HEINRICH HEINE
UNIVERSITÄT DÜSSELDORF

Protein interactions in living cells studied by multiparameter fluorescence imaging spectroscopy (MFIS)

Inaugural dissertation

for the attainment of the title of doctor
in the Faculty of Mathematics and Natural Sciences
at the Heinrich Heine University Düsseldorf

presented by

Qijun Ma

from Changchun, China

Düsseldorf, December 2015

from the institute for Physical Chemistry II
at the Heinrich Heine University Düsseldorf

Published by permission of the
Faculty of Mathematics and Natural Sciences at
Heinrich Heine University Düsseldorf

Supervisor: Prof. Dr. Claus A. M. Seidel
Co-supervisor: Prof. Dr. Rüdiger Simon

Date of the oral examination: 03 February 2016

Summary

Förster resonance energy transfer (FRET) is widely applied as a spectroscopic ruler to investigate the structures and interactions of labelled biomolecules exploiting its sensitivity to the distance. Multiparameter fluorescence image spectroscopy (MFIS) provides particular advantages to FRET imaging, because multiple fluorescence parameters can be monitored simultaneously with picosecond accuracy. In cellular studies, researchers performing image spectroscopy traditionally face the dilemma of either performing single point measurements or scanning a region of interest. Point measurements provide satisfactory photon statistics but at the expense of entirely relinquishing the image information; whereas imaging measurements contain the spatial information but with poor photon statistics in each pixel. With insufficient photon counts in FRET imaging, for example, the reason for a reduction in average donor fluorescence lifetime can hardly be assigned. The reduction can be caused by changes in FRET efficiency due to distinct protein-complex conformations, and/or changes in fraction of FRET-active species. To provide a solution to this long-standing dilemma, a novel workflow of generating population-specific pixel-integrated data for noise reduction and global analysis methods for a quantitative recovery of FRET parameters are introduced in this study. The newly developed MFIS-FRET analysis tools allow one to directly visualize and quantitatively analyze the fraction of FRET-active species and FRET efficiency. Using the determined fraction of FRET-active species and utilizing the intrinsic variations of protein concentration in each experiment, stoichiometry and dissociation constant of protein complexes can be characterized in living cells.

Characterization of the FRET efficiency enables detection of even subtle FRET variations and thus provides crucial information about the structural properties of molecular complexes. As also revealed in this study, fluorescent proteins in living cells have static majorly random distance distributions, thereby allowing for the distance estimation. Hence, the MFIS-FRET data can reach the quality of traditional *in vitro* cuvette experiments, which greatly facilitates the protein-interaction studies in living cells.

The newly developed MFIS-FRET methodology was employed in the research of membrane localized proteins: i) ligand-dependent receptor complex formation in plant cells, ii) oligomerization of guanylate binding proteins (GBPs) in murine embryonic fibroblasts (MEFs), and iii) oligomerization of G-protein coupled receptor (GPCR) in human cells. Several important and common features of proteins, such as homo- and heteromerization (i, ii and iii), changes in interaction dynamics triggered by outside stimuli, including peptide (i), pathogen (ii) and bile acid (iii), and clustering and aggregation (i and ii) are studied in detail.

i) Ligand-dependent receptor complex formation

MFIS-FRET was performed in individual living plant cells over time to study the initial interaction-events occurring at the receptor level following ligand perception for the two signaling pathways of the CLAVATA3 (CLV3) and flagellin (flg) peptides. The plant peptide CLV3 regulates stem cell homeostasis, whereas the bacterial flg22 peptide elicits defense responses. It shows that the CLV and the flg pathways represent two different principles of signal transduction: flg22 first triggered receptor-like kinase (RLK) heterodimerization, and later assembly into larger complexes through homomerization.

In contrast, CLV receptor complexes were preformed, and ligand binding stimulated their clustering.

ii) Oligomerization of murine GBPs (mGBPs) at membrane for pathogen defense

MFIS-FRET experiments are performed in uninfected and *Toxoplasma gondii* (*T. gondii*) infected MEFs, respectively, to determine the subcellular locations and concentrations of mGBPs, identify the interaction partners between the family members (mGBP1/2/3/5/6), and characterize their interaction affinities. The study shows that mGBPs can undergo concentration-dependent and species-specific oligomerization from monomeric to dimeric and oligomeric species. After the *T. gondii* invasion, mGBPs are recruited and thus highly enriched at the parasitophorous vacuole membrane, forming large, densely packed multimers comprising up to several thousand monomers.

iii) Oligomerization pattern of the membrane-localized G-protein coupled bile acid receptor TGR5

MFIS-FRET is performed on TGR5 wild type (wt) and its two variants, TGR5 Y111F and Y111A, to investigate TGR5 assembly, structure, and multimerization affinities in living cells. The study shows that all three variants form homodimers, however, only the TGR5 wt and Y111F variant are able to also form higher-order oligomers. The TGR5 Y111A variant dimerizes at an interface between transmembrane helix 1 (TM1) and helix 8, but is barred from oligomerization, likely because a clinically relevant mutation in TM5 markedly hinders its higher-order oligomerization.

In summary, this work demonstrates the unique advantages of the MFIS-FRET and new quantitative FRET analysis. The methodology introduced in this work allows one to investigate the spatiotemporally regulated protein interactions at a molecular resolution level. Researchers now can efficiently study protein localization, dynamics, concentration, aggregation, protein-complex formation, stoichiometry and binding affinity, and generate a panorama of proteins of interest in living cells.

List of Papers and Manuscripts

Chapter 2 Revealing structural features and affinities of protein complexes in living cells by MFIS-FRET analysis

Current status: manuscript in preparation

Qijun Ma, Marc Somssich, Stanislav Kalinin, Thomas-Otavio Peulen, Ralf Kühnemuth, Suren Felekyan, Yvonne Stahl, Rüdiger Simon, Stefanie Weidtkamp-Peters, Claus A.M. Seidel

- R.S., S.W.-P. and C.A.M.S. designed the research;
- Q.M. calibrated the experimental setup and performed the experiments;
- M.S. prepared the samples and performed the experiments;
- S.K. and S.F. developed the analysis software;
- T.-O.P. developed the simulation software;
- Q.M., M.S., T.-O.P., R.K., S.F., Y.S., R.S., S.W.-P. and C.A.M.S. analyzed and interpreted the data;
- Q.M., M.S., R.S., S.W.-P. and C.A.M.S. drafted and revised the manuscript.

AG Seidel in total: 65%					
Q.M.	S.K.	T.-O.P.	R.K.	S.F.	C.A.M.S.
30 %	5%	5%	5%	5%	15%

Chapter 3 Real-time dynamics of peptide ligand-dependent receptor complex formation in planta

Current status: published in “Science Signaling”

Marc Somssich, Qijun Ma, Stefanie Weidtkamp-Peters, Yvonne Stahl, Suren Felekyan, Andrea Bleckmann, Claus A.M. Seidel, Rüdiger Simon

- M.S., Q.M., S.W.-P., A.B., Y.S., R.S. and C.A.M.S. designed the research;
- M.S. and Q.M. performed the research;
- S.F. contributed new analytic tools;
- Q.M. and M.S. analyzed the data;
- M.S. and R.S. wrote the paper.

AG Seidel in total: 30%		
Q.M.	S.F.	C.A.M.S.
15%	5%	10%

Chapter 4 Guanylate binding proteins (GBPs) directly attack *T. gondii* via supramolecular complexes

Current status: published in "eLife"

Elisabeth Kravets, Daniel Degrandi, Qijun Ma, Thomas-Otavio Peulen, Suren Felekyan, Ralf Kühnemuth, Stefanie Weidtkamp-Peters, Claus A.M. Seidel, Klaus Pfeffer

- C.A.M.S. and K.P. designed the research;
- E.K., D.D., Q.M. and S.W.-P. performed the research;
- Q.M. and T.-O.P. performed the simulations;
- E.K., D.D., Q.M., T.-O.P., S.F., R.K., S.W.-P., C.A.M.S. and K.P. analyzed and interpreted the data;
- E.K., D.D., Q.M., S.W.-P., C.A.M.S., and K.P. drafted and revised the manuscript.

AG Seidel in total: 45%				
Q.M.	T.-O.P.	S.F.	R.K.	C.A.M.S.
19%	10%	5%	2%	9%

Chapter 5 Structural assemblies of the di- and oligomeric G-protein coupled receptor TGR5 in live cells: an MFIS-FRET and integrative modeling study

Current status: manuscript in preparation

Annemarie Greife, Suren Felekyan, Qijun Ma, Christoph G.W. Gertzen, Lina Spomer, Mykola Dimura, Thomas-Otavio. Peulen, Christina Wöhler, Dieter Häussinger, Holger Gohlke, Verena Keitel, Claus A.M. Seidel

- A.G., D.H, H.G., V.K. and C.A.M.S. designed the research;
- A.G., Q.M., L.S. and C.W. performed the experiments;
- C.G.W.G, M.D. and T-O.P. performed the computer simulation;
- A.G., S.F., Q.M., C.G.W.G, L.S., M.D., T.-O.P., H.G., V.K. and C.A.M.S. analyzed and interpreted the data;
- A.G., S.F., Q.M., C.G.W.G, L.S., M.D., T.-O.P., H.G., V.K. and C.A.M.S. drafted and revised the manuscript.

AG Seidel in total: 45%					
A.G.	S.F.	**Q.M.**	M.D.	T.-O.P.	C.A.M.S.
16%	8%	5%	4%	4%	8%

Contents

Chapter 1 General Introduction

1.1 Advantages of MFIS-FRET

Proteins, consisting of one or more long chains of amino acid residues, are the most versatile biological macromolecules in cells. They are essential players in the operations of life because they perform a huge array of functions within living organisms, such as cellular metabolism, transport, signaling, protection and defense against microorganisms, serving as building blocks and materials for energy storage in the body, etc. The spatiotemporally regulated interactions and assemblies of protein complexes constitute the foundation of multifarious cellular events. In this respect, protein-interaction research is a key research area in life science and medicine.

A plethora of biochemical assays, such as co-immunoprecipitation, protein microarray (MacBeath and Schreiber, 2000), surface plasmon resonance (Liedberg et al., 1983), mass spectrometry (Aebersold and Mann, 2003), were developed to detect protein interactions. However, most of these techniques only reflect the situation at the specific time point when the experiment is performed, thus the temporal resolution is limited; and they were not performed in the intact living cell, thus all spatial information is lost. For example, proteins originally localized in separate cellular compartments can be co-immunoprecipitated from cell lysate and generate false-positive results.

Fluorescence microscopy offers unique advantages for characterizing macromolecules under physiological conditions with high specificity and sensitivity. It benefits from the broad availability of fluorescent proteins (FPs) that can be genetically fused to the proteins of interest and report on protein dynamics without disturbing their functions (Prasher et al., 1992; Shaner et al., 2005; Shimomura et al., 1962; Tsien, 1998). Traditional far-field fluorescence microscopy alone, however, is intrinsically limited by optical resolution of ~200 nm, which is adequate to observe many cellular structures and compartments, but insufficient to disclose biomolecular interactions or structural features of individual molecules. Even for the latest super-resolution microscopy methodologies it is still challenging to achieve a resolution below 30 nm in cells (Betzig et al., 2006; Dickson et al., 1997; Grotjohann et al., 2011; Hell and Wichmann, 1994; Rust et al., 2006). Förster resonance energy transfer (FRET), on the other hand, is capable of reporting distance information (R_{DA}) between donor (D) and acceptor (A) fluorophores (Förster, 1948) below 15 nm. Hence it is an excellent technique that provides complementary information to fluorescence microscopy. FRET has been successfully employed as a 'spectroscopic ruler' (Stryer and Haugland, 1967) with molecular resolution to document biomolecule proximities occurring on the nm and sub-nm scale, such as protein-nucleic acid interactions (Rothwell et al., 2003), molecular motors motion (Rice et al., 1999), protein folding (Schuler and Eaton, 2008) or enzyme-substrate interactions (Ha et al., 1999). FRET imaging, combining the merits from both, FRET and fluorescence microscopy, can discern biological events at a molecular level while providing temporal and spatial information within the subcellular context, thereby greatly facilitating non-invasive studies of heterogeneous biological samples in living cells.

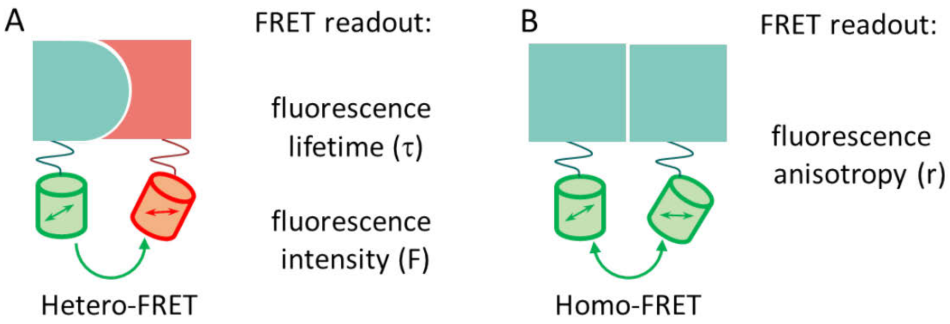

Figure 1-1 Sketch of Hetero-FRET and Homo-FRET modalities. Hetero-FRET occurs between distinct FPs, for example, from GFP (green) to mCherry (red). Homo-FRET occurs between identical FPs. The arrows inside the FPs depict their transition dipole moments.

As illustrated in Figure 1-1, FRET imaging experiments can adopt two modalities: In hetero-FRET imaging experiments one of the two putative interacting proteins is tagged with the donor FP (e. g. GFP), the other with the acceptor FP (e. g. mCherry) (Figure 1-1A). When the protein interaction occurs, their attached FPs come into close proximity inducing non-radiative energy transfer from the donor FP to the acceptor FP. Donor fluorescence intensity (F) will drop owing to the energy loss to the acceptor; and donor fluorescence lifetime (τ) will decrease as FRET adds an additional quenching pathway to depopulate the excited donor molecule (Lakowicz, 2006). In homo-FRET experiments, only one kind of FP is present (Figure 1-1B). Energy transfer among identical FPs does not alter their fluorescence intensity or lifetime, but it does reduce their fluorescence anisotropy (r) (Lakowicz, 2006). Hence, it is necessary to simultaneously record multiple fluorescence parameters in the study of heteromeric and homomeric protein interactions with FRET imaging.

Multiparameter fluorescence image spectroscopy (MFIS) (Kudryavtsev et al., 2006; Weidtkamp-Peters et al., 2009) provides particular advantages to FRET imaging because it allows monitoring multiple fluorescence parameters simultaneously. As empowered by pulsed laser excitation and time-correlated single photon counting (TCSPC) detection, MFIS can fully record eleven-dimensional information in parallel with picoseconds accuracy over time periods of hours. The eleven parameters are three spatial dimensions (x, y, z) and eight fluorescence parameters, namely fluorescence anisotropy, lifetime, intensity, detection time, excitation spectrum, emission spectrum, fluorescence quantum yield and distance between two fluorophores (Weidtkamp-Peters et al., 2009; Widengren et al., 2006). Registering the full information contained in a single experiment via MFIS therefore enables a thorough FRET analysis. Additionally, MFIS experiments permit other analyses to be employed if necessary, such as fluorescence correlation spectroscopy (FCS) (Sahoo and Schwille, 2011), fluorescence cross-correlation spectroscopy (FCCS) (Bacia and Schwille, 2007), raster image correlation spectroscopy (RICS) (Brown et al., 2008; Moens et al., 2010) or fluorescence intensity distribution analysis (FIDA) (Kask et al., 2000). The multidimensional readout of correlated changes in various parameters determined by these analyses maximizes the reliability of data interpretation. The economic use of photon information allows characterization of fluorescent fusion proteins that are expressed at very low levels. Therefore, MFIS-FRET is ideally suited to comprehensively investigate dynamic assemblies of heteromeric and homomeric protein complexes in living cells.

1.2 Challenges in data analysis

FRET imaging in principle allows the determination of structural and conformational features, as well as interaction affinities of molecular complexes in their natural cellular environment. The most frequently applied FRET analysis methods, however, miss to reveal all the information a dataset can provide. This is caused by the following four complications:

First, different molecular species are mixed together in FRET imaging experiments. The detection volume of a confocal microscope, typically ~200 nm in diameter, contains a mixture of proteins, belonging to either interacting or non-interacting molecular species. In consequence, changes in the FRET readout, for example a reduction in average donor fluorescence lifetime (τ) in a hetero-FRET experiment, could be due to changes in the FRET efficiency (E), and/or in the fraction of FRET-active species (x_{FRET}). To solve this ambiguity, analysis methods need to resolve different molecular species utilizing their distinct fluorescence properties. In homo-FRET analysis, both steady-state and time-resolved anisotropy are helpful indicators (Nguyen et al., 2012). The anisotropy values and decay patterns of different molecular species can be determined from control experiments or molecular simulations (Jares-Erijman and Jovin, 2003). In hetero-FRET analysis, both intensity-based and lifetime-based analysis methods are applicable. The latter is, however, superior to the former for two reasons: First, fluorescence lifetime is independent of the light path and molecule concentrations (Piston and Kremers, 2007). Second, intensity-based methods, such as measuring the ratio of donor and FRET-sensitized acceptor fluorescence F_D/F_A or the donor de-quenching by acceptor photobleaching (APB), require cumbersome instrument calibration. Therefore, lifetime-based methods are employed in MFIS-FRET analysis. But for traditional lifetime-based methods, it is still difficult to quantitatively resolve different molecular species and correctly assign the reasons for a reduction in τ.

Second, the fluorescence properties of both interacting and non-interacting molecular species are complex. Many donor FPs (e.g. GFP (Striker et al., 1999) and CFP (Tramier et al., 2002)) already show a bi-exponential fluorescence lifetime decay. The donor-acceptor species is more complex owing to its heterogeneous FRET distribution. Both N- and C-termini of a FP contain >10 amino acids that allow the FP to explore certain space around its host protein (Evers et al., 2006; Grünberg et al., 2013). Thus, FPs have countless conformations differing in donor-acceptor distances (R_{DA}) and relative dipole orientations (κ^2), which in the end translate into a broad distribution of FRET rate constants (k_{FRET}) that are difficult to determine. The lack of accurate fitting models describing such complex fluorescence decays of FPs in FRET-imaging experiments will lead to limited interpretations of a complex biological system.

Third, the orientation factor (κ^2) in FRET imaging experiments using FPs is unknown. Since the FRET rate constant (k_{FRET}) depends on both spatial distance (R_{DA}) and relative orientation (κ^2), to convert k_{FRET} to R_{DA}, the knowledge of κ^2 is required. For FRET experiments using organic dyes of small sizes (e.g. Atto488), the orientation factor in the dynamic averaging regime ($\langle\kappa^2\rangle = 2/3$) can be applied, because the orientations of donor and acceptor transition dipoles randomize by very fast rotation (~ps) before the donor emits fluorescence (~ns) (Hoi et al., 2013). However, bulky FPs undergo much slower rotation, of which the time scale (> 10 ns) can be even longer than the lifetime of the excited state in the presence of an acceptor (Hoi et al., 2013). It still remains unclear whether an average orientation factor can be applied to extract R_{DA} from k_{FRET}, and what that value should be.

Finally, the photon budget in living-cell experiments is very restricted. To increase photon counts, the excitation laser power can be increased or the measurement time can be extended, but both strategies may increase photo-bleaching (Cubitt et al., 1995), alter the photo-physical properties (e.g. fluorescence lifetime) of the FPs (Striker et al., 1999) and induce photo damage in cells by driving FPs into triplet state resulting in the production of reactive oxygen species (Goldman et al., 2010). Furthermore, increasing the laser power can result in severe detector saturation and the “pile-up” effect (Becker, 2005) once a certain photon count is reached. Enhancing the measurement time increases the risk of damaging the biological samples. Because of these limitations, only limited photon counts can be acquired from a single experiment in cells.

1.3 Outline of this thesis

To solve the complications involved in FRET imaging data analysis described in Section 1.2, Chapter 2 (titled “Revealing structural features and affinities of protein complexes in living cells by MFIS-FRET analysis”) provides a set of practical solutions. This chapter presents a new sub-ensemble global analysis method to dramatically improve the photon statistics, quantitatively determine FRET efficiency (E) and the fraction of FRET-active species (x_{FRET}), and thus maximally extract the information contained in a dataset. A novel illustration tool to directly visualize and resolve E and x_{FRET} is also introduced. With the newly developed analysis tools, Chapter 2 investigates the behavior of FPs in cells in detail. The study clarifies whether a FP is affected by other present biomolecules and cellular structures, and shows how to translate the quantitative FRET readouts into distance information. It also demonstrates the procedures of characterizing the stoichiometry and the dissociation constant of protein complexes. Therefore, the MFIS-

FRET data now can reach the quality of traditional *in vitro* cuvette experiments, which greatly facilitates the protein-interaction studies in living cells.

The newly developed MFIS-FRET methodology was employed in the research of membrane localized proteins: i) ligand-dependent receptor complex formation in plant cells (Chapter 3), ii) oligomerization of guanylate binding proteins (GBPs) in murine embryonic fibroblasts (MEFs) (Chapter 4), and iii) oligomerization of G-protein coupled receptor (GPCR) in human cells (Chapter 5). Several important and common features of proteins, such as homo- and heteromerization (i, ii and iii), changes in interaction dynamics triggered by outside stimuli, including peptide (i), pathogen (ii) and bile acid (iii), and clustering and aggregation (i and ii) are studied in detail.

Chapter 3 (titled “Real-time dynamics of peptide ligand-dependent receptor complex formation in planta”) presents a FRET study of the initial interaction events that occurred at the level of membrane receptors of two signaling pathways in living plant cells. One is the flagellin (flg) pathway, which initiates plant defense response in the presence of the bacterial peptide elicitor flg22 (Felix et al., 1999). The flg pathway involves the receptor FLAGELLIN-SENSITIVE 2 (FLS2) and its known coreceptor BRI1-ASSOCIATED KINASE 1 (BAK1) (Chinchilla et al., 2007; Felix et al., 1999). The rapid ligand-induced interaction between BAK1 and FLS2 upon perception of flg22 has been shown previously with conventional biochemical methods (Chinchilla et al., 2007; Schulze et al., 2010), and thus it serves as a test system for MFIS to unravel the assembly dynamics of plant receptor complexes in cells. The other pathway under study is the CLAVATA (CLV) pathway, which regulates plant stem cell homeostasis and involves the plant peptide CLV3, the receptor-like kinase (RLK) CLV1, the receptor-like protein CLV2 and the protein kinase CORYNE (CRN) (Brand et al., 2000; Clark et al., 1995, 1993; Fletcher et al., 1999; Kayes and Clark, 1998; Müller et al., 2008). Most of the previous studies on CLV-receptor-interactions only provided a static view on the capacity of the receptors to undergo molecular interactions (Bleckmann et al., 2010), or rely on genetic data (Müller et al., 2008). The study shown here is performed at the plasma membrane in individual living plant cells and in response to peptide treatment over time, thereby providing a higher spatial and temporal resolution of the interaction states of the receptors. The time-series experiments and the quantitative MFIS-FRET analysis enabled the simultaneous detection of changes in protein concentration and both homomeric and heteromeric interactions between the receptors with pixel-wise resolution, which allows one to compare the distinct work principles that the two signaling pathways adopt.

Chapter 4 (entitled "Guanylate binding proteins (GBPs) directly attack *T. gondii* via supramolecular complexes") presents a research on the subcellular localization, local concentration, homo- and hetero-multimerization, and interaction affinities of murine GBPs (mGBP1/2/3/5/6) in live murine embryonic fibroblasts (MEFs). This chapter also shows the impact of the parasite invasion on the localization and the molecular organization of mGBPs. GBPs are part of the dynamin superfamily, whose members are considered as universal membrane tubulation and fission molecules (Praefcke and McMahon, 2004). GBPs belong to the class of interferon-γ (IFNγ) induced effector molecules that combat intracellular bacteria and parasites (MacMicking, 2012). It was reported that mGBPs are essential for immunity against intracellular pathogens, especially for *Toxoplasma gondii* (*T. gondii*) control (Degrandi et al., 2007). To unravel the intricate host-pathogen interplay between *T. gondii* and the mGBPs (MacMicking, 2012; Praefcke and McMahon, 2004) in live murine embryonic fibroblasts (MEFs), a novel approach combining MFIS-FRET with mutational analyses and live cell imaging is employed.

To facilitate rational drug design, Chapter 5 (titled “Assemblies of the G-protein coupled receptor TGR5”) investigates TGR5 (GPBAR-1, M-BAR) oligomerization pattern, identifies the dimer and oligomer interfaces, and characterizes TGR5 multimerization affinities in living cells. G-protein coupled receptors (GPCRs) in general have received great attention due to their importance as receptors for almost half of all medicinal drugs (Gurevich and Gurevich, 2008; Kaczor et al., 2013; Lagerström and Schiöth, 2008; Maurel et al., 2008; Moreira, 2014; Overington et al., 2006; Terrillon and Bouvier, 2004). TGR5 is the first identified G-protein coupled bile acid receptor (Kawamata et al., 2003), and recently, it has been identified as a potential therapeutic target to treat metabolic disorders (Cao et al., 2013; Choi et al., 2012). However, no high-resolution crystal structure of TGR5 is available to date, knowledge on TGR5 regulation and oligomerization is scarce, and there are controversial data concerning the functional significance of oligomerization for class A GPCRs such as TGR5 (Ferre et al., 2014). This chapter proposes a model of TGR5 assembly that enlarges the knowledge of chemokine receptor structure, oligomerization and activation, and can have implications for drug development and screening.

Chapter 2 Revealing structural features and affinities of protein complexes in living cells by MFIS-FRET analysis

Authors: Qijun Ma[1], Marc Somssich[2], Stanislav Kalinin[1], Thomas-Otavio Peulen[1], Ralf Kühnemuth[1], Yvonne Stahl[2], Rüdiger Simon[2,3], Stefanie Weidtkamp-Peters[3*], Claus A.M. Seidel[1,3*]

Affiliations:

[1]Chair for Molecular Physical Chemistry, Heinrich Heine University, Düsseldorf, Germany.

[2]Institute for Developmental Genetics, Heinrich Heine University, Düsseldorf, Germany.

[3]Center for Advanced Imaging, Heinrich Heine University, Düsseldorf, Germany.

*Corresponding authors: Claus A.M. Seidel, Stefanie Weidtkamp-Peters

2.1 Introduction

In living cells, FRET microscopy is a widely-used technique to study interactions between biomolecules labeled with a donor and an acceptor, respectively (Laptenok et al., 2014; Somssich et al., 2015; Sun et al., 2011). In view of the current progress in super-resolution microscopy (Betzig et al., 2006; Dickson et al., 1997; Hell and Wichmann, 1994; Rust et al., 2006), the combined merits of FRET and confocal or wide-field microscopy techniques, in principle, allows one to achieve molecular resolution below 10 nm for studying protein complexes (Bonomi et al., 2014), while simultaneously providing spatial and temporal information. A catalog of methods for determining FRET, including ratiometric FRET, acceptor photobleaching FRET (abFRET), FRET-FLIM (fluorescence lifetime imaging microscopy), etc. are summarized in ref (Jares-Erijman and Jovin, 2003). Lifetime-based methods are significantly more robust in that the fluorescence lifetime (τ) measures the slope of a fluorescence decay ($f(t)$) and is independent of light path, molecule concentration and fluorescence intensity.

In FRET-FLIM, however, a reduction in an average τ can be caused by variations in the FRET efficiency (E) and/or in the fraction of FRET-active complexes (x_{FRET}). Biological samples are mostly heterogeneous and thus they may differ in both E and x_{FRET} which nevertheless give the same average τ. We demonstrate this drawback of traditional data analysis with two receptor complexes in living plant cells as an example (Figure 2-1): CORYNE (CRN) and CLAVATA2 (CLV2) versus CRN(del)kinase (CRNΔKi) and CLV2 (Bleckmann et al., 2010). Even with different molecule-complex geometries both experiments showed the same average lifetime (Figure 2-1), with one having fewer interacting molecules but compensating by shorter inter-label distance (CRNΔKi/CLV2) and the other being contrariwise (CRN/CLV2).

Another problem in FRET imaging is the limited number of registered photon counts. Imaging measurements provide spatial information in cells but has poor photon statistics in each pixel. Performing single point can improve the photon statistics but at the expense of entirely relinquishing the image information. Multiparameter fluorescence image spectroscopy (MFIS) suggested in (Weidtkamp-Peters et al., 2009) is the rescue to this dilemma. The precision and accuracy of data registration can be greatly boosted even with a restricted photon budget by operating a simultaneous eleven-dimensional signal recording (Figure 2-1), including eight fluorescence parameters (Widengren et al., 2006) and three optical dimensions (x, y, z) (Weidtkamp-Peters et al., 2009).

Here, we introduce an optimized MFIS global analysis workflow to achieve quantitative molecular description from FRET-FLIM data as from *in vitro* experiments (Figure 2-1). First, we applied statistically most efficient maximum likelihood estimator (MLE) to obtain multiple fluorescence parameters in each pixel (Kudryavtsev et al., 2006; Stahl et al., 2013; Weidtkamp-Peters et al., 2009). Then we displayed the 2D-histogram of two FRET indicators, green/red intensity ratio ($S_{G,G}/S_{R,G}$) versus donor fluorescence lifetime ($\langle\tau_D\rangle_f$) to identify and select individual pixel population (Weidtkamp-Peters et al., 2009). In the key step of the workflow, we integrated the photon counts from the selected sub-ensemble of pixels. This drastically improved photon statistics, so that the imaging data could be subjected to a very detailed and quantitative FRET analysis.

We introduce a graphical tool that can immediately illustrate and separate E and x_{FRET} of a FRET experiment. This approach is model-free and requires no fitting procedures. We applied it first to the study of FRET in a simple fusion protein expressed in living cells, which consists only of a tandem of GFP and mCherry (GFP-mCherry). Such a fusion protein is a prototype of many FRET-based biosensors (Boersma et al., 2015; Campbell, 2009) and thus has been extensively studied (Albertazzi et al., 2009; Millington et al., 2007; Tramier et al., 2006). Using this fusion protein as model system, we established a more comprehensive and appropriate fit model to quantify E and x_{FRET}.

Then we applied the analysis method in intermolecular-FRET studies, and showed that structural properties, stoichiometry and interaction affinities of a molecular complex can be quantitatively characterized *in planta*. We tested it on a total of 18 different samples and verified its general applicability on FRET-FLIM data to reveal the embedded information that traditional methods could not deliver.

The software for all the analysis procedures in the workflow is available at http://www.mpc.hhu.de/software.

2.2 Results

2.2.1 MFIS 2D-histogram unambiguously reveals FRET

As a starting point we studied FRET in a GFP-mCherry fusion protein in living plant tissue. The GFP-mCherry fusion and, as the reference, GFP alone were expressed in leaves of *Nicotiana benthamiana* (Section 2.4.1). In each recorded MFIS image, pixels containing at least 40 photons were processed with the established fitting protocol (Kudryavtsev et al., 2006; Stahl et al., 2013; Weidtkamp-Peters et al., 2009) (Section 2.4.3). For both experiments, we plotted the pixel-wise 2D frequency histogram of the two FRET indicators: $S_{G,G}/S_{R,G}$ versus $\langle\tau_D\rangle_f$ (Figure 2-2A). The subscript of $S_{G,G}$ or $S_{R,G}$ denotes green or red detection (first G or R) under green (second G) excitation. Via these two indicators, different pixel populations appear on different locations on the 2D-histogram (Sisamakis et al., 2010) (Figure 2-2A). The displacement of the GFP-mCherry pixel population to a lower $S_{G,G}/S_{R,G}$ and a shorter $\langle\tau_D\rangle_f$ is a visible hallmark for FRET. Photon counts from the pixels belonging to the same population can be integrated in one decay histogram as sub-ensemble data and analyzed together. Figure 2-2B compares the normalized donor fluorescence decays of the FRET ($f_{mix}(t)$) and the donor-only ($f_{(D,0)}(t)$) sub-ensembles in Figure 2-2A, in which the steeper slope of $f_{mix}(t)$ indicates FRET-induced donor quenching.

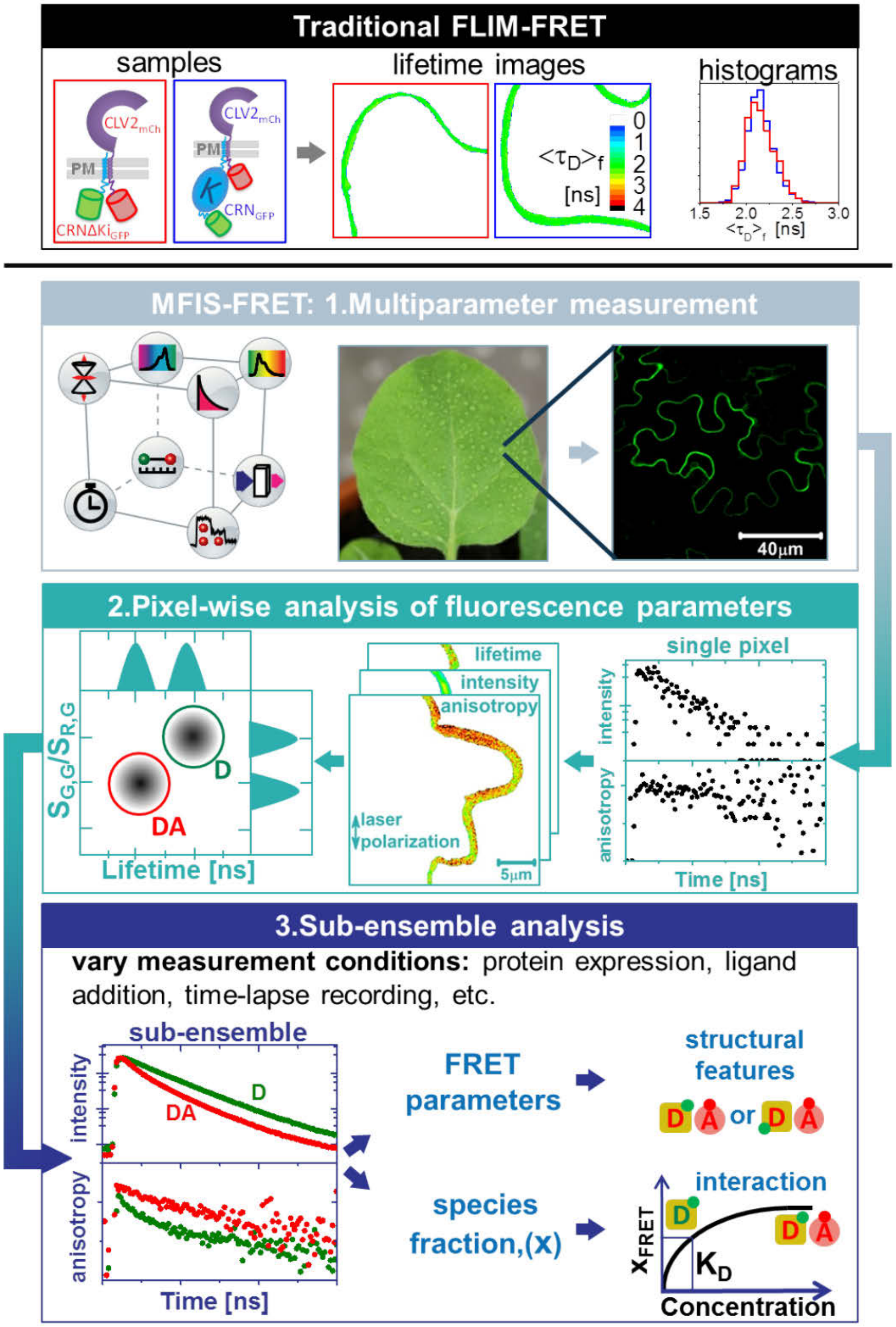

Figure 2-1 Maximal extraction of the information in FRET-imaging data by an optimized analysis workflow. Traditional methods deliver the same fluorescence lifetime readout for different protein interactions. For the two exemplary samples (CRNΔKi$_{GFP}$/CLV2$_{mCh}$ and CRN$_{GFP}$/CLV2$_{mCh}$), average fluorescence lifetime of both images is 2.16 ns The new workflow which is briefly described in 'Introduction' and will be shown in detail in later sections enabled us to infer the structural properties, molecular stoichiometry and interaction affinities of molecular complexes in living cells.

2.2.2 Visualization and recovery of FRET parameters in live cells

Comparing $f_{mix}(t)$ and $f_{(D,0)}(t)$ could only answer the basic question of whether FRET occurred or not. To directly and intuitively resolve the two main parameters of FRET-imaging data (E and x_{FRET}) without fitting, we introduce time-resolved FRET-specific donor quenching ($\varepsilon_{mix}(t)$) that directly displays the FRET parameters in a simple curve by computing the ratio between $f_{mix}(t)$ and $f_{(D,0)}(t)$. The resulting decay is typically comprised of both time-independent and dependent parts (Figure 2-2C).

As FRET is determined from the relative difference between FRET and donor-only samples, the latter is always indispensable, and thus it is essential to accurately describe its fluorescence decay in a fit model. Since most donor FPs (e.g. GFP) show a bi-exponential decay (Striker et al., 1999), the donor fluorescence decay $f_{(D,0)}(t)$ must be described by:

$$f_{(D,0)}(t) = \sum_{m=1}^{2} x_{D0}^{(m)} \cdot \exp(-t \cdot k_{D0}^{(m)}) \tag{2-1}$$

with the normalized donor species fraction, $x_{D0}^{(m)}$ $(\sum_{m=1}^{2} x_{D0}^{(m)} = 1)$, and the two (m = 2) donor decay rate constants, $k_{D0}^{(m)}$. These parameters can be pre-determined from donor-only reference samples and set as global restraints in the subsequent FRET analysis.

In FRET samples, FRET adds an additional quenching pathway with rate constant k_{FRET}. Due to the unstructured and flexible amino acids at the N- and C-termini of both FPs (PDB ID: 4EUL and 2H5Q) (Evers et al., 2006; Grünberg et al., 2013), the fusion protein has multiple conformations, which gives rise to multiple (l) FRET species (Vogel et al.,

2012) each with normalized fraction $x_{FRET}^{(l)}$ ($\sum_l x_{FRET}^{(l)} = 1$) and FRET rate constant, $k_{FRET}^{(l)}$. Since the two fluorescence species of GFP have almost the same emission spectrum (Jung et al., 2005; Striker et al., 1999) and the same distance to any nearby acceptor chromophore, the two donor lifetimes are quenched by associated FRET rates. Therefore, the donor fluorescence decay of the FRET-active species $f_{(D,A)}(t)$ is described as:

$$f_{(D,A)}(t) = \left(\sum_l x_{FRET}^{(l)} \exp\left(-t \cdot k_{FRET}^{(l)}\right) \right) \cdot f_{(D,0)}(t) \tag{2-2}$$

The ratio between $f_{(D,A)}(t)$ and $f_{(D,0)}(t)$ allows us to extract the FRET-induced donor quenching decay, $\varepsilon_{(D,A)}(t)$, from the fluorescence decay $f_{(D,A)}(t)$ (Förster, 1949; van der Meer et al., 1993), which is very convenient in graphically displaying the FRET features of the sample:

$$\varepsilon_{(D,A)}(t) = \frac{f_{(D,A)}(t)}{f_{(D,0)}(t)} = \sum_l x_{FRET}^{(l)} \exp\left(-t \cdot k_{FRET}^{(l)}\right),$$

$$\text{with } E = 1 - \frac{\int f_{(D,A)}(t)dt}{\int f_{(D,0)}(t)dt} \tag{2-3}$$

The steady-state FRET efficiency (E) of the FRET-active species, which is a key parameter in FRET data evaluation, can be determined via $\varepsilon_{(D,A)}(t)$ (Eq. (2-3) and Eq. (2-5)). Note that this procedure is equivalent to a global analysis of $f_{(D,0)}(t)$ (Eq. (2-1)) and $f_{(D,A)}(t)$ (Eq. (2-2)), which is used throughout this work for fitting the fluorescence decays (Section 2.4.4).

Another complication of FRET samples is that each pixel may consist of a mixture of FRET-active ($f_{(D,A)}(t)$) and inactive ($f_{(D,0)}(t)$) molecular species. Thus the donor fluorescence decay ($f_{mix}(t)$) has contributions from both molecular species. Consequently, the FRET-induced donor decay ($\varepsilon_{mix}(t)$-decay) of $f_{mix}(t)/f_{(D,0)}(t)$ consists of two parts:

$$\varepsilon_{mix}(t) = \frac{f_{mix}(t)}{f_{(D,0)}(t)} = \frac{x_{FRET}\, f_{(D,A)}(t) + (1 - x_{FRET})\, f_{(D,0)}(t)}{f_{(D,0)}(t)} = x_{FRET}\; \varepsilon_{(D,A)}(t) + (1 - x_{FRET}), \tag{2-4}$$

with $x_{FRET} = x_{(D,A)} - x_{NoFRET}$

Considering that a fraction of donor-acceptor complexes can have irresolvably low FRET efficiency (see Section 2.4.8 for details), and thus appears as FRET-inactive in experimental data, we denote such fractional contribution as x_{NoFRET}. The rest of the donor-acceptor complexes, $x_{(D,A)}$, is FRET-active (x_{FRET}). The time-dependent part $\varepsilon_{(D,A)}(t)$ displays the FRET, a steep or gentle decay slope denoting a large or small k_{FRET} (or E) respectively. A complex decay as in Figure 2-2C indicates a heterogeneous FRET distribution. The amplitude of $\varepsilon_{(D,A)}(t)$, which is the drop in a $\varepsilon_{mix}(t)$-diagram, gives the FRET-active species fraction (x_{FRET}) and is usually < 1 in FRET-imaging data.

Moreover, like time-resolved intensity decays, $\varepsilon_{mix}(t)$ can be subjected to phasor display (Figure 2-2D), then all the properties of the fluorescence-lifetime phasor (Digman et al., 2008) apply to the FRET phasor as well. The full range of FRET (0 - 100%) can be mapped into the phasor plot. If the $\varepsilon_{(D,A)}(t)$ of a $\varepsilon_{mix}(t)$-histogram contains only a single k_{FRET}, it will lie on the semicircle (open circles, in magenta); if more than single k_{FRET} is present, it will locate inside the semicircle (Digman et al., 2008). As an example, Figure

2-2D (red diamond) shows the location of the data in Figure 2-2B and 2-2C on the FRET phasor plot (see Section 2.4.6 for details).

We applied the quantitative model function (Eq. (2-1) - (2-4), Section 2.4.4) to the experimental data shown in Figure 2-2B. Initially only one k_{FRET} was included (i.e. $l = 1$) in Eq. (2-1) considering that the photon count is rather limited. This 1-k_{FRET} fit model mathematically assumes a unique donor-acceptor conformation in sub-ensemble data. It resulted in large correlated residuals (Figure 2-2B, in gray) indicating that the model could not fully describe the data. Next, 2-k_{FRET} fit model (l = 2) was tested and the fitting quality significantly improved (Figure 2-2B, in dark cyan). Even though a heterogeneous k_{FRET}-distribution was expected in sub-ensemble FRET-imaging data, due to the limited photon counts acquired in a typical *in vivo* experiment, the k_{FRET}-distribution in FRET-imaging data can be approximated by two discrete k_{FRET}, which is generally true for Gaussian-like distributions. It raises the question of how to further infer molecular properties with the quantified FRET parameters with this model.

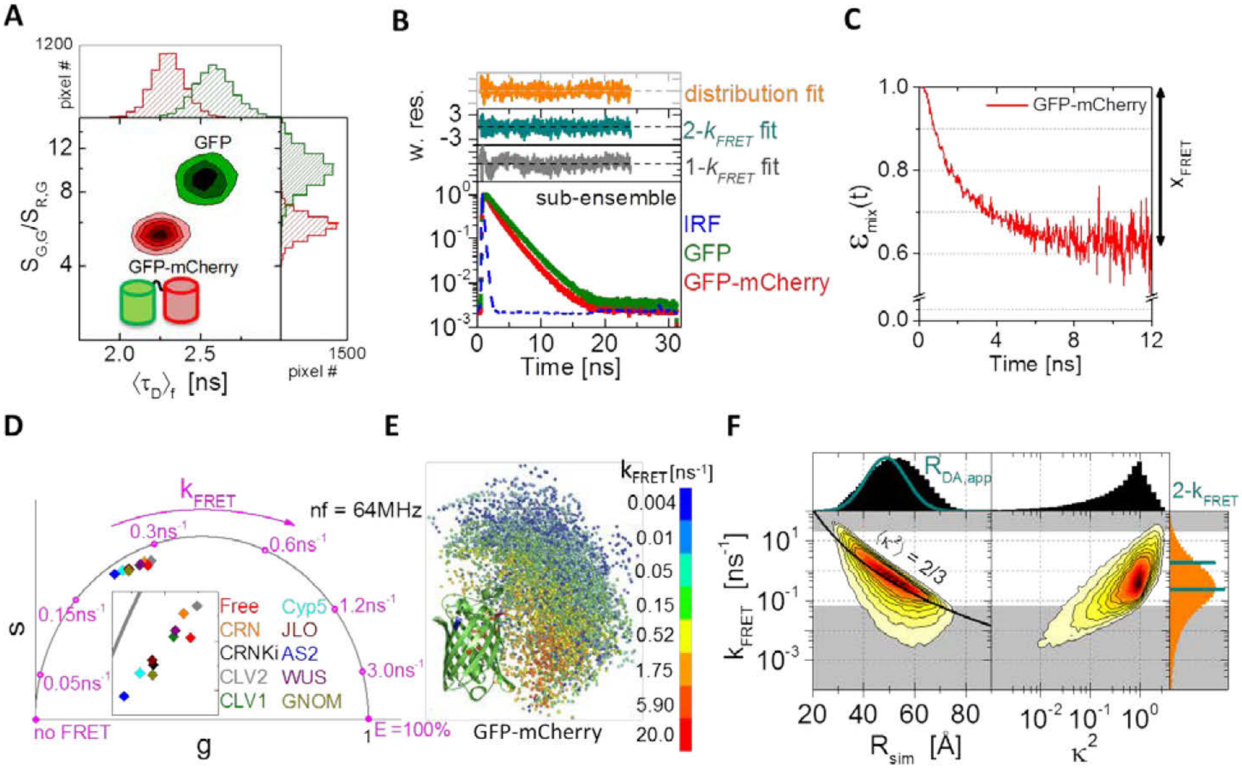

Figure 2-2 Comprehensive characterizations of FRET-FLIM data. (**A**) Two representative experiments of donor-only (GFP) and FRET (GFP-mCherry) samples are well separated on a MFIS 2D-histogram plotting two FRET indicators: $S_{G,G}/S_{R,G}$ versus $\langle\tau_D\rangle_f$. (**B**) Fitting the sub-ensemble fluorescence decay containing 3.96×10^6 photons of the GFP-mCherry experiment (**A**, in red) with 1-k_{FRET} (Eq. (2-1) - (2-4) with $l = 1$), 2-k_{FRET} (Eq. (2-1) - (2-4) with $l = 2$) and k_{FRET}-distribution (Eq. (2-1) - (2-4) with $\varepsilon_{(D,A)}(t)$ as obtained from Monte Carlo simulation, see below) models resulted in reduced chi^2 χ_r^2 = 1.41 (in gray), 1.03 (in dark cyan) and 1.08 (in orange) respectively. Pre-determined donor lifetime parameters were set as global restraints in all fits: $x_{D0}^{(1)}$ = 0.854, $x_{D0}^{(2)}$ = 0.146, $\tau_{D0}^{(1)}$ = 2.747 ns, $\tau_{D0}^{(2)}$ = 1.526 ns. Parameters obtained from the 1-k_{FRET} fit were x_{FRET} = 0.303 and k_{FRET} = 0.556 ns^{-1}; from the 2-k_{FRET} fit: x_{FRET} = 0.392, $x_{FRET}^{(1)}$ = 0.561, $x_{FRET}^{(2)}$ = 0.439, $k_{FRET}^{(1)}$ = 0.225 ns^{-1} and $k_{FRET}^{(2)}$ = 1.765 ns^{-1}; and from the k_{FRET}-distribution fit using the distribution in **F** and in Figure 2-7: $x_{(D,A)}$ = 0.652. (**C**) Plotting $\varepsilon_{mix}(t)$ diagram with the two normalized fluorescence decays of both sub-ensembles in **A** directly visualizes the fraction of FRET-active species (arrow) and FRET features. (**D**) $\varepsilon_{mix}(t)$ can be subjected to phasor display (FRET phasor). Difference in location shows difference in FRET. (**E**) Side view of a representative subset of GFP-mCherry

conformations sampled in the MC molecular simulation aligned according to GFP. Each mCherry is represented by a sphere pinpointing the middle position of its transition dipole moment. Each sphere is colored according to the k_{FRET} of that conformation. For GFP, only the beta-barrel which was kept rigid in the simulation is depicted, and the region colored in blue indicates its N-terminus side, in magenta indicates its C-terminus side. (**F**) With all the sampled conformations, dependence of k_{FRET} on R_{sim} (left panel) and on κ^2 (right panel) is plotted. The minimum and maximum R_{sim} in the simulation were 21.8 Å and 89.3 Å respectively. On the left panel, the overlaid curve in black assumes that the Förster radius between GFP and mCherry is 52 Å, unquenched GFP fluorescence lifetime is 2.6 ns and $\langle\kappa^2\rangle$ is 2/3. Areas tinted in gray indicate two time-ranges where k_{FRET} becomes irresolvable from typical experimental data (Section 2.4.8); in between is the experimentally resolvable range ($0.067\ ns^{-1} < k_{FRET} < 20\ ns^{-1}$). The two lines (in dark cyan) on the right-most panel represent the two fitted $k_{FRET}^{(l)}$ from the 2-k_{FRET} fit and their lengths are plotted in proportion to their fractions, $x_{FRET}^{(l)}$ (see the legend of (**B**)). In the upper-left panel, the $R_{DA,app}$-distribution reconstructed using the fit results from the 2-k_{FRET} model (Section 2.4.4) is overlaid with the R_{sim}-distribution.

2.2.3 Can FRET-imaging with FPs report distances *in vivo*?

To obtain molecular understandings from FRET imaging with FPs, first of all, one needs to be assured that FPs in living cells are not preferentially oriented, otherwise the observed FRET will not provide any geometry information of the host protein complex. We investigated the orientation of FPs in two different ways.

First, we examined whether the experimentally observed FRET in a GFP-mCherry fusion protein agreed with what Monte Carlo (MC) simulation of mobile fusion FPs predicted (a similar simulation method as employed in (Chiang et al., 2006; Drinkwater et al., 2014; Hunt et al., 2012; Miranda et al., 2013), Section 2.4.9 and Figure 2-7). In the MC simulation, the two beta-barrel structures in a GFP-mCherry fusion protein were kept as rigid bodies, while their interconnecting unstructured amino acid chain (28aa) were treated as a flexible chain that allowed the fusion protein to freely sample its conformational space. We applied the obtained k_{FRET}-distribution of GFP-mCherry fusion protein (Figure 2-7 and Figure 2-2F, right-most panel, in orange) to fit the experimental dataset displayed in Figure 2-2B. The pre-determined donor lifetimes (see legend of Figure 2-2B) and the k_{FRET}-distribution (i.e. $\varepsilon_{(D,A)}(t)$) were set as invariant restraints, only the fraction of donor-acceptor complex ($x_{(D,A)}$) was allowed to vary. The experimental data could be described very well by the k_{FRET}-distribution obtained from the MC simulation (Figure 2-2B, residuals in orange), suggesting that the FPs in the experiments were mobile as well. We found that the fraction of donor-acceptor complexes ($x_{(D,A)}$ in Eq. (2-4)) was 65%, thus about 35% of GFP-mCherry molecules exhibited non-FRET in the experiment, most likely owing to the presence of dysfunctional mCherry acceptors in cells. This percentage was in the same range as the 25 ± 5% (mean ± s.e.) that was later found in an independent set of intermolecular FRET experiments (discussed later, Figure 2-5B).

Second, we attached GFP-mCherry fusion to different host proteins (Host $_{\text{GFP-mCherry}}$) localizing in various cellular compartments and examined whether the FPs would be trapped in various cellular environments and therefore have largely distinct FRET features. As indicated by their close locations on the FRET phasor plot (Figure 2-2D), all the tested fusion constructs exhibited similar FRET features with only subtle variations. Such variations among them were caused by different excluded volumes (Lasker et al., 2010) of their individual host proteins. Thus, these experiments did not show interactions between FPs and their local environments.

We conclude that the random orientations of FPs conferred by their flexible N- and C-termini are not disrupted by cellular environment; hence FRET-imaging experiments with FPs are able to probe structural properties of biomolecules.

2.2.4 How to overcome the κ^2 problem in FRET imaging?

Clearly, the next step was to convert the FRET rate constants quantified with the 2-k_{FRET} model to donor-acceptor distances (R_{DA}). Such procedures required the knowledge of orientation factor (κ^2) in FRET imaging.

This information could be drawn from the MC molecular simulation. The left panel in Figure 2-2F plots the dependence of k_{FRET} on donor-acceptor distance (R_{sim}), overlaid with a function curve assuming the dynamic averaged κ^2 ($\langle\kappa^2\rangle = 2/3$). Although individual donor-acceptor conformations had random orientations, all the conformations if viewed as an ensemble overall followed the trend of the overlaid curve. It suggested that $\langle\kappa^2\rangle$ can be applied to sub-ensemble data to recover distance information. This theory was then tested with the experiments of GFP-mCherry fusion protein.

We converted the two fitted k_{FRET} from the sub-ensemble 2-k_{FRET} analysis (Figure 2-2F, right-most panel) to two apparent distances ($R_{DA,app}$) using $\langle\kappa^2\rangle = 2/3$, and then reconstructed a Gaussian-shape $R_{DA,app}$-distribution (Figure 2-2F, upper-left panel; Section 2.4.4). We found that the mean distance $\langle R_{DA,app}\rangle$ was 48.9 ± 1.8 Å (mean ± s.d., n = 16) in very good accordance with the 50.8 Å predicted by the MC simulation. But since only two k_{FRET} values could be directly recovered from experimental data, the width of the distance distribution ($w_{DA,app}$) was narrower than that in the MC simulation. According to the MC simulation, the fraction of FRET-inactive donor-acceptor complexes

(x_{NoFRET}) is 0.32 (Eq. (2-4); see Section 2.4.8 and 2.4.10 for details); and from the 2-k_{FRET} fit, that of FRET-active donor-acceptor complexes (x_{FRET}) is determined as 0.39 (Eq. (2-4), Figure 2-2B). Thus the total fraction of donor-acceptor complexes ($x_{(D,A)}$) in the GFP-mCherry experiment displayed in Figure 2-2B is 71% (Eq. (2-4)). The rest 29% of GFP-mCherry molecules indeed showed non-FRET owing to dysfunctional mCherries, highly consistent with the 35% according to the k_{FRET}-distribution fit (Figure 2-2B, in orange) and the 25 ± 5% (mean ± s.e.) in the intermolecular FRET experiments (Figure 2-5B). The different states of mCherry were also suggested in a previous study (Wu et al., 2009).

To summarize, analyzing sub-ensemble FRET-imaging data can handle the κ^2 problem and provides a convenient way to quantitatively approximate inter-fluorophore distances *in vivo*.

2.2.5 Testing the recovered distance distribution

The reliability of the recovered $R_{DA,app}$-distribution was tested using a set of FP-fusion constructs. We added a linker between both FPs (GFP-L(n)-mCherry) in addition to the 28 unstructured connecting amino acids, and the linker length was systematically varied (with n = 0, 8, 13 and 29). The FP-fusion constructs localized in the cytosol in plant cells. The same experiments were iterated with each fusion construct attached to a host protein, CLAVATA1 (CLV1), a membrane-localized receptor protein in plant cells.

As expected, the $\langle R_{DA,app} \rangle$ increased with lengthening the linker in both GFP-L(n)-mCherry and $\text{CLV1}_{\text{GFP-L(n)-mCherry}}$ experiments (Figure 2-3A). When the linker consists of only 0 or 8 amino acids, the $R_{DA,app}$-distributions of GFP-L(n)-mCherry and $\text{CLV1}_{\text{GFP-L(n)-mCherry}}$ were very similar with only subtle discrepancy coming from the excluded volume of the host protein CLV1, the same effect as shown in Figure 2-2D. Further lengthening the linker to 13 and 29 amino acids enlarged the accessible volume (AV) of the FPs, which might promote the impact from the surrounding protein domain and cellular environment respectively, and thus brought the difference between GFP-L(n)-mCherry and CLV1$_{\text{GFP-L(n)-mCherry}}$ to a larger extent. This observation suggests that to solely investigate the molecule complexes of interest, it is advisable to reduce undesirable external influences by shortening the linker length between a host protein and a FP.

From the above experimental and simulation studies on FP-fusion proteins, we conclude that the analysis workflow (Figure 2-1) using the 2-k$_{\text{FRET}}$ fit model (Eq. (2-1) - (2-4)) is able to correctly report and compare structure features of molecule complexes. Such essential information was embedded in all FRET-FLIM experiments but unattainable before.

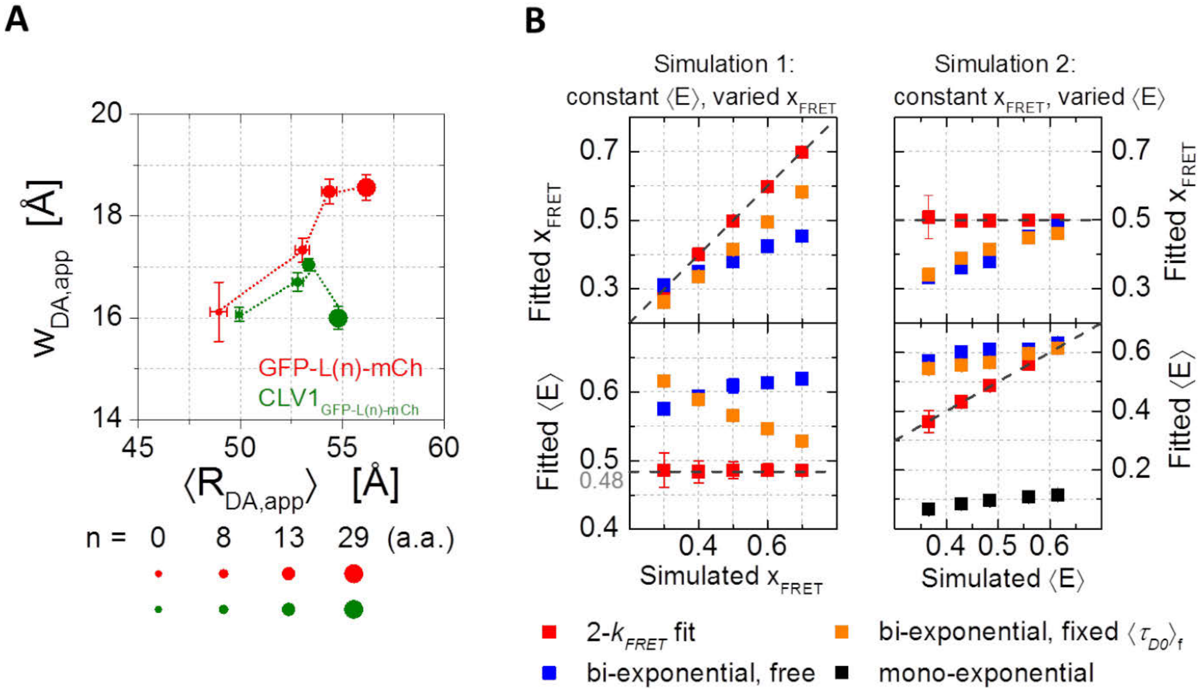

Figure 2-3 Influence of linker length and protein partner, and comparison of 2-k$_{\text{FRET}}$ fit to three traditional methods. (**A**) Systematically increasing the number of amino acids (n) in GFP-L(n)-mCherry and CLV1$_{\text{GFP-}}$

$_{\text{L(n)-mCherry}}$ result in longer $\langle R_{DA,app} \rangle$. The bars across the symbols indicate the standard error of the mean. Table 2-2 in Section 2.5.2 lists out all the FRET parameters determined from these experiments. (**B**) Simulations show that the 3 traditional models (Eq. (2-10) - (2-10) in Section 2.4.7) yield systematically deviated results in $\langle E \rangle$ and x_{FRET} from the simulated values (dashed lines). The bars across the symbols indicate the standard deviation. Section 2.5.3.3 details different simulated conditions. For each simulated condition 300 decay histograms each containing 3×10^6 photons were generated and fitted by the different models.

2.2.6 Quantitative comparison with traditional models for FRET-FLIM analysis

To quantitatively demonstrate the advantages of the 2-k_{FRET} model in properly recovering FRET parameters over traditional methods, we generated fluorescence decay histograms (Eq. (2-11)) and compared it with three models frequently applied in FRET-FLIM analyses via decay-histogram simulations: i) mono-exponential fit (Eq. (2-9)), the simplest model to determine the average fluorescence-weighted decay time ii) bi-exponential fit (Eq. (2-10)) with fluorescence lifetimes as fit parameters, which can resolve two lifetime species assigned as FRET-active and inactive respectively, and iii) bi-exponential fit (Eq. (2-10)) with pre-determined donor lifetime (an improved model of ii).

The simulations on the decay histograms were performed according to the three common complex characteristics shared by most FRET-FLIM data: 1) FRET-active and inactive molecular species coexist; 2) the decay of the latter is at least bi-exponential (Eq. (2-1)); and 3) the FRET feature of the FRET-active species can be formally described by two k_{FRET} as an approximation of a distribution. Such a multi-exponential model is given in Eq. (2-11) in Section 2.4.7. We systematically set the simulated conditions into two categories (Figure 2-3B): i) constant average FRET efficiency $\langle E \rangle$

(see Section 2.5.3.3) with varied FRET-active species fraction x_{FRET}, and ii) constant x_{FRET} with varied $\langle E \rangle$.

A total of 7 parameters (see Section 2.4.7 for details) need to be recovered in Eq. (2-11), which is impossible to directly obtain, given the limited fluorescence lifetime range and photon count. The 2-k_{FRET} model (Eq. (2-1) - (2-4)), however, globally analyzes the fluorescence decays of donor-only and FRET samples, therefore it reduces the number of fit parameters from 7 to 4 ($k_{FRET}^{(1)}, k_{FRET}^{(2)}, x_{FRET}$ and $x_{FRET}^{(1)}$) and properly recovers the FRET parameters.

In contrast, the three traditional models over simplify the fluorescence decay model, and thus lead to incorrect results in both categories of the simulated conditions (Figure 2-3B). It was most severe for the mono-exponential fit model (Figure 2-3B, black squares) as it does not resolve different molecular species. Both bi-exponential fit models (Figure 2-3B, blue and orange squares) suffered from the fact that donor fluorescence decay itself is bi-exponential. Thus the unquenched shorter donor-lifetime species was mixed with the longer donor-lifetime species quenched by FRET (Millington et al., 2007), which yielded incorrect results with deviations up to 30 % from the correct values (Figure 2-3B, dashed lines).

2.2.7 Application 1: Resolving protein complexes with different geometries by FRET

We applied the established workflow (Figure 2-1) to reanalyze the intermolecular-FRET experiments of the two membrane receptor complexes $CRN_{GFP}/CLV2_{mCh}$ and $CRN\Delta Ki_{GFP}/CLV2_{mCh}$ that the traditional mono-exponential analysis failed to distinguish between a change in E or x_{FRET} (Figure 2-1 and Figure 2-4A). In CRNΔKi (Figure 2-4A, lower panel), the kinase domain was deliberately removed, thus donor molecules are directly attached to the CRN transmembrane (TM) domain, therefore moving the donor molecules closer to the nearby acceptors attached to the intracellular side of the CLV2 TM domain.

The 2-k_{FRET} analysis (Figure 2-4B, black bars) proved that the mean apparent donor-acceptor distance ($\langle R_{DA,app} \rangle$) in CRNΔ$Ki_{GFP}$/CLV2$_{mCh}$ was indeed shorter than that in CRN_{GFP}/CLV2$_{mCh}$ (Figure 2-4B, dotted lines). The width of distance distribution ($w_{DA,app}$) in CRNΔKi_{GFP}/CLV2$_{mCh}$ was also narrower, possibly because the GFP was closer to the plasma membrane and therefore had a more confined accessible volume (AV).

To further reduce the number of fit parameters under limited photon budget, we imposed an additional restraint in the sub-ensemble analysis that the R_{DA}-distribution is a Gaussian distribution with a mean apparent distance $\langle R_{DA,app} \rangle$ and the width $R_{DA,app}$ (Section 2.4.4). This restraint is commonly employed in single-molecule FRET studies (Sisamakis et al., 2010) and also agreed with our MC simulation of FPs (Figure 2-2F, Figure 2-7). The fit results (Figure 2-4B, black dash lines) corroborated the conclusions drawn from the 2-k_{FRET} model. The mean distances determined with both models were in very good accordance; and as expected, with the Gaussian-distance model, a larger width was recovered (see the legend for Figure 2-4B). Additionally, for both receptor complexes we computed the R_{DA}-distributions (Figure 2-4B, histograms) by sampling the spatially allowed positions of the attached FPs (AV-simulations(Sindbert et al., 2011), Section 2.4.11). The AV-simulations recovered the experimental characterization to a great extent. To conclude, we can show that the donor-acceptor distance in the $\mathrm{CRN\Delta Ki_{GFP}/CLV2_{mCh}}$ is decreased by more than 10 Å.

Figure 2-4C (upper panel) plots the $\varepsilon_{mix}(t)$-diagrams of the two experiments shown in Figure 2-1. From the drop in each histogram one can immediately conclude that the $\mathrm{CRN\Delta Ki_{GFP}/CLV2_{mCh}}$ pixel population has a smaller x_{FRET}. Figure 2-4C (lower panel) isolates the FRET features ($\varepsilon_{(D,A)}(t)$) obtained from the 2-k_{FRET} analysis. The steeper slope for $\mathrm{CRN\Delta Ki_{GFP}/CLV2_{mCh}}$ indicates the higher FRET efficiency (Figure 2-4D), and thus shorter donor-acceptor distances between the attached FPs. Hence, the apparent similarity of the two traditional lifetime images (Figure 2-1), in fact, was caused by the compensating effect between E and x_{FRET}. Using the characteristic FRET efficiencies, we further quantified x_{FRET} in each pixel by a FRET pattern fit (Section 2.4.5). In contrast to a deceiving τ-histogram, the x_{FRET}-histogram (Figure 2-4E) directly displays the biologically relevant information as it reports the abundance of interacting complexes.

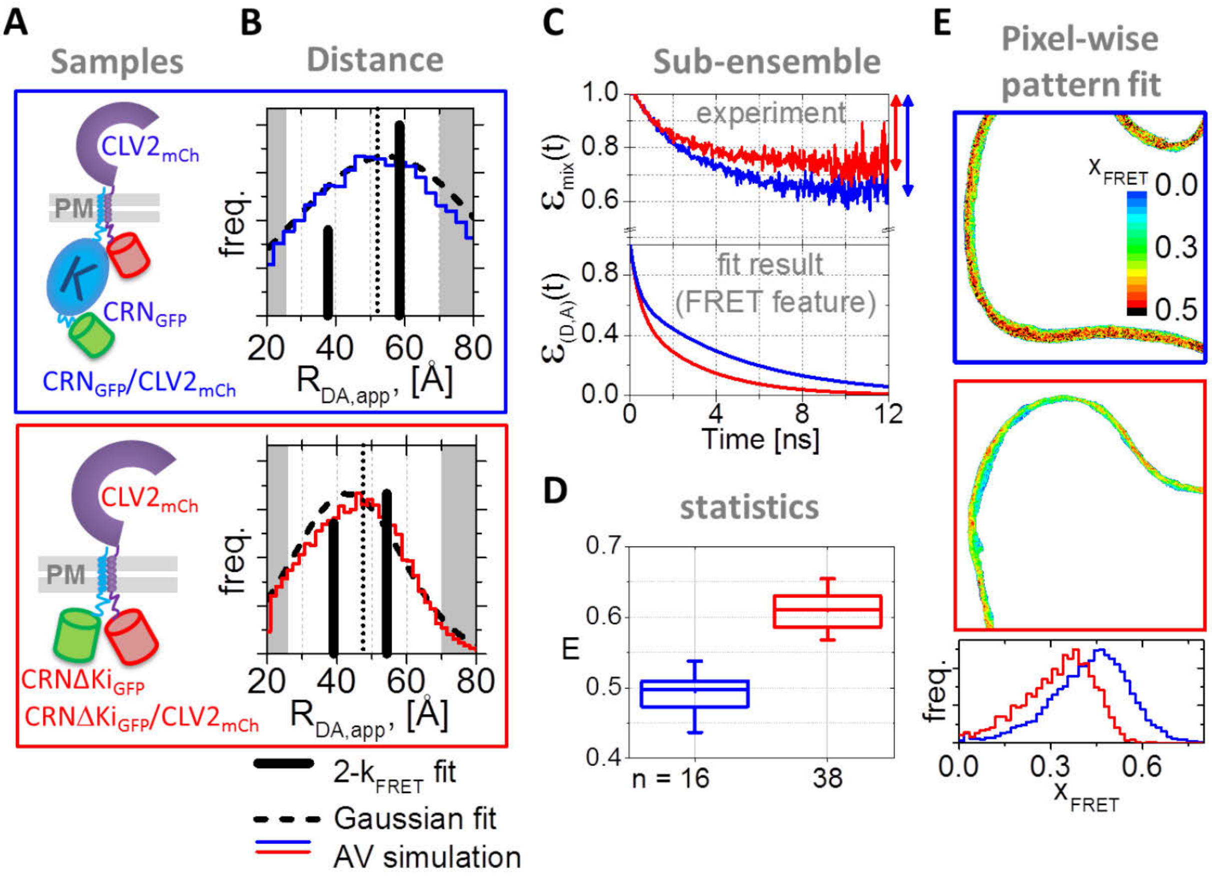

Figure 2-4 MFIS-FRET analysis resolves geometry differences between CRN/CLV2 and CRNΔKi/CLV2. (**A**) Molecular sketch of CRN$_{GFP}$/CLV2$_{mCh}$ (upper) and CRNΔKi$_{GFP}$/CLV2$_{mCh}$ (lower). (**B**) The areas tinted in gray mark the experimentally-irresolvable R_{DA}-ranges (beyond 27 – 70 Å) which correspond to the time-ranges tinted in gray in Figure 2-3B assuming $\langle\kappa^2\rangle = 2/3$. The amplitudes of both $R_{DA,app}$ (solid bars) from the 2-k_{FRET} fit are plotted in proportion to their corresponding fractions. See their values in Table 2-2. For CRN$_{GFP}$/CLV2$_{mCh}$ (upper), we determined with the 2-k_{FRET} fit: $\langle R_{DA,app}\rangle = 52.1$ Å (dotted line) and $w_{DA,app} = 19.2$ Å; with the Gaussian-distance fit: $\langle R_{DA,app}\rangle = 54.5$ Å and $w_{DA,app} = 52.0$ Å; and from the AV simulation: $\langle R_{DA}\rangle = 54.2$ Å and $w_{DA} = 44.5$ Å. For CRNΔKi$_{GFP}$/CLV2$_{mCh}$ (lower), we determined with the 2-k_{FRET} fit: $\langle R_{DA,app}\rangle = 47.5$ Å (dotted line) and $w_{DA,app} = 15.3$ Å; with the Gaussian-distance fit: $\langle R_{DA,app}\rangle = 43.0$ Å and $w_{DA,app} = 31.2$ Å; and from the AV simulation: $\langle R_{DA}\rangle = 44.6$ Å and $w_{DA} = 30.6$ Å. freq. = frequency. (**C**) The upper panel plots the two $\varepsilon_{mix}(t)$-diagrams of the two FRET-images in Figure 2-1, x_{FRET} in both images are marked with arrows. The lower panel compares their function-curves of $\varepsilon_{(D,A)}(t)$. (**D**) Steady-state FRET

efficiency differs in the two samples. (**E**) Images and histograms of pixel-wise x_{FRET} determined for the two FRET experiments as shown in Figure 2-1. freq. = frequency.

2.2.8 Application 2: Determining the stoichiometry and K_D of protein complexes

Besides the molecular geometry, information on molecule complex stoichiometry and interaction affinity is also contained in FRET-FLIM data and could be extracted with our analysis workflow. We demonstrate the key procedures taking CRNΔKi/CLV2 complex as an exemplary system.

A total of 38 measurements of different membrane regions on CRNΔKi_{GFP}/$CLV2_{mCh}$ interaction were individually analyzed with our workflow. Intrinsically, protein concentration varies between different cells and even at different locations of the same cell. Sample heterogeneity resulted in a broad range of x_{FRET} in these FRET images. Such a feature can be easily recognized via $\varepsilon_{mix}(t)$-diagrams (Figure 2-5A). In the following, we make use of the distinct protein concentration (see Section 2.4.12) to construct a binding isotherm.

First, to infer the stoichiometry of the protein complex, we checked the dependence of steady-state FRET efficiency E on acceptor concentration (Figure 2-5B, upper panel). The observed independence indicates that the CRNΔKi_{GFP}/$CLV2_{mCh}$ complex must have only one $CLV2_{mCh}$; otherwise, in the case of multiple acceptors, E would have shown an increase with increased acceptor concentration. Figure 2-8 shows that in the experiments with exchanged labeling, E of $CLV2_{GFP}$/CRNΔKi_{mCh} is independent of CRNΔKi_{mCh} concentration as well. Hence we can conclude that CRNΔKi/CLV2 complex is a heterodimer.

Next, to determine K_D we fit the relation between the x_{FRET} and the unbound CLV2 concentration assuming a (1:1) binding isotherm (Section 2.4.12; Figure 2-5B, lower panel). The variations in the data around the fitted curve are most likely due to the heterogeneous properties of mCherry in cells. Considering the CRNΔKi/CLV2 interaction, we fitted a value for K_D of 0.12 ± 0.03 μM (mean ± s.e.), and the fraction of mCherry functional as FRET acceptor of 75 ± 5% (mean ± s.e.). The rest 25 ± 5% (mean ± s.e.) were dysfunctional acceptors, consistent with the ~ 30% that were earlier found in GFP-mCherry fusion protein (Figure 2-2 and Section 2.4.10).

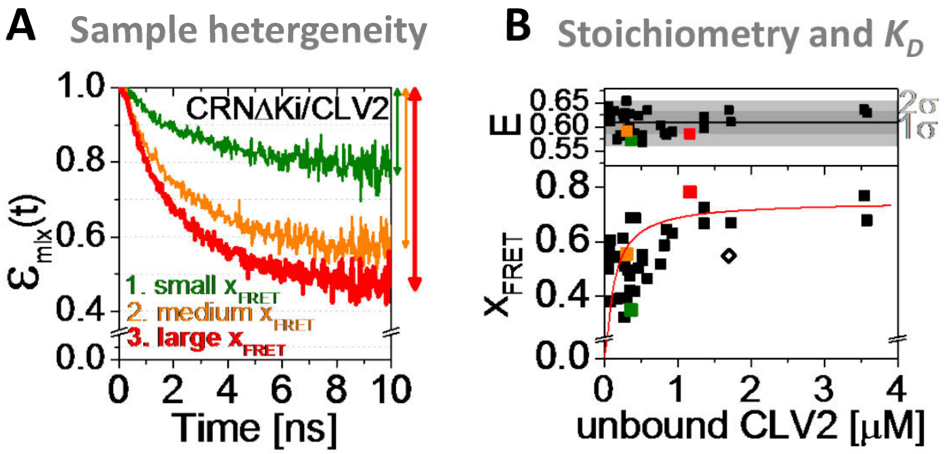

Figure 2-5 MFIS-FRET analysis determines the stoichiometry and K_D of CRNΔKi/CLV2 protein complex. (**A**) $\varepsilon_{mix}(t)$-diagrams of three experiments of CRNΔKi_{GFP}/$CLV2_{mCh}$ respectively containing low (olive), medium (orange) and high (red) FRET-active species fraction (x_{FRET}) are plotted together. Individual x_{FRET} is marked by an arrow beside the diagram. (**B**) In both panels, the data points colored in olive, orange or red correspond to the $\varepsilon_{mix}(t)$ in **A**. The upper panel plots steady-state FRET efficiency (E) versus concentration of unbound CLV2, E = 0.609 ± 0.024 (mean ± s.d., n = 38). The lower panel plots x_{FRET} versus concentration of unbound CLV2, and the fitting of K_D (Origin 8.6, OriginLab). An outlier (open diamond) marked out on the plot was not included in the fit. The reduced Chi^2 of the fit is 0.02.

2.2.9 FRET fingerprints

The structural features of a total of 18 different molecule complexes were characterized via the optimized MFIS analysis workflow. Figure 2-6 plots the two structure reporters, $\langle R_{DA,app} \rangle$ and $w_{DA,app}$, obtained from the 2-k_{FRET} fit as FRET fingerprints for these samples (circles) together with our previously published *in vitro* single-molecule FRET experiments on double-stranded RNA molecules (squares) labeled using organic dyes (Sindbert et al., 2011).

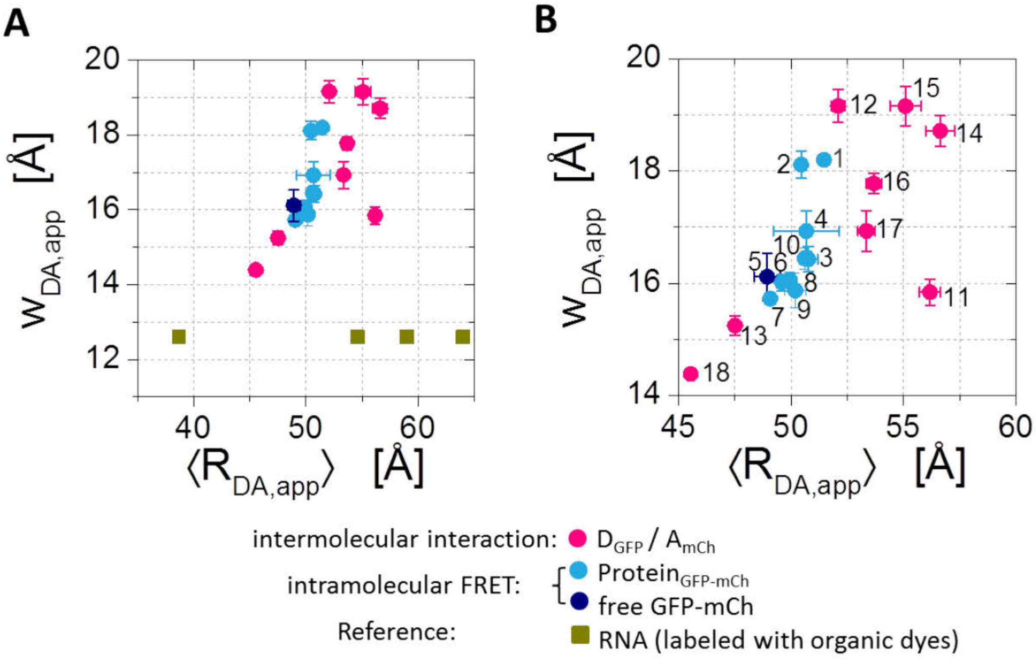

Figure 2-6 FRET fingerprints. (**A**) FRET fingerprints of 18 samples measured *in vivo* (circle) and 4 RNA molecules measured *in vitro* (square). (**B**) A zoom-in of the 18 samples in **A**. For each sample, the name and values of $\langle R_{DA,app} \rangle$ and $w_{DA,app}$ are listed in Table 2-2 according to the numbering labels beside each symbol.

Noticeably, Protein $_{GFP\text{-}mCherry}$ and free GFP-mCherry fusion constructs (Figure 2-6, in light blue and navy) are located closely together around $\langle R_{DA,app} \rangle$ = 50 Å. As shown in

Figure 2-2D, different host proteins impose different spatial restrictions on the GFP-mCherry conformational space (excluded volume effect (Lasker et al., 2010)), giving rise to slight FRET variations among different fusion constructs.

In intermolecular interactions studies (Figure 2-6, in pink), donor and acceptor FPs were separately attached to individual host proteins. Accordingly, molecular complexes of a variety of geometries produced a significantly larger spread of FRET fingerprints compared to the GFP-mCherry fusions. The flexible region between a host protein and its attached FP mainly consists of i) the unstructured amino acids at the C-terminus of the host protein, and ii) those at the N-terminus of the FP (12 amino acids in GFP and 17 in mCherry). Considering each amino acid is approx. 3.5 Å in length, such a flexible linkage is at least 42 Å when it is stretched, which is much longer than the accessible volume of flexibly linked organic dyes (20 Å) in double-stranded RNA molecule (Sindbert et al., 2011). Therefore, in contrast to the organic dyes in *in vitro* FRET experiments (Figure 2-6, dark yellow square), FPs in FRET-imaging experiments (Figure 2-6, circle) have a much wider R_{DA}-distribution covering a broader FRET efficiency (Figure 2-2), and the $\langle R_{DA,app} \rangle$ shows a weak correlation with the $w_{DA,app}$.

2.3 Discussion

In this study, we provide a global MFIS-FRET analysis workflow (Figure 2-1) to solve the dilemma of performing imaging measurements with poor pixel-wise photon statistics or measuring at a single point without any image information. Using this analysis workflow, we can characterize structural properties, stoichiometry and interaction affinities of molecular complexes in living cells while preserving the spatial image information, which remarkably excels traditional methods on all fronts.

The MC molecular simulation and experimental studies show that FPs have static majorly random distance distributions (Figure 2-2F). It allows us to handle the κ^2-effect and estimate the distance information. We show that if a GFP-mCherry protein is attached to different host proteins, the k_{FRET}-distribution will be altered according to the host proteins (excluded volume effect, Figure 2-2D and Figure 2-6). We also found that the impact of different molecular environment on FPs is usually small (Figure 2-5A).

The pixel-integration procedure increases the precision of analysis by dramatically improving the photon statistics in the imaging data, so that the sub-ensemble fluorescence decays *in planta* reach the quality of traditional *in vitro* cuvette measurements. This procedure is analogous to electron microscopy of single particles, in which the data noise is reduced by averaging of multiple particles. For the sub-ensemble data, we introduce the $\varepsilon_{mix}(t)$-diagram as an intuitive display, which allows one to inspect all FRET features immediately. We also establish a quantitative global fit model to correctly extract the true fraction of protein complexes and FRET efficiency. Using the determined fraction of protein complexes and utilizing the intrinsic variations of protein concentration in each experiment, stoichiometry and dissociation constant of protein complexes can be characterized in living cells. Characterization of the FRET efficiency enables detection of even subtle FRET variations and thus provides crucial information about the structural properties of molecular complexes.

To accurately recover distance information, on a theoretical level, our simulation suggests employing $\langle\kappa^2\rangle = 2/3$ to sub-ensemble FRET-imaging data; and on a practical level, we recommend reducing the linkage length between a host protein and its attached FP as much as possible during sample preparation. In future studies, provided with sufficient prior knowledge on the molecular structure and conformation, the κ^2-distribution can be obtained from the MC simulation and convoluted in the global fit to recover the R_{DA}-distribution.

The analysis workflow can be applied to any FRET-FLIM data, for example, to study biomolecular interactions, to characterize peptide linkers or to interpret behaviors of FRET sensor *in vivo*. The molecular interactions shown here are location-independent, yet the methodology can be easily adapted for location-dependent interactions (Somssich et al., 2015; Stahl et al., 2013). With MFIS images and/or histograms, such interactions can be identified and different populations separated. Moreover, combined with time-lapse recording (Somssich et al., 2015) the analysis tools allow one to monitor biomolecule conformational dynamics. Therefore, molecular descriptions powered by FRET and spatiotemporal information provided by imaging can be fully utilized to recover structural features, interaction affinities and stoichiometries of protein complexes in living cells.

2.4 Material and Methods

2.4.1 Sample preparation

Plant Reporter Lines. *Nicotiana benthamiana* plants were grown for four weeks in the greenhouse under controlled conditions. Transient transformation and the inducible expression system were performed as described in (Bleckmann et al., 2010).

Construction of Inducible Reporter Constructs. The CLV2, CRN and CRN(del)kinase (CRNΔKi) expression vectors are described in (Bleckmann et al., 2010). The cytoplasmic direct GFP-mCherry fusion was amplified from pABindFRET (Bleckmann et al., 2010) and cloned via the pENTR™/D-TOPO® and Gateway® LR Clonase® II Cloning Kits into the pMDC7 destination vector as described in (Curtis and Grossniklaus, 2003).

We chose a β-estradiol inducible system described in (Bleckmann et al., 2010). By doing so, we were able to time our measurements to be done exactly at the point when protein concentration reaches the lower detection limit, thereby reducing the chance of overexpression artifacts to the minimum.

2.4.2 MFIS experiments

Experiments were performed with a confocal laser scanning microscope (FV1000 Olympus, Hamburg, Germany) additionally equipped with a single photon counting device with picosecond time-resolution (Hydra Harp 400, PicoQuant, Berlin, Germany). GFP was excited at 485 nm with a linearly polarized, pulsed (32 MHz) diode laser (LDH-D-C-485, Pico-Quant, Berlin, Germany) at 0.8 µW at the objective (60x water immersion, Olympus UPlanSApo NA 1.2, diffraction limited focus). mCherry was excited at 559 nm with a continuous-wave laser (FV1000) at 5.4 µW at the objective. The emitted light was collected in the same objective and separated into its perpendicular and parallel polarization. GFP fluorescence was then detected by single photon avalanche detectors (PDM50-CTC, Micro Photon Devices, Bolzano, Italy) in a narrow range of its emission spectrum (bandpass filter: HC520/35, AHF, Tübingen, Germany). mCherry fluorescence was detected by hybrid detectors (HPMC-100-40, Becker&Hickl, Berlin, Germany, with custom designed cooling), of which the detection wavelength range was set by the bandpass filters (HC 607/70, AHF). Images were taken with 20 µs pixel dwell time. With 485 nm excitation, series of 40 frames were merged to one image; with 559 nm excitation, series of 10 frames were merged together; and the obtained images were further analyzed using custom-designed software (Kudryavtsev et al., 2006; Weidtkamp-Peters et al., 2009).

2.4.3 Pixel-wise analysis

The histograms presenting the decay of fluorescence intensity after the excitation pulse were built with 256 bins and 128 ps per bin to determine fluorescence-weighted donor lifetimes ($\langle\tau_D\rangle_f$) in each pixel. The fitting procedures have been described in (Stahl et al., 2013).

2.4.4 Sub-ensemble analysis

Photons from a sub-ensemble of pixels were integrated to an intensity decay histogram with 1024 bins and 32 ps per bin. The donor-only fitting with Eq. (2-1) was performed on every measured donor-only image, and the mean values of fit parameters ($x_{D0}^{(m)}$ and $k_{D0}^{(m)}$) were set as invariant restraints in the subsequent analysis of FRET samples. For a FRET sample, the donor fluorescence decay $f_{mix}(t)$ is a mixture of unquenched donor decay $f_{(D,0)}(t)$ and quenched donor decay $f_{(D,A)}(t)$. The latter given by Eq. (2-2) assumes that all the donor lifetimes are quenched by associated FRET rates, considering that the two states of GFP that relate to its two lifetimes have almost the same emission spectrum (Jung et al., 2005; Striker et al., 1999) and the same distance to any nearby acceptor chromophore. The $\varepsilon_{mix}(t)$ computes the ratio between $f_{mix}(t)$ and $f_{(D,0)}(t)$ to illustrate the time-resolved FRET processes, which is analogous to the time-resolved anisotropy (r(t)), in that r(t) computes the relative difference in fluorescence intensities between parallel and perpendicular polarizations to illustrate the time-resolved depolarization processes. The steady-state FRET efficiency of FRET-active species (E) is given by:

$$E = 1 - \frac{\langle \tau_{DA} \rangle_x}{\langle \tau_{D0} \rangle_x} = 1 - \frac{\sum_l x_{FRET}^{(l)} \sum_m x_{D0}^{(m)} \cdot \left(k_{D0}^{(m)} + k_{FRET}^{(l)}\right)^{-1}}{\sum_m x_{D0}^{(m)} \cdot \left(k_{D0}^{(m)}\right)^{-1}} \tag{2-5}$$

Here $\langle \tau_{DA} \rangle_x$ and $\langle \tau_{D0} \rangle_x$ are species weighted donor lifetimes in the presence and in the absence of acceptors (Sisamakis et al., 2010).

In the 2-k_{FRET} fit model (Eq. (2-1) - (2-4)), the obtained FRET parameters are two FRET rate constants ($k_{FRET}^{(1)}$ and $k_{FRET}^{(2)}$) and their normalized amplitudes ($x_{FRET}^{(1)}$ and $x_{FRET}^{(2)}$). To reconstruct an apparent distance distribution ($R_{DA,app}$-distribution), each FRET rate constant is converted to an apparent distance, $R_{DA,app}^{(1)}$:

$$R_{DA,app}^{(l)} = R_0 \cdot \left(k_{FRET}^{(l)} \cdot \tau_0\right)^{-\frac{1}{6}} \tag{2-6}$$

in which the unquenched GFP fluorescence lifetime τ_0 = 2.6 ns, and the Förster radius between GFP and mCherry R_0 = 52 Å (including κ^2 = 2/3). Then the mean ($\langle R_{DA,app}\rangle$) and the width ($w_{DA,app}$) of the $R_{DA,app}$-distribution are given by:

$$\left\langle R_{DA,app}\right\rangle = \sum_l x_{FRET}^{(l)} \cdot R_{DA,app}^{(l)}$$

$$w_{DA,app} = 2\cdot\sqrt{\sum_l x_{FRET}^{(l)} \cdot \left(R_{DA,app}^{(l)} - \left\langle R_{DA,app}\right\rangle\right)^2} \tag{2-7}$$

In the Gaussian-distance fit model (Eq. (2-1) - (2-4)), $\langle\kappa^2\rangle$ = 2/3 was employed to convert the $R_{DA,app}$-distribution to the k_{FRET}-distribution. The fit parameters are x_{FRET}, $\langle R_{DA,app}\rangle$ and $w_{DA,app}$.

The complete model function considering both polarizations is given in Section 2.5.3.1.

2.4.5 Determining pixel-wise species fractions by a pattern fit

After determining the fluorescence decay patterns of FRET-active ($f_{(D,A)}(t)$) and FRET-inactive species ($f_{(D,0)}(t)$) from the sub-ensemble analysis, they were set as restraints to fit the species fractions by our MLE in every pixel assuming that protein interaction feature ($\varepsilon_{(D,A)}(t)$) is localization-independent. Since the number of fitting parameters is reduced to the single parameter x_{FRET}, this procedure requires much less photon counts.

2.4.6 FRET phasor

To demonstrate the application of FRET phasor, we used the fit results obtained from our sub-ensemble analysis ($\varepsilon_{(D,A)}(t)$) to accurately pinpoint the phasor location. Similar to plotting fluorescence lifetime phasor (Digman et al., 2008), one could also plot phasor of $\varepsilon_{mix}(t)$ of experimental data without fitting.

At the n-th harmonic of the laser repetition rate f (f = 32 MHz in our measurement), the angular frequency ω equals $2n\pi f$. The coordinates, $g(\omega)$ and $s(\omega)$, of a given $\varepsilon_{(D,A)}(t)$ containing l FRET rates (Eq. (2-3)) in phasor plot are given by:

$$g(\omega) = \sum_{l} \frac{a_l}{1+(\omega / k_{FRET}^{(l)})^2}$$
$$s(\omega) = \sum_{l} \frac{a_l \cdot \omega / k_{FRET}^{(l)}}{1+(\omega / k_{FRET}^{l})^2} \tag{2-8}$$

$$\text{with } a_l = \frac{x_{FRET}^{(l)} \big/ k_{FRET}^{(l)}}{\sum_{l} (x_{FRET}^{(l)} \big/ k_{FRET}^{(l)})}$$

a_l is the intensity weighted fractional contribution of the l-th component with FRET rate constant $k_{FRET}^{(l)}$. The phasor location of a mixture of different FRET rates is the intensity-weighted average of the contributions of each FRET rate. Our phasor plot is calculated at 64 MHz, i.e. the second harmonic of the laser repetition rate, to have a better sensitivity to changes in the phasor location of different samples that have been measured.

2.4.7 Model functions used in traditional analysis of FRET-FLIM data

The following three models are arranged in the increasing order of their complexity. More details are given in Section 2.5.3.3.

Mono-exponential fluorescence decay model:

$$f(t) = \exp\left(-\frac{t}{\left\langle \tau_{DA} \right\rangle_x} \right) \tag{2-9}$$

Bi-exponential fluorescence decay model:

$$f(t) = (1 - x_{FRET})\exp\left(-\frac{t}{\langle \tau_{D0} \rangle}\right) + x_{FRET}\exp\left(-\frac{t}{\langle \tau_{DA} \rangle_x}\right) \tag{2-10}$$

Multi-exponential fluorescence decay model to resolve two FRET rates:

$$\begin{aligned} f(t) = {} & (1 - x_{FRET})\left(x_{D0}^{(1)} \cdot \exp(-t \cdot k_{D0}^{(1)}) + x_{D0}^{(2)} \cdot \exp(-t \cdot k_{D0}^{(2)})\right) \\ & + x_{FRET}\left(x_{DA}^{(1)} \cdot \exp(-t \cdot k_{DA}^{(1)}) + x_{DA}^{(2)} \cdot \exp(-t \cdot k_{DA}^{(2)})\right) \end{aligned} \tag{2-11}$$

In the 2-k_{FRET} model, using FRET rates reduces the required fitting parameters to a minimum while extracting the maximum information. In the Eq. (2-1) - (2-4) there are only 4 parameters needed to resolve FRET-active and inactive species (x_{FRET}) and recover two FRET rate constants ($k_{FRET}^{(1)}$ and $k_{FRET}^{(2)}$) and their fractions ($x_{FRET}^{(1)}$ and $x_{FRET}^{(2)}$). To obtain the same information using a multi-exponential model (Eq. (2-11)) one would need 7 parameters in total (two donor-only lifetimes and their normalized fractions, two donor-acceptor lifetimes and their normalized fractions, and the fraction of FRET-active species), which is impossible to obtain, given the limited fluorescence lifetime range and photon count.

2.4.8 Estimation of experimentally resolvable FRET-range

A resolvable FRET-range for a typical FRET-FLIM experiment (Figure 2-2F and Figure 2-4B) was estimated as follows: The minimum resolvable time constant (i.e. reciprocal of rate constant) is estimated as 0.05 ns for our instrument. The maximum is estimated according to when the fluorescence signal decays to a constant in a sub-ensemble decay histogram (for example in Figure 2-2B), which is 15 ns. Then the time range in between these two boundaries (i.e. 0.05ns <1/k_{FRET} < 15ns) is considered as experimentally resolvable. These two limiting time constants were converted to donor-acceptor distances assuming $\langle \kappa^2 \rangle = 2/3$ in Figure 2-4B.

2.4.9 GFP-mCherry fusion protein: sampling the conformational space

Based on the GFP and mCherry crystal structures (PDB-ID: 4EUL and 2H5Q respectively) homology models of the fusion protein were constructed using MODELLER (Fiser and Sali, 2003). The homology models were protonated using PDB2PQR (Dolinsky et al., 2007).Then the protonated full-length protein models were mapped to a reduced representation solely consisting of the C-, C_α-, N-, O- and the hydrogen atoms forming the NH-O bonds. The repulsion between the atom pairs (O, N), (C, O) and (C, N) were modeled as repulsive quadratic potential (Kalinin et al., 2012) and the existing hydrogen bonds as simple scaled attractive potential (1/r) preserving secondary structural elements. The sampling was performed on the φ and ψ torsion angles. In each iteration step the torsion angle of one amino acid was changed by random value taken from a Gaussian-distribution with a width of 0.025 rad. Only the internal coordinates of the connecting linker were altered while the internal coordinates of the beta-barrels were kept constant (Table 2-1).

A total of 179,276 sterically allowed conformations were captured, and a representative subset is displayed in Figure 2-2E. For each sampled conformation, its inter-chromophore distance (R_{sim}), orientation factor (κ^2), k_{FRET} and E were computed (Section 2.5.3.2). The obtained R_{sim}-distribution was close to a Gaussian distribution with a mean R_{sim} ($\langle R_{sim} \rangle$) of 50.8 Å and a width (w_{sim}) of 21.0 Å (Figure 2-7). The κ^2 of the sampled conformations ranged from 0 to 4 thus ensuring the extensiveness of the sampling. The mean κ^2 ($\langle \kappa^2 \rangle$) was 0.656, very close to the $\langle \kappa^2 \rangle$ in the dynamic averaging regime 2/3. Also, in agreement with (Vogel et al., 2012), the distribution of E approximately covered from 0 to 1.

2.4.10 GFP-mCherry fusion protein: comparison of simulation and experiment

We converted the FRET parameters fitted with the 2-k_{FRET} model to an apparent distance distribution ($R_{DA,app}$-distribution), and found that in experimental data the mean apparent distance ($\langle R_{DA,app} \rangle$) of GFP-mCherry fusion protein is 48.9 ± 1.8 Å (mean ± s.d.), and the width of apparent distribution ($w_{DA,app}$) is 16.1 ± 1.3 Å (mean ± s.d.). These values are very close to the simulation result if only evaluating its experimentally resolvable range: $\langle R_{DA} \rangle$ = 47.4 Å and w_{DA} = 17.7 Å.

However, since only two FRET rate constants could be directly recovered from experiments and some GFP-mCherry conformations with very low FRET efficiency become experimentally irresolvable, the reconstructed $R_{DA,app}$-distributions tended to be narrower than the physical distance distributions and slightly biased to shorter distances when compared to the simulation result of full range: $\langle R_{DA} \rangle$ = 50.8 Å and w_{DA} = 21.0 Å.

According to the MC simulation, of all the sampled GFP-mCherry conformations only a negligible portion (0.4%) showed irresolvably high FRET (i.e. $k_{FRET} > 20\ ns^{-1}$, see Section 2.4.8; Figure 2-2F). About 32% (x_{NoFRET}) showed irresolvably low FRET (i.e. $k_{FRET} < 0.067\ ns^{-1}$, see Section 2.4.8; Figure 2-2F), which would appear as FRET-inactive in experimental data resulting in an underestimation of the actual donor-acceptor species fraction ($x_{(D,A)}$) by 32% (Eq. (2-4)).

2.4.11 Accessible volume (AV) simulation of FP distributions

Due to the system complexity of the CRN/CLV2 and CRNΔKi/CLV2 protein complexes, to sample the sterically allowed conformations of their attached FPs at the intracellular side by MC molecular simulation was not feasible. Hence, we performed AV simulations to reduce the computational burden. As the AV simulations do not consider entropic effects (Sindbert et al., 2011), the uniform probability densities of the obtained AVs were then weighted by a Gaussian-chain distribution. We compared AV simulation with the experiments of GFP-mCherry fusion protein and found that persistence lengths of 1-3 amino-acids could be employed in the Gaussian-chain distribution. In the case of CRN/CLV2 and CRNΔKi/CLV2 protein complexes, 1 amino-acid serves best to reflect the experimental observables. The unresolved regions at the C-terminus of CRN where the FPs are attached were treated as flexible polypeptides. The orientation of the CRN kinase domain is unknown. Thus, we assumed two limiting cases: a sideways and an upright orientation. Both orientations are in good agreement with the experiments ($\chi^2_{r(sideways)}$ = 1.03 and $\chi^2_{r(upright)}$ = 1.05) though the sideways orientation is in better agreement.

2.4.12 Determination of the dissociation constant (K_D) of CRNΔKi/CLV2

The detection volume of our microscope was calibrated by FCS measurements of Rhodamine 110 (Rh110) to determine its shape and size. The fitting model applied to the obtained FCS curve assumes a 3-dimensional Gaussian-shaped volume, and a single diffusing species including transitions to a triplet state as shown in (Weidtkamp-Peters et al., 2009). From the Rh110 diffusion time of 32 μs and aspect ratio of 7, the detection volume for GFP was determined to be 0.5 fl. The detection volume for mCherry, 0.8 fl, is larger due to longer wavelength. The brightness of GFP and mCherry *in vivo* were individually characterized from FCS measurements of freely diffusing FPs in cytoplasm. By fitting the same model function as in Rh110 experiment, we found that with 5.4 μW of 559 nm laser excitation at the objective, mCherry brightness is 1.36 kcpm, and that with 0.8 μW of 485 nm laser excitation, GFP brightness is 1.12 kcpm.

The average mCherry fluorescence intensity of an image with mCherry excitation ($S_{R,R}$) was first corrected for detector dead time, t_d (Becker, 2005):

$$S_{R,R}^{m} = \frac{S_{R,R}}{1 - S_{R,R} \cdot t_d} \tag{2-12}$$

The dead time of the set-up was determined to be 80 ns from the linear auto-correlation curves of detection channels. $S_{R,R}^{m}$ was then used to calculate the total concentration of mCherry, $[A]_0$, with the determined detection volume and the mCherry brightness.

The average GFP fluorescence intensity of an image with GFP excitation was also first corrected for detector dead time (Becker, 2005) (see above), and then the obtained intensity ($S_{G,G}^{m}$) was further corrected for quenching effect due to FRET:

$$S_{G,G}^{u} = \frac{S_{G,G}^{m}}{\left(1 - x_{FRET}\right) + x_{FRET} \cdot \left(1 - E\right)} \tag{2-13}$$

$S_{G,G}^{u}$ is unquenched GFP fluorescence intensity in the absence of FRET. It was then used to calculate total concentration of GFP, $[D]_0$.

Assuming the total concentration of GFP and mCherry respectively reflects the total concentration of their host proteins, CRNΔKi$_{GFP}$ and CLV2$_{mCh}$, concentration of unbound

CLV2 (acceptor, [A]) is calculated as the total concentration minus the concentration of bound CLV2 ([DA]):

$$[A] = [A]_0 - [DA] = [A]_0 - [D]_0 \cdot x_{FRET} \tag{2-14}$$

Here, the FRET-active species fraction, x_{FRET}, is obtained directly by fitting each measurement in sub-ensemble analysis with 2-k_{FRET} model. Considering that the presence of dysfunction acceptors can result in underestimation of the interacting protein complexes, we introduced a fit parameter, C, to represent the fraction of mCherry functional as FRET acceptor. Therefore, the K_D is fitted by:

$$x_{FRET} = \frac{[A]}{K_D + \frac{[A]}{C}} \tag{2-15}$$

2.5 Supplementary Information

2.5.1 Supplementary Figures

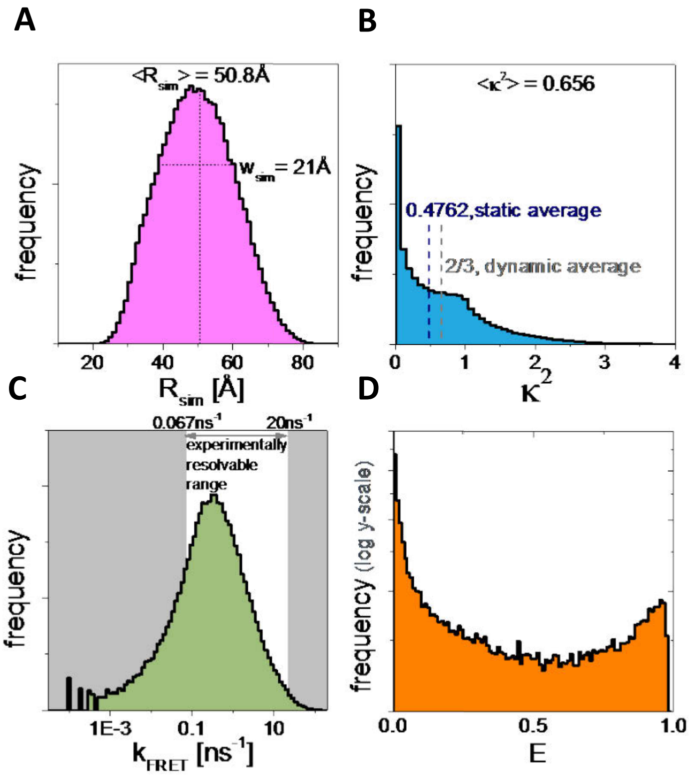

Figure 2-7 FRET parameters computed from all the sampled conformations of a GFP-mCherry fusion protein via MC molecular simulation. (**A** - **D**) The distribution of donor-acceptor distance (R_{sim}), orientation factor (κ^2), FRET rate constant (k_{FRET}), and FRET efficiency (E) respectively. In **C**, the experimentally resolvable k_{FRET}-range is indicated (Figure 2-2F; Section 2.4.8).

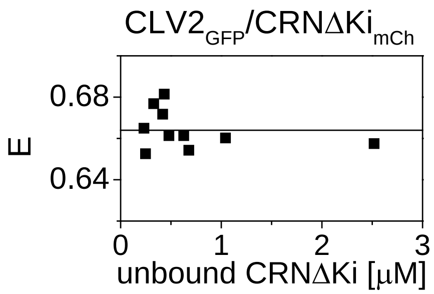

Figure 2-8 FRET efficiency (E) versus unbound $CRNKi_{mCh}$ concentration of 10 measurements on $CLV2_{GFP}/CRN\Delta Ki_{mCh}$. E = 0.664 ± 0.009 (mean ± s.d.).

2.5.2 Supplementary Tables

GFP	deleted	~~MVSKGEELFT GV~~
	kept rigid	VPILVELDGD VNGHKFSVSG EGEGDATYGK LTLKFICTTG KLPVPWPTLV TTLGYGVQCF SRYPDHMKQH DFFKSAMPEG YVQERTIFFK DDGNYKTRAE VKFEGDTLVN RIELKGIDFK EDGNILGHKL EYNYNSHNVY IMADKQKNGI KVNFKIRHNI EDGSVQLADH YQQNTPIGDG PVLLPDNHYL STQSALSKDP NEKRDHMVLL EFVTAA
	flexible	GITLGMDELY K
mCherry	flexible	MVSKGEEDNM AIIKEFM
	kept rigid	RFKVHMEGSV NGHEFEIEGE GEGRPYEGTQ TAKLKVTKGG PLPFAWDILS PQFMYGSKAY VKHPADIPDY LKLSFPEGFK WERVMNFEDG GVVTVTQDSS LQDGEFIYKV KLRGTNFPSD GPVMQKKTMG WEASSERMYP EDGALKGEIK QRLKLKDGGH YDAEVKTTYK AKKPVQLPGA YNVNIKLDIT SHNEDYTIVE QYERAEG
	deleted	~~RHSTGGMDEL Y~~

Table 2-1 Amino-acid sequence of GFP-mCherry fusion protein in the MC simulation. The first 12 amino acids of GFP and the last 11 of mCherry were omitted. The last 11 amino acids of GFP and the first 17 of mCherry were set as flexible. The rest corresponding to the beta-barrel structures of both FPs were kept rigid.

No.	Sample	⟨$R_{DA,app}$⟩	$w_{DA,app}$	$k_{FRET}^{(1)}$	$k_{FRET}^{(2)}$	$x_{FRET}^{(2)}$	N
		[Å]	[Å]	[ns^{-1}]	[ns^{-1}]		
			Protein $_{\text{GFP-mCherry}}$ fusion proteins				
1	$\text{AS2}_{\text{GFP-mCh}}$	51.5	18.2	0.207	2.476	0.318	1
2	$\text{Cyp5}_{\text{GFP-mCh}}$	50.5 ± 0.1	18.1 ± 0.2	0.218 ± 0.007	2.442 ± 0.065	0.354 ± 0.011	3
3	$\text{CRNKi}_{\text{GFP-mCh}}$/CLV2	50.8 ± 0.4	16.4 ± 0.2	0.223 ± 0.011	1.880 ± 0.079	0.366 ± 0.005	8
4	$\text{JLO}_{\text{GFP-mCh}}$	50.7 ± 1.5	16.9 ±0.4	0.225 ± 0.029	2.064 ± 0.230	0.363 ± 0.019	3
5	Free GFP-mCherry	48.9 ± 0.6	16.1 ± 0.4	0.245 ± 0.017	1.877 ± 0.097	0.453 ± 0.016	10
6	$\text{CRN}_{\text{GFP-mCh}}$/CLV2	49.6 ± 0.2	16.0 ± 0.1	0.251 ± 0.006	2.058 ± 0.051	0.379 ± 0.003	9

7	CRN/CLV2$_{\text{GFP-mCh}}$	49.1 ± 0.2	15.7 ± 0.1	0.259 ± 0.006	2.000 ± 0.052	0.404 ± 0.003	9
8	CLV1$_{\text{GFP-mCh}}$	49.9 ± 0.2	16.1 ± 0.1	0.239 ± 0.004	1.912 ± 0.043	0.389 ± 0.003	31
9	WUS$_{\text{GFP-mCh}}$	50.2 ± 0.5	15.9 ± 0.3	0.241 ± 0.013	1.890 ± 0.086	0.380 ± 0.010	15
10	GNOM$_{\text{GFP-mCh}}$	50.6 ± 0.2	16.4 ± 0.2	0.220 ± 0.005	1.827 ± 0.077	0.386 ± 0.007	18
intermolecular interactions							
11	AS2$_{\text{GFP}}$/AS1$_{\text{mCh}}$	56.2 ± 0.5	15.8 ± 0.2	0.157± 0.006	1.503± 0.057	0.228 ±0.010	8
12	CRN$_{\text{GFP}}$/CLV2$_{\text{mCh}}$	52.1 ± 0.3	19.2 ± 0.3	0.191± 0.006	2.643± 0.093	0.311 ±0.006	16
13	CRNΔKi$_{\text{GFP}}$/CLV2$_{\text{mC}}$	47.5 ±	15.3 ±	0.297±	2.170±	0.449 ±0.00	38

	h	0.2	0.2	0.006	0.051	3	
14	BAK1$_{GFP}$/FLS2$_{mCh}$+flg22	56.6 ± 0.6	18.7 ± 0.3	0.141± 0.006	2.207± 0.102	0.233 ±0.013	29
15	CLV1$_{GFP}$/CRN/CLV2$_{mCh}$+CLE40R	55.1 ± 0.7	19.2 ± 0.3	0.154± 0.009	2.282± 0.208	0.263 ±0.007	12
16	CRN$_{GFP}$/CLV2/CLV1$_{mCh}$+CLE40R	53.7 ± 0.3	17.8 ± 0.2	0.177± 0.006	1.973± 0.082	0.296 ±0.005	44
17	CLV2$_{GFP}$/CRN$_{mCh}$+CLE40R	53.4 ±0.4	16.9 ± 0.4	0.181± 0.008	2.124± 0.111	0.266 ±0.006	15
18	CLV2$_{GFP}$/CRNΔKi$_{mCh}$	45.5 ± 0.1	14.4 ± 0.1	0.348± 0.007	2.346± 0.053	0.510 ±0.004	10
GFP-L(n)-mCherry and CLV1$_{GFP-L(n)-mCherry}$							
	GFP-L(8)-mCherry	53.0 ± 0.3	17.3 ± 0.2	0.182± 0.007	1.738± 0.063	0.325 ±0.006	17

	GFP-L(13)-mCherry	54.3 ±0.4	18.5 ±0.2	0.158± 0.005	1.893± 0.116	0.299 ±0.010	17
	GFP-L(29)-mCherry	56.2 ± 0.3	18.6 ± 0.2	0.135± 0.004	1.532± 0.045	0.283 ±0.008	16
	$\text{CLV1}_{\text{GFP-L(8)-mCh}}$	52.8 ± 0.3	16.7 ± 0.2	0.196± 0.006	1.892± 0.082	0.299 ±0.006	16
	$\text{CLV1}_{\text{GFP-L(13)-mCh}}$	53.3 ± 0.2	17.0 ± 0.1	0.183± 0.003	1.814± 0.042	0.300 ±0.003	60
	$\text{CLV1}_{\text{GFP-L(29)-mCh}}$	54.8 ± 0.3	16.0 ± 0.2	0.177± 0.006	1.786± 0.075	0.237 ±0.009	13
RNA molecules in (Sindbert et al., 2011)							
		38.7	12.6				
		54.6	12.6				
		59	12.6				
		64	12.6				

Table 2-2 FRET parameters in the format of mean ± s.e.m.. Here includes the 18 samples displayed in Figure 2-6 according to the numbering labels (left-most column), and the 8 samples displayed in Figure 2-3A, in which the GFP-L(0)-mCherry and $\text{CLV1}_{\text{GFP-L(0)-mCherry}}$ (construct without a linker) are the same samples as No.5 and 8. N on the right-most column is number of measurements.

2.5.3 Supplementary Notes

2.5.3.1 Complete model function for polarization resolved detection

In MFIS measurements fluorescence decays in both polarizations ($f_{||}(t)$ and $f_{\perp}(t)$) are recorded, and coupled via the time-resolved anisotropy, r(t):

$$\begin{aligned} f_{||}(t) &= f(t)\cdot\left[1+(2-3l_1)\cdot r(t)\right]/3 \\ f_{\perp}(t) &= \frac{1}{G}\cdot f(t)\cdot\left[1-(1-3l_2)\cdot r(t)\right]/3 \end{aligned} \quad (2\text{-}16)$$

$$r(t) = b_1 e^{-\frac{t}{\rho_1}} + \left(r_0 - b_1\right)e^{-\frac{t}{\rho_2}} \quad (2\text{-}17)$$

G is the ratio between detection efficiencies of parallel and perpendicular detection channels. Factors l_1 and l_2 describe polarization mixing in objectives with high NA (Koshioka et al., 1995). Two rotational correlation times, ρ_1 and ρ_2, with amplitude b_1 and (r_0-b_1) are formally assigned to r(t), and r_0 is the fundamental anisotropy.

Besides fluorescence, the detected signal (S) in every measurement contains auto-fluorescence ($f_B(t)$), scattered photons ($b_{sc}(t)$) and constant background (B) as well. Thus, the detected signal in each polarization is given by:

$$\begin{aligned} s_{||}(t) &= f_{||}(t) + b_{||,sc}(t) + f_{||,B}(t) + B_{||} \\ s_{\perp}(t) &= f_{\perp}(t) + b_{\perp,sc}(t) + f_{\perp,B}(t) + B_{\perp} \end{aligned} \quad (2\text{-}18)$$

Measurements of unlabeled samples showed that auto-fluorescence contribution to the total intensity is negligible, therefore. $f_B(t)$ in both polarizations are ~ 0.

2.5.3.2 Computing FRET parameters from sampled GFP-mCherry conformations

To calculate FRET parameters (donor-acceptor distance, orientation factor, FRET rate constant and FRET efficiency) in every simulated structure, on each fluorophore, we chose two C-atoms on the beta-barrel (Asn122 and Asn147 on GFP, Ser356 and Glu388 on mCherry), so that the connecting vector of the two atoms is a good approximation of the transition dipole (Figure 2-9). The distance between the middle points of the connecting vectors of the donor and acceptor is taken as the distance between the chromophores, R_{sim}. Table 2-3 lists out the detailed calculation steps.

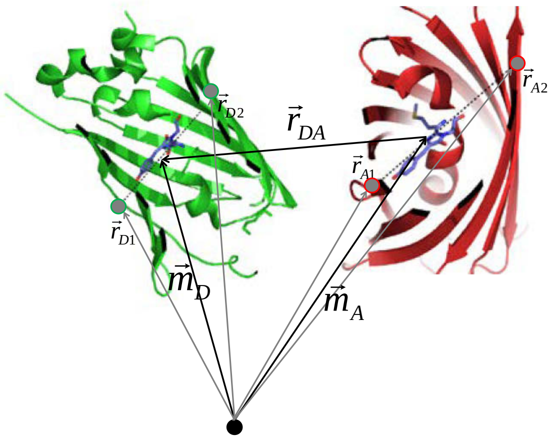

Figure 2-9 Illustration of FRET parameter calculation. Vectors and coordinates in this figure are listed in Table 2-3.

For every simulated structure, given the R_{sim} and the orientation factor (κ^2), the FRET rate constant (k_{FRET}) was calculated according to:

$$k_{FRET} = (3/2)\cdot\kappa^2\cdot(1/\tau_0)\cdot(R_0/R_{sim})^6 \tag{2-19}$$

in which τ_0 is 2.6 ns and the Förster radius (R_0) of GFP and mCherry is 52 Å (including $\kappa^2 = 2/3$). The steady-state FRET efficiency E was determined using

$$E = k_{FRET} / \left(k_{FRET} + 1/\tau_0 \right) \tag{2-20}$$

	Donor (GFP)	Acceptor (mCherry)
Coordinates of the two chosen C_α-atoms	$\vec{r}_{D1}$ and $\vec{r}_{D2}$	$\vec{r}_{A1}$ and $\vec{r}_{A2}$
Distance between the two C_α-atoms	$R_{D,21} = \left\Vert \vec{r}_{D2} - \vec{r}_{D1} \right\Vert_2$	$R_{A,21} = \left\Vert \vec{r}_{A2} - \vec{r}_{A1} \right\Vert_2$
Unit vector connecting the two C_α-atoms	$\hat{\mu}_D = \frac{\vec{r}_{D2} - \vec{r}_{D1}}{R_{D,21}}$	$\hat{\mu}_A = \frac{\vec{r}_{A2} - \vec{r}_{A1}}{R_{A,21}}$
Coordinates of the middle point of the connecting vector	$\vec{m}_D = \vec{r}_{D1} + \frac{R_{D,21}}{2} \hat{\mu}_D$	$\vec{m}_A = \vec{r}_{A1} + \frac{R_{A,21}}{2} \hat{\mu}_A$
Calculation of donor-acceptor distance and orientation factor	$\vec{r}_{DA} = \vec{m}_D - \vec{m}_A$ $R_{DA} = \left\Vert \vec{m}_D - \vec{m}_A \right\Vert_2$ $\hat{\mu}_{DA} = \frac{\vec{r}_{DA}}{R_{DA}}$ $\kappa^2 = \left(\langle \hat{\mu}_A, \hat{\mu}_D \rangle - 3 \cdot \langle \hat{\mu}_D, \hat{\mu}_{DA} \rangle \cdot \langle \hat{\mu}_A, \hat{\mu}_{DA} \rangle \right)^2$	

Table 2-3 Calculate R_{sim} and κ^2 from each sampled structure in steps.

2.5.3.3 Comparing the 2-k$_{FRET}$ fit model with 3 traditional models via simulation

Table 2-4 shows all the parameters set in the simulations. 300 decays of FRET samples were generated according each simulated condition. Each decay histogram contains 3×10^6 photons, which is a typical number for pixel-integrated sub-ensemble data.

The simulated decays were fitted by the 2-k$_{FRET}$ model and 3 traditional models that were most frequently applied in FRET-imaging studies, and based on fit results $\langle E\rangle$ was evaluated:

Mono-exponential model, see Eq. (2-9). Since only one lifetime ($\langle\tau_{DA}\rangle_x$) was determined, it is impossible to resolve different species using this model, thus $\langle E\rangle$ was evaluated assuming that the donor species weighted lifetime $\langle\tau_{D0}\rangle_x$ is 2.44 ns (Eq. (2-5)).

1) Bi-exponential model. Both lifetimes and x_{FRET} in Eq. (2-10) are fitting parameters. $\langle E\rangle$ was evaluated according to Eq. (2-5).
2) Bi-exponential model. The donor lifetime $\langle\tau_{D0}\rangle$ in Eq. (2-10) was fixed to its fluorescence weighted lifetime, 2.55 ns. Fitting parameters are $\langle\tau_{DA}\rangle_x$ and x_{FRET}. $\langle E\rangle$ was calculated according to Eq. (2-7) using donor species weighted lifetime 2.44 ns.
3) 2-k$_{FRET}$ fit model, see Eq. (2-1) - (2-4). The bi-exponential donor fluorescence decay was set as invariant. x_{FRET} was fit parameter; $\langle E\rangle$ was calculated according to Eq. (2-7).

In both simulations:
Donor-only fluorescence decay: $f_{(D,0)}(t) = 0.8e^{\frac{-t}{2.7ns}} + 0.2e^{\frac{-t}{1.4ns}}$. Time-resolved anisotropy: $r(t) = 0.028e^{\frac{-t}{1ns}} + 0.322e^{\frac{-t}{10^{6}ns}}$ Time-to-amplitude converter (TAC) channels: 4096. TAC channel width: 0.008 ns. Total photon count in each simulated decay histogram: 3×10^6. Background in both polarization channels: 0. G-factor: 1.
5 conditions in simulation I:
Constant ⟨E⟩: $\varepsilon_{(D,A)}(t) = 0.7e^{-0.2t} + 0.3e^{-2.0t}$, resulting in ⟨E⟩ = 0.484. Varied x_{FRET} = 0.3; 0.4; 0.5; 0.6; 0.7.
5 conditions in simulation II:
Constant x_{FRET} = 0.5. Varied ⟨E⟩: $\varepsilon_{(D,A)}(t) = 0.7e^{-0.1t} + 0.3e^{-1.2t}$, ⟨E⟩ = 0.366;

$\varepsilon_{(D,A)}(t) = 0.7e^{-0.15t} + 0.3e^{-1.5t}$, $\langle \mathrm{E} \rangle = 0.429$;
$\varepsilon_{(D,A)}(t) = 0.7e^{-0.2t} + 0.3e^{-2.0t}$, $\langle \mathrm{E} \rangle = 0.484$;
$\varepsilon_{(D,A)}(t) = 0.7e^{-0.3t} + 0.3e^{-2.5t}$, $\langle \mathrm{E} \rangle = 0.559$;
$\varepsilon_{(D,A)}(t) = 0.7e^{-0.4t} + 0.3e^{-3.0t}$, $\langle \mathrm{E} \rangle = 0.615$.

Table 2-4 Parameters in 10 different simulated conditions. In each simulated condition, 300 decays were generated and evaluated using 4 different models as explained in text.

Chapter 3 Real-time dynamics of peptide ligand-dependent receptor complex formation in planta

Authors: Marc Somssich[1], Qijun Ma[2], Stefanie Weidtkamp-Peters[3], Yvonne Stahl[1], Suren Felekyan[2], Andrea Bleckmann[1], Claus A.M. Seidel[1,2*], Rüdiger Simon[2,3*]

Affiliations:

[1]Institute for Developmental Genetics, Heinrich Heine University, Düsseldorf, Germany.

[2]Chair for Molecular Physical Chemistry, Heinrich Heine University, Düsseldorf, Germany.

[3]Center for Advanced Imaging, Heinrich Heine University, Düsseldorf, Germany.

*Corresponding authors: Rüdiger Simon, Claus A.M. Seidel

This chapter has been published as:

Somssich, M., Ma, Q., Weidtkamp-Peters, S., Stahl, Y., Felekyan, S., Bleckmann, A., Seidel, C.A.M., and Simon, R. (2015). Real-time dynamics of peptide ligand-dependent receptor complex formation in planta. Sci. Signal. 8, ra76–ra76.

3.1 Introduction

In multicellular organisms, growth and development is based on the coordination of cell proliferation and differentiation between single cells and within tissues. In every developmental step, communication between cells is essential. In plants, several signal transduction pathways coordinate growth or responses to various stimuli. Many of these pathways involve small signaling peptides, which are perceived by receptor-like kinase (RLK) proteins that transduce the signal into the cells. The CLAVATA (CLV) pathway is an example of RLK-mediated peptide signal transduction in *Arabidopsis thaliana*. Another example is the plant defense response initiated by the presence of the bacterial peptide flg22, which involves the receptors FLAGELLIN-SENSITIVE 2 (FLS2) and BRI1-ASSOCIATED KINASE 1 (BAK1). Here, we investigated the initial events that occurred at the receptors in each of these pathways using a multiparameter fluorescence imaging spectroscopy (MFIS) approach, combining fluorescence lifetime imaging with fluorescence polarization and anisotropy microscopy over time. With this approach, we simultaneously measured changes in protein concentration and both homomeric and heteromeric interactions between the receptors with pixel-wise resolution. This provided high spatial and temporal resolution of the interaction states of the receptors over time in individual living plant cells and in response to peptide treatments, which enabled the detection of rapid or transient changes in complex formation, arrangement, and intracellular localization.

The CLV pathway is the key regulatory pathway for stem cell homeostasis in the floral and shoot apical meristems of *A. thaliana*. *CLAVATA3* (*CLV3*) encodes a precursor protein that is processed into a 13–amino acid peptide, which is further modified by the addition of sugar moieties to hydroxyproline residues (Ohyama et al., 2009). The mature CLV3 peptide is secreted from stem cells and perceived by the CLAVATA1 (CLV1), CLAVATA2 (CLV2), and CORYNE (CRN) receptor-like proteins in underlying cells of the organizing center (OC) (Clark et al., 1995, 1997; Fletcher et al., 1999; Kayes and Clark, 1998; Müller et al., 2008). In the OC, the signal is transmitted intracellularly to repress the expression of *WUSCHEL* (*WUS*), encoding a stem cell regulatory transcription factor (Brand et al., 2000; Mayer et al., 1998).

CLV1 encodes an RLK with an extracellular leucine-rich repeat (LRR) receptor domain that binds the peptide CLV3 (Ogawa et al., 2008), a transmembrane domain that integrates into the plasma membrane, and an intracellular kinase domain for downstream signaling. Protein interaction studies showed that CLV1 preferentially forms homomers at the plasma membrane (Bleckmann et al., 2010). CLV2 also has a transmembrane domain for localization in the plasma membrane and an extracellular LRR receptor domain, which may possibly interact with a range of different peptides of the CLV3-related CLE family (Guo et al., 2010); however, direct binding of CLV3 to the purified LRR-domain of CLV2 could not be detected in (Shinohara and Matsubayashi, 2015). CLV2 carries a short juxtamembrane domain on the intracellular side but lacks a kinase domain. CRN is also localized to the plasma membrane through its transmembrane domain but lacks an extracellular LRR receptor domain (Müller et al., 2008). CLV2 and CRN interact through their transmembrane domains, and this interaction is required for the export of both proteins from the endoplasmic reticulum (ER) and delivery to the plasma membrane (Bleckmann et al., 2010). CRN may act as a co-receptor for CLV2; however, CRN may be a pseudokinase because the kinase domain does not autophosphorylate and is structurally atypical (Nimchuk et al., 2011).

Mutants in any of the genes *CLV1*, *CLV2*, *CLV3*, and *CRN* produce supernumerary stem cells because of a lack of *WUS* repression. In floral meristems, this can be quantified as the number of carpels that fuse to form the silique. Using this readout, none of the *clv1*, *clv2*, or *crn* single mutants is as strong as the *clv3* mutant, and *clv1*/*clv2* or *clv1*/*crn* double mutants show additive effects that reach the severity of the *clv3* mutant. In contrast, the phenotype of the *clv2*/*crn* double mutants resembles that of the *clv2* or *crn* single mutants, indicating that CLV2 and CRN function together but in parallel and independently of CLV1 (Clark et al., 1995, 1997; Kayes and Clark, 1998; Müller et al., 2008). CLV1 and CLV2 do not interact directly with each other (Bleckmann et al., 2010). However, recent evidence suggests that crosstalk exists between the two pathways, which could be mediated by a direct interaction of CRN with CLV2 and CLV1 (Bleckmann et al., 2010). Interaction studies using fluorescence resonance energy transfer (FRET) between fluorescently labeled receptor proteins show that CRN might act as the central component in a multimeric complex consisting of CLV1, CLV2, and CRN, which is detectable in the absence of CLV3.

The findings described above raise the question of how the assembly or reassembly of these different receptor complexes, consisting of CLV1 homomers (CLV1/CLV1), CLV2/CRN heteromers, and CLV1/CLV2/CRN multimers, is guided. Previous studies used methods such as coimmunoprecipitation experiments, genetic interaction studies, FRET acceptor photobleaching (APB) measurements, and structural analyses of protein crystals. A drawback of these methods is that they only reflect the static situation at the specific time point when the experiment is performed but lack any temporal dimension. Therefore, interaction dynamics over time could not be recorded. Furthermore, because most of these experiments were not performed in the intact living cell, all spatial information is lost, hence interactions taking place at the plasma membrane, in specific subdomains of the plasma membrane, or in other membranous compartments such as the ER or vesicles involved in receptor recycling cannot be discriminated.

By applying MFIS to *Nicotiana benthamiana* expressing the receptors in the CLV pathway, which were fused to fluorescent proteins, we showed that the CLV receptors were organized in preformed complexes before the addition of CLV3, indicating that the receptors exist in a “ready” state for rapid perception of the signal. We found that in the absence of CLV3, the CLV1/CLV1 homodimers and the CLV2/CRN heterodimers were evenly distributed along the plasma membrane, whereas larger multimers that contained all three receptors accumulated in small clusters along the plasma membrane. The addition of CLV3 triggered additional receptor clustering into more numerous and larger multimers, within specific domains along the plasma membrane.

In plant defense against bacterial pathogens, two LRR-RLKs, FLS2 and its co-receptor BAK1, detect the presence of potential pathogens by binding the bacterial peptide flg22 (Chinchilla et al., 2007; Felix et al., 1999). Both receptor proteins consist of an extracellular LRR domain, a transmembrane domain that integrates into the plasma membrane, and an intracellular kinase domain that transmits the signal within the cell (Gómez-Gómez and Boller, 2000; Li et al., 2002). The presence of flg22 triggers the formation of receptor complexes consisting of FLS2 and BAK1 (FLS2/BAK1), whereas the two receptors are kept separate when flg22 is not present (Chinchilla et al., 2007). Whether BAK1 is in a monomeric or dimeric state before complex formation with FLS2 is unknown. Different groups have reported monomeric or homomeric complexes for FLS2 in the absence of flg22: Using coimmunoprecipitation experiments from whole seedling tissue, Sun *et al*. (Sun et al., 2012) showed that some FLS2 molecules formed homomeric FLS2/FLS2 complexes, whereas, using FRET and fluorescence recovery after photobleaching (FRAP), Ali *et al*. (Ali et al., 2007) could not detect FLS2 homomeric complexes in protoplasts.

Applying our MFIS technique, we monitored the assembly of BAK1/FLS2 heteromeric complexes at the plasma membrane over time in living *N. benthamiana* cells before and after the addition of flg22. We found that BAK1/FLS2 heteromers were not present before ligand addition and that BAK1/BAK1 or FLS2/FLS2 homomers were not detectable at the plasma membrane before flg22 addition. We monitored the formation of the FLS2/BAK1 receptor complex over the course of 1 hour after the addition of flg22 and observed higher-order complexes with at least two BAK1 molecules, probably connecting two FLS2 molecules.

Our analysis indicated that the CLV and flg22 pathways exhibited distinct receptor behavior with the receptors of the CLV pathway, which is constitutively active throughout plant growth and development, existing in a preassembled ready state before ligand perception, and with the receptors of the flg22 pathway exhibiting ligand-induced receptor complex formation.

3.2 Results

3.2.1 Application of MFIS to monitor receptor complex dynamics in living cells

MFIS is used in mammalian and plant cells to study molecular interactions (Weidtkamp-Peters et al., 2009). MFIS, which is based on the detection of FRET between two fluorescent proteins or fluorophores that are fused to the proteins of interest (Weidtkamp-Peters et al., 2009), enables monitoring of various fluorescence parameters simultaneously and over time in living cells. We chose the FRET pair green fluorescent protein (GFP) and mCherry fused to the different *A*. *thaliana* receptor proteins and transiently coexpressed the fusion proteins in *N*. *benthamiana* with a β-estradiol–inducible system (Bleckmann et al., 2010). Although receptors could act differently in their native context than in the *N*. *benthamiana* system, we previously found good correspondence between observations on receptor interactions made for *A*. *thaliana* proteins expressed in *N*. *benthamiana* and *A*. *thaliana* (Bleckmann et al., 2010; Stahl et al., 2013). Furthermore, with the inducible system, we can perform measurements with low protein concentrations, thereby reducing the occurrence of overexpression artifacts.

To measure the effects of the ligands on the interaction state of their cognate receptors, we infiltrated a 1 μM peptide solution into the leaves. We assumed that the concentration of peptide initially reaching the receptors is much lower than 1 μM and continuously increases to a final concentration approaching 1 μM during the time course of the experiment.

After selecting multiple cells coexpressing the fusion proteins, we performed MFIS recordings of these cells every 10 min for 1 hour to monitor the interaction states of the receptors. We analyzed two main values: the fluorescence lifetime (τ) and the fluorescence anisotropy (r). The fluorescence lifetime of a fluorophore describes the time that the fluorophore remains in the fluorescent state after being excited by a laser pulse. Hetero-FRET between the GFP and mCherry quenches the fluorescence of GFP, which results in a shortened fluorescence lifetime for GFP (Gadella et al., 1993). The fundamental anisotropy (r_0) of free GFP in an aqueous solution and in the absence of any rotation is ~ 0.38. This anisotropy is altered by the rotational freedom of a fluorophore. Unbound GFP is free to rotate at all angles, although it rotates with a rather slow rotational diffusion time, $\rho \approx 15$ ns, because of its large hydrodynamic radius. With a fluorescence lifetime of $\tau = 2.6$ ns, GFP has a steady-state anisotropy of $r = 0.32$, which is derived from the Perrin equation [$r = r_0/(1 + \tau/\rho)$] (Perrin, 1929). If the GFP is fused to a protein, the rotational freedom of GFP is reduced and, therefore, the value of *r* increases. In contrast, indirect excitation of a GFP by another juxtaposed GFP (homo-FRET) leads to a depolarization of the signal and, therefore, a reduction in total GFP anisotropy. Because of these properties, anisotropy measurements provide additional information about the FRET state of a fluorophore (Gautier et al., 2001). The results of measurements at different time points were plotted in two-dimensional MFIS plots as steady-state anisotropy r versus lifetime τ (Figure 3-1A).

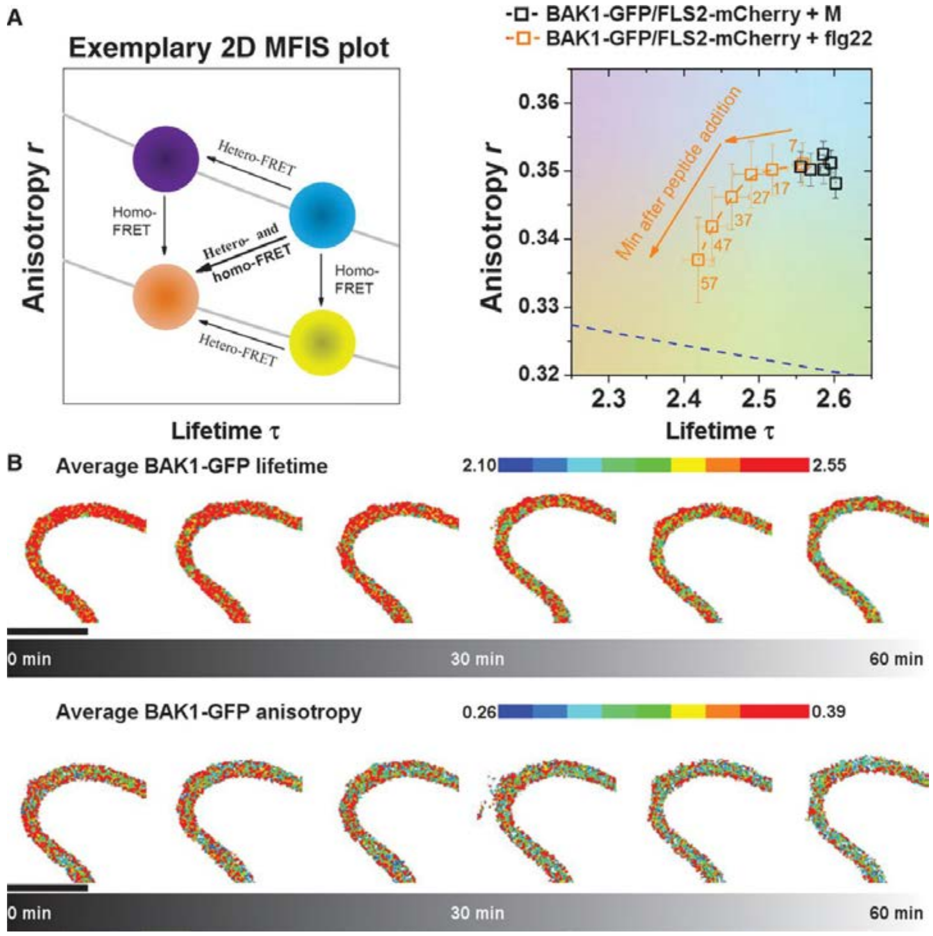

Figure 3-1 Changes in average BAK1-GFP fluorescence lifetime and anisotropy over time. (**A**) Left: Exemplary two-dimensional (2D) MFIS plot demonstrating the effects of various combinations of hetero- or homo-FRET on fluorophore lifetime and anisotropy. The blue sphere represents the fluorophore. The average donor fluorescence weighted lifetime (average $\langle \tau_D \rangle_f$), shortened to "lifetime (τ)," is plotted on the x axis, and the anisotropy (r) on the y axis. Hetero-FRET results in a decrease in τ and an increase in r. Hence, the data points would shift from the position of the blue to the violet sphere. Homo-FRET results in a decrease in r with no effect on τ. The data point would shift to the yellow sphere. A combination of homo- and hetero-FRET results in a decrease in both τ and r. The data point would shift to the orange sphere. Right: MFIS plot for BAK1-GFP in cells coexpressing FLS2-mCherry exposed to the indicated peptides. τ is the average of six cells per time point. The dashed line represents r and τ for free GFP according to the Perrin equation (23). min, minutes after peptide infiltration. Data are plotted as the average ± s.e.. (**B**) The top shows a magnified section of a cell, coexpressing BAK1-GFP and FL2-

mCherry, exposed to flg22 with the BAK1-GFP lifetime (τ) represented over a 60-min time period. The bottom shows the anisotropy of BAK1-GFP in the same area. Scale bar, 10 μm.

Furthermore, we quantified the distribution of different complexes, which exhibit different fluorescence lifetimes, by determining how heterogeneous the measured lifetimes from all pixels of the fluorescence lifetime imaging microscopy (FLIM) images were. If the same complexes are formed everywhere along the plasma membrane, then all the pixels will have comparable lifetimes and the heterogeneity of the sample will be low. If treatment with the receptor ligand results in the formation of different or unevenly distributed complexes, the lifetime heterogeneity will increase over time. This lifetime heterogeneity in a sample can be quantified as theta (θ). Finally, we analyzed if a change in average fluorescence lifetime resulted from the formation of more numerous FRET-active complexes (complexes containing misfolded mCherry are “FRET-inactive”) or from an altered arrangement of the measured molecules in which the two fluorophores are brought into closer proximity, which would affect the efficiency of FRET. To distinguish between these two possibilities (more FRET-active complexes or rearranged complexes with higher FRET efficiencies), we determined the fraction of FRET-active complexes (x_{FRET}) and the FRET efficiency (E) by pixel-integrated MFIS-FRET analysis (see Materials and Methods for details on the technical procedures).

3.2.2 Detection of flg22-dependent stepwise formation of multimeric BAK1/FLS2 complexes at the plasma membrane

Although MFIS measurements have been applied to plant cells before, real-time imaging over time has not (Weidtkamp-Peters et al., 2009). As a proof of principle, we monitored the ligand-triggered interaction between the flg22 receptors FLS2 and BAK1 (Chinchilla et al., 2007). We chose this interaction because it is well studied, and we therefore have a clear expectation: when treated with the flg22 peptide, the two receptors should interact and form complexes at the plasma membrane. Consequently, we should be able to monitor how the receptors change from a noninteracting into an interacting state over time after the addition of peptide.

We first tested if we detected preassembled BAK1 (BAK1/BAK1) and FLS2 (FLS2/FLS2) before flg22 is perceived. We performed FRET-APB measurements, which only detect hetero-FRET between GFP and mCherry, with GFP- and mCherry-tagged versions of the proteins. Although C-terminal fusions to BAK1 impair the protein's signaling capacity, ligand-dependent complex formation with FLS2 is not impaired by the tag (Ntoukakis et al., 2011). We measured donor dequenching, which we quantified as apparent FRET efficiency (ap. E%) after mCherry photobleaching (Karpova et al., 2003), to detect the interactions between BAK1-GFP and BAK1-mCherry (or FLS2-GFP and FLS2-mCherry). We measured, as a negative control, the ap. E% of BAK1-GFP (or FLS2-GFP) expressed without an mCherry fusion protein and, as a positive control, the ap. E% of a version of BAK1 (or FLS) tagged with both GFP and mCherry fused directly together. Control measurements resulted in an ap. E% of ~0 for the negative and ~18 for the positive controls (Table 3-1). Values for BAK1/BAK1 or FLS2/FLS2 were comparable to negative controls, indicating that these receptors did not interact.

Protein A	Protein B	ap. E%	s.d.
BAK1-GFP	-	- 2.6	1.6
BAK1-GFP-mCherry	-	16.7	6.0

BAK1-GFP	BAK1-mCherry	0.7	1.7
BAK1-GFP	FLS2-mCherry	- 1.0	1.7
FLS2-GFP	-	- 2.6	1.2
FLS2-GFP-mCherry	-	20.5	3.1
FLS2-GFP	FLS2-mCherry	0.7	1.3

Table 3-1 BAK1-BAK1 and FLS2-FLS2 interactions analyzed by FRET-ABP. Measurements for BAK1-GFP or FLS2-GFP alone are negative. BAK1-GFP-mCherry and FLS2-GFP-mCherry measurements are positive controls.

For all further experiments with a pixel-wise resolution, we used MFIS measurements of BAK1-GFP and FLS2-mCherry in control peptide (mock)–treated (Figure 3-5) or flg22-treated (Figure 3-6) cells over time (Figure 3-1A, B). The steady-state anisotropy of BAK1-GFP at the first time point was 0.35 for both treatments (Figure 3-1A, B, Figure 3-5 and Figure 3-6). This value is higher than the anisotropy value of free GFP (0.32), suggesting that the rotational freedom of BAK1-GFP is restricted. Furthermore, this indicated the lack of homo-FRET between two or more GFPs, and hence no BAK1-GFP homomer formation, which is consistent with the FRET-APB results showing that BAK1 did not interact with itself before complex formation with FLS2 (Table 3-1). Plotting the r-τ time series for cells expressing BAK1-GFP and FLS2-mCherry treated with the control peptide, we found no change in lifetime or anisotropy over time, indicating that BAK1 and FLS2 did not interact (Figure 3-1A and Figure 3-5). However, upon addition of flg22, both fluorescence lifetime and anisotropy decreased over time, indicating the formation of BAK1/FLS2 complexes (Figure 3-1A and B, and Figure 3-6). Notably, the lifetime decrease preceded the decrease in anisotropy, indicating that the formation of BAK1/FLS2 heterodimers preceded the formation of BAK1/FLS2 multimers: At ~17 min after peptide treatment, the lifetime of BAK1-GFP was reduced compared to that of the control, indicating that a fraction of BAK1-GFP molecules was in a complex with FLS2-mCherry. We detected a reduction in the anisotropy of BAK1-GFP after ~37 min, indicating that the occurrence of homo-FRET (and therefore BAK1/BAK1 homodimerization) occurred after BAK1/FLS2 heterodimerization (Figure 3-1A). These results indicated that in a first step after flg22 perception, BAK1/FLS2 heterodimers are formed, which would then in a second step aggregate to form larger complexes through interaction of the BAK1 molecules.

The measured lifetimes and anisotropy values are averages of all photons from all pixels collected in one image. This explains why the lifetime is only different from the negative control ~17 min after peptide infiltration, whereas complexes can be detected by coimmunoprecipitation after a few seconds (Schulze et al., 2010). Here, the number of molecules in a complex must be high enough to alter the mean of the entire pixel. The flg22-induced receptor complexes are internalized after ligand binding, with vesicles detectable after ~25 min (Robatzek et al., 2006). Nonetheless, we found that the total fluorescence intensity of BAK1-GFP or FLS2-mCherry was stable over the course of 1 hour (Figure 3-5 and Figure 3-6), most likely because only a small number of vesicles were targeted for degradation during this time. To verify that the reduced lifetime observed resulted from the formation of new complexes, rather than a change in FRET efficiencies of preexisting complexes, we determined the FRET efficiencies (E) and fraction of FRET-active complexes (x_{FRET}). Over time, the FRET efficiency was unchanged (Figure 3-7A, B), whereas the number of molecules in FRET complexes increased in the flg22-treated sample (Figure 3-2A and Figure 3-7A). Furthermore, we found that the lifetime was homogeneous along the entire membrane and did not change during the observation time of 1 hour, indicating that BAK1/FLS2 complexes were evenly distributed along the membrane (Figure 3-2B). Thus, the MFIS technique reliably reported the interaction states of receptor proteins in living plant cells over time.

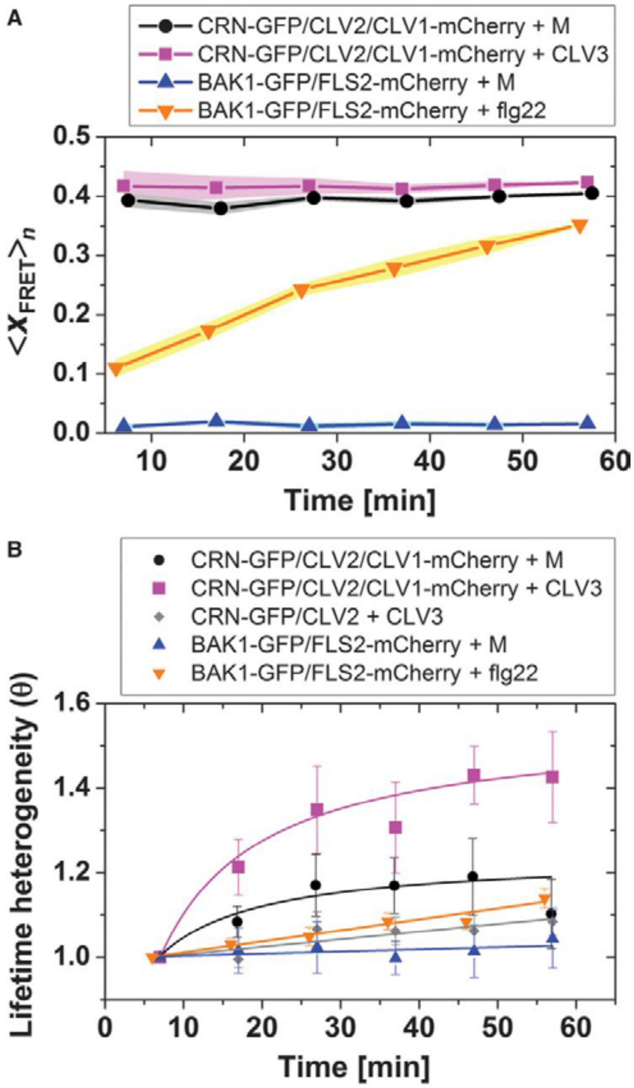

Figure 3-2 Quantification of BAK1-GFP and CRN-GFP lifetime heterogeneity (θ) and FRET efficiencies. (**A**) Time series for fractions of FRET-active complexes (x_{FRET}) in cells expressing the indicated receptors and exposed to the indicated peptides. n = 6 cells from two independent experiments for the cells expressing CRN-GFP, CLV2, and CLV1-mCherry exposed to CLV3; n = 4 for cells expressing CRN-GFP, CLV2, and

CLV1-mCherry exposed to the control peptide (M); n = 6 for cells expressing BAK1-GFP and FLS2-mCherry exposed to flg22; n = 5 for cells expressing BAK1-GFP and FLS2-mCherry exposed to the control peptide (M). Tinted areas represent the SEM. (**B**) Lifetime heterogeneity (θ) for cells expressing the indicated receptors exposed to the indicated peptides. n = 6 cells from two experiments for cells expressing BAK1-GFP and FLS2-mCherry exposed to flg22; n = 5 for cells expressing BAK1-GFP and FLS2-mCherry exposed to the control peptide (M); n = 3 for cells expressing CRN-GFP and CLV2 exposed to CLV3; n = 6 for cells expressing CRN-GFP, CLV2, and CLV1-mCherry exposed to the control peptide (M) or CLV3. Data are plotted as average ± s.e..

3.2.3 Detection of preformed receptor complexes in the CLAVATA pathway

We then used the MFIS technique to monitor the interaction states of the CLV3 receptors to investigate if the three reported complexes all formed at the plasma membrane at the same time and in the same regions, if the receptor complexes are evenly distributed at the plasma membrane, and how CLV3 alters the behavior of the receptors at the membrane. Similar to our approach for BAK1 and FLS2, we transiently coexpressed CRN-GFP, CLV2, and CLV1-mCherry in *N. benthamiana* and exposed the cells to either CLV3 or an inactive, but closely sequence-related, control peptide (mock). Because CRN-GFP is only exported from the ER to the plasma membrane when in a complex with CLV2, we interpreted the localization of CRN-GFP at the plasma membrane as indicator that CLV2, which did not have a fluorophore attached, was expressed. The initial lifetime of CRN-GFP, coexpressed with CLV1-mCherry, at the first time point was ~2.37 ns, independent of the treatment (Figure 3-3A, B, Figure 3-8 and Figure 3-9), compared to 2.57 ns when CRN-GFP and CLV2 were expressed without CLV1-mCherry (Figure 3-3A), indicating that the three proteins interacted and were present as part of the preassembled CLV1/CLV2/CRN receptor complexes at the plasma membrane even in the absence of CLV3.

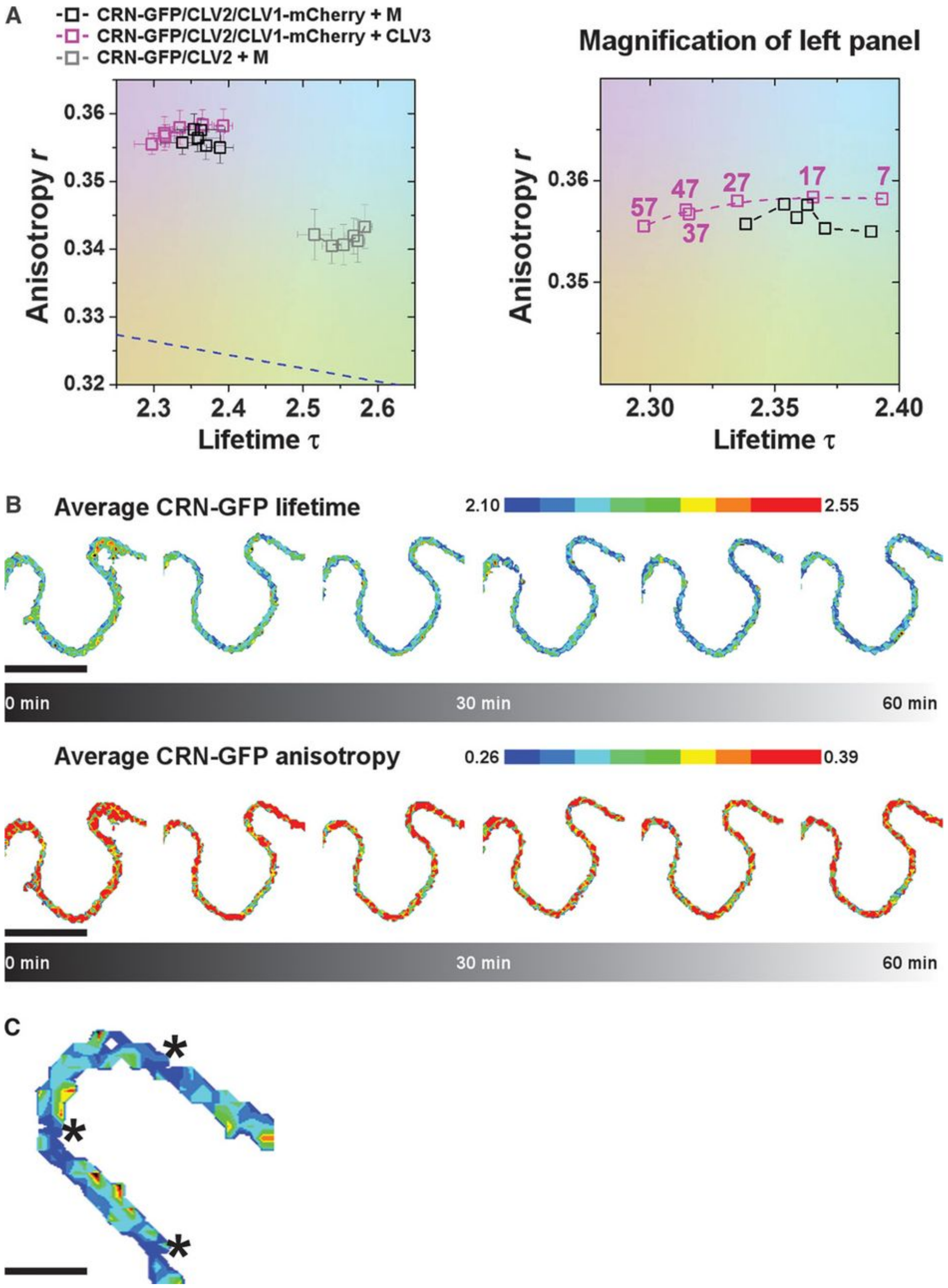

Figure 3-3 Changes in average CRN-GFP fluorescence lifetime (τ) and anisotropy (r) over time. Data were collected from cells expressing CRN-GFP, CLV2, and CLV1-mCherry that were exposed to the control peptide (M) or CLV3 or from cells expressing CRN-GFP and CLV2 that were exposed to the control peptide. (**A**) Left: MFIS plot of data for the indicated cells exposed to the indicated peptides. The dashed line represents r and τ for free GFP according to the Perrin equation (Perrin, 1929). Data are plotted as average ± SE. Right: Expanded view of the area containing the data from the cells expressing CRN-GFP,

CLV2, and CLV1-mCherry. Error bars were removed for easier viewing. Dotted lines connecting the data points represent the chronological order. min, minutes after peptide infiltration. n = 6 cells per time point. (**B**) Top: A magnified section of a representative cell expressing CRN-GFP, CLV2, and CLV1-mCherry that was exposed to CLV3 with the CRN-GFP lifetime (τ) represented over a 60-min time period. Bottom: Anisotropy of CRN-GFP over the same area. Scale bar, 10 μm. (C) A magnified region showing subdomains with reduced lifetime of CRN-GFP in CLV3-treated cells expressing CRN-GFP, CLV2, and CLV1-mCherry. The asterisks mark the regions with reduced lifetime. Scale bar, 2.5 μm.

We evaluated cells exposed to CLV3 to investigate if ligand perception altered the formation or distribution of these preexisting receptor complexes. CLV3 led to a continuous decrease of GFP lifetime from 2.37 to 2.30 ns within 1 hour (Figure 3-3A, B, and Figure 3-8). A smaller decrease occurred in mock-treated cells, where the lifetime varied in the range of 2.35 to 2.37 ns (Figure 3-3A and Figure 3-8). For both the CLV3- and mock-treated cells, the changes in lifetime were not accompanied by a visibly altered signal intensity for the GFP or mCherry channel, indicating that the total amount of receptor proteins detected at the plasma membrane remained constant (Figure 3-8 and Figure 3-9). Because for this experiment, we averaged the lifetimes over all pixels in a given image, which does not allow to resolve local differences, we next performed a pixel-wise analysis.

3.2.4 Receptor complex clusters along the plasma membrane triggered by CLV3

When the lifetimes of all collected photons were overlaid onto the FLIM image of the cells, we noticed the emergence of small regions along the plasma membrane that exhibited reduced lifetimes 1 hour after addition of CLV3 (Figure 3-3B, C). However, because the lifetime of the GFP fusion proteins in the other areas of the plasma membrane was stable, the average lifetime of all pixels was only weakly affected by these regional differences. To quantify this regional effect of CLV3 treatment, we compared the lifetime heterogeneity (θ) of cells expressing only CRN-GFP and CLV2-mCherry that were exposed to CLV3 to that of cells expressing CRN-GFP, CLV2, and CLV1-mCherry that were exposed to either CLV3 or the control peptide (Figure 3-2B). When expressed together without CLV1, CRN-GFP and CLV2-mCherry exhibited a smooth membrane distribution that was unaffected by the addition of CLV3, with an average θ close to 1. In contrast, in cells expressing CRN-GFP, CLV2, and CLV1-mCherry, exposure to the control peptide or CLV3 resulted in an increase in lifetime heterogeneity. However, the increase in lifetime heterogeneity for the cells exposed to the control peptide plateaued within 30 min at ~1.2, whereas the increase continued throughout the time course for cells exposed to CLV3, reaching 1.5 at 1 hour. These data indicated that CLV2/CRN heterodimers remained evenly distributed along the membrane (θ remained ~1 over time), whereas the CLV1/CLV2/CRN multimers localized slightly more heterogeneously in subdomains of the membrane (θ remained ~1.15 over time) and reacted to CLV3 with increasing clustering over time (θ increased up to 1.5 after 1 hour).

On the basis of this increase in fluorescence lifetime heterogeneity and the observed formation of regional lifetime differences along the plasma membrane in the images, we concluded that the binding of CLV3 to the receptor complexes triggered the clustering of more CLV1/CLV2/CRN multimers in subdomains of the plasma membrane. This observed CLV3-triggered clustering of smaller complexes into larger multimers should also be reflected in the measured FRET efficiencies and FRET-active complexes. In contrast to the BAK1/FLS2 interaction that we observed, the data indicated that the CLV3 receptors were already in FRET-active complexes before the addition of peptide.

Accordingly, the fraction of FRET-active complexes (x_{FRET}) should not change over time, but the FRET efficiency (E) should increase, because of more molecules being in closer proximity in these larger multimers. The FRET-active complex fraction x_{FRET} remained unchanged over time in cells expressing CRN-GFP, CLV2, and CLV1-mCherry that were exposed to CLV3 or the control peptide (Figure 3-2A), whereas the FRET efficiency between CRN-GFP and CLV1-mCherry in these cells exposed to CLV3 slightly increased from 0.36 to 0.45 (Figure 3-7). Therefore, we inferred that the molecular environment for CRN/CLV2/CLV1 multimers became more crowded after the addition of CLV3, suggesting the formation of larger clusters.

3.3 Discussion

To test whether the MFIS technique is suitable to monitor the interaction state of receptor proteins in living plant cells over time, we monitored the complex formation between BAK1 and FLS2 after the addition of the ligand flg22. With MFIS, we recorded the expected formation of receptor complexes, but we also obtained previously unknown insights on the nature of receptor complex assembly. We found that both FLS2 and BAK1 form neither homomers nor heteromers before flg22 recognition at the plasma membrane. This is in accordance with the findings of Ali *et al*. (Ali et al., 2007), who monitored FLS2 at the plasma membrane using FRET and FRAP with a protoplast system. This is in contrast to the results of Sun *et al*. (Sun et al., 2012), who detected FLS2 homomers in the absence of the ligand by coimmunoprecipitation experiments with cell extracts. A possible interpretation of both apparently contradictory results would be that FLS2 does not form homomers in the absence of flg22 at the plasma membrane but can homomerize upon internalization, which would be detected only in the coimmunoprecipitation experiments.

After ligand perception, we showed that heterodimeric FLS2/BAK1 complexes formed initially and subsequently aggregated to form larger complexes. These larger complexes likely consist of two BAK1 and two FLS2 molecules, with the two BAK1 molecules interacting directly with each other, flanked by FLS2 on each side to form an FLS2/BAK1/BAK1/FLS2 tetrameric arrangement (Figure 3-4A). Each of the two FLS2/BAK1 units would be active in both extracellular signal perception and intracellular transduction. This tetrameric arrangement could explain why Ali *et al*. (Ali et al., 2007) did not detect FLS2/FLS2 homomers after flg22 treatment: their position on the flanks of the complex would distance the FLS2 molecules too far apart for FRET. Our results also indicated that the composition of the formed complexes appeared the same along the entire plasma membrane because the BAK1-GFP fluorescence lifetime distribution was homogeneous.

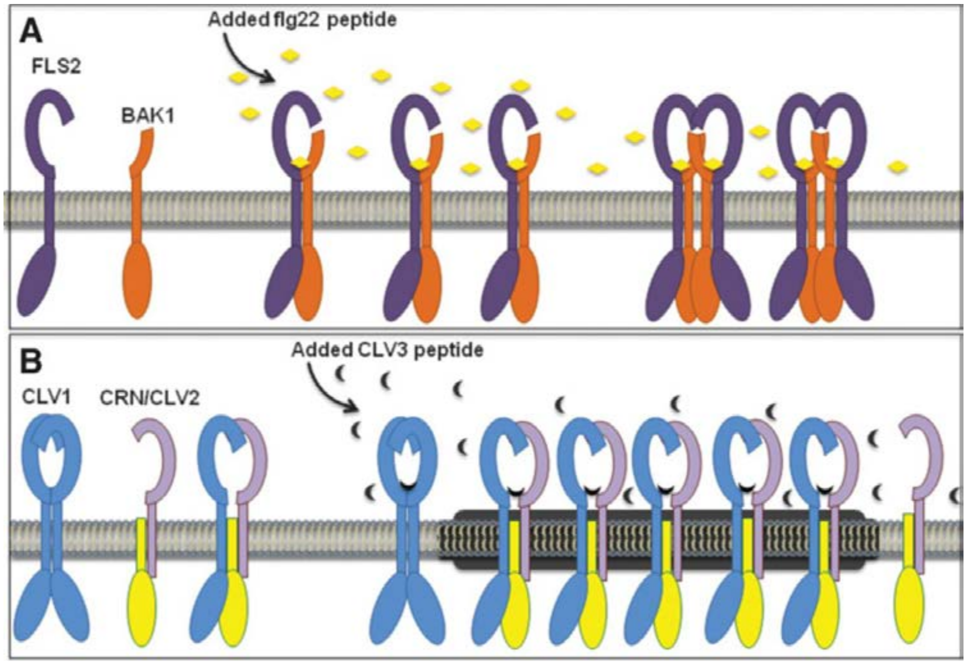

Figure 3-4 Models for stepwise assembly of complexes and clusters in the flg22 and CLV3 signaling pathways. (**A**) The flagellin pathway. In the absence of flg22, the two receptors FLS2 and BAK1 do not interact. When flg22 is present, complexes consisting of one BAK1 and one FLS2 molecule are formed in the first step. In the second step, these dimers form larger complexes consisting of two central BAK1 molecules with one FLS2 molecules on each flank. (**B**) The CLV pathway. Without CLV3 present, CLV1 forms preferentially homomers, CRN and CLV2 form heteromers, and only few CLV1/CLV2/CRN multimers are formed. When CLV3 is present, CLV1/CLV2/CRN multimers cluster in membrane subdomains.

We then applied MFIS to monitor the interaction states of the receptor proteins in the CLV signaling pathway. The CLV pathway is the key regulatory pathway in plant stem cell homeostasis. Plants maintain a constant number of stem cells in their aboveground stem cell niches, which are the shoot apical, axillary, and floral meristems. The key to the maintenance of these stem cell pools is a tight balance between stem cell proliferation and differentiation of their descendants. This regulation operates continuously, requiring the presence of receptor complexes at all times. We found that three different types of complexes were preformed at the plasma membrane and had the capacity to bind CLV3: these are CLV1/CLV1 homomers, CLV2/CRN heteromers, and CLV1/CLV2/CRN multimers. Of these three types of complexes, the CLV1/CVL1 homomers and CLV2/CRN heteromers were evenly distributed along the plasma membrane. Taking into account that the CLV2 receptor domain does not directly bind CLV3 and the atypical nature of the kinase domain of CRN, we expect that these CLV2/CRN heteromers require another active RLK to be fully functional. MFIS analysis indicated that CLV3 triggered the formation of the larger CLV1/CLV2/CRN multimers, preferentially in membrane subdomains (Figure 3-4B). Within these complexes, CLV2/CRN may act as co-receptors for CLV1, thereby increasing the specificity of the interaction between CLV3 and CLV1, or CLV2/CRN may aid in the assembly of signaling-competent complexes. Sequestration of receptor complexes into membrane subdomains might facilitate the assembly of additional factors necessary for downstream signaling, including the phosphatases that limit the kinase activities of RLKs (Simons and Toomre, 2000; Stone et al., 1998; Yu et al., 2003). Our model with both an active CLV1/CLV1 homomer and a CLV1/CRN/CLV2 heteromer is not in contrast to the published genetic data, which suggested two parallel and independently acting pathways (Müller et al., 2008) on the basis of the observation that *clv1*/*clv2* and *clv1*/*crn* double mutants are additive, whereas *clv2*/*crn* double mutants are not (Müller et al., 2008). This is consistent with all three receptors contributing to CLV3 signaling as components of CLV1/CLV1 homomers, CLV2/CRN heteromers, and CLV1/CLV2/CRN heteromeric complexes. An alternative function for the rapid clustering of CLV1/CLV2/CRN complexes in subdomains in the presence of ligand may be to sequester the receptors and enable their inactivation. In this case, the CLV1/CLV1 homomers and CLV2/CRN heteromers would signal in parallel and mostly independently, whereas the multimeric CLV1/CLV2/CRN complexes in the subdomains would be inactive. Clustering of the two otherwise independent signaling complexes in larger multimeric aggregates would provide a simple but effective means to facilitate the rapid and parallel down-regulation of both pathways in a situation with excess CLV3. The steady increase of clusters over time could then reflect the increasing amount of peptide that reaches the receptors, leading to their activation and subsequent sequestration. Such a mechanism may protect meristems from terminal stem cell loss after a transient surge in CLV3 abundance. Here, it is not clear how the membrane regions in which these multimers cluster are defined. These clusters may form at the contact sites of the cytoskeleton-guided ER or Golgi strands at the plasma membrane or within detergent-resistant membrane fractions (Gish et al., 2013).

A similar clustering of receptors upon ligand stimulation has been proposed for the epidermal growth factor receptor (EGFR) in mammalian cells (Kozer et al., 2013). By combining microscopy, image correlation spectroscopy, phosphorylation assays, and computational modeling of mass action kinetics, Kozer *et al*. (Kozer et al., 2013) suggested that EGFRs are localized at the plasma membrane as preformed dimers and that ligand leads to formation of higher-order oligomers in clusters along the plasma membrane, which then participate in transphosphorylation (Kozer et al., 2013). EGF-triggered clustering of EGFR is mediated by the scaffolding protein flotillin-1 (flot-1, also known as reggie-2), which localizes to lipid rafts in the plasma membrane and subsequently aids in the formation of larger EGFR-containing complexes that activate a downstream mitogen-activated protein kinase (MAPK) signaling cascade (Amaddii et al., 2012). In *Arabidopsis*, the protein family related to flot-1 is the HIR family, consisting of four proteins. HIRs localize to microdomains in the plasma membrane and are involved in LRR receptor–mediated signaling pathways (Qi et al., 2011). Furthermore, there is evidence that the CLV receptors regulate shoot meristem homeostasis partially through signaling through the MAPK cascades. CLV1 functions as a CLV3-dependent negative regulator of the activity of the MAPK MPK6 activity, whereas CLV2 appears to counter this effect, thereby providing another mechanism to fine tune CLV3-dependent signaling (Betsuyaku et al., 2011).

In the neuregulin (NRG) pathway, the EGFR-related ErbB4 is evenly distributed along the plasma membrane, with only some molecules in lipid rafts before ligand perception. Addition of the ligand NRG results in a relocalization and clustering of the existing protein complexes into lipid rafts, together with several associated signaling molecules, displaying a mechanism similar to our observations for the CLV3 receptors (Ma et al., 2003).

The observation that FLS2/BAK1 complexes only formed when the ligand was present is intriguing, especially when considered within the biological context. The FLS2/BAK1 complex is only required in the case of bacterial infection, and formation of this complex at the plasma membrane in the absence of ligand could result in basal activity of flagellin signaling and could compromise growth and development (Gómez-Gómez and Boller, 2000). Such inappropriate activation of immune responses would therefore incur a fitness penalty. Activation of the growth-promoting brassinosteroid receptor (BR) pathway, which is mediated by the receptor BRI1 and BAK1, inhibits immune signaling. This inhibition, however, does not occur through competition between FLS2 and BRI1 for the BAK1 co-receptor, but downstream of the receptors (Albrecht et al., 2012).

The observation that the flagellin receptors are kept separate and the CLV receptors form complexes independent of ligand availability seems to reflect the nature of the two pathways. In contrast to defense signaling, stem cell homeostasis is a continuous process, requiring the pathway to be active at all times. Our findings indicated that this physiological difference is reflected at the molecular level in the interaction properties of the signaling receptors. A similar observation was described by Bücherl *et al*. (Bücherl et al., 2013), who reported that ~7% of the BRI1 molecules interact with BAK1 in the absence of ligand. Addition of BR then results in an increase in heteromers. This is in accordance with our findings that in a constitutively active pathway involved in plant development, some receptors are maintained in a ready state to ensure ongoing signaling (Bücherl et al., 2013). Our study demonstrated that MFIS applied to living plant cells not only monitored the interaction states of several receptors over time but also detected changes in the composition of existing complexes, revealing a dynamic view of signaling in plants.

3.4 Materials and Methods

3.4.1 Plant Reporter Lines

Nicotiana benthamiana plants were grown in the greenhouse for 4 weeks before transient transformation. Transformation and expression were described before (Bleckmann et al., 2010).

3.4.2 Construction of Inducible Receptor Fusions

The CLV1, CLV2, CRN, and BAK1 expression vectors were described before (Bleckmann et al., 2010). The FLS2 fusions were created from complementary DNA using the pENTR/D-TOPO and Gateway LR Clonase II cloning kits, as well as the destination vectors pABindGFP, pABindmCherry, and pABindFRET, as described previously (Bleckmann et al., 2010).

3.4.3 Peptides

The peptides flg22 (QRLSTGSRINSAKDDAAGLQIA), CLV3 (RTV[Hyp]SG[Hyp]DPLHHH) and the inactive control peptide (LPQHPHGRSDVT) were ordered from ThermoFisher Scientific. They were infiltrated into the transformed plant leaves immediately before imaging at an initial concentration of 1 µM in infiltration medium using 1 ml flat-top syringes as described in Bleckmann et al. (Bleckmann et al., 2010).

3.4.4 Microscopy

Measurements were performed using a multiparameter fluorescence detection setup as described previously (Kudryavtsev et al., 2006; Weidtkamp-Peters et al., 2009). Experiments were performed with a confocal laser scanning microscope (FV1000, Olympus) additionally equipped with a single photon counting device with picosecond time resolution (Hydra Harp 400, PicoQuant). GFP was excited at 485 nm with a linearly polarized, pulsed (32 MHz) diode laser (LDH-D-C-485, PicoQuant) at 0.8 μW at the objective [60× water immersion, Olympus UPlanSApo NA (numerical aperture) 1.2, diffraction-limited focus]. mCherry was excited at 559 nm with a continuous wave laser (FV1000) at 5.4 μW at the objective. The emitted light was collected in the same objective and was separated into perpendicular and parallel polarization with respect to excitation polarization. GFP fluorescence was then detected by an avalanche photodiode (PDM50-CTC, Micro Photon Devices) in a narrow range of its emission spectrum (bandpass filter, HC520/35; AHF). mCherry fluorescence was detected by a hybrid photodetector (HPMC-100-40, Becker & Hickl), of which the detection wavelength range was set by the bandpass filters (HC 607/70, AHF). Images were taken with 20-μs pixel dwell time and a resolution of 103 nm/pixel. A series of 40 frames were merged into one image and further analyzed using custom-designed software (LabVIEW).

The FRET-APB measurements were done on a Zeiss LSM 780. GFP was excited with a continuous wave argon laser at 488 nm using a 40× water immersion objective (Zeiss C-Apochromat 40×/1.20 W Corr M27), and emission was detected between 498 and 524 nm by a GaAsP detector. mCherry was excited using a 561-nm continuous wave diode-pumped solid-state laser, and emission was detected between 578 and 639 nm. A series of 12 256 × 256 pixel frames with 0.18 μm pixel size, 47 μm^2 image size, and 1.27 μs pixel dwell time was recorded. After five frames, mCherry was photobleached in a region of interest along the plasma membrane by 80 iterations with 100% laser power. The FRET efficiency (ap E%) was determined as the change in GFP intensity after photobleaching of the acceptor mCherry by [(GFP_{after} − GFP_{before})/GFP_{after} × 100].

3.4.5 Pixel-wise fluorescence-weighted lifetime analysis

The histograms presenting the decay of fluorescence intensity after the excitation pulse were built for each pixel with 128 ps/bin. The fluorescence-weighted lifetime of the donor molecule in single pixel was determined using a model function containing only two variables ($\langle\tau_D\rangle_f$) and scatter contribution [for details, see (Stahl et al., 2013)], with maximum likelihood estimator (MLE). The instrument response function was measured with the back reflection of the laser beam and used for iterative reconvolution in the fitting process.

3.4.6 Pixel-wise anisotropy analysis

The steady-state anisotropy is given by $r_G = \frac{F_{\|} - G \cdot F_{\perp}}{F_{\|} + 2 \cdot G \cdot F_{\perp}}$, where $F_{\|}$ and $F_{\perp}$ are the average fluorescence count rates within a pixel, with a polarization parallel and perpendicular to that of the excitation light, respectively. Both were corrected for dead time of the detection electronics (Becker, 2005) and mixing of polarization in the high numerical aperture objective (Schaffer et al., 1999); $F = F_{\|} + 2GF_{\perp}$ is the total fluorescence intensity. Calibration measurements with Rhodamine 110 delivered the *G*-factor to correct the signal for orientational sensitivity differences of the detection system.

3.4.7 Fluorescence lifetime heterogeneity analyses

With MLE, the variance of fluorescence lifetime distribution ${\sigma_0}^2$ is inversely proportional to the number of photons in the decay histogram N under shot noise-limited conditions: $\theta_0 = {\sigma_0}^2 \cdot N$. The constant θ_0 that governs the width of the lifetime distribution can be calculated [for details see (Maus et al., 2001)]. For the experiments in living cells, lifetime distribution is wider than what is expected in the ideal condition due to detector noise and the heterogeneous cellular environment in biological samples. This will be reflected by a larger θ value than θ_0. To quantify the lifetime broadening, the θ value is calculated for each image according to $\theta = \sigma^2 \cdot \overline{N}$, in which σ^2 is the variance of the lifetime distribution and $\overline{N}$ is the mean photon count. Considering that each individual cell may have a different environment, which results in different absolute θ values, we normalized θ values of a set of k time-series measurements to that of the first measurement: $\overline{\theta^{(k)}} = \theta^{(k)} / \theta^{(l)}$. In this way, the time-independent lifetime broadening factors that exist in all the measurements are excluded by normalization, leaving only the time-dependent lifetime broadening due to peptide infiltration. After normalization the starting normalized θ value is always 1, so that different sets of time-series measurements can also be compared. An increasing θ value indicates that the lifetime distribution is wider, an indication that the whole population becomes more heterogeneous, and vice versa.

3.4.8 Quantitative MFIS-FRET pixel-integrated analysis

Noninteracting (donor-only) and interacting (donor-acceptor) species can be resolved in our lifetime-based FRET analysis. Two fluorescence lifetimes, $\tau_{D0}^{(1)}$ and $\tau_{D0}^{(2)}$, were assigned to donor-only species considering the typical bi-exponential characteristic of fluorescence proteins in vivo. When FRET occurs, the two donor lifetimes were quenched through (an) associated FRET rate(s): $\tau_{DA} = 1 / \left(\tau_{D0} + k_{FRET} \right)$. Using pre-determined donor lifetimes from donor-only sample, FRET rate constant(s) can be fitted for a subensemble of pixels. For the cells expressing BAK1-GFP and FLS2-mCherry and treated with flg22, pixels located at the plasma membrane of a given cell were selected as a subensemble, and two FRET rate constants were used in the fit. However, as additional selection criteria, only the pixels with lifetime shorter than 2.3 ns and green-to-red intensity ratio below 6.2 were selected as a subensemble to determine heterogeneity for cells expressing CRN-GFP, CLV2, and CLV1-mCherry and treated with CLV3 or mock peptide. One FRET rate was required in this case. FRET efficiency was calculated as $E = 1 - \langle \tau_{DA} \rangle_X / \langle \tau_{DO} \rangle_X$, $\langle \tau_{DA} \rangle_X$ and $\langle \tau_{DO} \rangle_X$ are the species-weighted donor lifetimes in the presence and in absence of acceptor, respectively.

3.4.9 Mean fraction of FRET active complexes, $\langle x_{FRET} \rangle_n$

To compare the peptide-induced effect in different cells (Figure 3-7), we computed the scaled fraction of FRET-active complexes ($\langle x_{FRET} \rangle_n$) for cell i at time point t: $x_{FRET,S}(t) = x_{FRET}(t) \cdot \frac{\frac{1}{n}\sum_{i=1}^{n}\left(x_{FRET}(t = end)\right)_i}{x_{FRET}(t = end)}$, where n is number of cells. The mean fraction of FRET-active complexes $\langle x_{FRET}(t) \rangle_n$ over n cells is calculated as $\langle x_{FRET}(t) \rangle_n = \frac{1}{n}\sum_{i=1}^{n}\left(x_{FRET,S}(t)\right)_i$.

3.5 Supplementary Figures

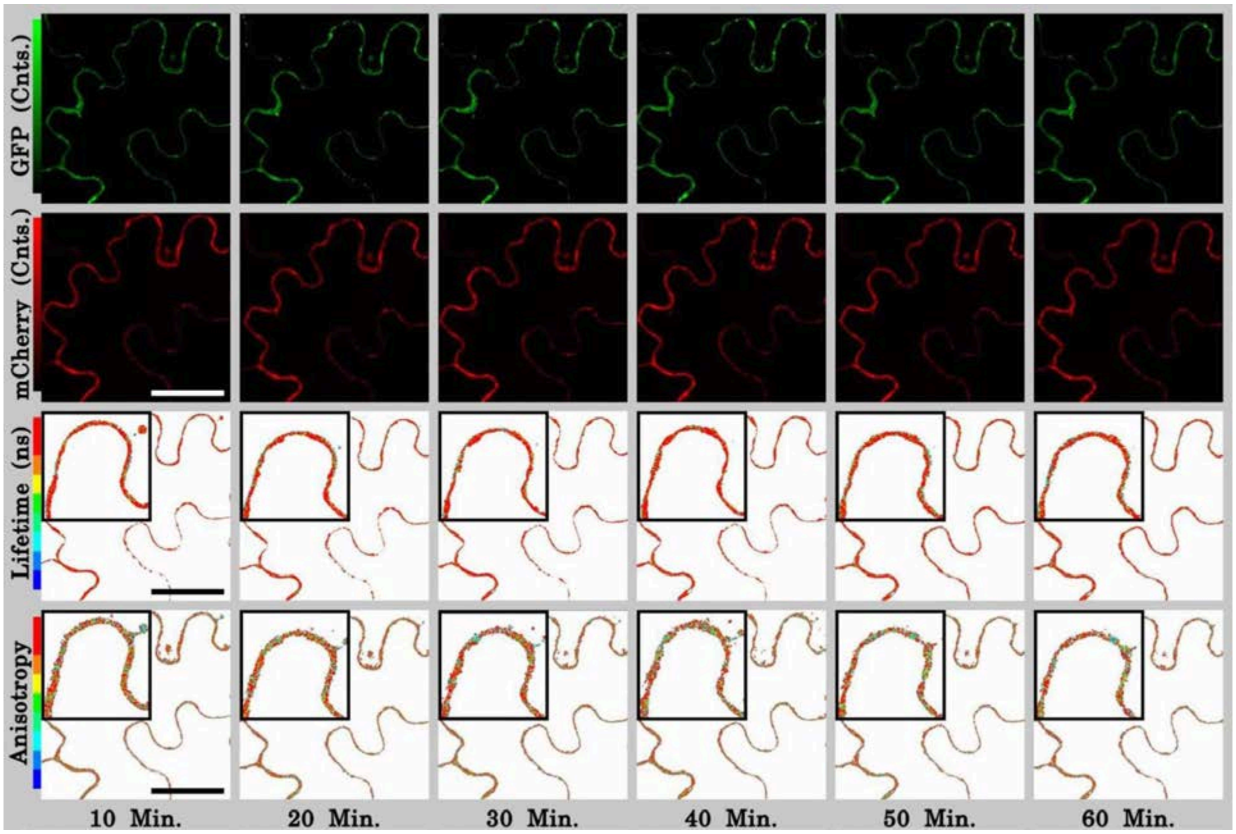

Figure 3-5 Fluorescence intensity, lifetime, and anisotropy projections on a cell expressing BAK1-GFP and FLS2-mCherry that was exposed to control peptide. Time series of a cell expressing BAK1-GFP and FLS2-mCherry exposed to an inactive control peptide. The average fluorescence intensities (top two rows), lifetime (third row), and anisotropy (bottom row) are unchanged over the course of one hour. Scales: GFP: 0 photons per pixel (ppp) (dark green) - 1600 ppp (light green); mCherry: 0 ppp (dark red) - 3600 ppp (light red); Lifetime: 2.0 ns (dark blue) - 2.9 ns (dark red); Anisotropy: 0.26 (dark blue) - 0.39 (dark red). ns = nanoseconds, Cnts. = photon counts per pixel, Min. = Minutes after peptide infiltration. Scale bar is 40 µm. Data are representative of two independent experiments.

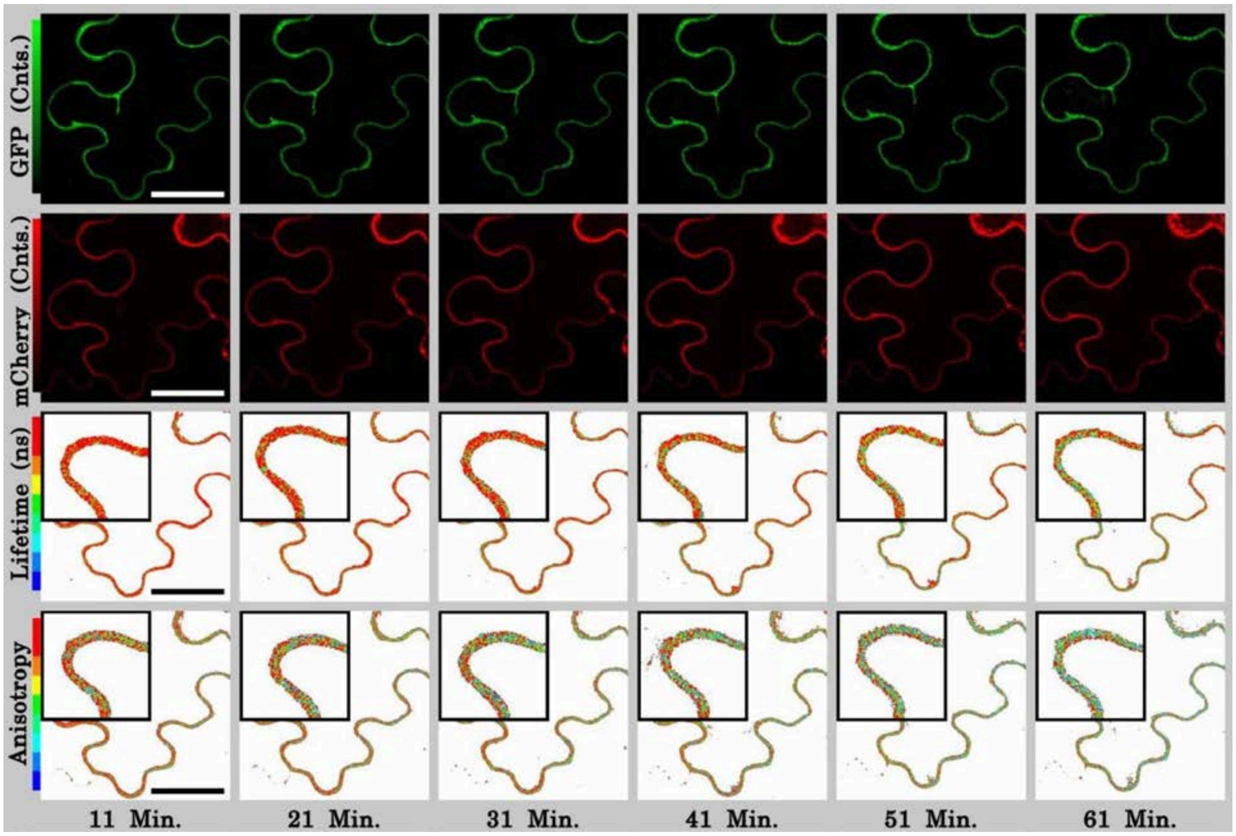

Figure 3-6 Fluorescence intensity, lifetime, and anisotropy projections on a cell expressing BAK1-GFP and FLS2-mCherry that was exposed to flg22. Time series of a cell expressing BAK1-GFP and FLS2-mCherry exposed to flg22. Although the average fluorescence intensities are unchanged for both BAK1-GFP and FLS2-mCherry over the course of one hour (top and second row), the average lifetime of BAK1-GFP (third row) drops from ~ 2.6 ns to ~ 2.43 ns over the course of one hour. The average anisotropy (lowermost row) drops from 0.35 to 0.325. Scales: GFP: 0 photons per pixel (ppp) (dark green) - 3600 ppp (light green); mCherry: 0 ppp (dark red) -5000 ppp (light red); Lifetime: 2.1 ns (dark blue) - 2.55 ns (dark red); Anisotropy: 0.26 (dark blue) - 0.39 (dark red). ns = nanoseconds, Cnts. = photon counts per pixel, Min. = Minutes after peptide infiltration. Scale bar is 40 µm. Data are representative of two independent experiments.

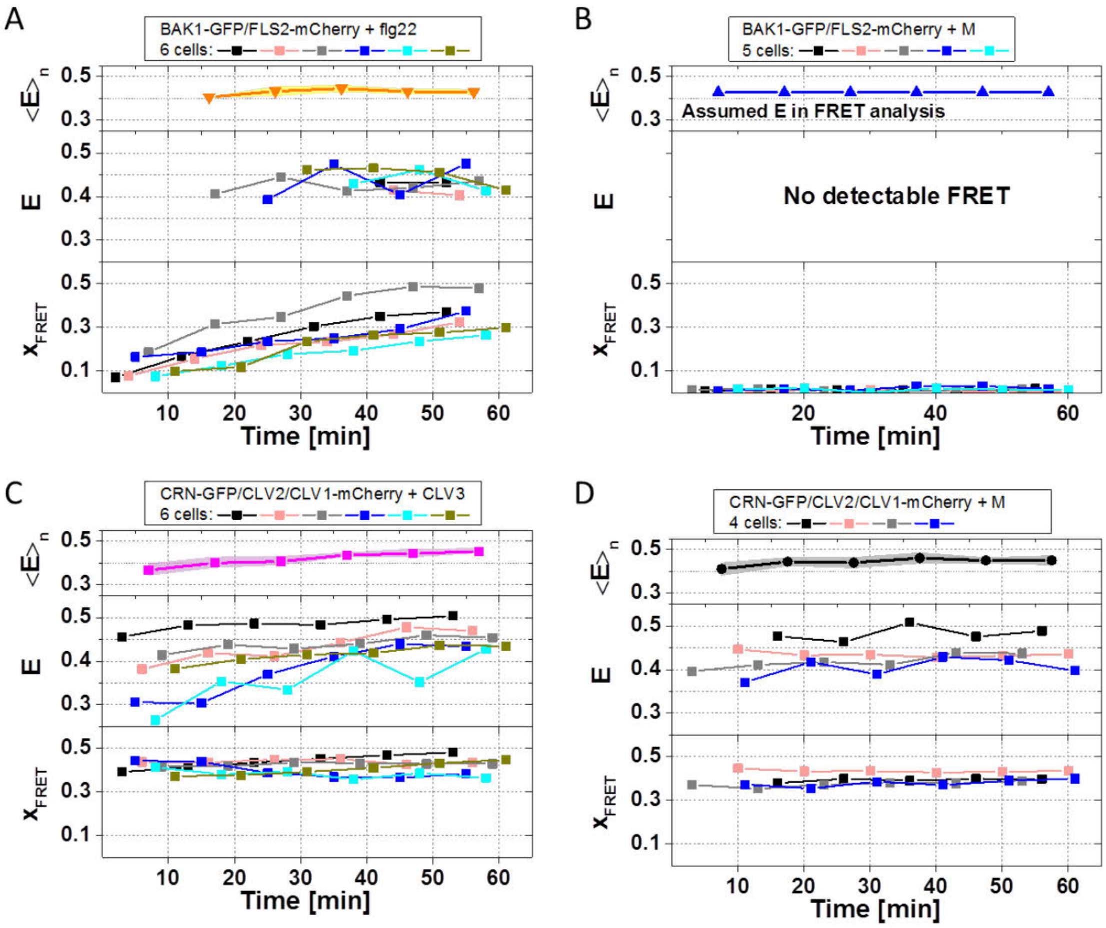

Figure 3-7 Time series of FRET efficiencies (E) and fraction of FRET-active complexes (x_{FRET}) of individual cells after peptide treatment. For individual cells, E (middle panel) and x_{FRET} (lower panel) determined from MFIS-FRET analysis are plotted. Average FRET efficiency ($\langle E \rangle_n$) was calculated for each round of the time-series measurement (upper panel). (**A**) After flg22 addition, FRET efficiency between BAK1-GFP and FLS2-mCherry remained unchanged but x_{FRET} increased over time. At early time points (< 20min) when the amount of FRET-active complexes started to increase but is still very limited, the applied fitting routines could not stably find the accurate FRET parameters, thus FRET efficiency in this case was not determined. (**B**) Analysis of the indicated cells exposed to control peptide (M). After addition of an inactive control peptide no detectable FRET was observed. In the FRET analysis, E was fixed to the average value obtained from the flg22 experiment, and x_{FRET} was determined to be close to ~0, proving that indeed no FRET occurred. (**C**) Upon CLV3 addition, FRET efficiency between CRN-GFP and CLV1-mCherry increased only slightly over time, whereas the fraction of interacting proteins remained constant. (**D**) Analysis of the indicated cells exposed to control peptide (M).

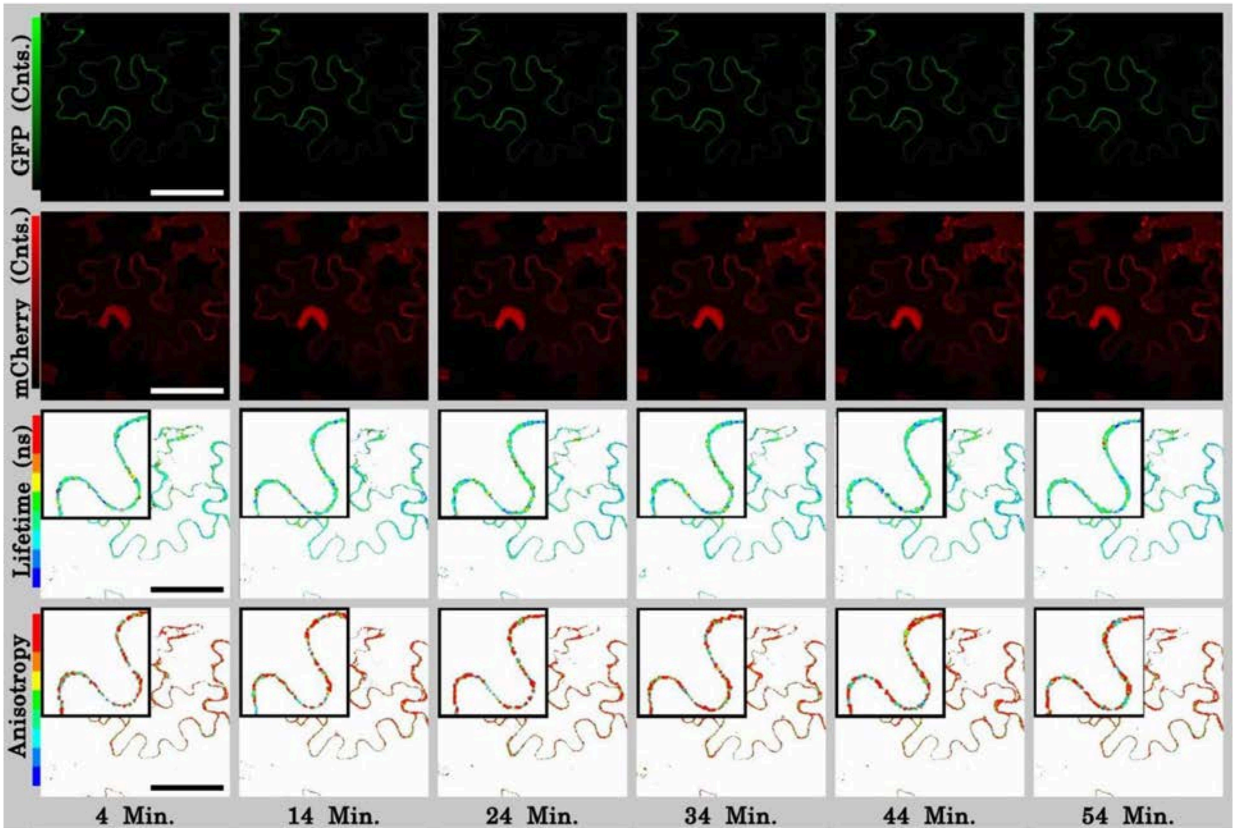

Figure 3-8 Fluorescence intensity, lifetime and anisotropy projections on a cell expressing CRN-GFP, CLV2 and CLV1-mCherry that was exposed to control peptide. Time series of a cell expressing CRN-GFP, CLV2, and CLV1-mCherry exposed to an inactive control peptide. The average fluorescence intensities, lifetime, and anisotropy are unchanged over the course of one hour. Scales: GFP: 0 photons per pixel (ppp) (dark green) - 3600 ppp (light green); mCherry: 0 ppp (dark red) - 5000 ppp (light red); Lifetime: 2.1 ns (dark blue) - 2.55 ns (dark red); Anisotropy: 0.26 (dark blue) - 0.39 (dark red). ns = nanoseconds, Cnts. = photon counts per pixel, Min. = Minutes after peptide infiltration. Scale bar is 40 µm. Data are representative of two independent experiments.

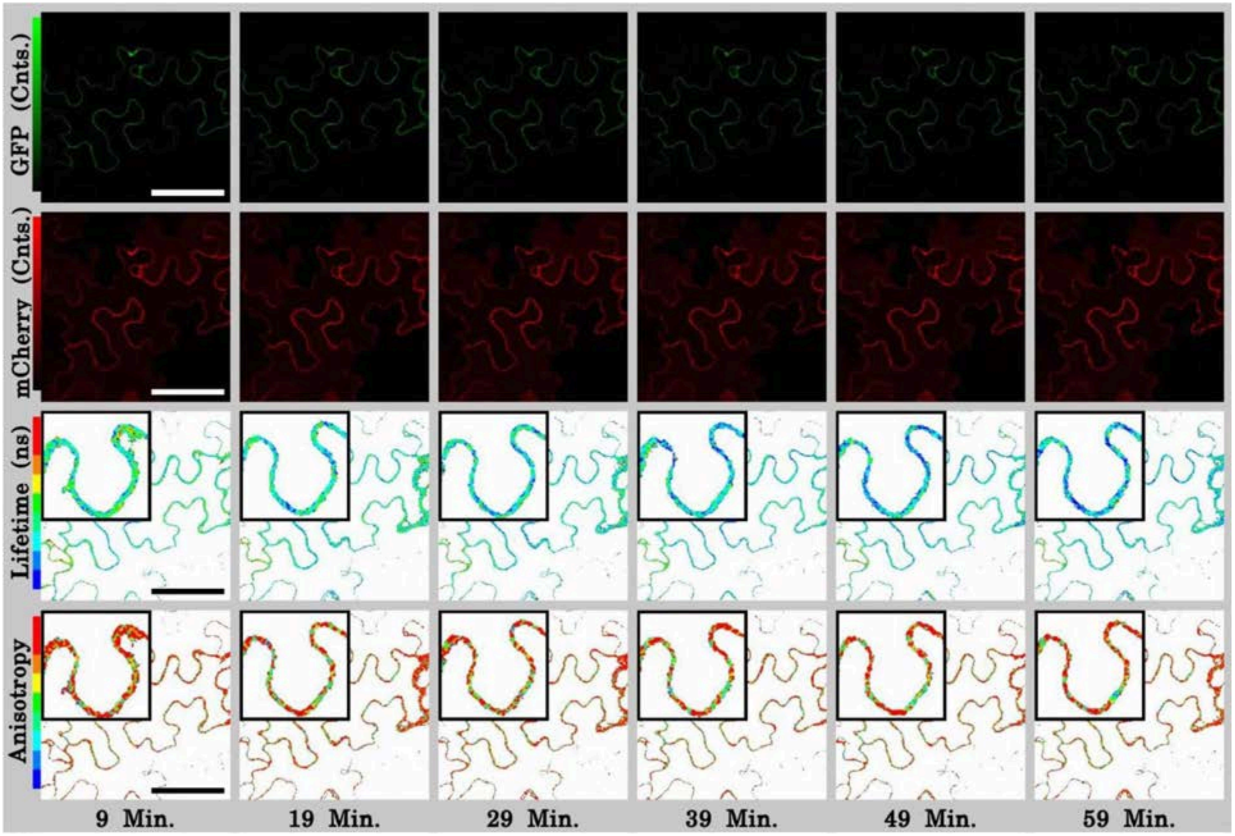

Figure 3-9 Fluorescence intensity, lifetime and anisotropy projections on a cell expressing CRN-GFP, CLV2 and CLV1-mCherry that was exposed to CLV3. Time series of a cell expressing CRN-GFP, CLV2, and CLV1-mCherry exposed to CLV3. Although the average fluorescence intensities of both CRN-GFP and CLV1-mCherry are unchanged over the course of one hour (top and second row), the average lifetime of CRN-GFP (third row) drops slightly from ~ 2.35 ns to ~ 2.30 ns on average. However, subdomains along the membrane (see insets for magnified example) display a lifetime reduction to ~ 2 ns. The average anisotropy remains unchanged over time (lowermost row). Scales: GFP: 0 photons per pixel (ppp) (dark green) - 2500 ppp (light green); mCherry: 0 ppp (dark red) - 5000 ppp (light red); Lifetime: 2.0 ns (dark blue) - 2.9 ns (dark red); Anisotropy: 0.26 (dark blue) - 0.39 (dark red). ns = nanoseconds, Cnts. = photon counts per pixel, Min. = Minutes after peptide infiltration. Scale bar is 40 µm. Data are representative of two independent experiments.

Chapter 4 Guanylate binding proteins (GBPs) directly attack *T. gondii* via supramolecular complexes

Authors: Elisabeth Kravets[1,4], Daniel Degrandi[1,4], Qijun Ma[2,4], Thomas-Otavio Peulen[2], Verena Klümpers[1], Suren Felekyan[2], Ralf Kühnemuth[2], Stefanie Weidtkamp-Peters[3], Claus A.M. Seidel[2,3*], Klaus Pfeffer[1*]

Affiliations:

[1] Institute of Medical Microbiology and Hospital Hygiene, Heinrich Heine University, Düsseldorf, Germany

[2] Chair for Molecular Physical Chemistry, Heinrich Heine University, Düsseldorf, Germany

[3] Center of Advanced Imaging, Heinrich Heine University, Düsseldorf, Germany

[4] Co-first authors

*Corresponding authors: Klaus Pfeffer, Claus A. M. Seidel

4.1 Introduction

IFNγ is an immunomodulatory cytokine that rapidly activates potent host cell effector mechanisms to confront a variety of intracellular pathogens (Decker et al., 2002). Some of the most abundantly IFNγ induced proteins are the 65-kDa guanylate-binding proteins (GBPs), which mediate cell-autonomous immunity (Degrandi et al., 2013; MacMicking, 2012; Meunier et al., 2015; Pilla et al., 2014). GBPs are related to the dynamin super family of GTPases (Praefcke and McMahon, 2004) and are highly conserved throughout the vertebrate lineage (Vestal and Jeyaratnam, 2011). The human genome harbors seven GBPs and at least one pseudogene, whereas the mouse genome contains 11 GBPs and two pseudogenes (Kresse et al., 2008; Olszewski et al., 2006). The gene loci of murine GBPs (mGBPs) are tandemly organized in clusters on chromosomes 3 and 5 (Degrandi et al., 2007; Kresse et al., 2008).

GBPs contain a conserved GTPase-domain which binds guanine nucleotides with low affinities. This induces nucleotide dependent GBP multimerization and cooperative hydrolysis of GTP via GDP to GMP (Ghosh et al., 2006; Kravets et al., 2012; Praefcke and McMahon, 2004; Prakash et al., 2000). Some GBPs are isoprenylated, endowing them with the ability to associate with intracellular membranous compartments (Degrandi et al., 2013; Vestal et al., 2000).

Murine GBPs (mGBPs) exert a major impact on cell-autonomous restriction of *Toxoplasma gondii* (Degrandi et al., 2007, 2013; Selleck et al., 2013; Yamamoto et al., 2012). *T. gondii* is an apicomplexan protozoan parasite with a broad host range, is distributed worldwide and causes serious and often fatal infections in immunocompromised hosts (Gazzinelli et al., 2014). *T. gondii* infection experiments in mice deficient for a cluster of mGBPs on chromosome 3 (Yamamoto et al., 2012) or solely for mGBP1 or mGBP2 (Degrandi et al., 2013; Selleck et al., 2013) prove that mGBPs are essential immune effector molecules mediating antiparasitic resistance. In several cell types distinct mGBPs accumulate at the parasitophorous vacuole membrane (PVM) of *T. gondii* (Degrandi et al., 2007, 2013; Kravets et al., 2012)

In previous studies, introduction of point mutations into the key positions of the conserved motifs of the G-domain (R48A, K51, E99A, D182N) and the isoprenylation site of mGBP2 (C586S), clearly showed that nucleotide binding, multimerization, GTP-hydrolysis and membrane anchoring, are essential for localization in vesicle-like structures (VLS) and the recruitment of mGBP2 to the PVM of *T. gondii* (Degrandi et al., 2013; Kravets et al., 2012). However, the assembly of homo- and hetero-mGBP multimers, their composition in distinct subcellular compartments, localization-dependent multimerization as well as their requirement for replication control of *T. gondii* in living cells remained enigmatic.

Therefore quantitative live-cell-imaging technologies were employed revealing seminal information on localization, interaction, concentration, structure and dynamics of biomolecules. To investigate the structure, composition and interaction of proteins, Förster resonance energy transfer (FRET) (Giepmans et al., 2006) is combined with multiparameter fluorescence image spectroscopy (MFIS) (Kudryavtsev et al., 2006; Weidtkamp-Peters et al., 2009), which enables unique advances in FRET imaging. In MFIS, a variety of fluorescence parameters is monitored simultaneously with picosecond accuracy, allowing the determination of many fluorescence parameters in a pixel-wise analysis such as number of photons, anisotropies, fluorescence lifetimes, and signal ratios by statistically most efficient estimators (Sisamakis et al., 2010) and to plot distinct parameters in MFIS pixel frequency histograms. The combination of MFIS and FRET experiments (MFIS-FRET) enables a quantitative analysis of the biophysical properties of homomeric and heteromeric molecular complexes in living cells (Stahl et al., 2013). This allows the identification and selection of pixel populations with unique properties for a detailed pixel-integrated analysis. Importantly, live cell measurements with MFIS can achieve the resolution and precision of traditional *in vitro* measurements of molecule ensembles with respect to the number of resolved species and rate constants.

Here, by advanced biophysical MFIS-FRET technology, it is demonstrated that the GTPase activity and isoprenylation of mGBP2 are prerequisites for its multimerization. The multimerization is essential for control of *T. gondii* replication. Colocalization and MFIS analysis of mGBPs showed intermolecular interaction of mGBP2 with itself, with mGBP1 and mGBP3, but not with mGBP6 in VLS in living cells. Interestingly, the interaction partnerships were recapitulated at the PVM of *T. gondii*. Moreover, characteristic interaction affinities of mGBP complexes were individually quantified. For the first time, we show that in the process of attacking *T. gondii*, mGBP2 directly targets the plasma membrane of the parasite after disruption and permeabilization of the PVM. These investigations enable a discrete understanding of the dynamics and intracellular interactions of mGBP effector molecules in *T. gondii* host defense.

4.2 Results

4.2.1 Multimerization of mGBP2 WT and mutants, determined by intracellular homo-FRET MFIS analysis

Site-directed mutagenesis of mGBP2 revealed that GTP-binding and hydrolysis as well as C-terminal isoprenylation affect the localization of mGBP2 in the cell (Degrandi et al., 2013; Kravets et al., 2012). However, the role of the GTPase activity and isoprenylation on the multimerization ability of mGBP2 in living cells is unknown.

Therefore, MFIS-FRET measurements and fluorescence-anisotropy-based homo-FRET analysis were employed in living IFNγ stimulated mGBP2$^{-/-}$ MEFs reconstituted either with GFP-fused mGBP2 WT protein (hereafter referred to as G-mGBP2 MEFs) or with one of the GTPase-domain mutants (R48A, K51A, E99A, D182N) or with the isoprenylation mutant (C586S) (Figure 4-1A).

The mean steady-state anisotropy of GFP was experimentally determined as $\langle r_D \rangle_{cytosol}$ = 0.328, which is in agreement with the value predicted by the Perrin equation (Lakowicz, 2006) using the known mean global rotational diffusion time $\rho_{global} \approx 15$ ns for freely diffusing GFP. When GFP is fused to mGBP2, two opposing effects need to be considered (Figure 4-1B). First, its rotational freedom is restricted and therefore r_D increases; second, homo-FRET between G-mGBP2 complexes reduces r_D by depolarization of the total GFP signal. Consequently, the average steady-state anisotropy of WT G-mGBP2 in the cytosol $\langle r_D \rangle_{cytosol}$ remained comparable to the value for free GFP (Figure 4-1C). In contrast, the GFP signal intensity ($S_{G,G}$) in VLS increased significantly, indicating an enrichment of mGBP2 molecules in these structures (Figure

4-1C) accompanied by a significant reduction of the average anisotropy $\langle r_D \rangle_{VLS}$, suggesting an increased mGBP2 homo-multimerization (Figure 4-1A, C).

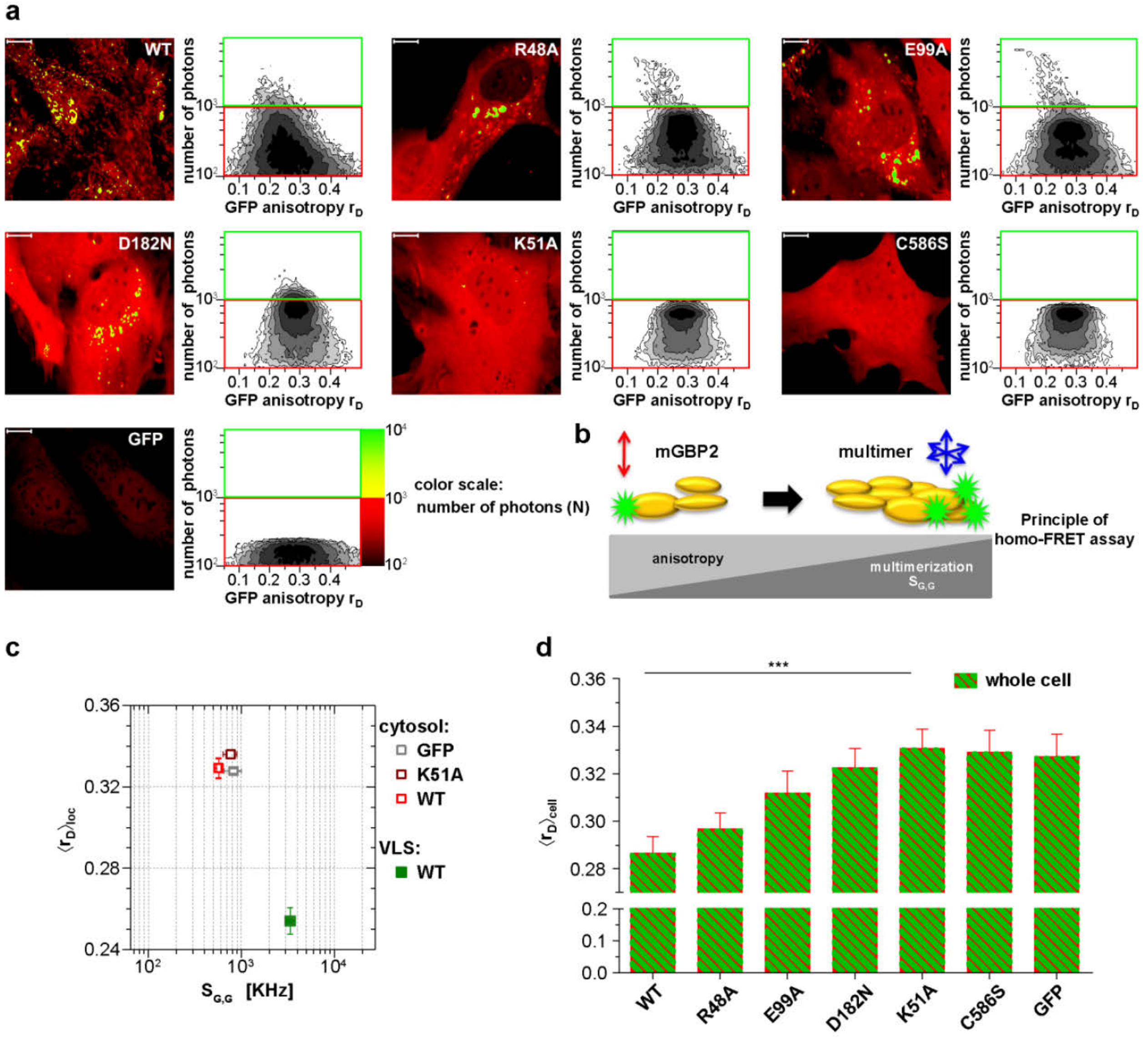

Figure 4-1 Intracellular homo-multimerization of WT and mutant mGBP2. All cells were pre-treated with IFNγ for 16h prior investigation (**A**) Left panel. GFP fluorescence intensity ($S_{G,G}$) images of GBP2-/- MEFs expressing G-mGBP2-WT (G-mGBP2 MEFs), mutants (R48A, K51A, E99A, D182N, C586S) or GFP highlighted with selections of pixels within different cellular compartments. Right panel. MFIS 2D-histograms of GFP anisotropy (r_D) on x axis vs. photon number per pixel on y axis, the frequency of pixels color coded from white (lowest) to black (highest). This allows the identification and selection of pixel

populations with unique fluorescence properties for a detailed subsequent pixel integrated analysis. The pixels with low photon numbers (below 1000) are selected in red boxes (defined as cytosol) and those with more than 1000 photons in green boxes (defined as VLS). Bars, 10 µm. (**B**) Scheme of the principle of homo-FRET assays. Compared to G-mGBP2 monomers, r_D in G-mGBP2 multimers decreases due to depolarization of GFP fluorescence while GFP $S_{G,G}$ increases. (**C**) For specific compartments (cytosol and VLS, respectively), the anisotropy values are averaged over all cells generally denoted as $\langle r_D \rangle_{loc}$. $\langle r_D \rangle_{loc}$ and $S_{G,G}$ in cytosol and VLS were plotted for G-mGBP2-WT, and the K51A mutant and GFP in the cytosol. (**D**) Mean anisotropy of averages over whole cells $\langle r_D \rangle_{cell}$ for G-mGBP2 WT and mutant proteins. GFP expressing cells served as controls (***P<0.0001).

The nucleotide binding and hydrolysis impaired K51A mutant does not localize in VLS (Kravets et al., 2012). This mutant showed a higher average anisotropy ($\langle r_D \rangle_{cytosol} = 0.336$) as compared to the cytosolic WT mGBP2 (Figure 4-1A, C) due to the absence of homo-FRET, proving its incapability to form multimers. Next, the mean anisotropies of averages over whole MEFs $\langle r_D \rangle_{cell}$ were determined (Figure 4-1D). The hydrolytically impaired mGBP2 mutants R48A and E99A (Kravets et al., 2012) showed significantly increased $\langle r_D \rangle_{cell}$ values (Figure 4-1A, D), further proving that the GTPase activity is essential for multimerization in living cells. The nucleotide binding deficient mGBP2 mutant D182N showed significantly increased $\langle r_D \rangle_{cell}$ value (Figure 4-1A, D) as compared to WT mGBP2 and mutants R48A and E99A reflects the low multimerization capability of this mutant. The recombinant isoprenylation mutant (C586S) did not show altered nucleotide binding, hydrolysis activity or multimerization of mGBP2 in cell-free analyses (Figure 4-11). Nevertheless, this mutant did not localize in VLS (Degrandi et al., 2013) and showed anisotropy values comparable to the dysfunctional K51A mutant (Figure 4-1D).

Altogether, these data provide compelling evidence that nucleotide binding and membrane anchoring are prerequisites for multimerization of mGBP2 in living cells. The degree of multimerization of mGBP2 increases from cytosol to VLS.

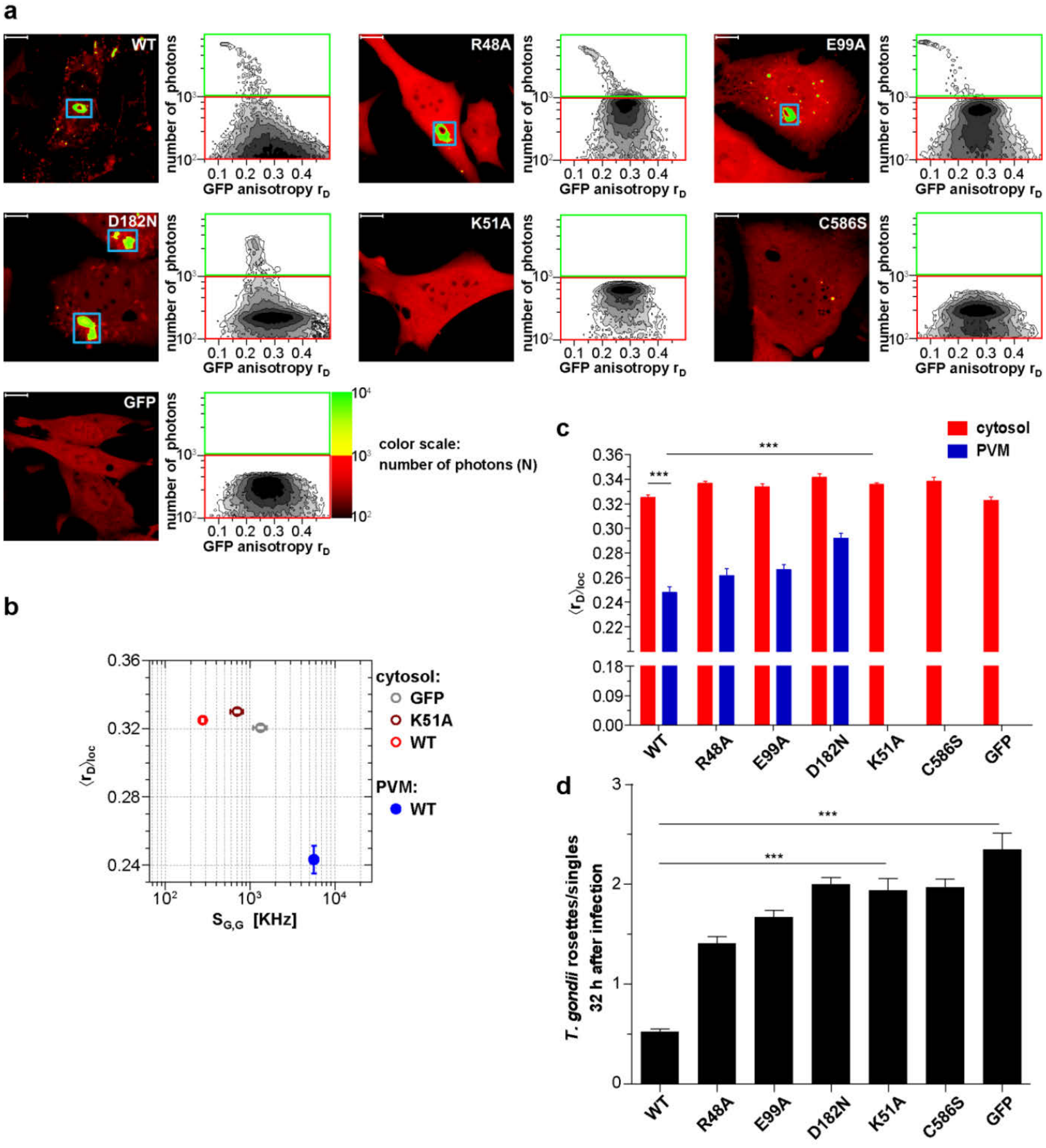

Figure 4-2 Intracellular homo-multimerization of WT and mutant mGBP2 at the PVM of *T. gondii* and parasite inhibition. Cells were pre-treated with IFNγ for 16h prior infection with *T. gondii* ME49 (**A**) Left panel. GFP fluorescence intensity images of G-mGBP2-WT, mutants or GFP MEFs highlighted with

selections of pixels with low and high numbers of photons. Blue boxes mark the PVM area. Bars, 10 µm. Right panel. MFIS 2D-histograms of GFP r_D on x axis vs. photon number per pixel on y axis. The pixels with low photon numbers (below 1000) are selected in red boxes and the pixels containing more than 1000 photons in green boxes. (**B**) Mean values of $\langle r_D \rangle_{loc}$ and mean GFP $S_{G,G}$ were plotted for G-mGBP2-WT in the cytosol and at the PVM of *T. gondii* and for the K51A mutant and GFP in the cytosol. (**C**) Mean anisotropy $\langle r_D \rangle_{loc}$ of WT and mutants in the cytosol and at the PVM (blue boxes in A). GFP expressing cells served as controls (ns=not significant; *P<0.05; **P<0.01; ***P<0.0001). (**D**) Replication inhibitory capacity of G-mGBP2-WT and mutants. After fixation *T. gondii* were stained with the α-SAG1 antibody and the cell nuclei with DAPI. Slides were analyzed by confocal microscopy. Replication inhibition was calculated by the ratio of *T. gondii* single parasites versus replicative units (rosettes) in at least 100 infected cells (****P*<0.0001).

4.2.2 Multimerization of mGBP2 WT and mutants at the PVM of *T. gondii*

mGBPs were reported to be involved in rupture of *T. gondii* PVMs few hours after infection and are important for *T. gondii* control *in vivo* (Degrandi et al., 2013; Kravets et al., 2012; Selleck et al., 2013; Yamamoto et al., 2012). Previously, it could be determined that the GTPase activity as well as isoprenylation regulate the recruitment of mGBP2 to the PVM of *T. gondii* (Degrandi et al., 2013; Kravets et al., 2012). The next step therefore was to elucidate the impact of the GTPase activity and the isoprenylation of mGBP2 on the ability to multimerize at the PVM and to control intracellular *T. gondii* replication. Hence, G-mGBP2 MEFs as well as MEFs expressing GTPase and isoprenylation mutants were infected with *T. gondii* and analyzed by MFIS homo-FRET assays. Also, the ratio of replicative units, so called rosettes, versus single parasites was determined 32 hours after infection (Figure 4-2).

A marked decrease of fluorescence intensities of WT mGBP2 in the cytosol of infected cells (Figure 4-2A, B) compared to uninfected cells (Figure 4-1C) concurrent with a strong increase of the mGBP2 concentration at the PVM of *T. gondii* was observed along with a further decrease in anisotropy (Figure 4-2A, B; Figure 4-12). This raises the question on a distinct composition of the mGBP2 complexes at the PVM, which will be addressed below by pixel-integrated MFIS analysis.

As shown previously, the enzymatically dysfunctional K51A and the isoprenylation C586S mutants showed nearly no recruitment to the PVM (Degrandi et al., 2013; Kravets et al., 2012). Interestingly, as shown here, the corresponding anisotropies (Figure 4-2A, B, C) did not significantly change in comparison to the uninfected situation (Figure 4-1). These mutants were incapacitated in controlling *T. gondii* replication (Figure 4-2D). The R48A and E99A mutants, which have reduced capacity to recruit to the PVM (Kravets et al., 2012), showed slightly increased anisotropy at the PVM as compared to WT mGBP2 (Figure 4-2C) and a reduced capability to restrict *T. gondii* growth (Figure 4-2D). For the D182N mutant a higher anisotropy at the PVM in comparison to WT mGBP2 could be determined, suggesting a lower degree of multimerization. This correlated with insufficient control of *T. gondii* growth, comparable to the K51A and C586S mutants (Figure 4-2D).

In summary, it can be concluded that at the PVM the enrichment of mGBP2 is increased compared to VLS. Nucleotide binding, GTPase activity as well as membrane anchoring regulate the multimerization capability of mGBP2 at the PVM and are prerequisites for the control of *T. gondii* replication.

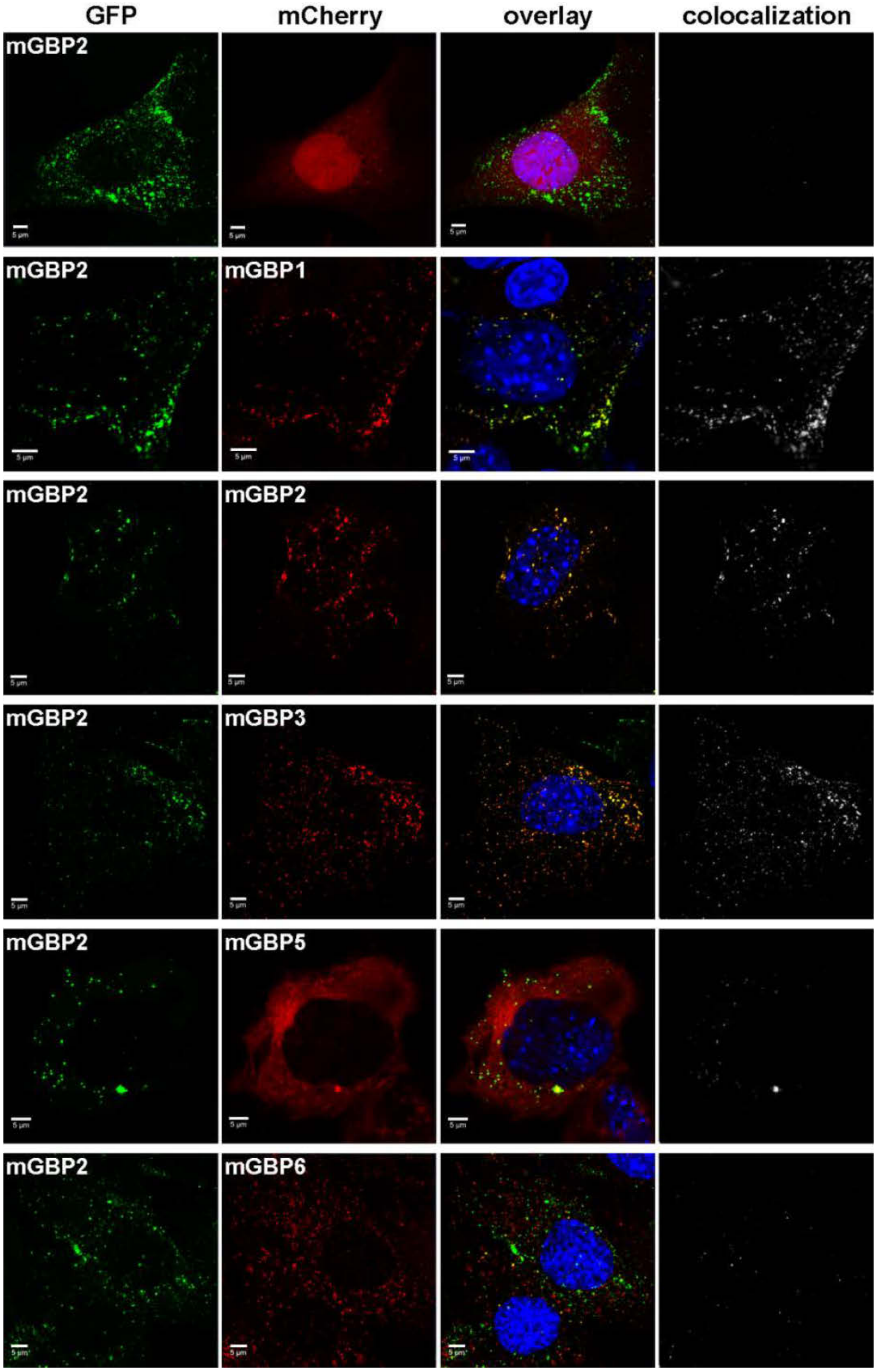

Figure 4-3 Intracellular colocalization of mGBP proteins. Subcellular localization of mGBPs was analyzed in G-mGBP2 coexpressing one of the mCh-mGBPs (1, 2, 3, 5 or 6). mCherry expressing cells served as controls. Cells were pre-treated with IFNγ for 16 h. After fixation, nuclei were stained with DAPI. Glass

slides were analyzed by confocal microscopy. Bars, 5 µm. Colocalization analysis was performed with Imaris (Bitplane).

4.2.3 Colocalization and hetero-FRET studies of mGBPs

Several members of the mGBP family localize in VLS in IFNγ stimulated cells (Degrandi et al., 2007). However, it is unclear whether co-compartmentalization of mGBPs and molecular interactions between them in VLS occur. For this purpose, G-mGBP2 MEFs were cotransduced with mCherry fusion proteins of mGBP1, mGBP2, mGBP3, mGBP5, and mGBP6 (hereafter referred to as G-mGBP2/mCh-mGBPx) and confocal imaging studies were performed (Figure 4-3, Figure 4-13). All of the analyzed mGBPs showed a vesicular distribution except for mGBP5 (Figure 4-3). A correlation of localization could be computed employing the Pearson´s coefficient, P. G-mGBP2/mCh-mGBP2 MEFs showed the most pronounced colocalization indicating that the fluorescence tags do not affect protein localization (P = 0.758 ± 0.093). Confocal images revealed a high correlation of G-mGBP2 positive VLS with mCh-mGBP1 (P = 0.516 ± 0.132) and mCh-mGBP3 VLS (P = 0.65 ± 0.121). mCh-mGBP5 (P = 0.108 ± 0.104) and mCh-mGBP6 (P = 0.338 ± 0.126) scarcely overlapped with G-mGBP2. Thus, the subcellular reservoir of mGBP1, mGBP2 and mGBP3 differed from mGBP6, whereas mGBP5 showed no compartmentalization.

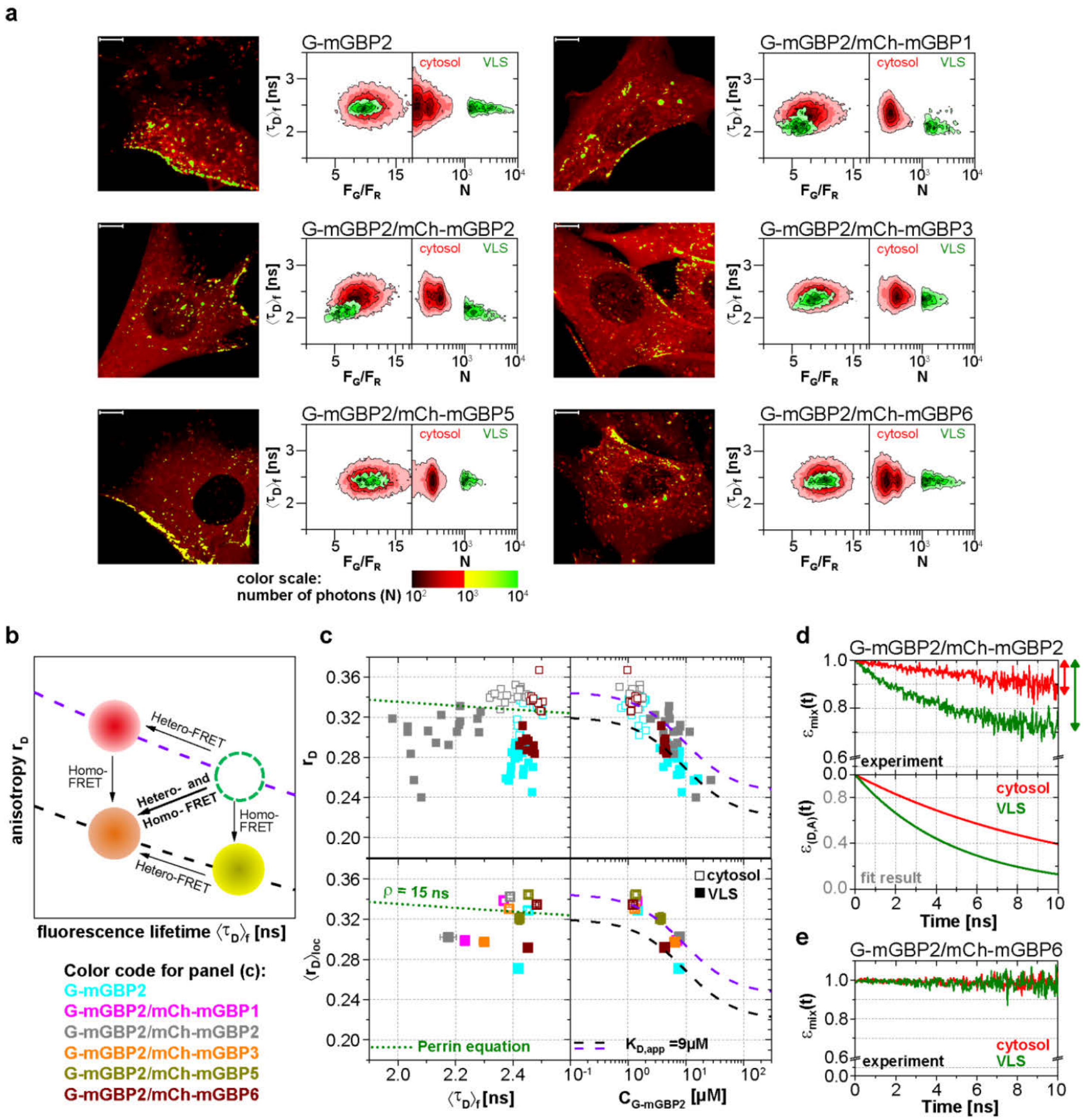

Figure 4-4 Intracellular homo- and hetero-multimerization of mGBPs. All cells were pre-treated with IFNγ for 16h prior investigation (**A**) Left panels. GFP fluorescence intensity images of G-mGBP2 or G-mGBP2/mCh-mGBP(1,2,3,5,6) MEFs highlighted with selections of pixels with different intensities. Bars, 10 µm. Right panels. Two MFIS 2D-histograms of GFP fluorescence lifetimes ($\langle\tau_D\rangle_f$) on y axes, GFP/mCherry fluorescence intensity ratios (F_G/F_R) or photon number per pixel (N) on x axes. The pixel populations locating in cytosol (N < 1000: red island) and VLS (N > 1000: green island) were separated according to photon numbers. (**B**) Schematic 2D MFIS plot detailing the effects of hetero- and/or homo-

FRET on a reference data set (green circle). The average GFP $\langle\tau_D\rangle_f$ is plotted on the x axis from short to long, while the average steady-state r_D is plotted on the y axis. For detailed explanation refer to results section. (**C**) Upper panel. For individual G-mGBP2, G-mGBP2/mCh-mGBP2 or G-mGBP2/mCh-mGBP6 MEFs, mean values of r_D in the cytosol (empty squares) and in the VLS (solid squares) were plotted against $\langle\tau_D\rangle_f$ and G-mGBP2 concentrations ($C_{G\text{-}mGBP2}$). Lower panel. Mean anisotropy $\langle r_D\rangle_{loc}$ values (average over all cells weighted by $C_{G\text{-}mGBP2}$) were plotted against $\langle\tau_D\rangle_f$ or $C_{G\text{-}mGBP2}$. The two left panels contain an overlay calculated according to the Perrin equation: $r_D = r_0 /(1+\langle\tau_D\rangle_f / \rho_{global})$ with GFP fundamental anisotropy r_0 = 0.38 and rotational correlation time ρ_{global} = 15 ns. The two right panels are overlaid with function curves plotting $r_D = r_{\max} - (r_{\max} - r_{\min})\cdot C_{G-mGBP2} /(C_{G-mGBP2} + K_{D,app})$ which assumes a mGBP2 Langmuir binding model with an apparent dissociation constant $K_{D,app}$. In all the donor-only experiments the formation of mGBP2 homo-multimers could be described by $K_{D,app}$ = 9 μM, r_{max} = 0.32 and r_{min} = 0.22 (black curve). If other interaction processes interfere with homo-FRET between G-mGBP2 proteins, this curve is shifted upwards (violet curve) while keeping $K_{D,app}$ invariant (r_{max} = 0.345 and r_{min} = 0.245). (**D, E**) $\varepsilon_{mix}(t)$ and $\varepsilon_{(D,A)}(t)$ diagrams of a representative G-mGBP2/mCh-mGBP2 MEF (**D**) and G-mGBP2/mCh-mGBP6 MEF (E). The drop in $\varepsilon_{mix}(t)$ curves, as marked by the arrows, represents the species fractions of FRET-active complexes (x_{FRET}) in the VLS (green) and in the cytosol (red). In (**D**), the FRET rate constant (k_{FRET}) in the cytosol is 0.09 ns^{-1} and in the VLS 0.20 ns^{-1}.

To elucidate whether the colocalization of mGBPs is due to specific protein interactions, MFIS-hetero-FRET measurements were performed using G-mGBP2 as donor and mCh-mGBPx as acceptors (Figure 4-4). In the FRET analysis GFP and mCherry fluorescence intensities (F_G and F_R) and the mean fluorescence-weighted donor lifetime $\langle\tau_D\rangle_f$ were determined for each pixel (Figure 4-4A). By displaying the frequency of pixels in color scales for the two localizations (red: cytosol, green: VLS), the VLS-population exhibits a correlated shift in the MFIS 2D-histogram of the FRET indicators F_G/F_R and $\langle\tau_D\rangle_f$ towards smaller values with respect to the population in the cytosol. This is a clear indicator for the presence of hetero-FRET, which proves the interaction between molecules. Furthermore, GFP r_D was plotted versus $\langle\tau_D\rangle_f$ as well as the G-mGBP2 concentration ($C_{\text{G-mGBP2}}$) derived from F_G (see Section 4.4.12) (Figure 4-4B, C, Figure 4-14). A $\langle\tau_D\rangle_f - r_D$ diagram is essential to determine homo- and hetero-oligomerization between mGBPs sensed by hetero- and homo-FRET. Figure 4-4B illustrates the interpretation of a $\langle\tau_D\rangle_f - r_D$ diagram based on the Perrin equation to visualize the effects on a donor-reference data set (green circle) by selective hetero- (red sphere) or homo-FRET (yellow sphere) or simultaneous homo- and hetero-FRET (orange sphere). Comparing G-mGBP2 MEFs (Figure 4-4C) with G-mGBP2/mCh-mGBP2 MEFs, both homo- and hetero-FRET were visible for the latter cells indicated by a simultaneous reduction of $\langle\tau_D\rangle_f$ and an increase of r_D. Moreover, analyzing the cells individually, the anisotropy dropped with increasing G-mGBP2 concentrations. The variation of mGBP2 concentrations between individual cells allowed the estimation of the spatially resolved apparent dissociation constant ($K_{D,app}$) of the mGBP2 homomultimer of approx. 9 μM in the VLS (Figure 4-4C, upper right panel, black curve). Note that any interactions interfering with G-mGBP2 homomerization will result in a $K_{D,app}$-curve shifted upwards (purple curve).

To attain an overview of all experimental data, we computed the averaged values of $\langle\tau_D\rangle_f$ and fluorescence intensity weighted anisotropy $\langle r_D\rangle_{loc}$ for all cells of the specified FRET pair (Figure 4-4C, lower panel). Both in cytosol and in VLS, the strongest fluorescence lifetime reduction compared to the donor-only sample could be measured for combinations of G-mGBP2 with mCh-mGBP2 and to a lesser extent for mCh-mGBP1 and mCh-mGBP3 (Figure 4-4A, C), proving that mGBP1, 2, and 3 do not only colocalize but also directly interact. Although no detectable lifetime reduction could be observed between G-mGBP2 and mCh-mGBP5, data showed a higher anisotropy compared to the donor reference, indicating interference of mGBP5 with mGBP2 homomerization (Figure 4-4C). No fluorescence lifetime reduction (Figure 4-4C, left panel) or interaction-induced anisotropy increase (Figure 4-4C, right panel) could be observed for mGBP2 and mGBP6 coexpressing cells.

To elucidate the reason for the donor lifetime reduction in VLS by determining the fraction of FRET-active complexes (x_{FRET}) together with their FRET properties given by the rate constants of FRET (k_{FRET}), pixel-integrated MFIS-FRET analysis was applied by computing the FRET-induced donor-quenching decay $\varepsilon_{mix}(t)$ (Eq. (2-4) in Section 2.2.2) to graphically display the FRET effect (Figure 4-4D) .The larger drop of $\varepsilon_{mix}(t)$ (Figure 4-4D, upper panel) directly shows the difference in x_{FRET} which proves that more interacting mGBP2 complexes reside in the VLS than in the cytosol. The FRET-induced donor decay $\varepsilon_{mix}(t)$ displays the interaction state of an ensemble of proteins, which includes both FRET-active and -inactive species. To separate the effects of both FRET-species on the decay, it is necessary to determine the characteristic k_{FRET} of the populations in the cytoplasm and the VLS. The formally fitted decay curves of FRET-active complexes $\varepsilon_{(D,A)}(t)$ are separately plotted (Figure 4-4D, lower panel), because this allows to remove the influence of the offset on the decay due to FRET-inactive species. The $\varepsilon_{(D,A)}(t)$ clearly differ for cytosol and VLS suggesting a higher degree of multimerization of mGBP2 in VLS. The $\varepsilon_{mix}(t)$-curve of a representative cell expressing G-mGBP2/mCh-mGBP6 (Figure 4-4E) had random fluctuations around 1, which is consistent with the data in Figure 4-4A and C showing no FRET events and confirms the absence of heteromeric complexes.

In summary, in the cytosol and VLS mGBP2 forms homo-multimers and hetero-multimers with mGBP1 and mGBP3, but not with mGBP6.

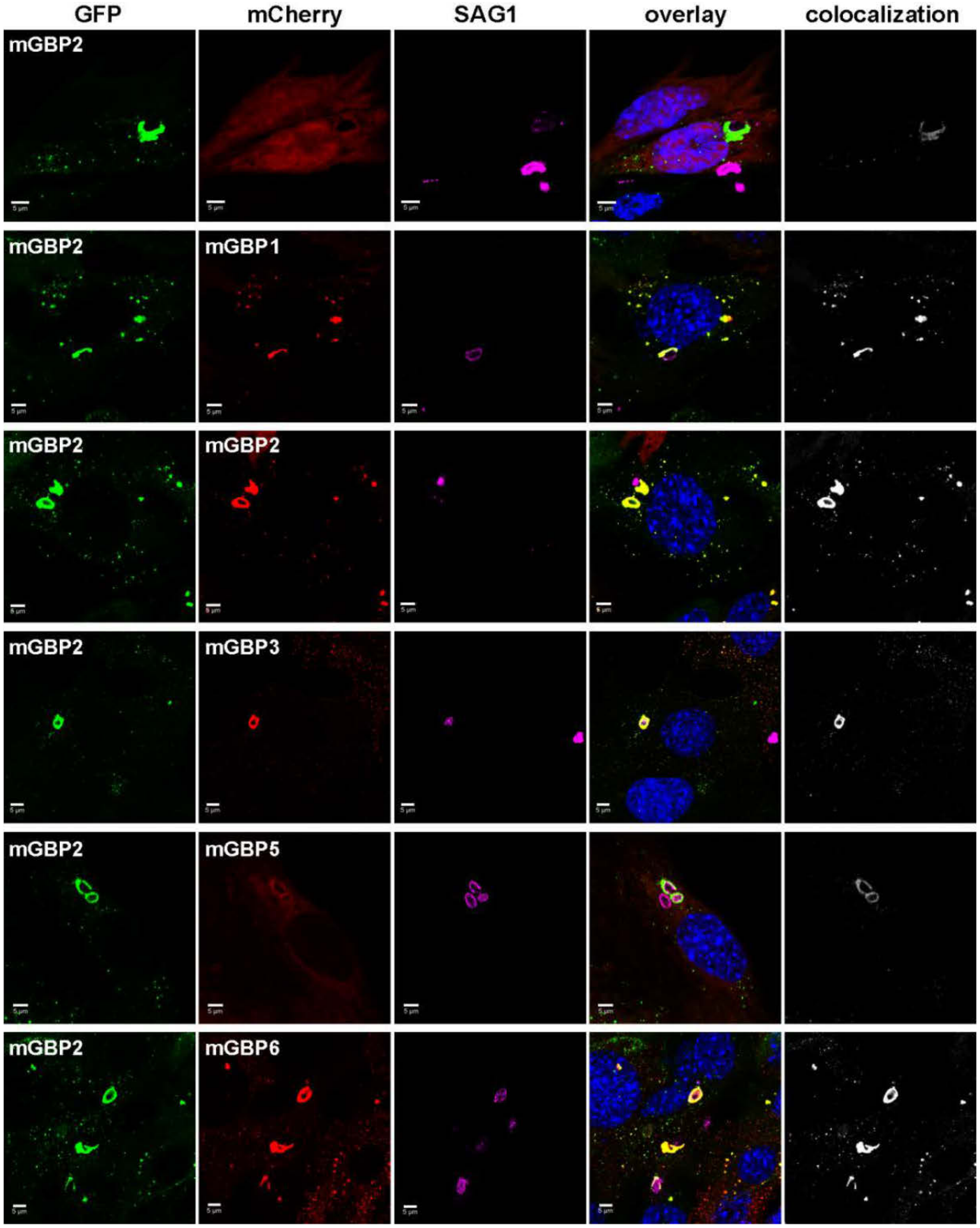

Figure 4-5 Intracellular colocalization at the PVM of *T. gondii* and enrichment of mGBP proteins. Recruitment and colocalization of mGBPs was analyzed in G-mGBP2/mCh-mGBP(1,2,3,5,6) MEFs. mCherry expressing cells served as controls. Cells were stimulated with IFNγ for 16 h and subsequently infected with *T. gondii* for 2 h. After fixation, *T. gondii* were stained with an α-SAG1 antibody and cell and *T. gondii* nuclei with DAPI. Glass slides were analyzed by confocal microscopy. Bars, 5 µm. Colocalization analysis was performed with Imaris (Bitplane).

4.2.4 Colocalization and hetero-FRET studies of mGBPs at the PVM of *T. gondii*

Individual members of the mGBP family are able to recruit to the PVM (Degrandi et al., 2007). To investigate the colocalization of several mGBPs at the PVM, G-mGBP2/mCh-mGBPx MEFs were infected with *T. gondii* (Figure 4-5). A colocalization of all investigated mGBPs with mGBP2 could be detected at distinct PVMs for each pairwise combination of proteins.

To investigate whether the colocalized mGBPs interact at the PVM, MFIS-FRET measurements were applied in G-mGBP2/mCh-mGBPx MEFs (Figure 4-6). A strong decrease of both FRET indicators, GFP fluorescence lifetimes $\langle\tau_D\rangle_f$ and intensity ratio F_G/F_R, could be detected in the cytosol and at the PVM of G-mGBP2/mCh-mGBP1 and G-mGBP2/mCh-mGBP2 MEFs and, to a lesser extent, in G-mGBP2/mCh-mGBP3 MEFs (Figure 4-6A, B).

For individual cells, MFIS diagrams plotting the r_D values against donor lifetimes $\langle\tau_D\rangle_f$ and G-mGBP2 concentrations were generated (Figure 4-6B upper panels, Figure 4-14B). The $K_{D,app}$-curves describing the relationship between r_D and $C_{G\text{-}mGBP2}$ in uninfected cells (Figure 4-4C) fitted also very well to the infected situation (Figure 4-6B). The averaged values of $\langle\tau_D\rangle_f$, $\langle r_D\rangle_{loc}$ and $C_{G\text{-}mGBP2}$ over individual cells are depicted in Figure 6B (lower panels). An even stronger reduction in $\langle\tau_D\rangle_f$ was observed at the PVM for combinations of G-mGBP2 with mCh-mGBP2 and to a lesser extent with mCh-mGBP1 and mCh-mGBP3 as compared to the VLS in uninfected cells (Figure 4-4C), proving that the observed colocalization at the PVM (Figure 4-5) enables direct protein interactions. For G-mGBP2/mCh-mGBP5 MEFs the situation is more complex: in the cytosol the anisotropy was slightly increased but the donor lifetime was unchanged, whereas at the

PVM an increase in anisotropy was absent (Figure 4-6B, lower right panel). In G-mGBP2/mCh-mGBP6 MEFs no interactions were detected, neither in the cytosol nor at the PVM.

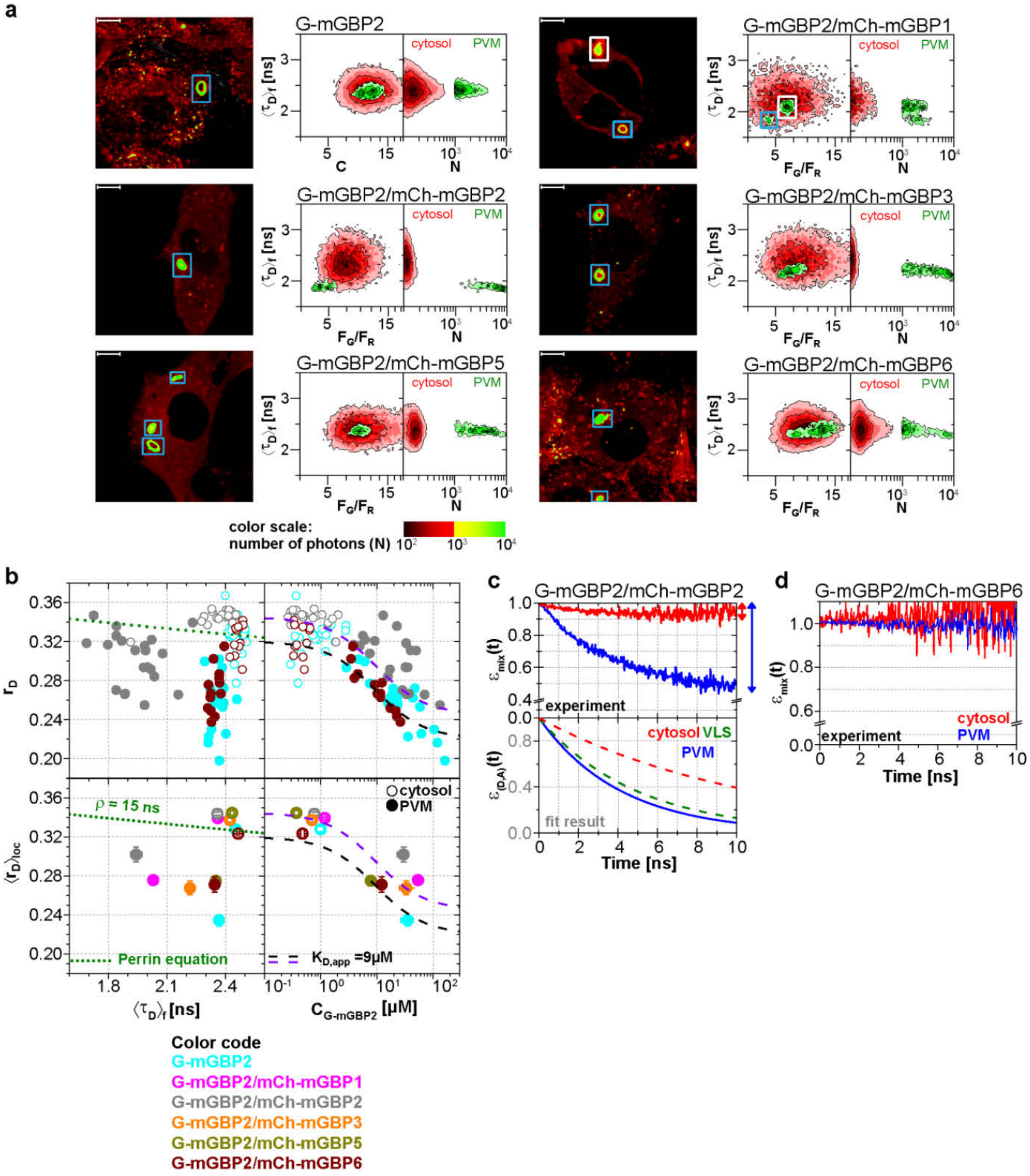

Figure 4-6 Intracellular homo- and hetero-multimerization of mGBPs at the PVM of *T. gondii*. All cells were pre-treated with IFNγ for 16h prior investigation (**A**) Left panels. GFP fluorescence intensity images of

living G-mGBP2 or G-mGBP2/mCh-mGBP(1,2,3,5,6) MEFs infected with *T. gondii* highlighted with selections of pixels within different intracellular localizations. Right panels. Two MFIS 2D-histograms of GFP $\langle\tau_D\rangle_f$ on y axes, GFP/mCherry F_G/F_R and photon number per pixel (N) on x axes. The pixel populations locating in cytosol (N < 1000: red island) and at the PVM (N > 1000: green island) were separated according to photon numbers. (**B**) Upper panel. For individual G-mGBP2, G-mGBP2/mCh-mGBP2 or G-mGBP2/mCh-mGBP6 MEFs pixel averages of r_D in the cytosol and at the PVM were plotted against $\langle\tau_D\rangle_f$ or $C_{G\text{-mGBP2}}$. Lower panel. Averages of $\langle r_D\rangle_{loc}$ were plotted against $\langle\tau_D\rangle_f$ and $C_{G\text{-mGBP2}}$. Please refer to Figure 4-4C for further information on the legend and overlaid curves. (**C, D**) $\varepsilon_{mix}(t)$ and $\varepsilon_{(D,A)}(t)$ diagrams of a representative *T. gondii* infected G-mGBP2/mCh-mGBP2 MEF (**C**) and G-mGBP2/mCh-mGBP6 MEF (**D**). The drop in $\varepsilon_{mix}(t)$ curves, as marked by the arrows, represents x_{FRET} at the PVM (blue) and in the cytosol (red). The dashed curves representing the $\varepsilon_{(D,A)}(t)$ diagrams of G-mGBP2/mCh-mGBP2 interactions in the cytosol (red) and VLS (green) in uninfected cells are inserted for comparison from Figure 4-4D. In (**C**), k_{FRET} at the PVM is 0.24 ns^{-1}.

The FRET-related donor quenching $\varepsilon_{mix}(t)$ of one representative G-mGBP2/mCh-mGBP2 cell (Figure 4-6C) exhibited a larger drop, which indicates a higher x_{FRET}, i.e. more interacting protein complexes were located at the PVM compared to VLS in uninfected cells (Figure 4-4D). Nevertheless, their slopes (k_{FRET}) of $\varepsilon_{(D,A)}(t)$ are comparable within the precision of the analysis (Figure 4-6C, green dashed line), suggesting an unchanged local environment in the oligomer. Furthermore, the $\varepsilon_{mix}(t)$ diagram for one representative G-mGBP2/mCh-mGBP6 cell revealed no interaction between these mGBPs.

In conclusion, mGBP2, besides its homo-interaction, directly interacts with mGBP1, and, to a lesser extent, with mGBP3 at the PVM. Although other mGBPs, such as mGBP5 and mGBP6 were recruited to the same PVMs, no direct interaction could be detected suggesting the formation of specific mGBP supramolecular complexes.

4.2.5 Quantitative species-resolved pixel-integrated MFIS-FRET analysis of mGBPs multimers

In addition to the formal analysis (Figure 4-15) of the hetero-FRET data, an additional inspection of the time-resolved donor anisotropy ($r_D(t)$) (Figure 4-7A) revealed that cells with a higher mGBP2 concentration (C_{mGBP2}) exhibited a larger drop in initial anisotropy, which is evidence for ultrafast depolarization processes due to the formation of densely packed mGBP2 homo-oligomers with multiple GFPs. These processes were too fast to be resolved by hetero-FRET analysis (Figure 4-6C), but combining both homo- and hetero-FRET, global pattern based, pixel-integrated MFIS-FRET analysis could be performed to resolve the individual mGBP species (Figure 4-7B and C) and to characterize the composition of FRET-active homo- and hetero-complexes of mGBP2 (Eq. (4-1) and (4-2)) in distinct localizations. The information content in the experimental fluorescence decays is restricted by their noise (Köllner and Wolfrum, 1992). Given the limited amount of photons of the pixel-integrated fluorescence intensity histograms, the pattern fit uses structural information of molecular simulations (Figure 4-17) to obtain population fractions of all species. The structural information is based on prior knowledge of the dimerization interface (Vöpel et al., 2014) and on Monte Carlo simulations of the linkers (see Section 4.4.11) connecting the fluorescent proteins to the GBPs (Evers et al., 2006; Pham et al., 2007). The obtained species fractions of mGBP2 monomers, homo- or hetero-dimers and oligomers are displayed in Figure 4-7C. The obtained species fraction of mGBP2 monomers, homo- or hetero-dimers and oligomers are displayed in Figure 4-7B. The homo- and hetero-dimer formation is very similar in G-mGBP2 MEFs and G-mGBP2/mCh-mGBP1, 2 or 3 MEFs as expected for the highly conserved GTPase-domains of mGBPs. Dimeric complexes are primarily formed with a small fraction of monomers in the cytosol (Figure 4-7C, middle panel, see methods). The obtained $K_{D,dim}$ of ~24 nM is close to previous biochemical studies (Kravets et al., 2012). In the VLS an equilibrium of mGBP dimers and oligomers existed which was shifted towards oligomers with increasing protein concentration so that, the fraction of oligomers at the PVM is even higher than in the VLS. However, the dissociation constants for oligomerization $K_{D,oligo}$ differ significantly between the mGBPs: 70 µM for G-mGBP2/mCh-mGBP1, 8 µM for G-mGBP2/mCh-mGBP2 and 208 µM G-mGBP2/mCh-mGBP3 (Figure 4-7C lower panel).

Global analysis of G-mGBP2 MEFs and G-mGBP2/mCh-mGBP2 MEFs, revealed the heterogeneity in size of the mGBP2 oligomers via the broad distribution of FRET rate constants for small and large oligomers, $k_{Olig,s}$ and $k_{Olig,l}$, respectively (Figure 4-7D). While $k_{Olig,s}$ did not change with increasing protein concentration, $k_{Olig,l}$ increased and reached a saturation level of ~15 ns^{-1} at ~50 µM (Figure 4-7D, red line), which is expected for a maximal local packing of FRET acceptors around the donor (see Section 4.4.14) and proved the growth of oligomers. Notably FRET senses only the local environment in a distance range limited to ~10 nm, however the continuous increase in brightness suggests also the formation of larger oligomers. Therefore we introduced scanning fluorescence intensity distribution analysis (FIDA) ((Kask et al., 2000), Section 4.4.15) to determine the mean number and brightness of the large oligomers for all pixels of the PVM in one infected MEF. The obtained oligomer brightness allowed us to derive the mean number of mGBP2 units in an oligomer using the specific brightness of one GFP under these measurement conditions. With increasing local mGBP2 concentration, scanning FIDA suggests also an increasing oligomer size (Figure 4-7E). The mean number of mGBP2 monomer units in the oligomer ranges between 1000 and

6000 at the PVM. Remarkably the FRET rate constants in large oligomers $k_{Olig,s}$ saturated at approximated 2000 monomer units, which corresponds to a total local concentration of mGBP2 monomer units of ~ 30 µM (Figure 4-7E).

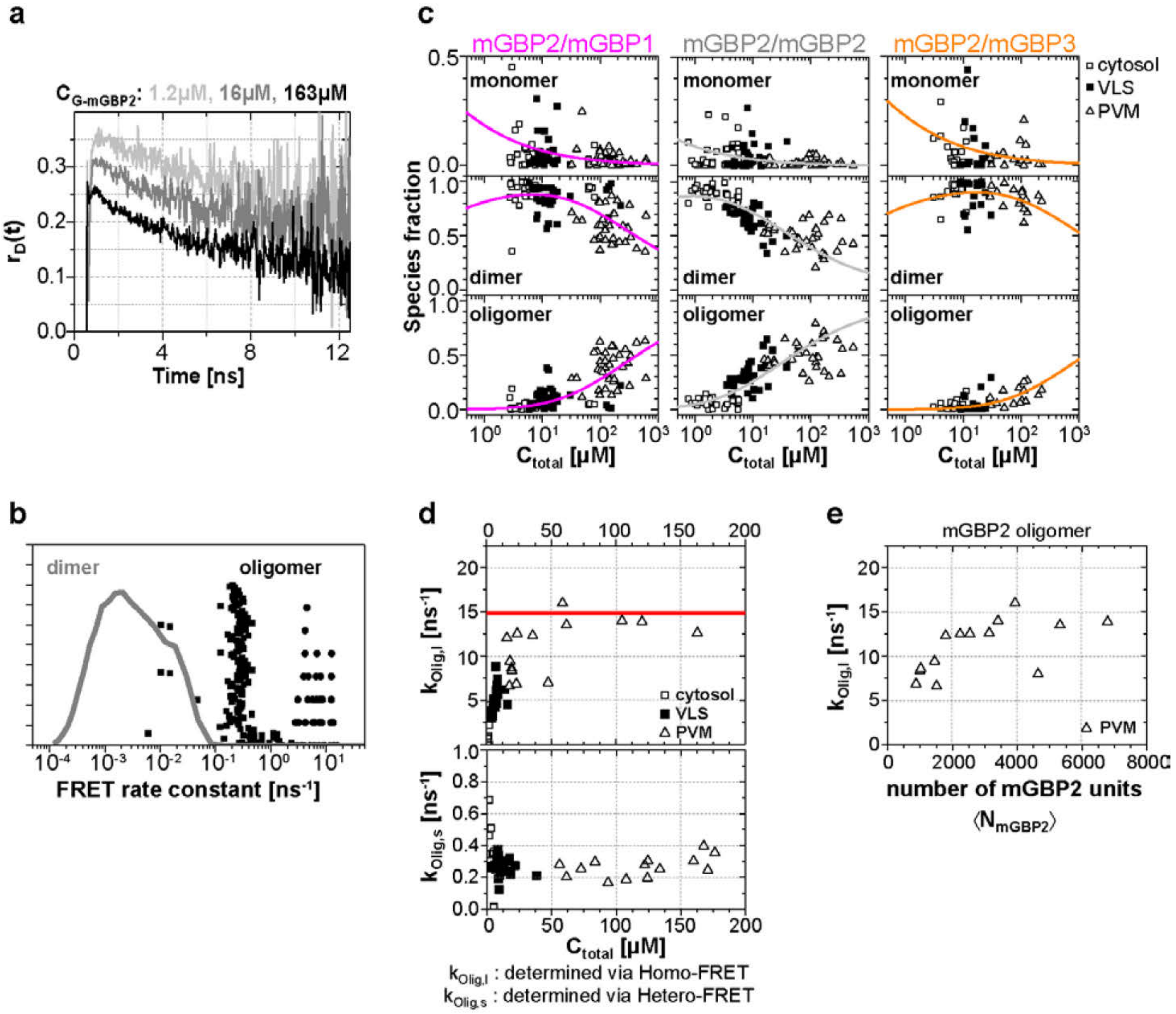

Figure 4-7 Species-resolved analysis of mGBP2 homo- and hetero-complexes (**A**) G-mGBP2 MEFs with higher concentration exhibited larger quasi instantaneous drop of $r_D(t)$ from its initial value of ~0.35, which proves the appearance of a very fast depolarization process due to homo-FRET in mGBP2 oligomers. (**B**) Distribution of FRET rate constants (k_{FRET}) for mGBP2 dimer (gray curve) and oligomer species (black symbols). Small (black squares) and large (black dots) oligomers, as formally differentiated in the pattern-based MFIS-FRET analysis, show generally higher k_{FRET} than that of the mGBP2 dimer estimated by the

MC simulation. (**C**) Concentration dependence of the three mGBP species (monomer, dimer and oligomer) obtained by the global pattern fit (Eq. (4-1) and (4-2)) of $r_{mix}(t)$ and $\varepsilon_{mix}(t)$ for two localizations VLS and PVM. The line depicts the fit (Section 4.4.10 and 4.4.13) to the corresponding binding equilibrium with $K_{D,dim}$ and $K_{D,oligo}$ (values are given in the text). (**D**) Concentration dependence of FRET rate constants for mGBP2 oligomers which formally differentiated as small ($k_{Olig,s}$) and large ($k_{Olig,l}$). (**E**) $k_{Olig,l}$ versus the number of monomer units in mGBP2 multimers at the PVM determined by scanning FIDA (Section 4.4.15).

In summary, with increasing protein concentration the fraction of mGBP2 dimers decreases due to the formation of large oligomers of heterogeneous size. The formation of mGBP2 homo-oligomers is preferred over heteromers with mGBP1 and mGBP3 as $K_{D,oligo}$ dropped by a factor of 9 and 25, respectively. The mean size of large mGBP2 oligomers can reach up to several thousand monomer units.

4.2.6 mGBP2 directly targets the parasite membrane

mGBP2 was shown to rapidly accumulate at the PVM after active invasion of the parasite in IFNγ activated cells (Degrandi et al., 2013). To further investigate the spatio-temporal behavior of mGBP2, 3D live cell imaging was performed in mGBP2-/- MEFs stably expressing G-mGBP2 or mCh-mGBP2 (Figure 4-8 and Video 1-3). mGBP2 localized in VLS of heterogeneous size, morphology, and velocity within the cytosol. In IFNγ stimulated uninfected cells the diameter of VLS reaches up to several microns. No obvious directional movement could be observed (Video 1). After *T. gondii* infection of IFNγ stimulated MEFs, mGBP2 accumulated rapidly at the PVM (Figure 4-8A, B and Video 1). Image analysis revealed that accumulation initiated simultaneously at different sites around the PVM (Figure 4-8B). Quantification of the overall G-mGBP2 fluorescence in regions containing the PVM and the remaining cell revealed a constant reduction of the cytosolic and VLS G-mGBP2 concentrations after infection, paired with a reciprocal increase at the PVM (Figure 4-8C). Thus, accumulation of mGBP2 at the PVM occurs by redistribution of the protein, leading to a depletion of mGBP2 reservoirs and a reduction of the number of VLS (Figure 4-8D) within the cytosol. However, no directional movement of VLS towards the parasite could be observed (Video 1).

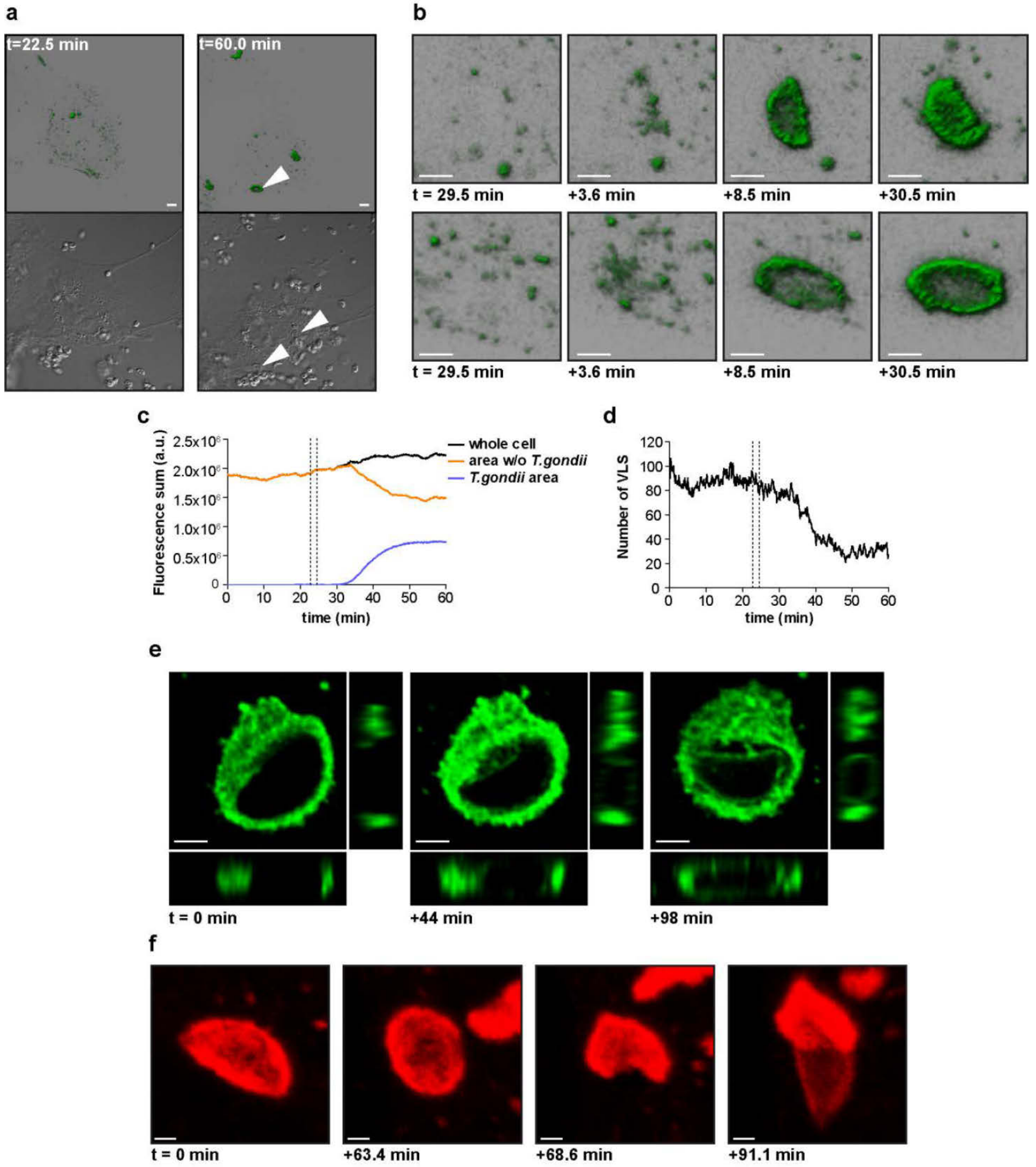

Figure 4-8 Live-cell imaging of mGBP2 in *T.gondii* infection. (**A**) G-mGBP2 MEFs were treated o/n with IFNγ and infected with *T.gondii* ME49. Living cells were observed by confocal microscopy at 37°C and a z-stack was recorded every 5-10 s. 4D data were processed and rendered in normal shading mode (upper panels) and the DIC images are displayed (lower panels) for the indicated time points. One out of at least

3 similar experiments is shown. Bar = 5µm. (**B**) Magnification from Video 1 and Figure 4-8A of G-mGBP2 accumulation around two *T. gondii* parasites at time points indicated. Bar = 2 µm. (**C**) Quantification of the total fluorescence intensity over the indicated voxels from Video 1. Vertical lines indicate the time points of *T. gondii* infection of MEFs. One representative analysis out of at least 3 similar experiments is shown. (**D**) Number of cytosolic VLS with at least approx. 0.25 µm diameter from Video 1 over time. Fluorescence signals close to the *T. gondii* area were excluded from the analysis. Vertical lines indicate the time points of *T. gondii* infection of MEFs. One representative analysis out of at least 3 similar experiments is shown (**E**) XY, XZ, and YZ projections of G-mGBP2 around one *T. gondii* PVM are shown for the indicated time points. Bar = 2 µm. (**F**) Maximum intensity projections of mCh-mGBP2 around one *T. gondii* are shown for the indicated time points. Bar = 1 µm.

After accumulation of mGBP2 at the PVM of *T. gondii*, different fates of the parasite could be observed within the recording period by live cell imaging. mGBP2 remained at the PVM for more than 16 hours without any noticeable change in PVM or parasite morphology (not shown), mGBP2 penetrated through the PVM into the vacuolar space and accumulated at the parasite membrane (Figure 4-8E and Video 2), or the mGBP2-associated PVM acquired a rounded shape immediately followed by disruption of the PVM and subsequent accumulation of mGBP2 at the parasite membrane (Figure 4-8F and Video 3). Importantly, the behavior of mGBP2 was independent of the mCherry or GFP fusion.

Additionally, the events following mGBP2 recruitment to the PVM were documented and quantified. For this, IFNγ stimulated G-mGBP2 MEFs were infected with *T. gondii* for 6 hours, fixed and the plasma membrane of *T. gondii* was stained with anti-SAG1. To determine the precise localization of mGBP2 at this time point, intensity profiles of G-mGBP2 and Alexa633-SAG-1 were determined encompassing the PVM, the plasma membrane of the parasite and the cytosol of the parasite (Figure 4-9). A total of 110 intracellular mGBP2-positive *T. gondii* PVs out of two independent experiments were evaluated. About 1.8% of the parasites acquire mGBP2 on the plasma membrane without apparent loss of PV integrity (Figure 4-9C). For 37.1% of counted parasites disruption of PVM and direct targeting of mGBP2 to the plasma membrane of the parasite was observed (Figure 4-9B). The remaining 61.1% revealed mGBP2 targeting at the PVM without apparent disruption or permeabilization and targeting of the parasite plasma membrane (Figure 4-9A). Occasionally, after 6 hours of infection, parasites with very aberrant SAG1 localization, providing evidence that these parasites were already non-viable. In such cases G-mGBP2 fluorescence inside the cytosol of the parasite could be found, suggesting a loss of the membrane integrity of the parasite (Figure 4-9D).

As previously reported, a rapid colocalization of mGBP2 with the PV of *T. gondii* type II strain ME49 but not of *T. gondii* type I strain BK in IFNγ–activated MEFs was observed (Degrandi et al., 2007). After infection with *T. gondii* ME49, selective permeabilization experiments revealed that immunofluorescence labeling of SAG1 at the *T. gondii* plasma membrane could be detected for mGBP2-positive PVMs in the absence of saponin. In contrast, after infection with the virulent BK *T. gondii*, almost no SAG1-labeled parasites could be detected (Table 4-2). Please note that after saponin permeabilization virtually all ME49 or BK parasites could be labeled with anti-SAG1. This shows that targeting of mGBP2 to the PVM promotes permeabilization or disruption of the PVM, allowing influx of proteins into the PV space.

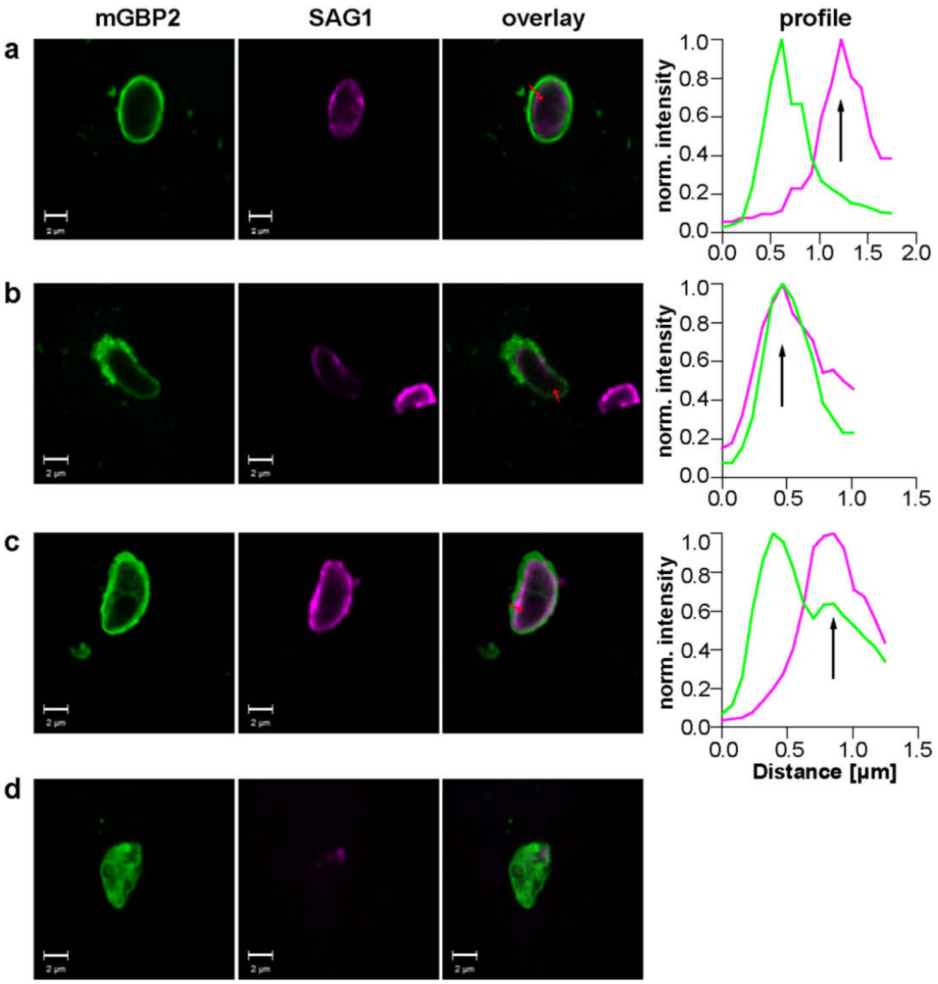

Figure 4-9 Localization of mGBP2 at the PVM, the plasma membrane, or the cytosol of *T. gondii*. G-mGBP2 cells were stimulated with IFNγ for 16 h and subsequently infected with *T. gondii* ME49 for 6 h. After fixation, *T. gondii* were stained with an α-SAG1 antibody. Glass slides were analyzed by confocal microscopy. Bars, 2 µm. Profiles show individually normalized intensities of GFP (mGBP2, green) or Alexa633 (SAG1, magenta) fluorescence along the indicated red arrows. Black arrows indicate the localization of the *T. gondii* plasma membrane, as identified by the SAG1 staining. (**A**) Example of mGBP2 accumulation at the PVM of *T. gondii* without disruption or permeabilization of the PVM. (**B**) Example of mGBP2 accumulation at the plasma membrane of *T. gondii* with obvious disruption of the PVM. (**C**) Example of mGBP2 accumulation at the plasma membrane of *T. gondii* without apparent PVM disruption. (**D**) Example of *T. gondii* death and accumulation of mGBP2 in the cytosol of the parasite.

Additionally, we have monitored the influx of cytosolic mCherry protein into the PV space after PVM disruption of GFP-mGBP2 positive *T. gondii* PV (Video 4). This observation corroborates former experimental approaches, showing a disruption of the PVM after IRG recruitment (Zhao et al., 2009).

Taken together, these observations show direct evidence that mGBP2 promotes PVM permeabilization and disruption and provide novel evidence that mGBP2 translocates into the PV space targeting the plasma membrane of the parasite, presumably delivering a direct attack on the parasite.

4.3 Discussion

The localization, molecular dynamics, interactions, and the formation of mGBP supramolecular complexes in the context of defense against *T. gondii* could be directly visualized in living cells using MFIS and live cell imaging within this study. Our data demonstrate that GTP binding and hydrolysis as well as membrane anchoring enable the pre-assembly of multimeric complexes containing mGBP2 in VLS. mGBP2/mGBP2, mGBP2/mGBP1 and mGBP2/mGBP3 complexes in the form of dimers and multimers with distinct composition are recruited at considerably high concentrations (10 - 200 µM) to the PVM of *T. gondii*. Moreover, the GTPase activity and isoprenylation of mGBP2 are crucial for the control of *T. gondii* proliferation within the PV. Eventually, mGBP2 multimers target the plasma membrane of *T. gondii*, thus establishing the immune function of GBPs to directly attacking intracellular pathogens.

To extract structural information from the MFIS-FRET data (Kalinin et al., 2012), we performed Monte Carlo sampling of the donor-acceptor conformational space of the mGBP2 dimer to compute the expected FRET parameters (Section 4.4.11, Figure 4-17B). The sterically accessible volume of flexibly attached fluorescent proteins (green (GFP) and red (mCherry)) are depicted as fuzzy clouds. The prediction that more than 60% of all D-A configurations are FRET-inactive due to their large distances between the fluorophores is confirmed by the formal MFIS-FRET analysis (Figure 4-15D). Our data argue that GTP binding is a prerequisite to induce dimer-and multimerization of mGBP2 in living cells. Indeed, the simulated FRET parameters of the mGBP2 homodimer (Figure 4-17B-D) interacting via the GTPase domains are in good agreement with MFIS pixel integrated analysis (Figure 4-4D, Figure 4-6C and Figure

4-15). Moreover, the K51A mutant, which is predicted to be predominantly nucleotide-free (Kravets et al., 2012), shows higher anisotropy values compared to WT, is entirely delocalized in the cytosol, and is monomeric in living cells (this study). However, GTPase-domain dimerization is not sufficient to determine the targeting of mGBP2 to the PVM.

Interestingly, individual murine and human GBPs (hGBPs) harbor C-terminal CaaX motifs (GBP1, GBP2, GBP5), targeting them for isoprenylation, which provides anchorage to different membranous compartments distributed within the host cell (Britzen-Laurent et al., 2010; Degrandi et al., 2007; Vestal et al., 2000). As described for hGBP1, the dimerization of the GTPase-domains enables contact formation between the two C-terminal α13 helices resulting in a juxtaposition which is crucial for their membrane localization through the attached farnesyl groups (Vöpel et al., 2014). The purified CaaX mutant of mGBP2 (C586S) shows GTP binding and hydrolysis properties as well as nucleotide dependent dimerization like the WT protein (Figure 4-11). However, the C586S mGBP2 mutant renders the protein non-functional and it is found ubiquitously within the cytosol. Noteworthy, the isoprenylation mutant C586S shows similar localization and anisotropy values as the K51A mutant in living cells, also indicating a monomeric species. Altogether these studies suggest an assembly mechanism for mGBP2 complexes in living cells that connects the GTPase activity of mGBP2 with membrane association leading to the stabilization of mGBP2 multimers, which is essential for its biological function. Moreover, MFIS measurements with high-precision FRET and brightness analysis allowed us to characterize the dynamic equilibrium between mGBP2 multimers. Their size distribution is heterogeneous ranging from dimers to large multimers (Figure 4-7C, D). The dependence of FRET rate constants on the mGBP2 concentration and their saturation level proves dense packing of the mGBP2 protomers in multimers (Section 4.4.14) as suggested for the related mechanochemical GTPase dynamin forming large helical oligomers (Faelber et al., 2011). While FRET characterizes the molecular environment of GFPs, scanning FIDA shows that the average number of mGBP2 units in the oligomers can reach several thousands. Considering the predicted size of the mGBP2 monomer (~ 4 × 6 × 12 nm, according to PDB-ID 1F5N of hGBP1), it is expected that the oligomers should reach a size of several hundred nanometers. Remarkably, confocal live cell imaging (Figure 4-8E and Video 2) resolves the enrichment of mGBP2 at the PV membrane resulting in a rough surface with elongated very bright features, that are sufficiently large to be resolved by far field confocal microscopy.

Figure 4-10 provides a scheme derived from the observed mGBP interactions in living cells with molecular resolution at various stages after T. gondii infection. Our hetero-FRET data of MFIS measurements clearly reveal interactions of mGBP2 in multimers with itself, mGBP1, and, to a lesser extent, with mGBP3, but not with mGBP6. However, the interplay between mGBP2 and mGBP5 is different. The two proteins can be coprecipitated (Figure 4-16), but the complex shows no FRET (Figure 4-4, Figure 4-6). Given the experimentally achieved concentrations in the cytosol and the corresponding enrichment in the VLS, the observation that fluorescence anisotropy of G-mGBP2 increased while its donor lifetime remained unchanged suggests either an interaction of mGBP2 and mGBP5 via adaptor molecules, so that they are not in close proximity and hence FRET inactive, or the rather unlikely case of an unfavorable static orientation of the fluorophores. It is noteworthy that, upon infection, oligomerization and accumulation of the mGBPs in VLS is reversible, so that the VLS serve as protein reservoir to accomplish a fast attack of the parasite after infection.

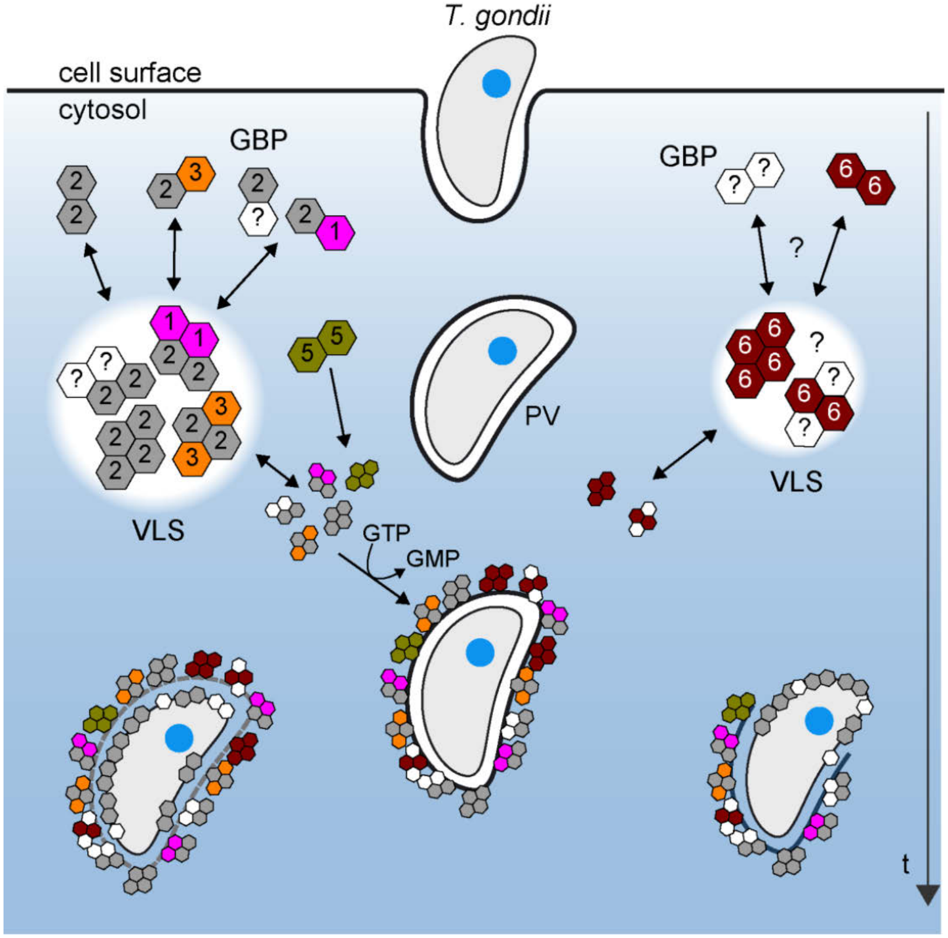

Figure 4-10 Schematic view of mGBP dynamics and multimerization in *T.gondii* infected cells. For details see Results and Discussion.

Both mGBP1 and mGBP2 have been implicated in *T. gondii* defense in single gene deficient mice (Degrandi et al., 2013; Selleck et al., 2013). Since mGBP1 still recruits to *T. gondii* in mGBP2$^{-/-}$ cells (Degrandi et al., 2013), the high level of colocalization and interaction between mGBP1 and mGBP2 and their important roles in *T. gondii* control strongly argue for a cooperative effect at the PVM of *T. gondii*. Interestingly, reconstitution of mGBP2 in mGBP^{chr3}-deleted MEFs did not allow a sufficient control of *T.*

gondii replication, while reconstitution of mGBP1 partially restored the WT phenotype (Yamamoto et al., 2012). Although more studies on the hierarchy of mGBPs are needed to fully understand the individual roles of each GTPase, this might hint that mGBP2 acts in concert with mGBP1 and possibly other mGBPs to exert its molecular antiparasitic activity.

The dissociation constant $K_{D,oligo}$ of mGBP2/mGBP3 heteromers is 25 times larger than that of mGBP2/mGBP2 homomers. Thus, it is not surprising that mGBP3 colocalized only partially in the same VLS (Figure 4-3, Figure 4-10). Strikingly, mGBP6, which also localizes in VLS and recruits to the PVM of *T. gondii*, is predominantly found in different VLS and shows no interaction with mGBP2 by FRET and co-IP. The different localizations of mGBP multimers argue for distinct individual functional roles in *T. gondii* immunity to be elucidated in the future.

Recently, an essential function for the cassette of autophagy proteins, including Atg7, Atg3, and the Atg12-Atg5-Atg16L1 complex was demonstrated in cellular anti-*T. gondii* immunity by facilitating IRG and GBP recruitment to the PVM (Choi et al., 2014; Haldar et al., 2014; Ohshima et al., 2014). This function appears to be independent of the classical autophagy degradation pathway (Zhao et al., 2008), but rather to play a role in the delivery of effectors to pathogen containing vacuoles (Selleck et al., 2013). Performing live cell imaging and MFIS analysis it could be shown that mGBP2 is loaded on the PVM of *T. gondii* within a few minutes post-infection, assembling a machinery of supramolecular complexes with mGBP1 and mGBP3.

It has been recently shown, that mGBP and IRG host proteins cooperate in destruction of PVs of *T. gondii* (Haldar et al., 2013, 2015; Yamamoto et al., 2012). Previous studies in astrocytes and macrophages infected with type II *T. gondii* strains have shown that IRGs participate in mediating vesiculation of the PVM, resulting in the exposure of disrupted parasites to the host cytosol (Ling et al., 2006; Martens et al., 2005; Melzer et al., 2008; Zhao et al., 2010, 2009). However, no colocalization of IRG proteins with the parasite plasma membrane has been reported previously. Here, we unambiguously show that mGBP2 directly targets the membrane of the parasite after penetration or disruption of the PVM.

Interestingly, GBP proteins, especially mGBP2, were shown to stimulate caspase-11-dependent pyroptosis in macrophages infected with Gram-negative bacteria which reside in vacuoles. There, GBP dependent induction of lysis of the pathogen-containing vacuoles and release of cytoplasmic LPS leads to the activation of the noncanonical inflammasome (Meunier et al., 2014; Pilla et al., 2014). Strikingly, a novel study suggests a direct bacteriolytic function of mGBPs, releasing pathogen-associated molecular patterns into the cytosol, resulting in activation of the AIM2 inflammasome (Man et al., 2015; Meunier et al., 2015). Thus, based on our observations, it is likely that mGBPs promote not only disruption of the PVM, but also directly induce lysis of the plasma membrane of *T. gondii*. The hierarchy of events which might be involved in *T. gondii* targeting and elimination, such as autophagic degradation (Choi et al., 2014) and/or inflammasome activation (Ewald et al., 2014; Gorfu et al., 2014; Meunier et al., 2014, 2015) have yet to be determined.

These studies define mGBP2 as an important effector molecule of innate immunity in the host parasite interaction with apicomplexan parasites such as *T. gondii*, by providing seminal insight into its supramolecular assembly and cellular function. Further studies will be performed to address the question how this information can be exploited for anti-parasitic therapy.

4.4 Material and Methods

4.4.1 Expression Constructs

The WT ORF of mGBP2 (NCBI accession numbers: mGBP-2, NM_010260.1) was subjected to site directed mutagenesis (QuikChange II Mutagenesis kit, Stratagene) for generation of GTPase mutants R48A, K51A, E99A and D182N (Kravets et al., 2012) and isoprenylation mutant C586S (Degrandi et al., 2013) in the pEGFP-C2 plasmid (Clontech). The respective genes were then cloned into the pWPXL plasmid (Trono lab) as N-terminal GFP-fusion constructs. For the cloning of mCherry constructs, the pWPXL plasmid was modified by exchanging of the gene for GFP by the gene for mCherry. The ORFs of mGBP1 (NM_010259.2), mGBP2, mGBP3 (NM_001289492.1), mGBP5 (NM_153564.2), mGBP6 (NM_194336.2) were then cloned into the modified pWPXL plasmid as N-terminal mCherry-fusion constructs. The lentiviral envelope vector pLP/VSVG (Invitrogen) and the packaging vector psPAX2 (Trono lab) were used for the lentiviral genetic transfer.

4.4.2 Cell culture and transduction

MEFs were cultured in Dulbecco's modified Eagle's medium (DMEM, Invitrogen/Gibco) supplemented with 10% (v/v) heat-inactivated low endotoxin fetal bovine serum (FBS, Cambrex), 100 U/ml penicillin, 100 µg/ml streptomycin, 2 mM L-glutamine (Biochrom) and 0.05 mM β-mercaptoethanol (Invitrogen/Gibco). Human foreskin fibroblasts (HS27, ATCC CRL-1634) were hold in culture in Iscove's Modified Dulbecco's Medium (IMDM, Invitrogen/Gibco) with the same supplementations. 293FT cells were cultivated in DMEM supplemented with 10% FBS, 100 U/ml penicillin, and 100 µg/ml streptomycin. All recombinant lentiviruses were produced by transient transfection of 293FT cells according to standard protocols. Briefly, subconfluent 293FT cells were cotransfected with 20 µg of a plasmid vector, 10 µg of psPAX2, and 5 µg of pLP/VSVG by calcium chloride precipitation in FBS free medium. After 6 h medium was changed (10% FBS), and supernatants with recombinant lentivirus vectors were harvested 48 h later. Alternatively, the trasfection was performed utilizing the jetPRIME® trasfection reagent (Polyplus) in medium supplemented with 10% FBS. MEFs were seeded in 24 well plates (Corning Incorporated) and transduced with 600 µl of lentivirus with 25 µg Polybrene (Millipore). After 4 h of incubation medium was changed. The transduction efficacy was analyzed by flowcytometry. Subsequently, GFP or GFP/mCherry positive cells were sorted and cultivated.

Tachyzoites from *T. gondii* strain ME49 were maintained by serial passage in confluent monolayers of HS27 cells. After infection of fibroblasts, parasites were harvested and passaged as described previously (Degrandi et al., 2007).

4.4.3 Infection of murine MEFs with *T. gondii*

Cells were stimulated with 200 U/mL IFNγ (R&D Systems) 16 h before infection. For immunofluorescence, MEFs were cultured in 24-well plates (Falcon, BD Biosciences) on cover slips (ø 13 mm, VWR International) and inoculated with freshly harvested *T. gondii* at a ratio of 50:1. To remove extracellular parasites, cells were washed with PBS.

4.4.4 Immunofluorescence analysis

Cells were fixed in 4% paraformaldehyde (PFA, Sigma-Aldrich) permeabilized with 0.02% saponin (Calbiochem-Merck) and blocked in 0.002% saponin with 2% goat serum (DaKoCytomation). The outer membrane of *T. gondii* was visualized by anti-SAG1

(Abcam) at a concentration of 1/700. As secondary reagents, 1/200 concentrated Cy2-conjugated goat anti-rabbit IgG and Cy3-conjugated goat anti-mouse IgG plus IgM (Jackson ImmunoResearch Laboratories) were used. Nuclei were counterstained with 1/2500 4',6-diamidino-2-phenylindole (DAPI, Invitrogen). The cover slips were fixed in fluorescence mounting medium (Fluoromount-G, Southern Biotechnology Associates). Fluorescence was visualized using a LSM780 confocal microscope (Zeiss). Image analysis and processing was performed with the ZEN (Zeiss) and Imaris (Bitplane) softwares.

4.4.5 Confocal live cell imaging

Live cell imaging was performed using an LSM780 confocal microscope (Zeiss, Germany) at 37°C with 8% CO_2 and humidity saturated air. Cells were cultured and imaged on imaging dishes CG (MoBiTec, Germany) with Phenol-free cell culture media. Image analysis was performed with the software ZEN (Zeiss), Imaris (Bitplane) and AutoquantX3 (MediaCy/Bitplane).

4.4.6 MFIS experiments

MFIS experiments (Kudryavtsev et al., 2006; Weidtkamp-Peters et al., 2009) were performed with a confocal laser scanning microscope (Olympus FV1000, IX81 inverted microscope) additionally equipped with a single photon counting device with picosecond time-resolution (PicoQuant Hydra Harp 400, PicoQuant, Berlin, Germany). GFP was excited at 485 nm with a linearly polarized, pulsed (32 MHz) diode laser (LDH-D-C-485) at 0.4 µW at the objective (60x water immersion, Olympus UPlanSApo NA 1.2, diffraction limited focus). mCherry was excited at 559 nm with a continuous-wave laser (FV1000) at 0.54 µW at the objective. The emitted light was collected in the same objective and separated into its perpendicular and parallel polarization (PBS 101, Thorlabs). GFP fluorescence was then detected by SPADs (PD5CTC, Micro Photon Devices, Bolzano, Italy) in a narrow range of its emission spectrum (bandpass filter: HC520/35 (AHF, Tübingen, Germany)). mCherry fluorescence was detected by HPDs (HPMC-100-40, Becker&Hickl, Berlin, Germany), of which the detection wavelength range was set by the bandpass filters (HC 607/70, AHF). Images were taken with 20 µs pixel time and a resolution of 276 nm/pixel. With 485 nm excitation, series of 40-100 frames were merged to one image and further analyzed with custom-designed software (Widengren et al., 2006).

4.4.7 Pixel-wise MFIS analysis of fluorescence parameters

From the recorded GFP (S_G) and mCherry (S_R) signal intensities, background intensities of the regions where no cells localize were subtracted to determine fluorescence intensities of GFP (F_G) and mCherry (F_R) respectively. To determine fluorescence anisotropy (r_D) and fluorescence-weighted donor lifetimes ($\langle\tau_D\rangle_f$) in each pixel, the histograms presenting the decay of fluorescence intensity after the excitation pulse were built with 256 bins and 128 ps per bin. The fitting procedures were described in (Stahl et al., 2013) and (Kravets et al., 2012).

4.4.8 Formal pixel-integrated MFIS-FRET analysis

In each obtained MFIS image, pixels in the VLS and in the cytosol in uninfected cells, and pixels at the PVM and in the cytosol in infected cells were separately selected according to fluorescence photon number (Figure 4-1A, 2A, 4A and 6A). Photons from each pixel selection were integrated to an intensity decay histogram with 1024 bins and

32 ps per bin. The pixel-integrated histograms were formally fitted according to the 1-k_{FRET} model introduced in Section 2.2.2 (Eq. (2-1) - (2-4)) to quantitatively determine x_{FRET} and k_{FRET}. This formal analysis revealed that mGBPs exhibit distinct FRET features in different cellular compartments (Figure 4-15).

4.4.9 $\varepsilon_{mix}(t)$ and $\varepsilon_{(D,A)}(t)$ diagrams

FRET-related donor quenching histogram ($\varepsilon_{mix}(t)$) was plotted to directly separate different molecular species and visualize FRET efficiency in the pixel-integrated data. The mathematical formalism of $\varepsilon_{mix}(t)$ and $\varepsilon_{(D,A)}(t)$ is introduced in Section 2.2.2 (Eq. (2-3) – Eq. (2-4)) To directly compare different experiments, $\varepsilon_{(D,A)}(t)$ diagrams were plotted in Figure 4-4D. A steeper slope in $\varepsilon_{(D,A)}(t)$ diagram indicates that the experiment showed higher k_{FRET}. This formal analysis revealed that mGBPs exhibit distinct FRET features in different cellular compartments (Figure 4-15).

4.4.10 Pattern based pixel-integrated MFIS-FRET analysis

To resolve three characteristic protein species, namely mGBP monomer (with specie fraction x_{mono}), dimer (x_{di}) and oligomers (x_{oligo}) by analyzing time-resolved anisotropy $r_{mix}(t)$ (Eq. (4-1)) and time-resolved FRET-induced donor decay $\varepsilon_{mix}(t)$ (Eq. (4-2)) for homo- and hetero-FRET, respectively, both decays were fitted with a linear combination of three species-specific patterns.

Homo-FRET. The $r_{mix}(t)$ of homo-FRET data was fitted with:

$$r_{mix}(t) = r_0 \cdot \left(x_{mono} + x_{di} \left(\int p(k_{di}) e^{-2 \cdot k_{di} \cdot t} dk_{di} \right) + x_{oligo} \left(x_s e^{-2 \cdot k_{oli,s} \cdot t} + x_l e^{-2 \cdot k_{oli,l} \cdot t} \right) \right) e^{-t/\rho_{global}} \qquad (4\text{-}1)$$

Here $p(k_{di})$ is the FRET-rate distribution of mGBP2 dimer complex as determined by the conformational sampling of the sterically allowed space (see Section 4.4.11, Figure 4-7B and Figure 4-17D). $k_{olig,s}$ and $k_{olig,l}$ are formally assigned as the FRET rate constants of mGBPs oligomers of small and large sizes respectively (Figure 4-7B), and x_s and x_l are their normalized fractions. It has to be considered that energy can be transferred in forward and backward direction which doubles the rate constants. The monomer is described by a constant offset, because there is no FRET. The fundamental anisotropy r_0 for GFP molecules is known as 0.38. The global rotational correlation time ρ_{global} was estimated as 15 ns given the molecular weight of G-mGBP2 fusion protein. Oligomer species which produced ultrafast decay components in $r_{mix}(t)$ resulted in a drop in the initial anisotropy (Figure 4-6D). With the knowledge of r_0 they can be determined together with other species in homo-FRET data.

Hetero-FRET**.** An analogous analysis was applied to the hetero-FRET data. The $\varepsilon_{mix}(t)$ was fitted with:

$$\varepsilon_{mix}(t) = x_{mono} + x_{di}\left(\int p(k_{di})e^{-k_{di}\cdot t}dk_{di}\right) + x_{oligo,s}e^{-t\cdot k_{oli,s}} \tag{4-2}$$

in which $x_{oligo,s}$ denotes the species fraction of small oligomers. In the case of hetero-FRET, donor molecules in large oligomers (with species fraction $x_{oligo,l}$) could be strongly quenched by nearby acceptors up to nearly 100% and thus became irresolvable owing to the finite width of the instrument response function. Therefore the information of large oligomers in hetero-FRET data needed to be recovered according to the homo-FRET data. In the latter, the species fractions of small and large oligomers were found equal in various compartments. Based on the relation $x_{oligo,s} = x_{oligo,l}$ the large oligomer fractions in hetero-FRET data were extrapolated. Moreover, such a coherent behavior between small and large oligomers indicated that they have a common origin; and the broad distribution of their rate constants showed that oligomers may consist of a variety number of units (Figure 4-7B). Hence, it is more meaningful to combine both oligomer species and generally sort protein species as monomer, dimer and oligomer as displayed in Figure 4-6C. The fits were performed by custom software programmed in MATLAB.

4.4.11 Monte Carlo sampling of the donor-acceptor conformational space of mGBP2 dimer

Based on the hGBP1 crystal structure (Prakash et al., 2000) homology models of the G-mGBP2 (PDB-ID: 1F5N , 4EUL) and mCherry-mGBP2 fusion protein (PDB-ID: 1F5N, 2H5Q) (Table 4-3) were constructed using MODELLER (Fiser and Sali, 2003). The homology models were protonated using PDB2PQR (Dolinsky et al., 2007). Then the protonated full-length protein models were mapped to a reduced representation solely consisting of the C-, C_α-, N-, O- and the hydrogen atoms forming the NH-O bonds. The repulsion between the atom pairs (O, N), (C, O) and (C, N) were modeled as repulsive quadratic potential (Kalinin et al., 2012) and the existing hydrogen bonds as simple scaled attractive potential (1/r) preserving secondary structural elements. The sampling was performed on the φ and ψ torsion angles. In each iteration step the torsion angle of one amino acid was changed by random value taken from a Gaussian-distribution with a width of 0.025 rad. The sampling of the conformational space was restricted to the linkage region. Thus, only the internal coordinates of the connecting linker were altered while the internal coordinates of the beta-barrels as well as the internal coordinated of the mGBP2 model were kept constant. Given the sampled conformation of the mCh-mGBP2 and the G-mGBP2 constructs a putative head-to-head dimer structures was created by superimposing the LG-domains onto the LG-domains in the dimer structure of hGBP1 in presence of GppNHp (PDB-ID: 2BC9) and discarding conformations with clashes (Vöpel et al., 2014). To calculate the donor-acceptor distance, R_{sim}, in every simulated structure, on each fluorophore, two Cα-atoms on the beta-barrel (Asn122 and Asn147 on GFP, Tyr125 and Glu149 on mCherry) were chosen (Figure 4-17A, Table S2), so that the connecting vector of the two atoms is a good approximation of the transition dipole. The distance between the middle points of the connecting vectors of the donor and acceptor is taken as the distance between the chromophores ($R_{DA,sim}$). Table 4-4 lists out the detailed calculation steps to determine the ($R_{DA,sim}$) and orientation factor (κ^2). For each simulated mGBP2 dimer conformation, its k_{di} value was calculated according to:

$$k_{di} = (3/2) \cdot \kappa^2 \cdot (1/\tau_{D(0)}) \cdot (R_0/R_{DA,sim})^6 \tag{4-3}$$

in which $\tau_{D(0)} = 1/k_0$ is 2.6 ns and the Förster radius (R_0) of GFP and mCherry is 52Å including $\kappa^2 = 2/3$.

The donor-acceptor distance distribution obtained from the MC simulation of the mGBP2 dimer (Figure 4-17, blue curve) was used as the prior input, and was further optimized according to experimental data measured in the cytosol using the maximum entropy method (MEM) (Vinogradov and Wilson, 2000). The optimized distance distribution (MEM-MC) is plotted in Figure 4-17E (red curve). The difference between both distributions is primarily in the short distance range, because a small fraction of oligomers is present in the experimental data (Figure 4-7C), but of course absent in the

MC simulation of a dimer. The two distributions agree very well in the longer distance range, therefore the distribution from the MC dimer simulation (k_{di}) (Figure 4-7B) describes the experimental data in a valid manner.

4.4.12 Determination of mGBP protein concentrations and binding curves

mGBP protein concentrations. The protein concentration is monitored via the fluorescence intensity of the fused fluorescent proteins. The detection volume of the MFIS microscope was calibrated by Fluorescence Correlation Microscopy (FCS) measurements of Rhodamine 110 (Rh110) to determine its shape and size. The fitting model applied to the obtained FCS curve assumes a 3-dimensional Gaussian-shaped volume, and a single diffusing species including transitions to a triplet state as shown in (Weidtkamp-Peters et al., 2009). From the Rh110 diffusion time of 32 μs and aspect ratio of 7, the detection volume $V_{det\text{-}GFP}$ of GFP was determined as 0.5 fl. The detection volume of mCherry $V_{det\text{-}mCherry}$ is larger (0.8 fl) because of the longer wavelength. The brightness of GFP or mCherry in living cells was individually characterized from FCS measurements of freely diffusing fluorescent proteins in the cytosol. By fitting the same model function as in Rh110 experiment, it was found that with 0.54 μW of 559 nm laser excitation at the objective, mCherry brightness is $Q_{mCherry}$ = 0.1 kcpm (kilo counts per molecule) in the cytosol and that with 0.4 μW of 485 nm laser excitation, GFP brightness is Q_{GFP} = 0.56 kcpm in the cytosol.

The average mCherry fluorescence intensity of an image with mCherry excitation was first corrected for detector dead time (Becker, 2005), and then used to calculate the mCherry concentration with the determined detection volume and the mCherry brightness.

The average GFP fluorescence intensity of an image with GFP excitation was first corrected for detector dead time, and then the obtained intensity ($S_{G,G}^{m}$) was further corrected for quenching effect due to FRET:

$$S_{G,G}^{u} = \frac{S_{G,G}^{m}}{\left(1 - x_{FRET}\right) + x_{FRET} \cdot \left(1 - E\right)} \tag{4-4}$$

$S_{G,G}^{u}$ denotes unquenched GFP fluorescence intensity in the absence of hetero-FRET and was used to calculate the GFP concentration.

The average mCherry fluorescence intensity of an image with mCherry excitation was first corrected for detector dead time (Becker, 2005), and then used to calculate the mCherry concentration with the determined detection volume and the mCherry brightness.

The concentration of GFP (C_{GFP}) was determined by

$$C_{GFP} = \frac{S_{G,G}^{u}}{Q_{GFP} \cdot V_{\det - GFP}} = \frac{S_{G,G}^{u}}{0.56kcpm \cdot 0.5fl} \tag{4-5}$$

The concentration of mCherry ($C_{mCherry}$) was determined by

$$C_{mCherry} = \frac{S_{R,R}}{Q_{mCherry} \cdot V_{\det - mCherry}} = \frac{S_{R,R}}{0.1kcpm \cdot 0.8fl} \tag{4-6}$$

We note that we do not measure intensities of single-molecule events as described by (Wu et al., 2009) but intensity averages of pixel populations so that it is sufficient to use an average brightness Q for the calculation of the FP concentrations. In our pattern fits we usually find on average less than 10% of non-FRET species (Figure 4-7C). From this we conclude that under our conditions with one photon excitation of donors with low irradiance (as compared to the two photon excitation used by (Wu et al., 2009) and low FRET efficiency most of the mCherry molecules are active FRET-acceptors. The $K_{D,\mathrm{dim}}$ of ~24 nM of mGBP2 dimerization determined in this way is very close to previous biochemical studies (Kravets et al., 2012).

In Eq. (4-4), the FRET-active species fraction (x_{FRET}) is obtained from fitting of each measurement in pixel-integrated MFIS-FRET analysis using the 1-k_{FRET} model. FRET efficiency, E, was calculated as:

$$E = 1 - \frac{\sum_m x_{D0}^{(m)} \cdot \left(k_{D0}^{(m)} + k_{FRET}\right)^{-1}}{\sum_m x_{D0}^{(m)} \cdot \left(k_{D0}^{(m)}\right)^{-1}} \tag{4-7}$$

4.4.13 Determination of association constants

To quantify the dependence of the dimeric species fraction on the total protein concentration (initial increase, stationary phase followed by a decrease) we used the simplest possible model that can approximate such a behavior. In this model we assume the formation of a dimer and a subsequent formation of a tetramer formed by two dimers. The formation of a dimer and a tetramer can be described by two reactions with corresponding dissociation equilibrium constants:

$$\begin{aligned} &A_1 + A_1 \to A_2 \qquad K_{D,\mathrm{dim}} = \frac{c(A_1)c(A_1)}{c(A_2)}, \\ &A_2 + A_2 \to A_4 \qquad K_{D,oligo} = \frac{c(A_2)c(A_2)}{c(A_4)} \end{aligned} \tag{4-8}$$

For given of equilibrium constants and a total protein concentration $c_T = c(A_1) + 2 \cdot c(A_2) + 4 \cdot c(A_4)$ the species concentrations $c(A_1), c(A_2), c(A_4)$ were determined numerically by solving the fourth polynomial equation $c_T(A_1)$ by a simple root-finding algorithm (Ridders, 1979) and minimize the disagreement between the modeled species fractions and the fitted fractions by a Quasi-Newton method (Shanno and Kettler, 1970). We extended this model of stepwise oligomer formation by the stepwise binding of dimer in a non-cooperative fashion (i.e. all equilibrium constants are equal to $K_{D,oligo}$) up to a dodecamer. If the total concentration of all oligomers is used to display the binding isotherm, one obtains an only slightly broadened binding isotherm compared to the tetramer system. If this binding isotherm is fitted with the simpler tetramer model, a binding constant for dimer binding $K_{D,app\text{-}oligo}$ is obtained, which is slightly (factor 1.6) larger than the simulated value.

As no information on the cooperativity of binding and the spatially resolved GTP concentration was available, the formation of higher order oligomers was approximated by the minimal tetramer model for the following reasons: (1) FRET only senses its local environment (i.e. a limited oligomer size) thus the contribution of each monomer unit to the measured signal decreases with increasing oligomer size. (2) This simple model reduces the number of fitting parameters to an adequate level given the spread of the data-points. To conclude, a simple model with a Langmuir binding isotherm (i.e. non-cooperative binding) describes all experiments very well. The simulation showed that the obtained apparent dissociation constant $K_{D,app\text{-}oligo}$ is a good approximation for the true $K_{D,oligo}$.

Note that the observed reduction in steady-state anisotropy (r_D) for cells of high mGBP2 concentration as displayed in Figure 4-4C, was mainly due to the large drop in the initial anisotropy of their time-resolved anisotropy ($r_D(t)$) as plotted in Figure 4-6D. Therefore the $K_{D,app}$ value (9 μM) derived from r_D in fact reports the mGBP2 oligomerization processes that could produce such ultrafast depolarizing effect, and is very close to the 8 μM obtained by fitting $r_D(t)$ with the species-resolved model. Hence, the two independent approaches interrogating the same oligomerization process delivered very consistent results, verifying the reliability of the analyses.

4.4.14 Maximum FRET rate constants

Due to its inverse sixth-power distance dependence (Eq. (4-9)), FRET depends on molecular proximity and cannot occur between remotely located fluorescent proteins. Consequently, in large mGBP oligomers, the FRET-induced donor quenching will eventually saturate regardless of the presence of more acceptors simply because they are too distant. If assuming that the mGBP proteins are arranged homogeneously in mGBP oligomers, the maximum k_{FRET} can be estimated following the ideas of T. Förster (Förster, 1949).

Here, the case of a single donor is considered, the FRET rate constant k_{FRET} from the donor to N surrounding acceptors is given by Eq. (4-9) using the parameter in Eq. (4-3).

$$k_{FRET,\max} = \frac{1}{\tau_{D0}} \sum_{k=1}^{N} \left(\frac{R_0}{R_{DA,k}} \right)^6 \tag{4-9}$$

with $R_{DA,k}$ being the distance between the donor and the k-th acceptor k_{FRET}. Assuming that the acceptors that attached on mGBPs are homogeneously distributed around the donor and closed packed with a minimum inter-fluorophore distance R_{min}, which is ~ 26 Å given by the molecular dimensions of fluorescent proteins, a similar estimation of the maximum k_{FRET} as in (Förster, 1949) can be performed.

To determine the maximum FRET-rate constant at which a donor molecule is quenched by multiple acceptors it was assumed that at saturation protein concentrations the space around the donor is fully filled by acceptors and the space that is occupied by the donor cannot be occupied by the acceptor. If a donor is homogenously surrounded by acceptors, given a constant molecular density ρ (number of acceptors per volume), which are separated at least by a distance of Rmin from the donor, the FRET-rate constant is given by:

$$\begin{aligned} k_{FRET} &= \frac{1}{\tau_0} \int_{R_{\min}}^{\infty} \rho \cdot 4\pi R^2 \left(\frac{R_0}{R} \right)^6 dR = \rho \frac{R_0^6}{\tau_0} \frac{4}{3} \pi \cdot \frac{1}{R_{\min}{}^3} \\ &= \frac{1}{\tau_0} \frac{R_0{}^6}{R_{\min}{}^3 \cdot R_{\mathrm{mol}}{}^3} \end{aligned} \tag{4-10}$$

R_{mol} is the mean radius of the acceptor molecules and relates to molecular density ρ. Given the molecular structure of mCherry in mCh-mGBPs fusion proteins, R_{mol} is approximated by 31 Å. The minimum possible distance R_{mol} is given by the structure of the fluorescent proteins (~20-30 Å). Therefore, the maximum possible FRET rate constant k_{FRET} was approximated by 15 ns^{-1}.

4.4.15 Scanning fluorescence intensity distribution analysis (FIDA) for determination of oligomer size

To investigate the size (composition) of mGBP2 oligomer locating at the PVM which can exceed the detectable range of FRET technique (> 10 nm), FIDA from (Kask et al., 2000) was adapted for imaging measurements and employed in infected G-mGBP2 expressing cells. Given the recorded photon trace in the image line of selected PVM area, 20 µs binned new sliding with 2.5 µs (1/8 × pixel time) steps intensity traces were computed. Then a corresponding 2D matrix of green versus red photon counts from all the time windows is generated and analysed by 2D FIDA. The average brightness, $\langle Q_{oligo} \rangle$, and average number, $\langle N_{oligo} \rangle$, of the mGBP2 oligomers could be determined. The average number of mGBP2 units (Figure 4-7E) per oligomer $\langle N_{mGBP2} \rangle$ is calculated as the ratio of obtained $\langle Q_{oligo} \rangle$ to single GFP brightness Q_{GFP}:

$$\left\langle N_{mGBP2} \right\rangle = \frac{\left\langle Q_{oligo} \right\rangle}{Q_{GFP}} \tag{4-11}$$

Based on these two average numbers of oligomers and mGBP2 units per pixel and knowing the excitation volume of the setup, the average mGBP2 concentration $\langle c_{mGBP2} \rangle$ is calculated as:

$$\left\langle c_{mGBP2} \right\rangle_{FIDA} = \frac{\left\langle N_{oligo} \right\rangle \cdot \left\langle N_{mGBP2} \right\rangle}{N_A \cdot V_{\det-GFP}} \tag{4-12}$$

where $N_A = 6.022 \times 10^{23}$ mol^{-1} is the Avogadro‘s number and $V_{det\text{-}GFP} = 0.5$ fl – excitation volume of the used laser. The mGBP2 concentration calculated from scanning FIDA was compared with that directly derived from the GFP intensity as a control. Figure 4-17F shows the good agreement between both methods.

4.5 Supplementary Figures

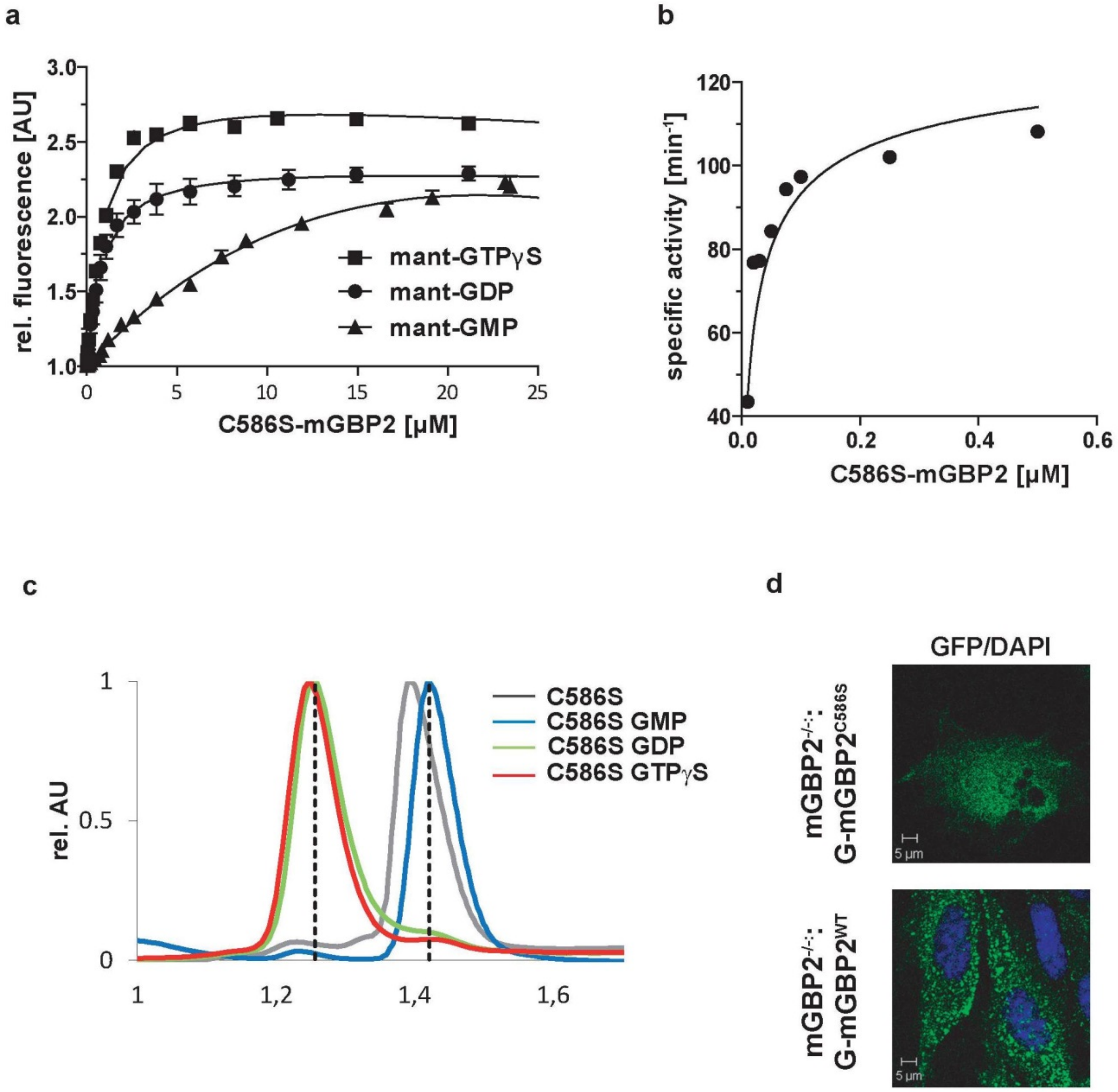

Figure 4-11 Biochemical properties and intracellular localization of the C586S mutant of mGBP2. (**A**) Nucleotide binding. A solution containing 0.5 µM mant-GTPγS, mant-GDP and mant-GMP was titrated with C586S mutant of mGBP2. The fluorescence was excited at 355 nm and detected at 448 nm. The values were normalized to the fluorescence of the nucleotide alone. Dissociation constants are calculated from the fit of the binding curves as in (Kravets et al., 2012). The results averaged over two to four experiments each are given in the Table 4-3. (**B**) GTP-hydrolysis. Concentration-dependent GTP-hydrolysis catalyzed by the C586S mutant was measured with a fixed concentration of GTP (1 mM) at

37°C. The initial rates were measured (< 30% GTP hydrolyzed) from the linear parts of time-course experiments and normalized to the protein concentrations used (specific activity). The specific activities were then plotted against protein concentrations. The data were fitted to a model describing the interaction of two molecules of mGBP2, yielding K_D (µM) and the maximal specific activity K_{max} (min^{-1}). The maximum specific GTPase activitiy, the dimer dissociation constant and the amount of GMP production are summarized in the Table 4-3. (**C**) Nucleotide-dependent multimerization. Size-exclusion chromatography of the C586S mutant of mGBP2 bound to GTPγS, GDP, GMP and in the nucleotide free state at 4°C. Elution of all proteins was followed using absorbance by 280 nm. The protein size was estimated by appropriate standard proteins and the absorbance values were normalized to the peaks of the curves. (**D**) Intracellular localization of WT and C586S-mGBPs was analyzed by transduction of the GFP fusion constructs in mGBP2$^{-/-}$ MEFs. Cells were stimulated with IFNγ for 16 h. Glass slides were analyzed by confocal microscopy. Bars, 5 µm.

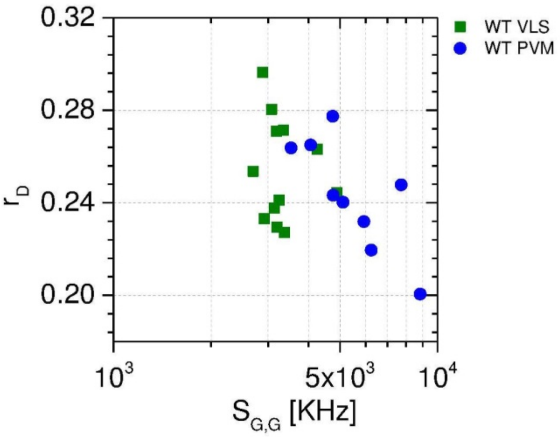

Figure 4-12 Spectroscopic characterization of G-mGBP2 WT in VLS in non-infected cells and at the PVM in *T. gondii* infected cells via homo-FRET assay. Average values of GFP fluoresecnce anisotropy (r_D) and signal intensity ($S_{G,G}$) over single-cell measurements are plotted, in which $S_{G,G}$ values are proportional to protein concentration. A much wider distribution of $S_{G,G}$ can be observed for G-mGBP2 localizing at the PVM (blue circles) comparing to the $S_{G,G}$ values for G-mGBP2 localizing in the VLS (green squares).

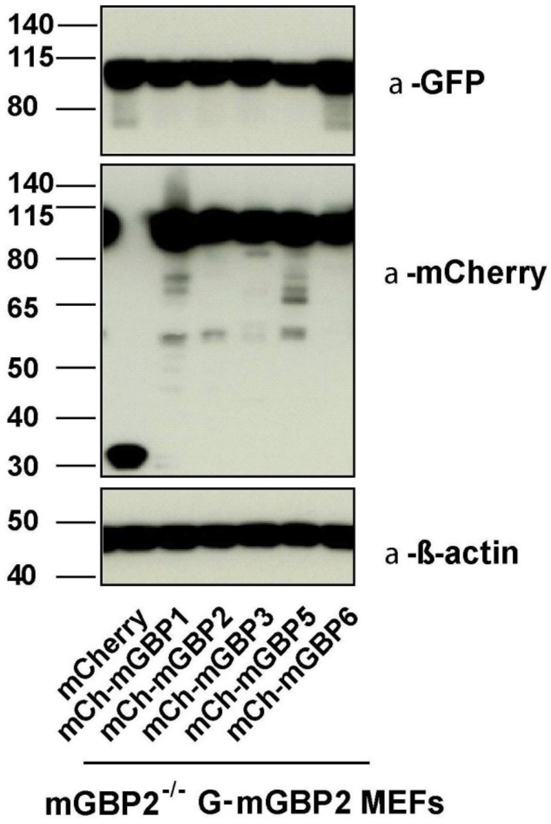

Figure 4-13 Expression analysis of coexpressed mGBP proteins. Expression levels of mGBPs in postnuclear supernatants of mGBP2$^{-/-}$ MEFs reconstituted with G-mGBP2 and coexpressing one of the mCh-mGBPs (mGBP1, mGBP2, mGBP3, mGBP5, mGBP6) were analyzed by Western Blotting. mCherry protein expressing cells served as controls. Cells were stimulated with IFNγ for 16 h. Blots were stained with the α-mCherry antibody.

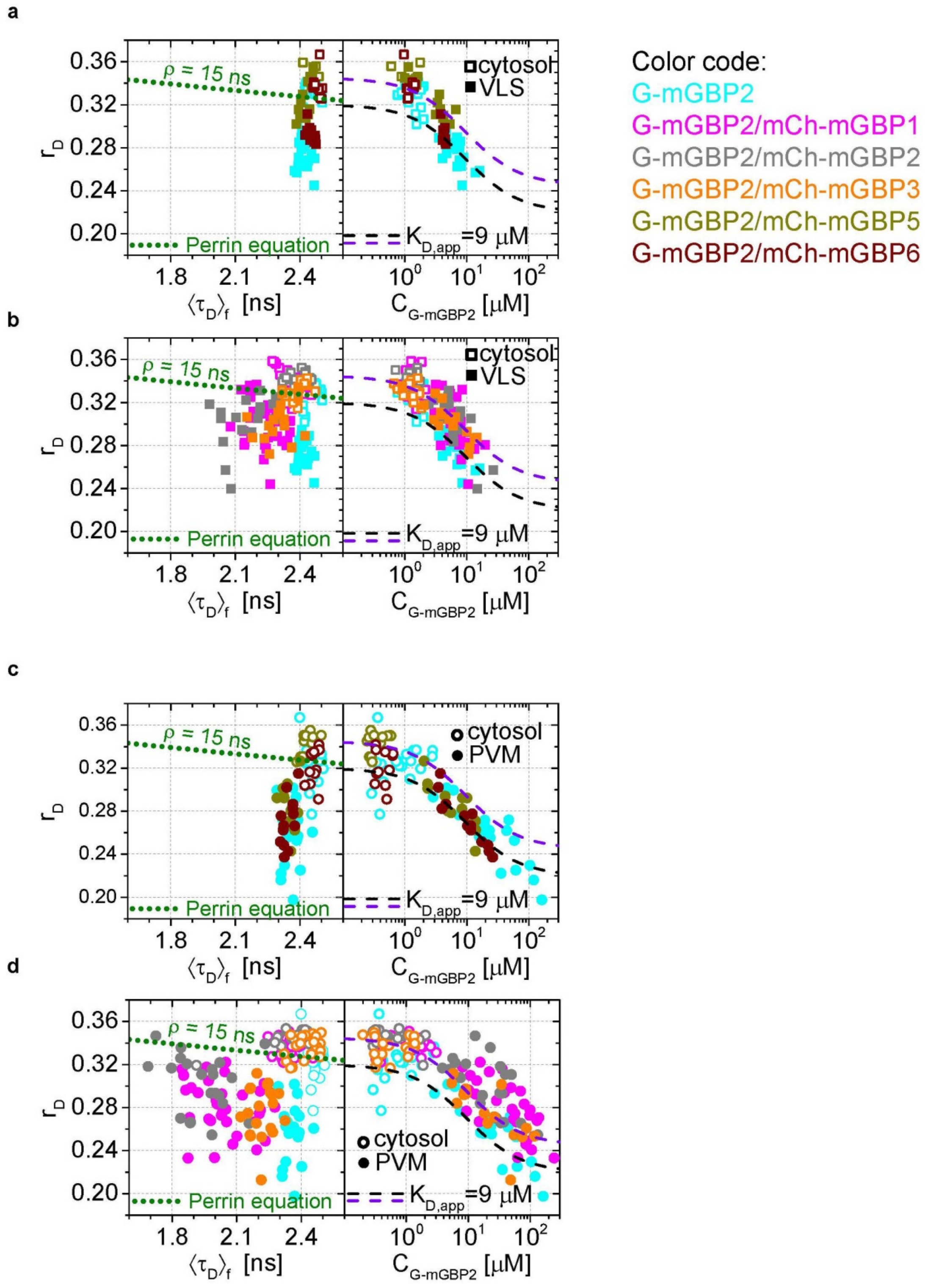

Figure 4-14 Intracellular homo- and hetero-multimerization of mGBPs in cells. (**A**) For single IFNγ stimulated mGBP2$^{-/-}$ MEFs expressing G-mGBP2 alone or coexpressing G-mGBP2/mCh-mGBP5, and G-mGBP2/mCh-mGBP6, average values of r_D in the cytosol (empty) and in the VLS (solid) were plotted

against $\langle \tau_D \rangle_f$ or G-mGBP2 concentrations ($C_{G\text{-}mGBP2}$). See the legend of Figure 4-4C for the description of the overlay curves in both panels. (**B**) Corresponding plots as in (A) for single cells expressing G-mGBP2 alone or coexpressing G-mGBP2/mCh-mGBP1, G-mGBP2/mCh-mGBP2 and G-mGBP2/mCh-mGBP3. (**C**) Corresponding plots as in (**A**) for *T. gondii* infected cells. (**D**) Corresponding plots as in (**B**) for *T. gondii* infected cells.

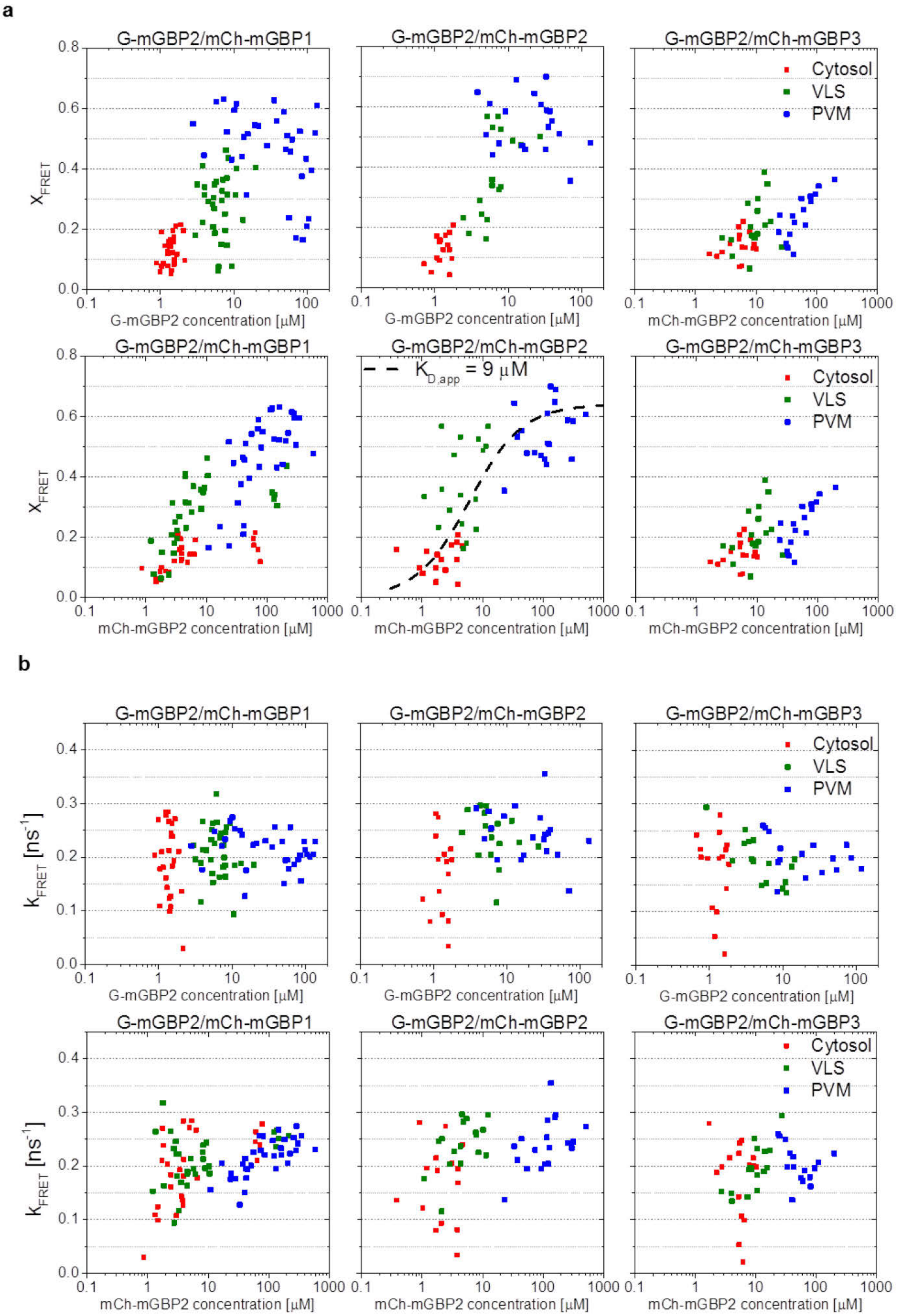
a
G-mGBP2/mCh-mGBP1
G-mGBP2/mCh-mGBP2
G-mGBP2/mCh-mGBP3
Cytosol
VLS
PVM
x$_{FRET}$
0.0
0.2
0.4
0.6
0.8
0.1
1
10
100
1000
G-mGBP2 concentration [µM]
mCh-mGBP2 concentration [µM]
K$_{D,app}$ = 9 µM
b
k$_{FRET}$ [ns^{-1}]
0.0
0.1
0.2
0.3
0.4

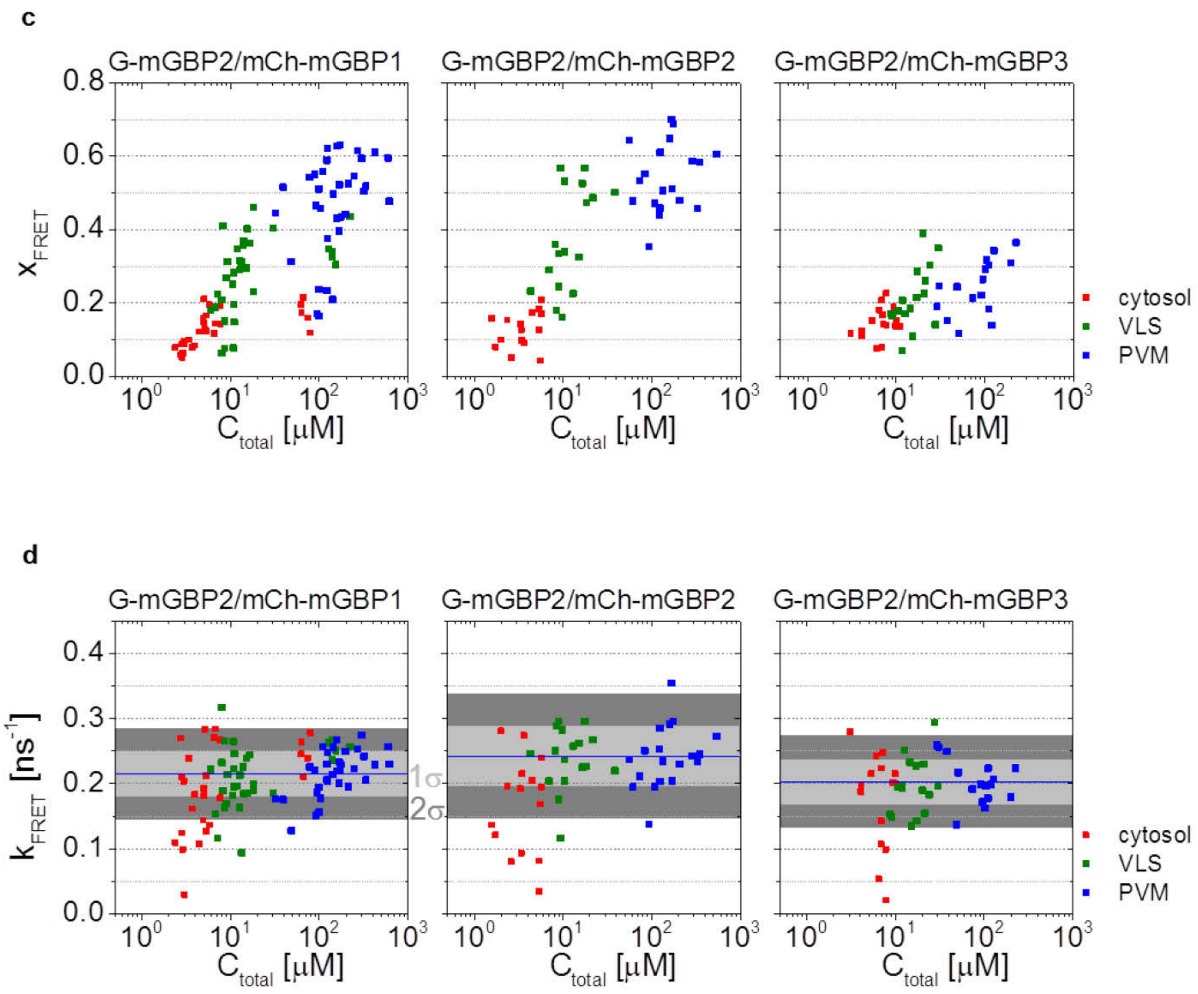

Figure 4-15 Quantitative MFIS-FRET analysis of mGBP2 hetero-multimerization in living IFNγ stimulated cells. (**A**) All the experiments on G-mGBP2/mCh-mGBP1, G-mGBP2/mCh-mGBP2 and G-mGBP2/mCh-mGBP3 interactions were formally analyzed according to the 1-k_{FRET} model (Section 0). Fit results of species fraction of FRET-active complex (x_{FRET}) is plotted against G-mGBP2 and mCh-mGBPs concentrations determined in cytosol (red), in VLS (green) and at PVM (blue). The overlaid fuction curve plotting $x_{FRET} = S \cdot C_{mCh-mGBP2} / \left(C_{mCh-mGBP2} + K_{D,app} \right)$ assumes a mGBP2 Langmuir binding model with apparent dissociation constant, $K_{D,app}$ = 9 μM, the same value as applied in Figure 4-4C and Figure 4-6B. The scaling factor S = 0.64 was adjusted according to the saturation level of x_{FRET}. (**B**) For the same experiments as in (**A**), FRET rate constants (k_{FRET}) are plotted versus G-mGBP2 and mCh-mGBPs concentrations. (**C**) x_{FRET} in (**A**) is plotted versus total protein concentration. (**D**) k_{FRET} in (**B**) is plotted versus total protein concentration.

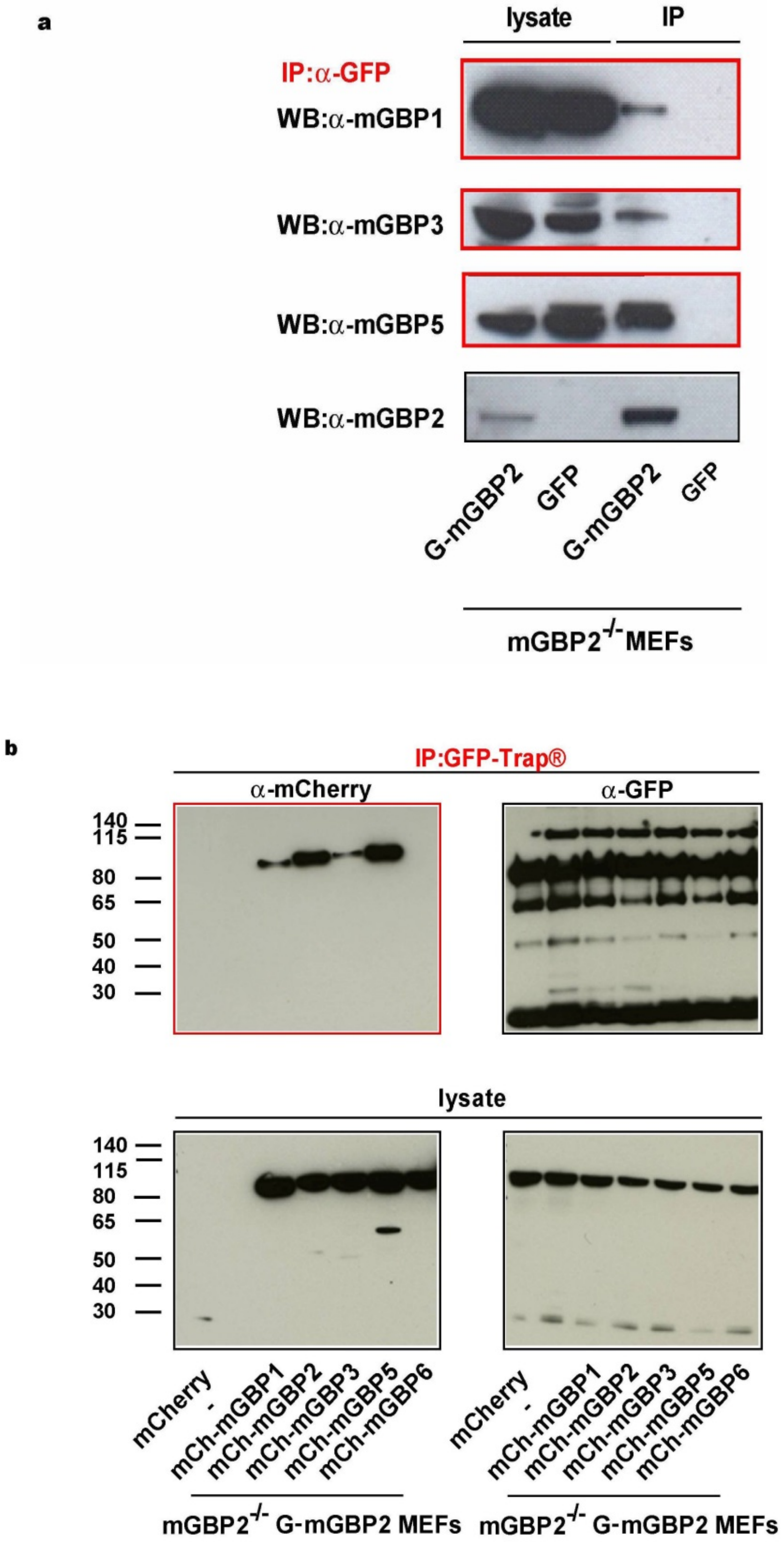

Figure 4-16 Immunoprecipitation analysis of mGBP proteins. (**A**) mGBP2$^{-/-}$ MEFs reconstituted with G-mGBP2 or GFP were stimulated with IFNγ for 16 h, subsequently lysed and postnuclear supernatants

were incubated o/n with G-sepharose beads and the α-GFP antibody at 4°C. IP probes were subjected to Western Blotting. Blots were stained with the α-mGBP2, α-mGBP1, α-mGBP3, α-mGBP5 antibodies. (**B**) Postnuclear supernantants of mGBP2$^{-/-}$ MEFs reconstituted with G-mGBP2 and coexpressing mCherry protein or one of the mCherry fused mGBPs (mGBP1, mGBP2, mGBP3, mGBP5, mGBP6) were incubated o/n with GFP-Trap® beads at 4°C. IP probes were subjected to Western Blotting. Blots were stained with the α-GFP and α-mCherry antibodies.

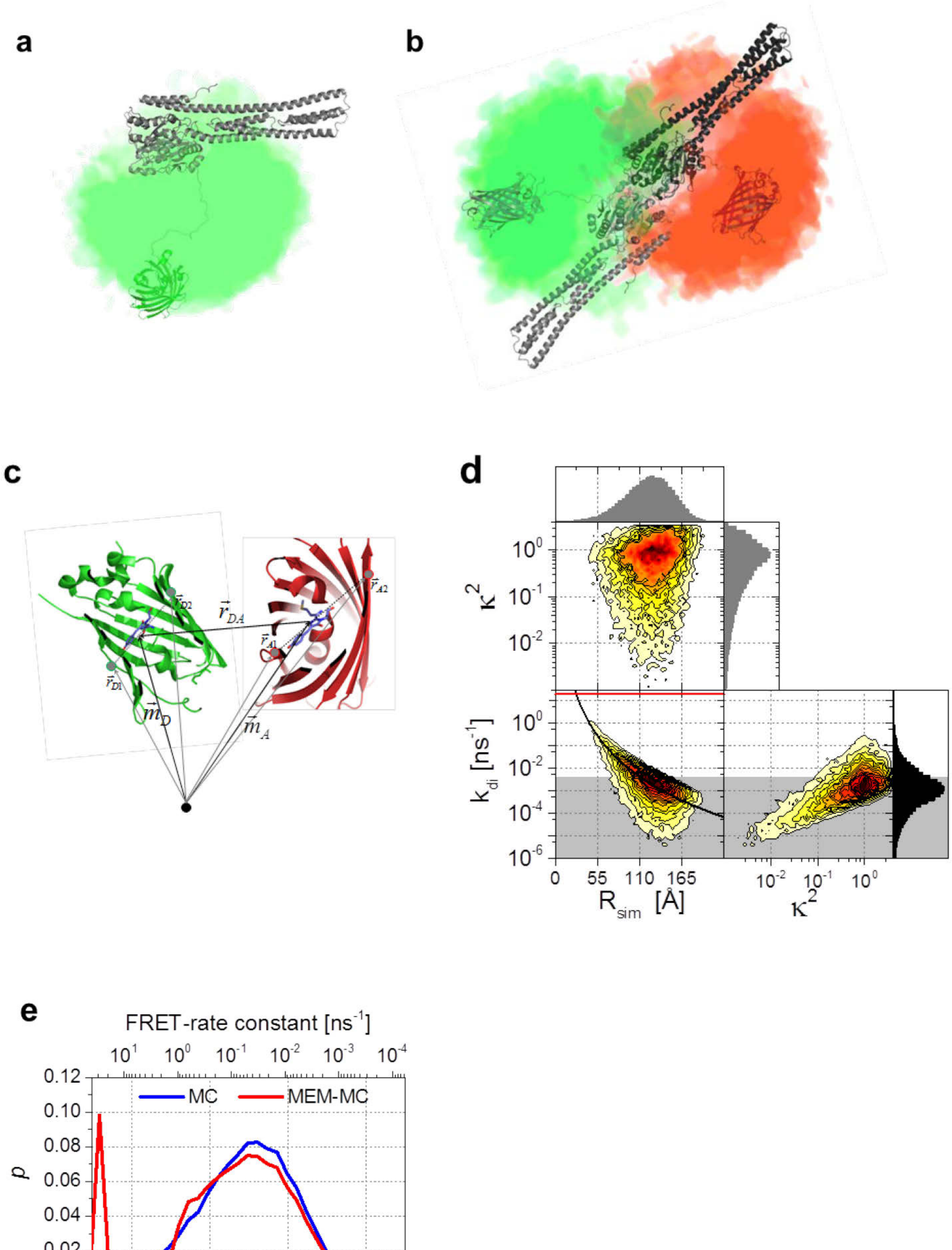
a
b
c
$\vec{r}_{D2}$
$\vec{r}_{DA}$
$\vec{r}_{A2}$
$\vec{r}_{A1}$
$\vec{r}_{D1}$
$\vec{m}_D$
$\vec{m}_A$
d
κ^2
10^0
10^{-1}
10^{-2}
k_{di} [ns^{-1}]
10^0
10^{-2}
10^{-4}
10^{-6}
0
55
110
165
R_{sim} [Å]
10^{-2}
10^{-1}
10^0
κ^2
e
FRET-rate constant [ns^{-1}]
10^1
10^0
10^{-1}
10^{-2}
10^{-3}
10^{-4}
0.12
0.10
0.08
0.06
0.04
0.02
0.00
p
MC
MEM-MC
50
100
150
200
R_{DA} [Å]

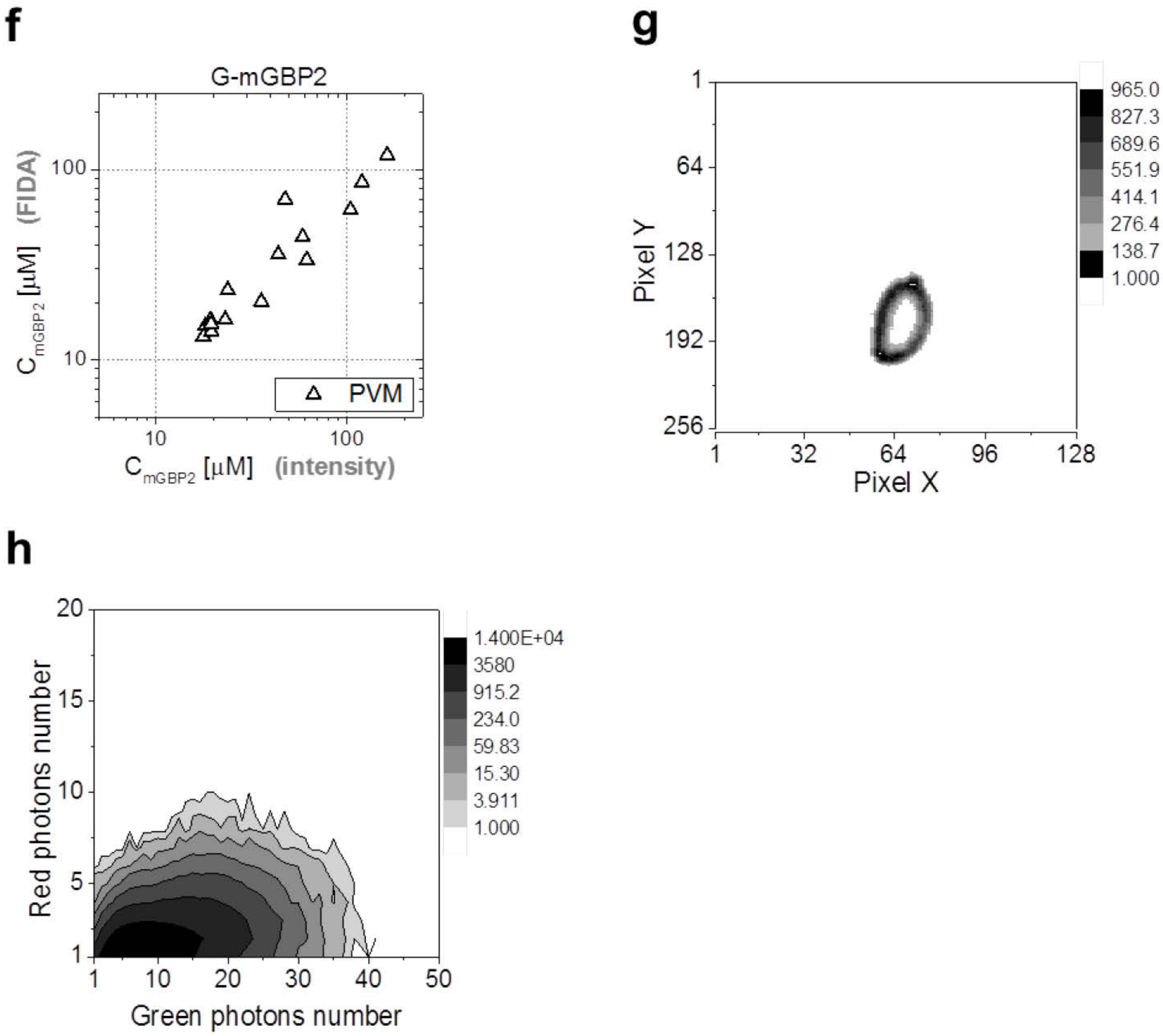

Figure 4-17 Sample mGBP2 dimer conformations by MC molecular simulation. (**A**) Conformational space sampled by the MC simulations of free mGBP2 is illustrated by the density of the GFP-chromophore, one conformation is shown using cartoon representation. (**B**) Structural properties of a predicted mGBP2 dimer based on the crystal structure of the hGBP1 dimer (PDB-ID 2BC9). The characteristic FRET features of the dimer with flexibly linked fluorescent proteins can be predicted by calculating inter fluorophore distances from the space that is sterically accessible to the fluorescent proteins. The accessible space of attached fluorescent proteins (green (GFP) and red (mCherry) is depicted as fuzzy cloud; ≥ 60% of all D-A configurations are FRET-inactive due to their large distances between the fluorophores, Section 4.4.11). (**C**) Illustration of FRET parameter calculation on each sampled G-mGBP2/mCh-mGBP2 dimer conformation in the MC simulation. Vectors and coordinates in the figure are listed in Table 2-3. GFP:

green, mCherry: red. (**D**) Donor-acceptor orientation factor (κ^2), spatial distance (R_{sim}) and FRET rate (k_{di}) were computed for each sampled mGBP2 dimer conformation, and their relation is plotted in the histogram. In the left panel, the overlay curve in black assumes that the Förster radius between GFP and mCherry is 52 Å, unquenched GFP fluorescence lifetime is 2.6 ns and $\langle\kappa^2\rangle$ is 2/3. The red line indicates the maximum resolvable FRET rate constant for our detection system (20 ns^{-1}). The area shade in grey indicates the irresolvable low FRET rate constant ($E < 1\%$, $k_{di} < 0.004$ ns^{-1}), in which the conformations constitute ~73% of the whole population. (**E**) The donor-acceptor distance distribution (R_{DA}) obtained from the Monte Carlo (MC) simulation of mGBP2 dimer (blue) and its optimized distance distribution according to the experimental data using maximum entropy method (MEM-MC, in red), see Section 4.4.11 for details. (**F**) mGBP2 concentration determined by 2D FIDA analysis is plotted versus that directly derived from G-mGBP2 fluorescence intensity. (**G**) A typical image showing the pixels at the PVM area which were analysed by scanning FIDA. The grey scale indicates acquired photon count per pixel. (**H**) The corresponding 2D FIDA matrix analysing the fluorescence intensity in the green and red detection channel of (**G**) (the details of FIDA are given in Section 4.4.15).

4.6 Supplementary Tables

	Nucleotide-binding					
	mant-GTPγS	mant-GDP	mant-GMP	GFP-hydrolysis		
	K_D (µM)	K_D (µM)	K_D (µM)	K_{max} (min^{-1})	Dimer K_D (µM)	GMP (%)
WT	0.45	0.54	14.4	102	0.029	74
C586S	0.50	0.45	15.5	133	0.026	72
The % GMP indicates the relative amount of the two products, GDP and GMP						

Table 4-1 Dissociation constants K_D of mant-nucleotides for mGBP2 WT and C586S mutant determined by fluorescence titrations and GTPase activity parameters obtained by protein concentration-dependent hydrolysis.

	ME49 *T. gondii*			BK *T. gondii*		
	mGBP2**+**	mGBP2**+**	mGBP2**-**	mGBP2**+**	mGBP2**+**	mGBP2**-**
	SAG1**-**	SAG1**+**	SAG1**+**	SAG1**-**	SAG1**+**	SAG1**+**
w/o Saponin	50 %	38 %	12 %	n.d.	n.d.	3 %
0,15 % Saponin	n.d.	57 %	43%	n.d.	1 %	99 %

Table 4-2 G-mGBP2 cells were stimulated with IFNγ for 16 h and infected with *T. gondii* ME49 or BK strains for 2 h. After fixation and permeabilization with the indicated amounts of saponin, *T. gondii* were stained with an α-SAG1 antibody and DAPI. *T. gondii* were counted and categorized according the indicated mGBP2 and SAG1 fluorescence. N.d = not detected.

GFP	kept rigid	MVSKGEELFTGVVPILVELDGDVNGHKFSVSGEGEGDATYGKLTLKFICTTGKLPVPWPTLVTTLTYGVQCFSRYPDHMKQHDFFKSAMPEGYVQERTIFFKDDGNYKTRAEVKFEGDTLV**N**RIELKGIDFKEDGNILGHKLEYNY**N**SHNVYIMADKQKNGIKVNFKIRHNIEDGSVQLADHYQQNTPIGDGPVLLPDNHYLSTQSALSKDPNEKRDHMVLLEFVTAA
	flexible	GITLGMDELYKSGLRSELNFEFPGASEIHMSEP
mGBP2	kept rigid	MCLIENTEAQLVINQEALRILSAITQPVVVVAIVGLYRTGKSYLMNKLAGKRTGFSLGSTVQSHTKGIWMWCVPHPKKAGQTLVLLDTEGLEDVEKGDNQNDCWIFALAVLLSSTFIYNSIGTINQQAMDQLHYVTELTDLIKSKSSPDQSGVDDSANFVGFFPTFVWTLRDFSLELEVNGKPVTSDEYLEHSLTLKKGADKKTKSFNEPRLCIRKFFPKRKCFIFDRPAQRKQLSKLETLREEELCGEFVEQVAEFTSYILSYSSVKTLCGGIIVNGPRLKSLVQTYVGAISNGSLPCMESAVLTLAQIENSAAVQKAITHYEEQMNQKIQMPTETLQELLDLHRPIESEAIEVFLKNSFKDVDQKFQTELGNLLVAKRDAFIKKNMDVSSARCSDLLEDIFGPLEEEVKLGTFSKPGGYYLFLQMRQELEKKYNQAPGKGLQAEAMLKNYFDSKADVVETLLQTDQSLTEAAKEVEEERTKAEAAEAANRELEKKQKEFELMMQQKEKSYQEHVKKLTEKMKDEQKQLLAEQENIIAAKLREQEKFLKEGFENESKKLIREIDTLKQNKSSGKCTIL
mCherry	kept rigid	MVSKGEEDNMAIIKEFMRFKVHMEGSVNGHEFEIEGEGEGRPYEGTQTAKLKVTKGGPLPFAWDILSPQFMYGSKAYVKHPADIPDYLKLSFPEGFKWERVMNFEDGGVVTVTQDSSLQDGEFI**Y**KVKLRGTNFPSDGPVMQKKTMGW**E**ASSERMYPEDGALKGEIKQRLKLKDGGHYDAEVKTTYKAKKPVQLPGAYNVNIKLDITSHNEDYTIV
	flexible	EQYERAEGRHSTGGMDELYKEFPGASEIHMSEP
mGBP2	kept rigid	MCLIENTEAQLVINQEALRILSAITQPVVVVAIVGLYRTGKSYLMNKLAGKRTGFSLGSTVQSHTKGIWMWCVPHPKKAGQTLVLLDTEGLEDVEKGDNQNDCWIFALAVLLSSTFIYNSIGTINQQAMDQLHYVTELTDLIKSKSSPDQSGVDDSANFVGFFPTFVWTLRDFSLELEVNGKPVTSDEYLEHSLTLKKGADKKTKSFNEPRLCIRKFFPKRKCFIFDRPAQRKQLSKLETLREEELCGEFVEQVAEFTSYILSYSSVKTLCGGIIVNGPRLKSLVQTYVGAISNGSLPCMESAVLTLAQIENSAAVQKAITHYEEQMNQKIQMPTETLQELLDLHRPIESEAIEVFLKNSFKDVDQKFQTELGNLLVAKRDAFIKKNMDVSSARCSDLLEDIFGPLEEEVKLGTFSKPGGYYLFLQMRQELEKKYNQAPGKGLQAEAMLKNYFDSKADVVETLLQTDQSLTEAAKEVEEERTKAEAAEAANRELEKKQKEFELMMQQKEKSYQEHVKKLTEKMKDEQKQLLAEQENIIAAKLREQEKFLKEGFENESKKLIREIDTLKQNKSSGKCTIL

Table 4-3 Amino-acid sequence settings in the MC molecular simulation. The residues used to define the dipole of the chromophoric groups are indicated.

	Donor (GFP)	Acceptor (mCherry)
Coordinates of the two chosen C$_\alpha$-atoms	$\vec{r}_{D1}$ and $\vec{r}_{D2}$	$\vec{r}_{A1}$ and $\vec{r}_{A2}$
Distance between the two C□-atoms	$R_{D,21} = \left\lVert \vec{r}_{D2} - \vec{r}_{D1} \right\rVert_2$	$R_{A,21} = \left\lVert \vec{r}_{A2} - \vec{r}_{A1} \right\rVert_2$
Unit vector connecting the two C$_\alpha$-atoms	$\hat{\mu}_D = \frac{\vec{r}_{D2} - \vec{r}_{D1}}{R_{D,21}}$	$\hat{\mu}_A = \frac{\vec{r}_{A2} - \vec{r}_{A1}}{R_{A,21}}$
Coordinates of the middle point of the connecting vector	$\vec{m}_D = \vec{r}_{D1} + \frac{R_{D,21}}{2}\hat{\mu}_D$	$\vec{m}_A = \vec{r}_{A1} + \frac{R_{A,21}}{2}\hat{\mu}_A$
Calculation of donor-acceptor distance and orientation factor	$\vec{r}_{DA} = \vec{m}_D - \vec{m}_A$ $\quad R_{DA} = \left\lVert \vec{m}_D - \vec{m}_A \right\rVert_2$ $\quad \hat{\mu}_{DA} = \frac{\vec{r}_{DA}}{R_{DA}}$ $\kappa^2 = \left(\langle \hat{\mu}_A, \hat{\mu}_D \rangle - 3 \cdot \langle \hat{\mu}_D, \hat{\mu}_{DA} \rangle \cdot \langle \hat{\mu}_A, \hat{\mu}_{DA} \rangle \right)^2$	

Table 4-4 Calculations of donor-acceptor distances (R_{sim}) and orientation factors (κ^2) from each sampled conformation from MC molecular simulation of G-mGBP2/mCh-mGBP2 dimer in steps. See Section 4.4.11 and Figure 4-17 for details.

4.7 Supplementary Videos

Video 1. mGBP2$^{-/-}$ MEFs transduced with G-mGBP2 were treated o/n with IFNγ and infected with *T. gondii*. The living cells were observed with a confocal microscope at 37°C and a z-stack was recorded every 5-10 s. 4D data were processed and rendered in normal shading mode. Bar = 5 µm.

Video 2. mGBP2$^{-/-}$ MEFs transduced with G-mGBP2 were treated o/n with IFNγ and infected with *T. gondii*. The living cells were observed with a confocal microscope at 37°C and a z-stack was recorded every 5-10 s. 4D data were processed and rendered as maximum intensity projection. Bar = 2 µm.

Video 3. mGBP2$^{-/-}$ MEFs transduced with mCh-mGBP2 were treated o/n with IFNγ and infected with *T. gondii*. The living cells were observed with a confocal microscope at 37°C and a z-stack was recorded every 5-10 s. 4D data were processed and rendered as maximum intensity projection. Bar = 1 µm.

Video 4. mGBP2-/- MEFs transduced with G-mGBP2 and cytosolic mCherry were treated o/n with IFNγ and infected with *T. gondii*. The living cells were observed with a confocal microscope at 37°C.

Chapter 5 Assemblies of the G-protein coupled receptor TGR5

Full title: Structural assemblies of the di- and oligomeric G-protein coupled receptor TGR5 in live cells: an MFIS-FRET and integrative modeling study

Authors: Annemarie Greife[1], Suren Felekyan[1], Qijun Ma[1], Christoph G.W. Gertzen[2], Lina Spomer[3], Mykola Dimura[1], Thomas-Otavio Peulen[1], Christina Wöhler[3], Dieter Häussinger[3], Holger Gohlke[2*], Verena Keitel[3*], Claus A.M. Seidel[1*]

Affiliations:

[1] Chair for Molecular Physical Chemistry, Heinrich Heine University, Düsseldorf, Germany

[2] Institute for Pharmaceutical and Medicinal Chemistry, Heinrich Heine University, Düsseldorf, Germany

[3] Clinic for Gastroenterology, Hepatology and Infectious Diseases, Heinrich Heine University, Düsseldorf, Germany

[*] Corresponding authors: Claus A.M. Seidel, Holger Gohlke, Verena Keitel

5.1 Introduction

TGR5 (GPBAR-1, M-BAR) is the first identified G-protein coupled bile acid receptor (Kawamata et al., 2003) and is widely expressed in tissues, including liver, intestine, and the central and enteric nervous system (Jensen et al., 2013; Keitel and Häussinger, 2012; Keitel et al., 2009). Animal studies suggest that TGR5 activation leads to anti-inflammatory effects and influences energy homeostasis and glucose metabolism, thereby playing a role in the pathogenesis of obesity and diabetes (Cao et al., 2013; Choi et al., 2012). Therefore, TGR5 has emerged as a potential therapeutic target to treat metabolic disorders. The most potent TGR5 bile acid agonist is taurolithocholic acid (TLCA/TLC). In model cell lines it was shown that TGR5 couples to $G\alpha_s$, leading to stimulation of adenylate cyclase (AC) and formation of cyclic AMP (cAMP) (Duboc et al., 2014). Homology models of TGR5 have been presented based on template structures of other seven transmembrane (7TM) domain receptors (D'Amore et al., 2014; Gertzen et al., 2015; Macchiarulo et al., 2013; Sindhu and Srinivasan, 2015; Yu et al., 2015), but no high-resolution crystal structure of TGR5 is available to date, and knowledge on TGR5 regulation and oligomerization is scarce. We previously reported that the amino acids 285-294 at the TGR5 C-terminus form an alpha-helical stretch, which is important for plasma membrane localization and thus responsiveness to extracellular ligands (Spomer et al., 2014).

It is now well established that class C GPCRs form homo- and hetero-oligomers (Ferre et al., 2014). However, for class A GPCRs such as TGR5, there are controversial data about the functional significance of forming homo- and hetero-oligomers (Ferre et al., 2014). Studies with rhodopsin (Bayburt et al., 2007; Whorton et al., 2008), µ-opioid

(Kuszak et al., 2009) and β_2-adrenergic receptors trapped as either monomers or dimers in nanodiscs demonstrated that monomers are functional and are able to activate G-proteins; sometimes monomers are even more efficient than homo-dimers (Ferre et al., 2014). The same GPCRs were also shown to be stable as dimers or tetramers in living cells (Bayburt et al., 2007; Kuszak et al., 2009; Whorton et al., 2008). Dimerization has been proved using biophysical approaches such as bioluminescence and Förster Resonance Energy Transfer techniques (BRET and FRET), as well as single molecule analysis (Calebiro et al., 2013) and atomic force microscopy in native disc membranes (Fotiadis et al., 2003). Total internal reflection fluorescence microscopy (TIRFM) in live cells transfected with GPCR at expression levels comparable to native tissues suggested for β_1- and β_2-adrenergic receptors that the presence of monomers and formation of dimers and higher-order oligomers (tetramers and octamers) is dependent on the GPCR density at the cell membrane (Calebiro et al., 2013).

Several oligomer models exist for GPCRs. Extended biased molecular dynamics simulations suggested a model in which homo-dimers characterized by stable interactions involving TM1 transiently interact with the other protomer via other helices such as TM4 (Johnston et al., 2012). Bioinformatics studies predicted a role for transmembrane helices TM1 and TM4 to TM6 in dimerization; mutation of residues there disrupted dimerization (Filizola and Weinstein, 2005; Simpson et al., 2010). AFM, crystallography, and FRET studies of the β_1- and β_2-adrenergic receptors (Huang et al., 2013), muscarinic receptor M_3 (Patowary et al., 2013), rhodopsin (Duboc et al., 2014; Fotiadis et al., 2003; Salom et al., 2006) and the μ-opioid receptor (Manglik et al., 2012) suggested that oligomerization interfaces are most probably formed by TM1-TM2-H8 and TM4-TM5 or TM5-TM6. So far, several spatial arrangements of tetrameric GPCRs are discussed. For muscarinic receptor M_3 a rhombic arrangement of tetramers seems to be preferred than linear or squared ones (Patowary et al., 2013), whereas for rhodopsin either a more linear or squared arrangement is discussed (Ferre et al., 2014; Fotiadis et al., 2003; Patowary et al., 2013).

To perform protein-protein interaction studies in living cells without disturbance and with high spatial resolution, we applied Multiparameter Image Fluorescence Spectroscopy (MFIS) that combines fluorescence lifetime imaging and fluorescence anisotropy microscopy allowing a comprehensive analysis of the biophysical properties of homo- and heteromeric molecular complexes by FRET. MFIS is based on multiparameter fluorescence detection (MFD), which has been established as a standard tool to investigate biomolecules in *in vitro* experiments (Kudryavtsev et al., 2006, 2012; Sisamakis et al., 2010). Similar to MFD, MFIS records photons one by one, which allows for fully parallel recording of all fluorescence (fundamental anisotropy, fluorescence lifetime, fluorescence intensity, time, excitation spectrum, fluorescence spectrum, fluorescence quantum yield, and distance between fluorophores) and additionally pixel/image information over time periods of hours with picosecond accuracy. The multidimensional analysis of correlated changes of several parameters measured by FRET, FCS, fluorescence lifetime, and anisotropy increases the reliability of data interpretation (Stahl et al., 2013; Weidtkamp-Peters et al., 2009). Especially, the economic use of photon information greatly facilitates studies in cells where fluorescent fusion proteins are expressed at low concentration levels and the acquired photon counts are limited.

In this study, we pursued a combined strategy applying cellular biology, Co-immunoprecipitation experiments, MFIS-FRET, and molecular modelling and simulations to obtain information about dimerization and/or higher-order oligomerization of TGR5 and the influence of a mutation in the TGR5 ERY111 motif on oligomerization. FRET between C-terminal TGR5-GFP (donor) and TGR5-mCherry (acceptor) fusion proteins was measured for three different variants: TGR5 wt, TGR5 Y111A and TGR5 Y111F. Homo-dimerization could be detected in all three variants, but interestingly, raising the abundance of acceptor molecules did not alter the FRET efficiency (E) in TGR5 Y111A, but significantly increased the E in TGR5 wt and TGR5 Y111F. Together with our molecular modelling and simulations, we could conclude that the majority of TGR5 Y111A proteins only form dimers, whereas TGR5 wt and TGR5 Y111F proteins primarily assemble into higher-order oligomers, at least tetramers which are formed from dimer of dimers. In view of the growing interest in GPCR oligomerization, dynamics (Thelen et al., 2010) and ligand-induced effects, the proposed model of TGR5 assembly enlarge the knowledge of GPCR oligomerization patterns and affinities, and can have implications for drug development and screening.

5.2 Results

5.2.1 Different TGR5 variants form homo-complexes with different affinities

To characterize the localization and activity of TGR5 protein three TGR5 variants were studied: TGR5 wt and the two variants Y111A and Y111F. The tyrosine residue at position 111 is part of the ERY motif, which is important for GPCR function (Rovati et al., 2007) and also predicted to be phosphorylated by EGFR using NetPhos (Blom et al., 1999, 2004).

Immunofluorescence staining in MDCK and HEK293 cells as well as FACS analysis of transfected HEK293 cells demonstrated that all TGR5 variants were correctly localized at the plasma membrane in about 92% of the transfected cells (Figure 5-1A, B). Furthermore, TGR5 responsiveness towards TLC was investigated using a cAMP-responsive luciferase assay (Hov et al., 2010; Spomer et al., 2014), where luciferase activity served as a measure for the second messenger cAMP following TGR5 activation. Forskolin (F) elevates cAMP independent of TGR5 and was used as positive control. Stimulation of TGR5 wt, TGR5 Y111A, or TGR5 Y111F with TLC led to a significant dose-dependent increase in luciferase activity in all three cases, which proves correct TGR5 function (Figure 5-1C).

To analyze the interaction between TGR5 wt proteins or TGR5 wt with TGR5 Y111A, we performed Co-immunoprecipitation (Co-IP) experiments. His-tagged TGR5 wt and either TGR5 wt-YFP or TGR5 Y111A-YFP proteins were transfected into HEK293 cells. Immunoprecipitation of His-tagged TGR5 wt was carried out with an anti-His antibody. The interaction of TGR5 proteins was visualized using an anti-GFP antibody that recognized the TGR5 C-terminal YFP (Figure 5-2A, lane 3). Co-IP clearly showed that

TGR5 forms homo-complexes. Compared to the interaction between TGR5 wt proteins, the interaction between TGR5 wt and TGR5 Y111A is significantly reduced by about 40% as measured by densitometry (Figure 5-2B).

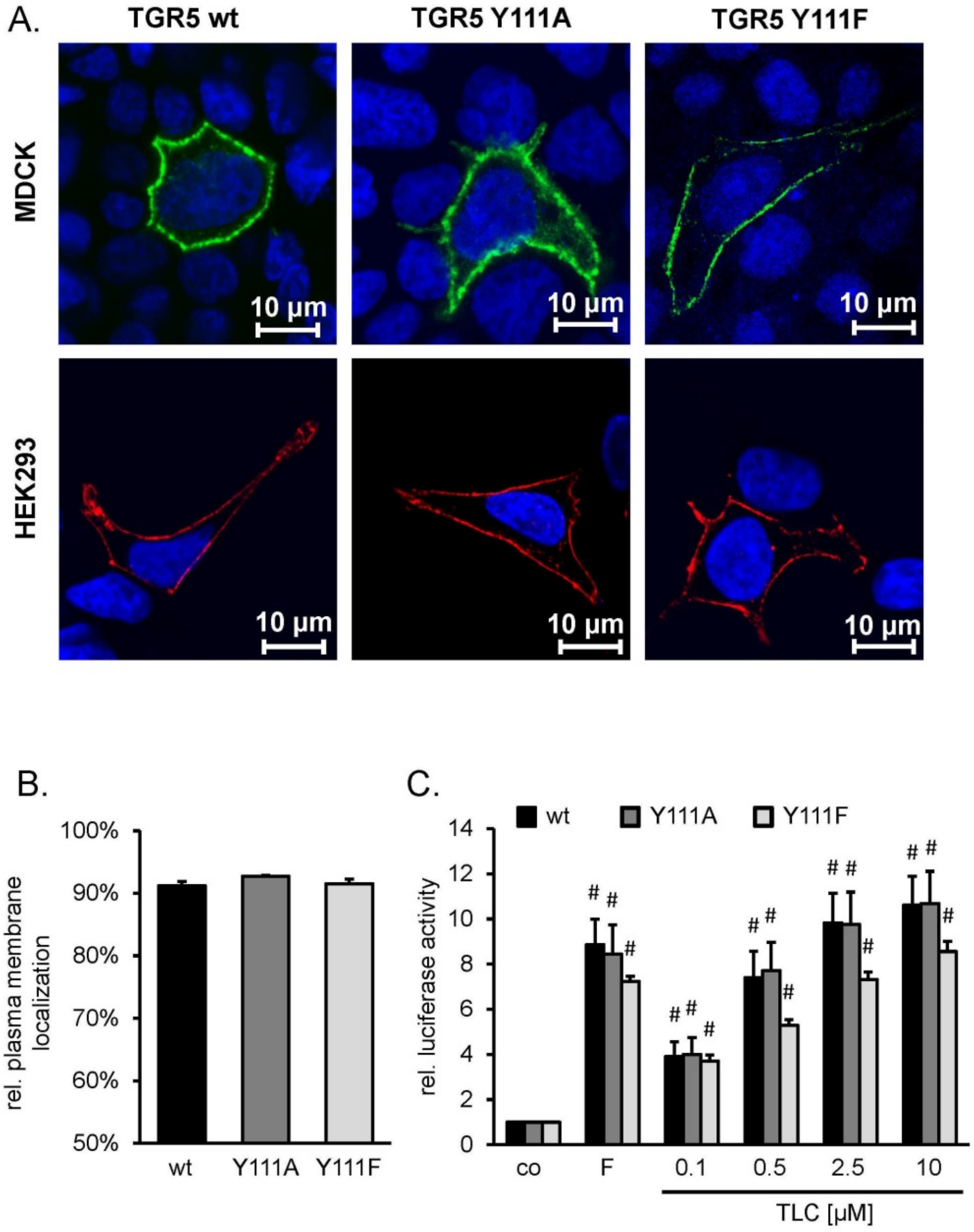

Figure 5-1 Localization und functional analysis of TGR5 wt and Y111 variants. (**A**) Localization of TGR5 by confocal laser scanning microscopy. MDCK cells (upper panels) were transiently transfected with FLAG-TGR5-YFP constructs. The YFP-fluorescence was detected in the plasma membrane for TGR5 wt

as well as for the TGR5 Y111A and TGR5 Y111F variants. HEK293 cells (lower panels) were transiently transfected with TGR5-pcDNA constructs. TGR5 was stained using the RVLR2 antibody (in red). TGR5 as well as the TGR5 Y111A and TGR5 Y111F variants were present in the plasma membrane. Nuclei were stained with Hoechst (blue). Bars = 10 µm (**B**) Relative quantification of TGR5 plasma membrane localization using flow cytometry. The amount of FLAG-TGR5-YFP within the plasma membrane corresponds to the amount of positive FLAG-tag labelling (= extracellular labelling) divided by the total amount of YFP-fluorescence. TGR5 Y111A and TGR5 Y111F were detected on the cell surface in 92.7% and 91.5% of the transfected cells, which was similar to the TGR5 wt with 91.2% (n = 3 independent transfection experiments). (**C**) TGR5 receptor activity was determined using a cAMP responsive luciferase assay. HEK293 cells were co-transfected with TGR5 (pcDNA3.1+), a cAMP responsive luciferase reporter construct, and a Renilla expression vector. Luciferase activity served as a measure of the rise in intracellular cAMP following activation of TGR5. Forskolin (F, 10 µM) was used as TGR5-independent positive control. TGR5 Y111A and TGR5 Y111F did not affect receptor responsiveness to the bile acid taurolithocholate (TLC). Results (wt n = 8; TGR5 Y111A n = 9; TGR5 Y111F n = 6) are expressed as mean + s.e. # = significantly different (p ≤ 0.01) from DMSO (co = control).

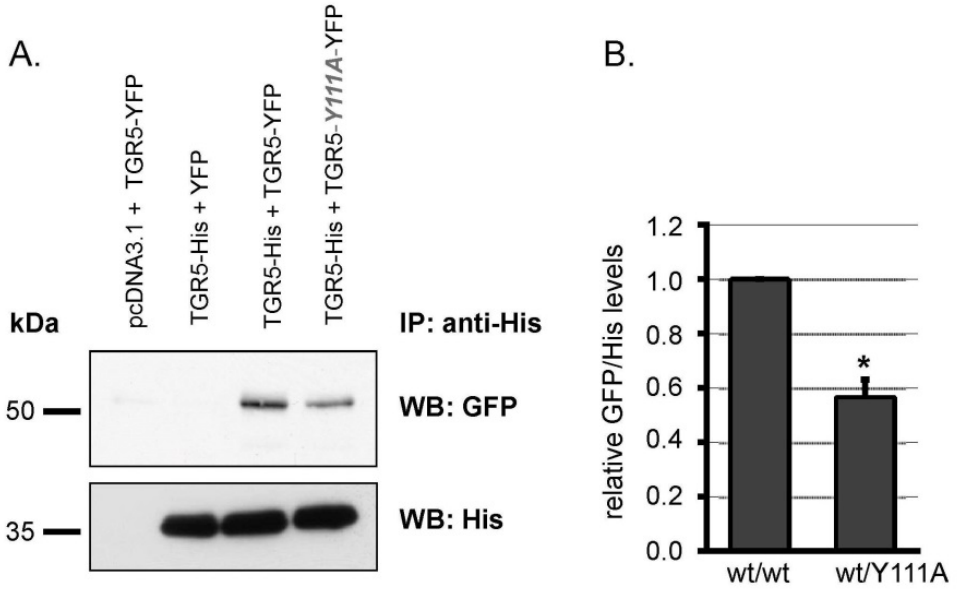

Figure 5-2 Detection of TGR5 multimerization by co-immunoprecipitation. (**A**) HEK293 cells were transiently transfected with pcDNA3.1 and TGR5-YFP, TGR5-His and pEYFP, TGR5-His and TGR5-YFP,

or TGR5-His and TGR5 Y111A-YFP. Immunoprecipitation (IP) was carried out using an anti-His antibody. Equal volumes of the precipitate were deglycosylated with N-glycosidase-F, separated by SDS-PAGE, and blotted onto PVDF membranes. For Western blotting (WB) horseradish-peroxidase-coupled primary antibodies against His and GFP were used. TGR5-YFP was co-precipitated with TGR5-His. Mutation of tyrosine 111 to alanine in TGR5-YFP reduced the amount of co-precipitated variant receptor. (**B**) Densitometric analysis of the anti-GFP and anti-His Western blots. Relative TGR5-TGR5 interaction was determined as relative GFP to His levels. Results are expressed as mean + s.e. (n = 4), *=significantly different from wt-His/wt-YFP interaction, $p < 0.05$.

5.2.2 Pixel-wise MFIS-FRET analysis reveals remarkable differences in FRET properties between TGR5 variants

Next, we performed MFIS-FRET experiments in HEK293 cells transfected by C-terminal TGR5-GFP and TGR5-mCherry fusion proteins to further analyze the differences in the complex formation found by Co-IP. GFP and mCherry are commonly used as a FRET pair with a Förster radius R_0 = 52 Å (Akrap et al., 2010). As shown in Figure 5-3A and Figure 5-9A (right panel), TGR5-GFP and TGR5-mCherry are clearly co-localized at the cell membrane in all the tested variants (TGR5 wt, Y111A and Y111F).

To analyze FRET and to visualize the heterogeneity within and between cells, the MFIS-FRET images were accurately analyzed in a pixel-wise manner to compute all relevant fluorescence parameters. For a direct proof of FRET, it is necessary to show that the observed signal changes are due to differences in FRET efficiency and not due to local changes of fluorophore properties or transfection artifacts. Thus, it is mandatory to analyze both FRET indicators: (i) FRET-induced donor quenching due to the presence of acceptor and (ii) the occurrence of FRET-sensitized acceptor fluorescence (Sisamakis et al., 2010).

Figure 5-3B and Figure 5-3C compare the images of signal intensities (S) and donor fluorescence lifetime ($\langle\tau_D\rangle_f$) between donor-only reference and FRET samples of the three variants. In the donor-only sample, the mCherry emission under direct excitation ($S_{em,ex} = S_{Y,Y}$) and the FRET-sensitized mCherry emission ($S_{Y,G}$) were close to zero as expected. FRET-induced donor quenching is judged by comparing the fluorescence-weighted average lifetimes of the donor in the absence $\langle\tau_{D(0)}\rangle_f$ and presence of acceptor $\langle\tau_{D(A)}\rangle_f$, respectively. FRET samples of all TGR5 variants clearly showed an increase in $S_{Y,G}$ and a reduction in $\langle\tau_{D(A)}\rangle_f$ (Figure 5-3C and Figure 5-9B).

The correlated FRET-specific change of both FRET indicators is best visualized in a 2D-histogram of both FRET indicators, ratio of the corrected fluorescence intensities of donor and acceptor (F_D/F_A) (Section5.5.10, Eq.(5-2) - (5-3) and Table 5-1) versus donor fluorescence lifetime ($\langle\tau_D\rangle_f$), of which the color scale corresponds to the pixel frequency with black being the highest (Figure 5-4A). The correlated shift of both indicators in FRET samples (Figure 5-4A, in orange and red) with respect to the donor-only sample (in green) proves the molecular proximity of TGR5 monomers, therefore confirming the homomerization of TGR5 wt and TGR5 Y111A/F variants.

To study whether also higher-order oligomers form, we systematically titrated donor-to-acceptor concentration ratio from 1:3 to 1:40 in the cell transfection. Two representative experiments of each variant are displayed the in the 2D-MFIS histogram (Figure 5-4A). Here, the FRET-indicators (F_D/F_A) and $\langle\tau_{D(A)}\rangle_f$ allow for a qualitative interpretation of the measurements without applying a specific model. FRET senses the local proximity of binding partners, i.e. the donor is quenched by all surrounding acceptors within ~ 80 Å. Hence, if small oligomers exist, the fluorescence-averaged donor lifetime in the presence of the acceptor $\langle\tau_{D(A)}\rangle_f$ and the fluorescence intensity ratio (F_D/F_A) will decrease with increasing acceptor concentration, whereas they do not change if only dimers exist. Notably, this increase in donor quenching levels off for larger oligomers, because all FRET active sites in close proximity are already occupied in the small oligomers.

Notably, raising the abundance of acceptor molecules from D/A ratio of 1:10 (Figure 5-4A, in orange) to 1:40 (in red) only gave rise to minor correlated changes in both FRET indicators in TGR5 Y111A experiments (7%). But it resulted in a more noticeable change for TGR5 wt (17%) and TGR5 Y111F (14%) experiments. Such distinct behaviors suggest a significant formation of TGR5 wt and TGR5 Y111F oligomers but no or only few oligomers for TGR5 Y111A. These qualitative indications were later verified by pixel-integrated MFIS analysis (discussed later).

In addition, we noticed that the distinct properties of Y111A variant already existed in donor-only samples. The fluorescence lifetime of TGR5 Y111A-GFP ($\langle\tau_{D(0)}\rangle_f$) is 2.8 ns, remarkably longer than that of TGR5 wt-GFP and TGR5 Y111F-GFP, which is 2.4 ns (Figure 5-9B). Moreover, we found that with laser excitation at 488 nm, the emission spectrum of TGR5 Y111A exhibited a 13 nm red shift compared to that of TGR5 wt (Figure 5-9C). These spectroscopic differences of GFP revealed the differences in the local micro-environment between TGR5 Y111A and the other two variants.

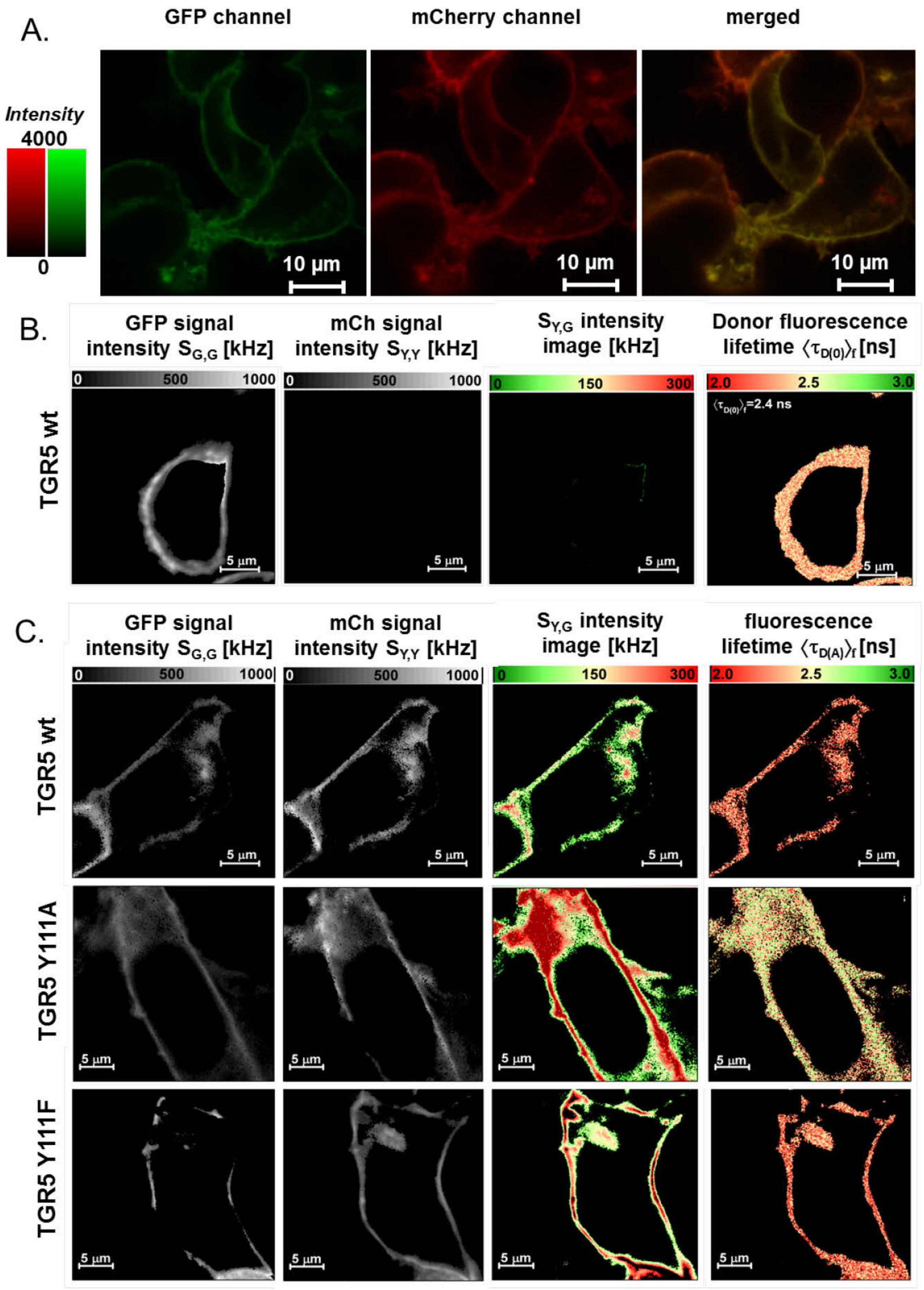

Figure 5-3 Detection of TGR5 multimerization by pixel-wise MFIS-FRET analysis. (**A**) HEK293 cells, transiently transfected with TGR5-GFP and TGR5-mCherry (transfection ratio 1:10), were imaged for co-

localization of GFP and mCherry using sequential scanning and a scanning resolution of 1024 x 1024 pixels. Each TGR5-GFP and TGR5-mCherry picture is shown in a false color saturation mode and then overlaid by using green and yellow intensity colors. TGR5 wt-GFP and TGR5 wt-mCherry are clearly co-localized at the cell membrane. Scale bar 10 µm. The TGR5 Y111 variants are shown in Figure 5-9A. (**B**) MFIS analysis of TGR5 wt-GFP transfected HEK293 cells by comparing (from left to right) the fluorescence intensity of the donor GFP, fluorescence intensity of the acceptor mCherry, the detection of yellow mCherry photons after excitation of GFP ($S_{Y,G}$, S: signal, Y: yellow emission, G: green excitation) as a result of FRET, and changes in the donor fluorescence lifetime $\langle\tau_{D(0)}\rangle_f$. For TGR5 wt-GFP only the donor signal but no acceptor signal is detected. The MFIS analysis of TGR5 Y111 variants is shown in Figure 5-9B. (**C**) The same parameters were used for TGR5 GFP/mCherry samples. The MFIS measurements show FRET ($S_{Y,G}$ and changes in $\langle\tau_{D(A)}\rangle_f$) in all TGR5 variants, which indicates at least homo-dimerization.

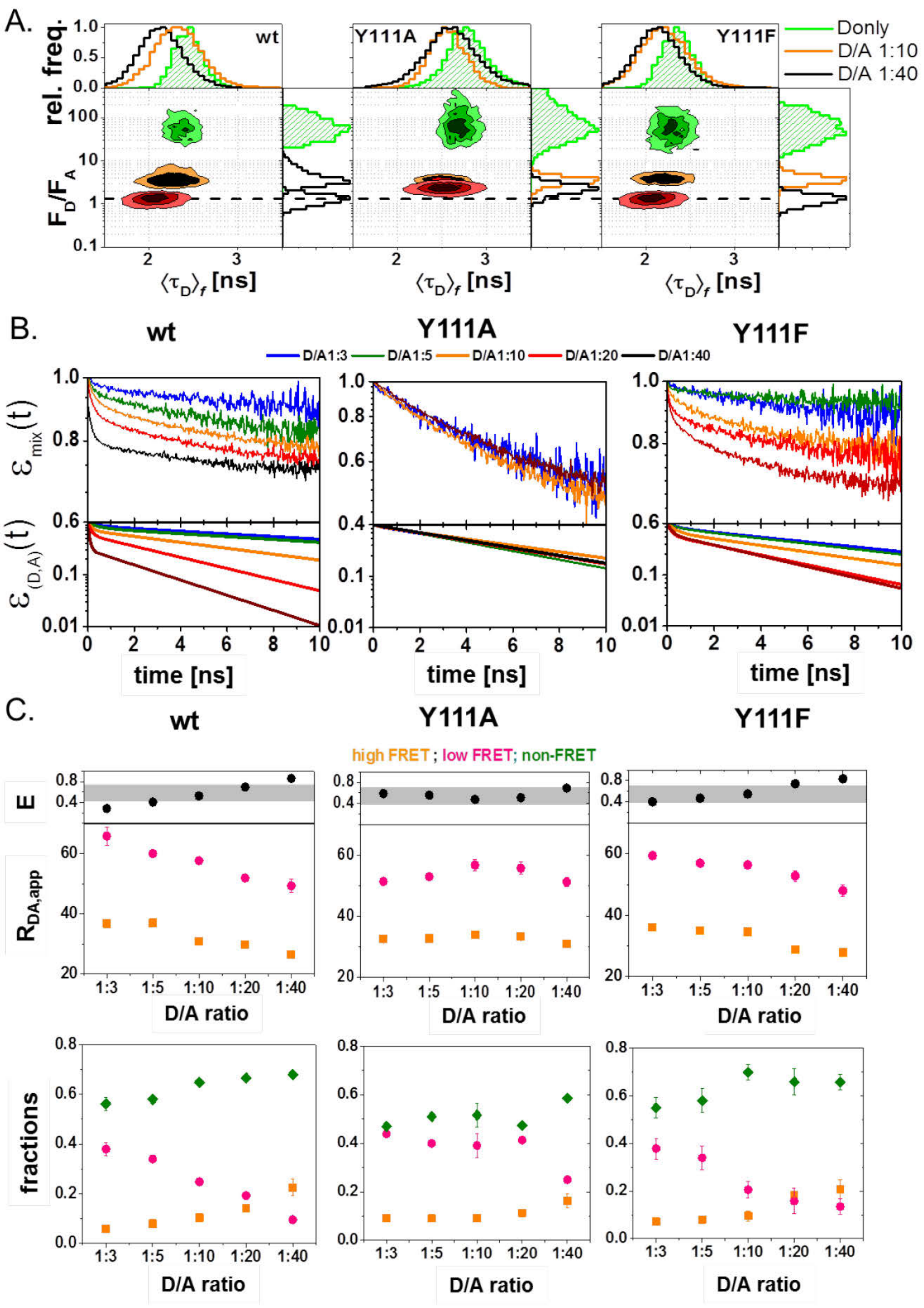

Figure 5-4 Pixel-integrated analyses of TGR5 FRET properties. (**A**) The MFIS-FRET 2D plots are generated with Origin 8.6 and show an overlay of two histograms of (F_D/F_A) vs. $\langle\tau_{D(A)}\rangle_f$. TGR5 wt and

TGR5 Y111F donors (in green) showed a $\langle\tau_{D(0)}\rangle_f$ = 2.4 ns and a high green to yellow signal. With increasing amounts of the acceptor mCherry (orange and red islands) both parameters were strongly reduced in TGR5 wt and TGR Y111F, but not in TGR5 Y111A. All samples were corrected for relative brightness, relative direct mCherry excitation in the green detection channel, spectral shift of the Y111A variant, and background in the green and yellow channels (see Section 5.5.10). The color scale corresponds to the pixel frequency with black being highest. (**B**) FRET-induced donor quenching $\varepsilon_{mix}(t)$ derived from sub-ensemble fluorescence measurements on TGR5 variants at different donor-to-acceptor ratios. The time-axis measures the time between excitation and detection of donor photons. The upper row shows the experimental data. In the bottom row the offset is subtracted and the result is termed $\varepsilon_{(D,A)}(t)$. In TGR5 wt and TGR5 Y111F, FRET clearly increased in a mCherry-dependent manner, whereas in TGR5 Y111A all $\varepsilon_{(D,A)}(t)$ curves behaved similar. (**C**) FRET-decays from sub-ensemble analysis at different donor-to-acceptor ratios were fitted with a 2-k_{FRET} fit to obtain two apparent distances $R_{DA,app}^{(1)}$ and $R_{DA,app}^{(2)}$ (upper row) with their corresponding FRET fractions (lower row) and to calculate the mean transfer energy efficiency E. E increased in an acceptor-dependent manner in TGR5 wt and TGR5 Y111F, whereas E changed only slightly in TGR5 Y111A. These changes in E correlate with a reduction of both apparent distances $R_{DA,app}^{(1)}$ and $R_{DA,app}^{(2)}$ in TGR5 wt and TGR5 Y111F: In the lower row, the $R_{DA,app}^{(1)}$ fractions increase, whereas the $R_{DA,app}^{(2)}$ fractions decrease in an acceptor-dependent manner. Orange: $R_{DA,app}^{(1)}$ and $R_{DA,app}^{(1)}$ fraction, pink: $R_{DA,app}^{(2)}$ and $R_{DA,app}^{(2)}$ fraction, green: non-FRET fraction, the grey bar in E represents average E for TGR5 Y111A.

5.2.3 TGR5 wt and TGR5 Y111F form higher-order oligomers, whereas TGR5 Y111A forms primarily dimers

The pixel-wise analysis of the fluorescence data by the fluorescence-averaged lifetimes $\langle\tau_D\rangle_f$ and the fluorescence intensity ratios (F_D/F_A) does not allow us to resolve multiple species as the information contained in the recorded fluorescence decays is reduced to two numbers. Hence, sample heterogeneities that naturally arise in imaging cannot be resolved. For instance, changes of the average FRET levels might arise due to changes of the donor-acceptor distances or due to changes of the fraction of non-FRET molecules (molecules that lack an acceptor).

To unravel molecular mechanism give rise to the distinct FRET properties in the three TGR5 variants observed in the pixel-wise analysis, high-precision pixel-integrated MFIS-FRET analyses were performed. We plotted the ratio of the fluorescence decay histograms between FRET and donor-only experiments. The obtained histogram depicts the time-resolved FRET-induced donor decay $\varepsilon_{mix}(t)$ (Section 5.5.11 Eq.(5-5)), which allows visually separating various molecular species. The FRET-inactive molecular species is represented by a constant offset in the $\varepsilon_{mix}(t)$-diagram, and the FRET-active species by a decay. The fraction of FRET-inactive or -active species can be directly read out from the amplitude of the offset or of the decay respectively. The slope of the decay in a $\varepsilon_{mix}(t)$-diagram is determined by the geometry of the protein complex: a steeper decay slope is caused by a higher FRET rate constant (k_{FRET}), which corresponds to a shorter donor-acceptor distance (R_{DA}), and vice versa. If a mixture of FRET-active complexes with various R_{DA} is present in the FRET-active species, the slope of the decay will become heterogeneous and thus non-exponential. Therefore by reading a $\varepsilon_{mix}(t)$-diagram one can immediately infer the species composition and molecular geometry from a FRET experiment.

The $\varepsilon_{mix}(t)$-diagrams of all variants are displayed in semi-logarithmic plot in Figure 5-4B, (upper panels). Differences in the constant offset and the slope of the decays are clearly visible. Since we are interested in the geometry of the TGR5 complexes of each variant, which is represented by the decay slope in the $\varepsilon_{mix}(t)$-diagrams, we isolated the decay part (ε_{FRET}(t)) of each ε_{mix}(t)-diagram (Section 5.5.11 Eq.(5-5), Table 5-2) and displayed them in Figure 5-4B (lower panels). For TGR5 wt and Y111F, the decay slope has two characteristic regions: a steeper region and a shallower region. The former corresponds to a higher k_{FRET}, while the latter to a lower k_{FRET}. When varying the donor-to-acceptor transfection ratio from 1:3 to 1:40, the slope of ε_{FRET}(t) in both regions become even steeper. But for TGR5 Y111A variant, only one homogeneous decay slope is present and acceptor titration has almost no influence on the ε_{FRET}(t).

To quantify the observed trend, we formally describe the FRET-induced donor decay (ε_{mix}(t)) by two FRET rate constants, which are for convenience converted to two apparent distances ($R_{DA,app-1}$ and $R_{DA,app-2}$, Eq. (5-10)) with $R_{DA,app-1}$ being longer than $R_{DA,app-2}$. Their species fractions are denoted as $x_{DA,app-1}$ and $x_{DA,app-2}$ respectively (the 2-k_{FRET} fit model function is detailed in Section 5.5.12, an exemplar fit decay is shown in Figure 5-10 and fitted results in Table 5-2). As shown in Figure 5-4C, with increasing acceptor concentration, in TGR5 wt and TGR5 Y111F both apparent distances became shorter: $R_{DA,app-1}$ changed from 40 to 20 Å and $R_{DA,app-2}$ from 75 to 50 Å. Their species fractions were also affected: the fraction of short distance $x_{DA,app-1}$ increased from 7% to 30%, whereas that of long distance $x_{DA,app-2}$ reduced from 39% to 12%. We summarized this tendency with one parameter, the mean FRET efficiency of the FRET-active species (E, Section 5.5.12 Eq. (5-11)). E markedly increased for TGR5 wt and Y111F with the acceptor concentration; while remaining almost constant for Y111A (Figure 5-4C).

To summarize, both ε_{FRET}(t) diagrams and 2-k_{FRET} analysis show that for TGR5 Y111A, the FRET efficiency is independent of the relative amount of fluorescent reporters, showing that each donor molecule can maximally have one acceptor in its vicinity.

5.2.4 The TGR5 ligand TC has no influence on the oligomerization state of TGR5

It has been shown that activation by ligands can influence GPCR oligomerization (Ferre et al., 2014). To study the ligand-induced effects on TGR5, we tested whether taurocholate (TC), a bile acid less cytotoxic than TLC for live cells, affects oligomerization of TGR5 wt, TGR5 Y111A, and TGR5 Y111F. A time series analysis was designed, where MFIS-FRET measurements in each chosen cell were performed at four time points: before addition of 10 µM water soluble TC, directly after addition, 10 min after and 20 min after. FRET properties as reported by the species-averaged donor fluorescence lifetime $\langle\tau_{D(A)}\rangle_x$ remained almost unchanged in the time-series experiments (Figure 5-5). A detailed pixel-integrated FRET analysis showed that neither the FRET-active species fraction nor the molecular geometry changed markedly after the TC addition (Figure 5-11). These results indicate that TC does not influence the oligomerization state of TGR5 variants.

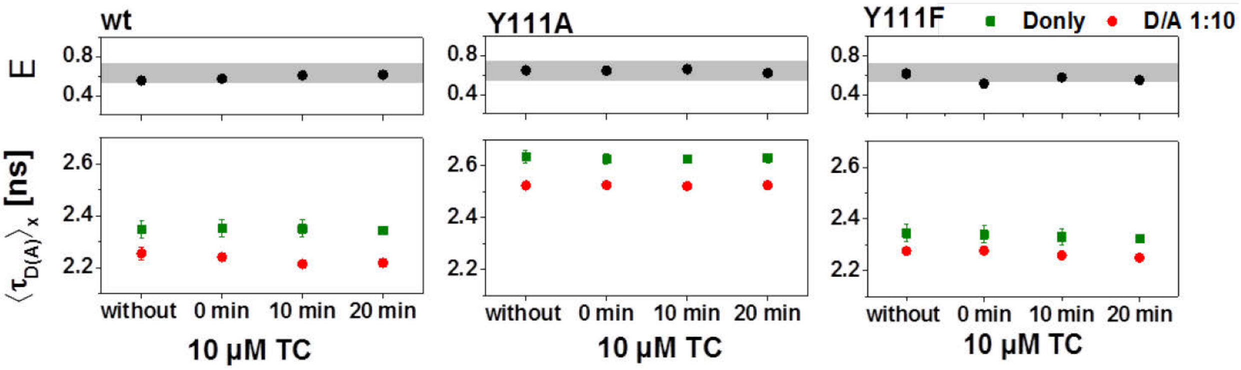

Figure 5-5 Influence on FRET after treatment with TGR5 ligand TC. HEK293 cells were transiently transfected with TGR5-GFP alone (Donly, green) or with TGR5-GFP and TGR5-mCherry at a ratio D/A 1:10 (DA, red). For time-series analysis three cells were selected using the Olympus time laps function, and MFIS-FRET measurements were taken before addition of 10 µM TC (without), immediately after addition of TC (t = 0), and after 10 min and 20 min, respectively. The species-averaged donor

fluorescence lifetime $\langle\tau_D\rangle_x$ was determined and plotted against time, as well as the mean efficiency E, which was calculated from data shown in Figure 5-11. Each point represents the average of nine cells. No lifetime changes were observed for Donly samples and DA samples in the presence of the agonist TC.

5.2.5 Structural arrangement of di- and oligomeric TGR5

Next, we analyzed which structural features of the TGR5 complexes can be extracted from the observed FRET parameters. Previous work by (Sindbert et al., 2011) and (Kalinin et al., 2012) has shown that the extent of FRET between two flexibly linked fluorescent probes can be accurately predicted by calculating the distance distribution between all fluorophore positions that are sterically accessible (accessible volume, AV) for a given structural model. As both fused fluorescent proteins have flexible connecting amino acid residues (Table 5-3) creating a large, widely distributed structural ensemble (Evers et al., 2006), computer simulations generating probe distributions can be readily applied to study TGR5 assemblies by FRET.

5.2.6 Simulation of the expected FRET properties

The structural model of the TGR5 monomer required for modelling of FRET was generated by performing multi-template homology modelling based on seven template structures of related class A GPCRs (Section 5.5.14 and (Gertzen et al., 2015)). As shown in Figure 5-6A**,** we generated three possible homo-dimerization models with interfaces involving TM1-TM2-H8 (1/8 dimer), TM4-TM5 (4/5 dimer), or TM5-TM6 (5/6 dimer).

To assure accuracy we compared two procedures for calculating the distance distributions between fluorophore positions for the TGR5 models: (i) Explicit linker simulations based on explicit peptide linker/GFP MD simulations followed by calculations of conformational free energies to weight each linker-GFP configuration in the presence of a TGR5 dimer and an implicit membrane bilayer (Figure 5-14A, B, Section 5.5.15). This thermodynamic ensemble (TE) approach is expected to be more accurate than the following procedure but the computations are time consuming. (ii) Implicit linker simulations by AV calculations weighted by a Gaussian chain distribution, so that entropic effects and geometric factors in terms of steric exclusion effects by the TGR5 oligomer and the membrane are taken into account (Section 5.5.16). The AV approach has to be calibrated to be accurate (Section 5.5.16) but it has the advantage that the computation is very fast.

The TE approach results in a hemispherical arrangement of GFP on the cytoplasmic side, which is centred on the attachment point at helix 8 of TGR5 (Figure 5-14D, E) and where each linker/GFP configuration is Boltzmann weighted according to the conformational free energy (Figure 5-14C see Section 5.5.15.3). Configurations of lower probability are found when GFP approaches TGR5 due to energetically unfavourable contacts (Figure 5-14C, D). The Boltzmann-weighted distribution of distances between the linker N-terminus and the GFP fluorophore shows a peak distance of about 45 Å, while the minimal distance is about 35 Å. This is due to the fact that the fluorophore is located 20 Å away from the linker C-terminus inside the β-barrel structure of GFP and thus is inaccessible to the linker’s N-terminus. The peak linker length (without considering GFP) is about 25 Å. This is about 5 Å longer than the average radius of gyration of a Gaussian chain polypeptide of the same number of residues (33 amino acids yielding 3.5 Å * $33^{0.5}$ = 20 Å (Grosberg and Khokhlov, 1994). The deviation shows that the linker with GFP does not exactly behave like a ‘perfect’ Gaussian chain. The

Boltzmann-weighted fluorophore position map (Figure 5-6C, Figure 5-14D) was used for inter-dye distance distribution calculations (Figure 5-6B).

The implicit model (Figure 5-6C) was tested as an alternative to account for dye-linker diffusion. The accessible volume (AV) approach was used to estimate all possible dye positions within the linker length from the attachment point without steric clashes with the macromolecular surfaces. The fluorophores are approximated by a sphere with a defined radius, which is estimated from the physical dimensions of the molecules (left panel). The connecting linker is modelled as a flexible cylinder. To take entropic effects into account the linker was assumed to obey Gaussian chain behaviour. Thus, the fluorophore distribution density gradually drops as the distance from the attachment point increases. For the implicit model, the 55 amino acid residues (Section 5.5.16, Table 5-3) between the structured parts of the TGR5 C-terminus and GFP were considered as a flexible sequence with unknown structure with a length of ~203.5 Å at maximal extension.

Both methods for linker simulations gave very similar results. The (1/8) dimerization model shows a distance distribution between fluorophore positions between 25-150 Å with the highest probability at 55 and 60 Å for the explicit and implicit linker models, respectively. The distances between fluorophores in models (4/5) and (5/6) are similarly distributed with the highest probability at around 95-110 Å; i.e. the distance of most conformers is too large for significant FRET. Implicit and explicit linker models thus show very similar inter-dye distance distributions for all dimer models: The implicit model shows a 5 Å shift towards the higher length for the (1/8) dimer and a 15 Å shift towards the shorter length for the (4/5) dimer model.

Finally we can conclude that both linker simulation techniques predicted FRET should distinguish a 1/8 dimer from 4/5 dimer and 5/6 dimer, respectively, because the FRET probe distance distributions has a characteristic peak at short distances (Figure 5-6B). However, the FRET probe distance distributions of the two dimers involving TM5 are expected to be not distinguishable in our FRET experiments (Figure 5-6B).

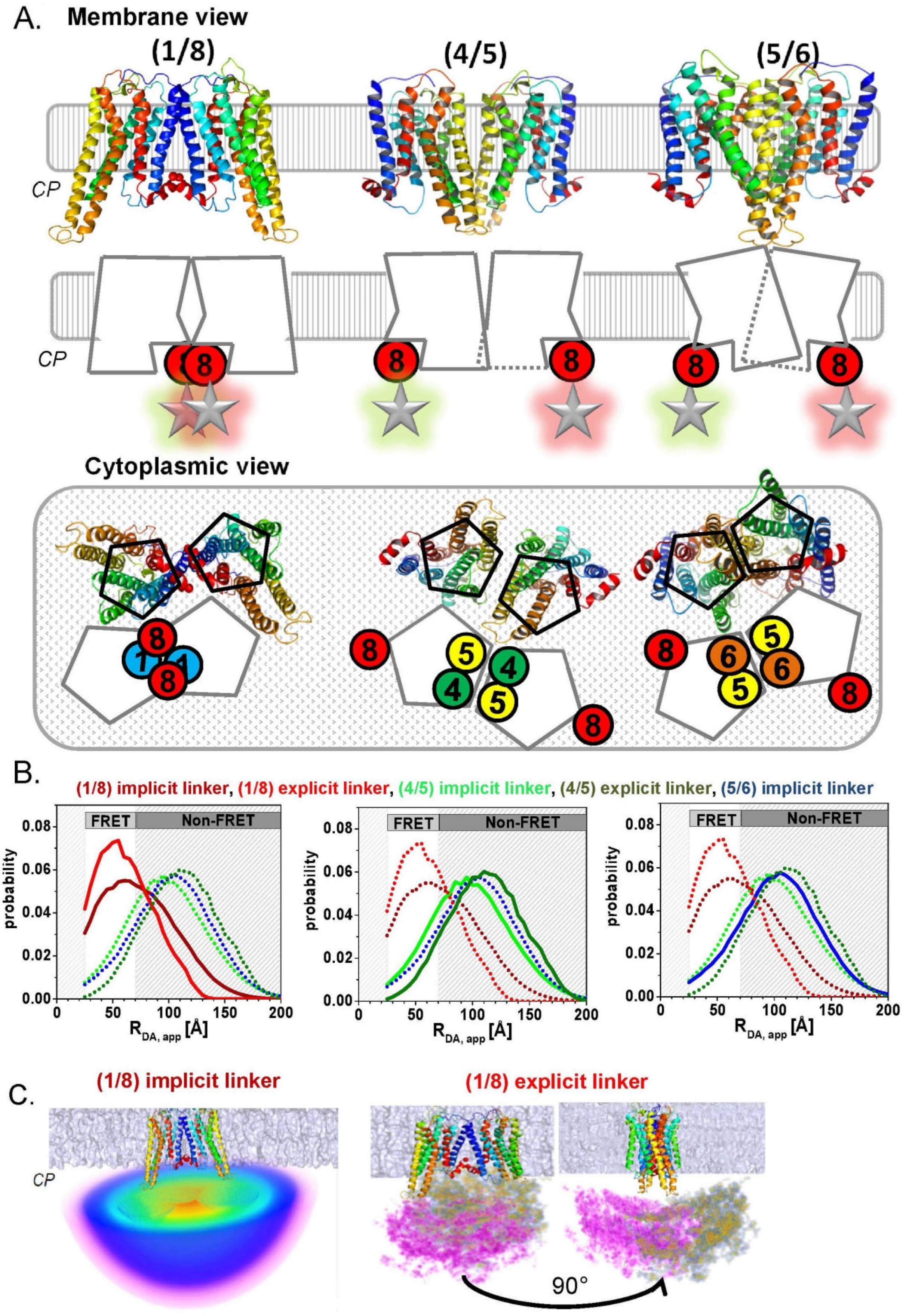
A.
Membrane view
(1/8)
(4/5)
(5/6)
CP
CP
8
Cytoplasmic view
1
4
5
6
B.
(1/8) implicit linker, (1/8) explicit linker, (4/5) implicit linker, (4/5) explicit linker, (5/6) implicit linker
FRET
Non-FRET
probability
0.00
0.02
0.04
0.06
0.08
0
50
100
150
200
R_DA, app [Å]
C.
(1/8) implicit linker
(1/8) explicit linker
CP
90°

Figure 5-6 Homo-dimerization models and their distance distributions. (**A**) Homo-dimerization models with the following interfaces from left to right: (1/8), (4/5) and (5/6). TGR5 monomer chains are rainbow coloured starting with TM1 in blue to H8 in red. Top row: membrane view of models displayed in PyMol and schematic models. Bottom row: cytoplasmic view of models displayed in PyMol and schematic models. The attachment point for the fluorescent proteins (FP) at the cytoplasmic H8 is labelled with red circles, and FPs are presented as glowing stars in green for donor and red for acceptor. Abbreviation: CP = cytoplasm. (**B**) Distance probability distributions with two methods (explicit and implicit linker) for the homo-dimerization models (1/8) (red), (4/5) (green), and (5/6) (blue). The non-FRET area is shaded in grey. (**C**) Positional distributions of the fluorescent probes for the TGR5 dimer (1/8). The implicit linker simulations yield weighted AVs for both fluorophores which overlap and create one huge sphere (left panel). The probability of the allowed fluorophore positions decrease from red, yellow over green, blue to pink. The explicit linker simulations yield a thermodynamic ensemble (right panel) depicted as an orange-blue and purple volume map, respectively. The ensembles also overlap to a high degree. Higher saturation represents higher fluorophore position occupancy. Both methods gave very similar results.

5.3 Discussion

In the present study, we pursued a combined strategy applying cellular biology, MFIS-FRET and molecular simulations to obtain information about dimerization and higher-order oligomerization of TGR5 and to study the influence of a mutation in the TGR5 D/ERY motif (TGR5 Y111A and Y111F) on oligomerization. We could show that TGR5 forms homo-complexes.

5.3.1 Pixel-wise and pixel-integrated MFIS-FRET analyses indicate the presence of several TGR5 oligomerization patterns.

The pixel-wise analysis of the fluorescence data by the fluorescence averaged lifetimes $\langle\tau_D\rangle_f$ and the fluorescence intensity ratios (F_D/F_A) does not allow us to resolve multiple species. However, using three TGR5 variants, we could show strong differences in the FRET properties in TGR5 Y111A compared to wt and Y111F (Figure 5-4A). These effects were only detectable in an acceptor concentration dependent manner. Thus we tested whether the observed FRET could be simply caused by a very high local concentration of acceptor proteins in the membrane, so that donor and acceptor are in proximity even though they do not interact. Due to the single-molecule sensitive of our confocal microscope, we could perform at acceptor concentrations of ~ 1 µM, which corresponds to a molecule density of less than ~ 0.002 acceptor molecules/nm^2. According to (King et al., 2014) proximity FRET is negligible ($E < 0.1$) at these concentrations. Furthermore, the pixel-integrated, time-resolved analysis $\varepsilon_{mix}(t)$ supported the pixel-wise analysis and clearly indicated the presence of different FRET species in wt and Y111F and therefore higher-order oligomers as compared to Y111A.

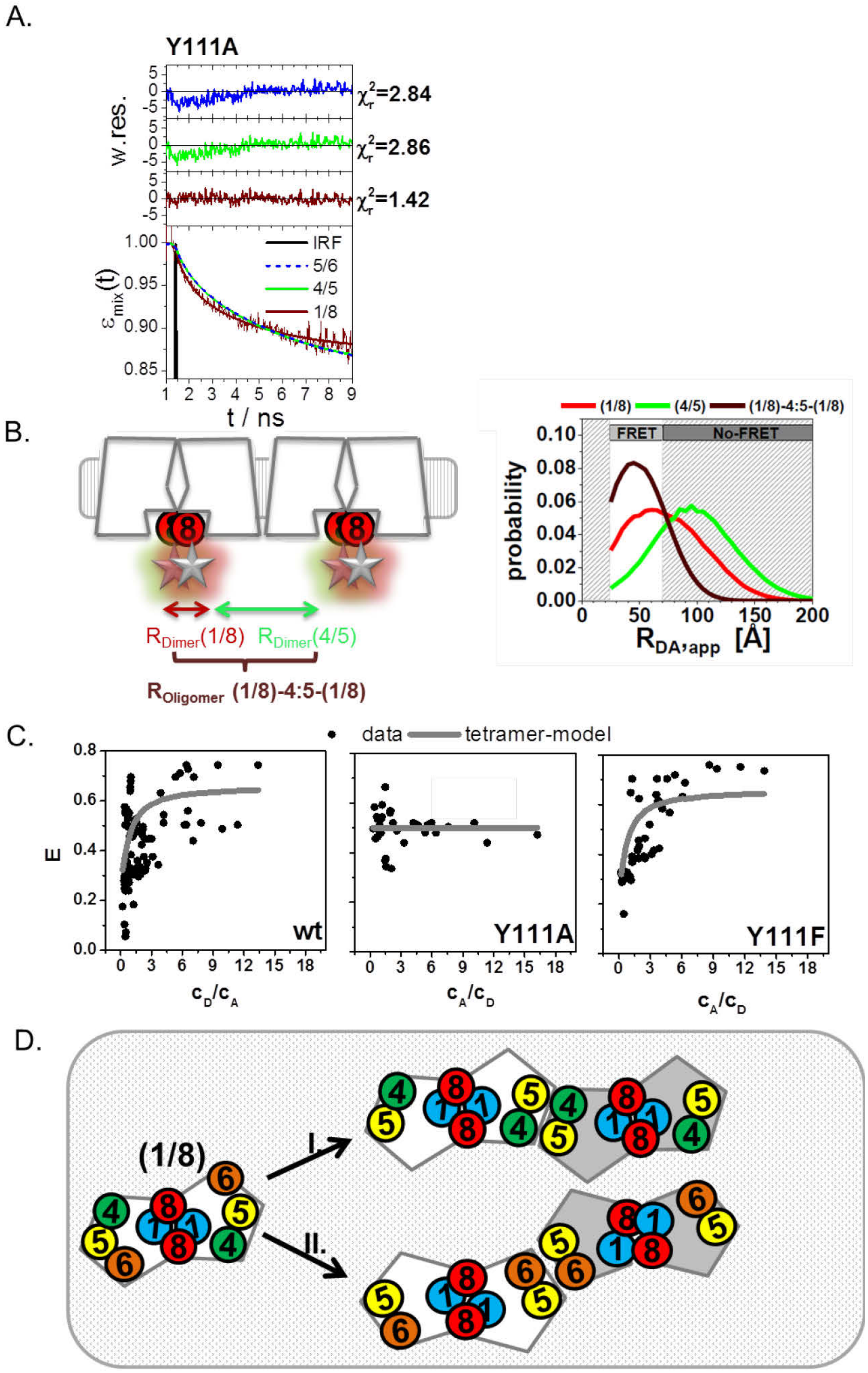

A.
Y111A
w.res.
χ_r^2=2.84
χ_r^2=2.86
χ_r^2=1.42
ε_mix(t)
IRF
5/6
4/5
1/8
t / ns
B.
R_Dimer(1/8)
R_Dimer(4/5)
R_Oligomer (1/8)-4:5-(1/8)
(1/8)
(4/5)
(1/8)-4:5-(1/8)
FRET
No-FRET
probability
R_DA,app [Å]
C.
data
tetramer-model
E
wt
Y111A
Y111F
c_D/c_A
c_A/c_D
c_A/c_D
D.
(1/8)
I.
II.

Figure 5-7 TGR5 oligomerization models. (**A**) Fit of the FRET-induced donor quenching decay ε(t) derived from sub-ensemble fluorescence measurements on TGR5 Y111A with two species with the fractions normalized to unity: (i) Dimer (fraction x_{Dimer}) with the complete distance distribution (FRET and Non-FRET) of the corresponding dimer models (Figure 5-6B) and (ii) donor only/ FRET inactive molecules. Only the distance distribution of the 1/8 dimer model gives a satisfactory fit as judged by the weighted residuals and the reduced chi squared χ_r^2. Fit results of TGR5 Y111A for x_{Dimer}: 1/8 dimer: 0.27; 4/5 dimer: 0.59; 5/6 dimer: 0.73. (**B**) The schematic presentation shows the two individual apparent distances from the interfaces (1/8) and (4/5). Both R_{Dimer} can be converted into FRET rates. In an oligomer the two FRET rates add up and have to be convolved to calculate the new apparent distance $R_{\text{(oligomer)}}$. The resulting distance distribution is similar to the dimer (1/8). (**C**) Dependence of the TGR5 oligomerization monitor by the FRET efficiency (experiment (black) and modeled (grey)) on the donor acceptor ratio c_A/c_D. In case of the TGR5 wt, Y111F and Y111A overall 100, 42 and 43 cells were analysed, respectively. In the cells the donor, acceptor and total TGR5 concentration (including inactive mCherry (30 %)) (Section 5.6.3.1) varied between 0.25 - 6.3 µM, 0.1 - 5.0 µM and 0.5 - 13 µM, respectively, which causes the spread in the observed FRET efficiencies for projection onto the c_A/c_D axis. The fits, however, were performed in the three dimensional space (c_D, c_A and E; Figure 5-13D), so that the differences in the protein concentrations are properly accounted. The modeled transfer efficiency was calculated by a simple dimer/tetramer model (see Section 5.6.3.2). The dimer is composed of a donor acceptor distance of 45 Å, and the tetramer is composed out of two dimers separated by 100 Å. The modeled dissociation constant of the dimer K_{D1} was fixed to 10 nM for all TGR5 variants. The values for the modeled dissociation constants of the oligomer (Tetramer) were: (K_{D2}(TGR5 wt) = 70 nM, K_{D2}(TGR5 Y111F) = 200 nM, K_{D2}(TGR5 Y111A) = 2000 nM). (**D**) Suggested oligomerization model originating from the (1/8) dimer. Two possible oligomers are reasonable ((1/8)-4:5-(1/8) (I) and (1/8)-5:6-(1/8) (II) shown as schematic representations): TGR5 monomers form a dimer with the contact sites in TM1 (blue circle) and H8 (red circle). H8 is attached to fluorescent fusion proteins (GFP and mCherry). If a tetramer is formed as a dimer of a dimer, then contact sites in TM4 (green circle) and TM5 (yellow) (I) or TM5 (yellow) and TM6 (orange) (II) create a second interface promoting a linear oligomer organization. A third less reasonable oligomer configuration is shown in Figure 5-12.

5.3.2 The FRET-induced donor quenching curve $\varepsilon_{mix}(t)$ identifies the 1/8 interface as the dimerization interface

The TGR5 Y111A variant forms predominantly homo-dimers at our measurement conditions, because this TGR5 variant showed FRET with rather constant energy transfer efficiency throughout the titration experiments (Figure 5-4B, C). Therefore it is perfect variant to test which of our distance probe distributions calculated for three potential interfaces describes the FRET-induced donor quenching curve $\varepsilon_{mix}(t)$ best. Figure 5-7A shows the fits using a model with the complete distance distribution (FRET and Non-FRET) of the corresponding dimer models (Figure 5-6B) and donor only/ FRET inactive molecules (for details see caption). As judged by the weighted residuals and the reduced chi squared χ_r^2 only the distance distribution of the 1/8 dimer model gives a statically satisfactory fit, so that the dimerization of TGR5 via the 4/5 or 5/6 interface can be ruled out.

5.3.3 The mutations in ERY motif affect TGR5 oligomerization

The so-called “D/ERY” motif is a highly conserved triplet of the Glu/Asp-Arg-Tyr residues in the second intracellular cytoplasmic loop (ICL2) between the transmembrane helices 3 and 4 and belongs to one of two clusters important for structural stability in GPCRs (Unal and Karnik, 2012). Mutation studies in Rhodopsin suggested that the D/ERY motif has importance for G-protein coupling, Arrestin binding and is sensitive to phosphorylation by kinases (Karnik, 2002). Further D/ERY mutation studies in class A GPCRs led to a classification of two phenotypes which either show constitutive active signaling caused by retained G-protein coupling and agonist-induced response with increased affinity for the agonist (e.g. Rhodopsin, µ-opioid receptor) or no constitutive active signaling caused by impaired agonist-induced receptor responses (muscarinic M1, M5 receptors) (Capra et al., 2004; Rovati et al., 2007). In all these mutation studies either glutamic acid and/or aspartic acid was responsible for the observed effects.

However, the tyrosine (Y) mutation often did not or only marginally affect receptor function (Auger et al., 2002) regarding receptor expression, G-protein binding and ligand affinity. In our studies the TGR5 Y111 variants, Y111A and Y111F, were normally localized at the plasma membrane and activated by both bile acid agonists TLC and TC to a level comparable to TGR5 wt. These findings implicated no obvious impaired ligand binding affinities or G-protein coupling consistent with literature results (Auger et al., 2002). However, we observed significant differences in oligomer formation as assessed by Co-IP experiments and FRET measurements in live cells, but especially for TGR5 Y111A and not for TGR5 Y111F. This shows that an aromatic side chain contributes significantly the stabilization of oligomers.

5.3.4 TGR5 tetramers with a linear organization assembled from (1/8) dimers can form a second interface via TM5

The titration experiments strongly suggest that TGR5 wt and TGR5 Y111F are able to form dimers and higher-order oligomers under our measurement conditions (Figure 5-4B). Increasing amounts of acceptor mCherry strongly increased E. The concentration dependence suggests that oligomers – (with a formation of tetramers as first step) - are formed from dimers (dimer of dimer model). Therefore, this finding implies at least a second interface for TGR5 homo-oligomer formation involving the ERY motif and TM5.

As shown in Figure 5-6B the average apparent distances between fluorescent proteins attached to TGR5 helix 8 (without a coupled G-protein) were 120 Å for the (4/5) dimer model and 103 Å for (5/6) model, respectively. If we expect oligomers formed by the (1/8) dimer (abbreviated as (1/8)-4:5-(1/8)), then a second interface with contacts in TM4 and TM5 are possible and the effective apparent oligomer distance is approximately 49 Å (Figure 5-7B). To compute the apparent distance distribution shifts towards shorter distances for the case of two acceptors being in the vicinity of one donor which would happen if higher order oligomers are formed, the two inter-probe distance distributions ((1/8) and (4/5)) were convoluted (Figure 5-7B). An essentially identical distance distributions is expected for (1/8)-5:6-(1/8)) tetramer.

This becomes clear in the following Gedankenexperiment: If we think of a tetramer, then it can be formed by one donor, three acceptors (1D-3A) or two donors, two acceptors (2D-2A), or three donors, one acceptor (3D-1A) (Figure 5-13E). The most ideal case would be a tetramer formed by donor-acceptor dimers (DA-DA). For this two acceptor cases (Figure 5-7B) the FRET rates from each interface ((1/8) and (4/5)) add up and result in an apparent distance distribution slightly similar to the (1/8) dimer model but narrower and with a significantly increased FRET population. Further possible oligomers can be formed from (1/8) and (5/6) interfaces (abbreviated as (1/8)-5:6-(1/8)) or (5/6) and (4/5) interfaces ((5/6)-4:5-(5/6)). For all these oligomer models the Gedankenexperiment is true and the average effective apparent oligomer distance is approximately 50 Å. Furthermore we applied a dimer/tetramer simulation on our MFIS data which considers all donor-acceptor configurations to estimate the association constants (Figure 5-7C, Figure 5-13E-G). For TGR5 wt and Y111F the fit model indicates that almost all dimers have formed tetramers, whereas TGR5 Y111A forms predominantly dimers. The measurements do not allow us to determine the dissociation constants very precisely. However, we see that the dimerization constant K_{D1} must be very small (< 20 nM) and we can estimate the dissociation constant K_{D2} of the TGR5 tetramers to be in the range of 100 nM for wt and Y111F and several µM for Y111A; i.e. the replacement of Y by A at position 111 approximately reduces the tetramer affinity by factor of 10. This strongly indicates that the equilibrium between dimer and higher order oligomer formation is primarily on the dimer side in TGR5 Y111A and on the tetramer side in TGR5 wt and Y111F. Notably, the spread in the FRET efficiencies observed in Figure 5-7C is caused by the distinct protein concentrations in the cell and is taken into account in the simulations (Figure 5-13, Section 5.6.3.2).

All mentioned dimer interfaces are supported for class A GPCRs by literature (Fotiadis et al., 2003; Huang et al., 2013; Patowary et al., 2013). The known dimer of dimers either has a row or a rhomboid tetramer organization as shown in Figure 5-7D, Figure 5-12 and Figure 5-13. We suggest that the TGR5 oligomers must resemble a one-dimensional array mediated by a single oligomerization interface, because one mutation in the ERY motif Y111A in intracellular loop (ICL2) affects the association significantly. As shown in Figure 5-8 the Y111 residue can interact with TM5 or/and TM6 dependent on its structural behavior, which could be either helical or flexible. In both cases (4/5) and (5/6) as potential interaction sites can be affected during oligomerization. This observation is supported by two crystal structures: In the (4/5) model, as shown in CXCR4 (3ODU), a 7 Å salt bridge between Y111 and R146 is possible, as well as in the (5/6) model, as shown in µ-opioid receptor (4DK2), between Y111 and R280.

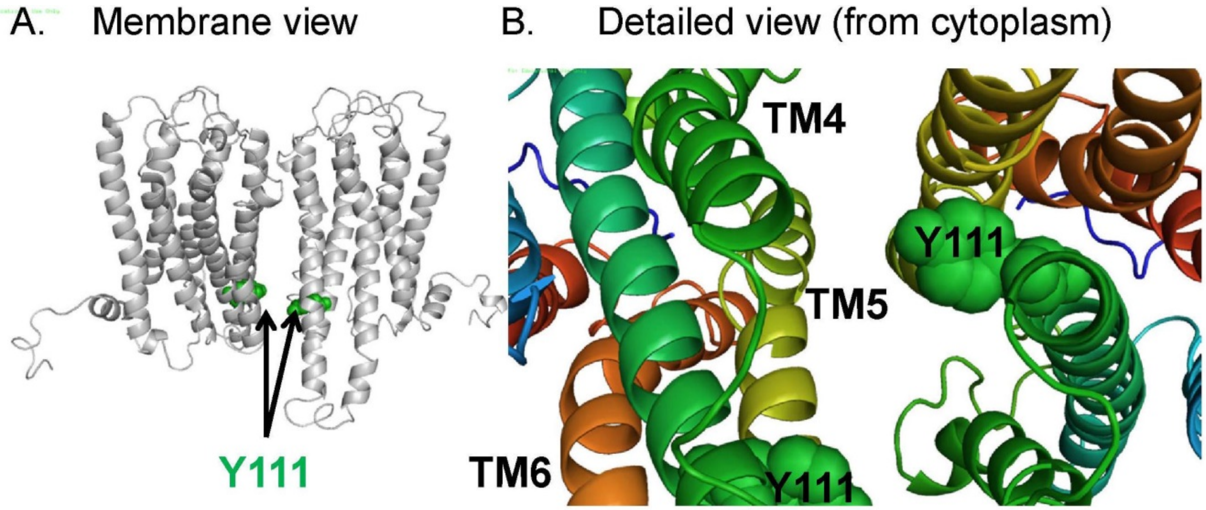

Figure 5-8 Influence of the Y111 residue on oligomerization. (**A**) The dimerization model (4/5) is displayed as a grey cartoon viewed from the membrane. Residue Y111 located in ICL2 is depicted as a green sphere in each TGR5 monomer. (**B**) Blow-up of the region around residue Y111 to show possible interactions between Y111 from one TGR5 molecule with residues in TM4 (green) and TM5 (yellow) in a second TGR5 molecule.

As we lack detailed structural information of the TGR5 ICL2 and based on our experimental data, we cannot distinguish oligomerization interfaces (4/5) from (5/6). Therefore both patterns, (1/8)-5:6-(1/8) and (1/8)-4:5-(1/8), are currently possible with Y111 forming salt bridges and/or hydrophilic interactions with residues within the mentioned interfaces. In literature, there is evidence for a helical structure of the ERY motif (e.g. neurotensin receptor) (White et al., 2012), however, this has to be validated for TGR5. The oligomer (5/6)-4:5-(5/6) which forms a rhomboid tetramer can be excluded for the same reason: disruption of the (4/5) and (5/6) interface would result in monomers.

One-dimensional arrays forming mainly (1/8)-4:5-(1/8) oligomers have also been found for rhodopsin (Fotiadis et al., 2003; Salom et al., 2006) and (1/8)-5:6-(1/8) oligomers for the µ-opioid receptor (Manglik et al., 2012). Therefore, FRET and mutagenesis corroborate formation of TGR5 oligomers with row organization formed mainly from (1/8), thereby creating possible new interfaces with contact sites involving TM5.

5.3.5 TGR5 oligomerization is not affected by ligand binding and subsequent G-protein coupling.

It was reported that GPCR oligomerization could be affected by ligand binding (Ferre et al., 2014). As has been shown by recent research (Duboc et al., 2014; Jensen et al., 2013; Spomer et al., 2014), we could also prove cAMP increase after ligand treatment in all TGR5 variants as an indicator of G-protein binding. However, competitive cAMP independent signalling pathways e.g. by interaction with EGFR (Jensen et al., 2013) are also possible. From simulation experiments we expect that after G-protein binding the average apparent distances get longer, but effective R_{DA} distributions of oligomers with and without G-protein are indistinguishable, because a distance distribution difference of less than 8 Å is smaller than the anticipated accuracy of the models (see Table 5-4).

In fact, the MFIS-FRET measurements showed no change in FRET properties after TC treatment - an observation that is also supported by literature (Patowary et al., 2013). The assumption that G-proteins can bind transiently after activation for cAMP dependent signal transduction is reasonable. Recent G-Protein-receptor coupling models suggest transient binding after ligand activation (collision model and compartmentalization model) or pre-coupling even in absence of the ligand (Hein et al., 2005). From our data we conclude that the major amount of TGR5 molecules is uncoupled, even after TC stimulation. Our findings are also consistent with the observations of (Jensen et al., 2013) that TGR5 does not interact with β-arrestins, internalize, or desensitize, but transmits sustained signals close to the cell surface.

In summary, we have no evidence, that TGR5 oligomerization is affected by ligand treatment and subsequent G-protein coupling. It’s however largely unknown how many G-proteins interact with TGR5 oligomers. A possible scenario for GPCR-G-Protein coupling is suggested for class A GPCR dimers (Breitwieser, 2004; Ciruela et al., 2010; Filizola, 2010; Gurevich and Gurevich, 2008; Moreira, 2014; Park et al., 2004; Parker et al., 2011; Pfleger and Eidne, 2005), where a stoichiometry of 2:1 (two GPCRs, one heterotrimeric G-protein complex) is most likely formed. However, this has also to be validated for TGR5 in future research.

5.4 Conclusions

In the present study we characterized TGR5 oligomerization by combined molecular biology, fluorescence microscopy approaches, as well as bioinformatics modelling and simulations. From these data TGR5 wt forms homo-oligomers and localizes to the plasma membrane in a G-protein uncoupled state. TGR5 oligomers are formed from dimers of dimers involving interaction contact sites in transmembrane helix 1 (TM1) and Helix 8 and transmembrane helix 5 (TM5).

5.5 Methods

Cell culture media were from PAA (Coelbe, Germany). Foetal calf serum (FCS) was from Biochrom (Berlin, Germany). Taurolithocholic acid (TLC), Taurocholic acid (TC) and Forskolin (F) were purchased from Sigma-Aldrich (Taufkirchen, Germany) and Calbiochem (San Diego, CA, USA), respectively.

5.5.1 Cloning of TGR5

Human TGR5 was cloned as previously described (Spomer et al., 2014). Constructs were cloned into the pcDNA3.1+ (TGR5-pcDNA: complete CDS; TGR5-His: stop codon in complete CDS replaced by C-terminal 8xHis-tag), pGFP-N1, and pmcherry-N1 (stop codon in the complete CDS replaced by a restriction site) vectors. The FLAG-TGR5-YFP construct with an N-terminal FLAG-tag and a C-terminal YFP-tag was cloned into the pEYFP-N1 vector. All vectors were from Clontech, Palo Alto, CA. The Y111A and Y111F mutations were introduced into different TGR5 cDNA constructs using the QuikChange Site-Directed Mutagenesis Kit (Agilent Technologies, Santa Clara, USA) (Spomer et al., 2014). All cloning strategies and mutagenesis primer sequences can be obtained upon request. Successful cloning and mutagenesis was verified by sequencing (GenBank accession numbers: TGR5:NM_001077191.1).

5.5.2 Immunofluorescence and confocal laser scanning microscopy

Human embryonic kidney 293 (HEK293) cells and Madin Darbin canine kidney cells (MDCK), grown on glass coverslips or transparent filter wells, were transiently transfected with TGR5 wt, Y111A or Y111F in pcDNA3.1+ and pEYFP-N1 vectors using Lipofectamine2000 (Invitrogen) for 48 h according to the manufacturer's recommendations. After fixation with -20°C cold methanol for 30 sec, cells were incubated with RVLR2 (Keitel et al., 2009) antibody against TGR5 and Cyanine-3 (1:500) conjugated secondary antibodies, which were purchased from Dianova (Hamburg, Germany). Nuclei were stained with Hoechst 34580 (1:20000; Invitrogen). Images were analysed on a Zeiss LSM510META confocal microscope using a multi-tracking modus. A 63 x objective and a scanning resolution of 1024 x 1024 pixels was used for all samples.

5.5.3 Flow cytometry

TGR5 plasma membrane protein amount was quantified by flow cytometry (FACS) using a FACS-CANTO-II (BD Biosciences; Heidelberg, Germany) as previously described (Hov et al., 2010; Spomer et al., 2014). HEK293 cells were transiently transfected with the FLAG-TGR5-YFP constructs using Lipofectamine2000. The N-terminal FLAG-tag was detected with the anti-FLAG M2-antibody (Sigma-Aldrich) using the Zenon PacificBlue Label-Kit (Invitrogen) according to manufacturer's instructions. TGR5 plasma membrane expression was calculated by the amount of FLAG-tag positive cells divided by the total amount of TGR5 positive cells as determined by YFP-fluorescence.

5.5.4 Reporter gene assay

HEK293 cells were transiently transfected with TGR5 wt and TGR5 Y111A and TGR5 Y111F variants in the pcDNA3.1+ construct (0.5 ug), pEYFP-N1-empty vector (1.1 ug), reporter PlasmLuc (1.6 ug; Bayer AG; Leverkusen, Germany), and Renilla expression vector (0.1 µg; Promega; Madison, WI, USA) using Lipofectamine2000. The PlasmLuc-reporter gene construct contains 5 cAMP-responsive elements (CREs) upstream of the luciferase gene. Luciferase activity was normalized to transfection efficacy, which was monitored by cotransfection with the Renilla expression vector, and served as measure for the rise in intracellular cAMP. Luciferase activity was determined 16 hours after stimulation with DMSO, TLC or Forskolin (Hov et al., 2010; Spomer et al., 2014). The increase in TLC- and Forskolin-dependent luciferase activity is relative to the DMSO stimulation, which was set equal to 1.0.

5.5.5 Co-immunoprecipitation

HEK293 cells were cotransfected with TGR5-YFP and TGR5-His. Cells transfected with the empty vector (pcDNA or pEYFP-N1) and only one of the TGR5 cDNAs (TGR5-His or TGR5-YFP) served as controls. Cells were lysed with a buffer containing 50 mM Tris-HCl pH 8.0, 1% Nonidet® P40 (AppliChem) and complete protease inhibitor cocktail tablets (Roche). Protein concentration was determined by Bradford assay, and 1.6 mg protein from each sample was used for immunoprecipitation with the uMACS HIS-tagged protein isolation kit (Miltenyi Biotec, Bergisch-Gladbach, Germany). His-tagged TGR5 was labelled with the anti-His microbeads and loaded onto the MACS columns. His-tagged proteins were eluted from the columns with 60 µl elution buffer and divided into two equal samples of 30 µl each. These were subjected to deglycosylation using the N-glycosidase-F Kit (Roche Diagnostics, Mannheim, Germany) for 10 min at 37°C. The deglycosylation reaction was stopped with 10% Laemmli buffer, heated to 95°C for 3 min, and separated by SDS page. Proteins were transferred to PDVF membranes. His-tagged proteins were detected with the HRP-coupled anti-His antibody (dilution 1:5000, Miltenyi Biotec). YFP-coupled proteins were detected using the HRP-coupled anti-GFP antibody (1:5000, Miltenyi Biotec). Densitometry was performed using the Totallab-100 software (Nonlinear Dynamics, Durham, NC). The relative amount of TGR5 oligomerization was calculated by dividing the amount of TGR5-YFP protein through the amount of TGR5-His protein. TGR5-wt-YFP/TGR5-His was set to 1.0.

5.5.6 Multiparameter fluorescence imaging spectroscopy (MFIS)

For live cell experiments HEK293 were seeded on 8 well chambered glass slides (Labtek, Nunc, USA) one day before transfection. Cells were transiently transfected with 0.5 µg DNA at a density of about 80% using FuGene6 (Promega) according to the manufacturer's protocol 24 to 48 h before analysis. Cell vitality and successful transfection was visually inspected before MFIS measurements. All measurements in live cells were performed on an inverted confocal laser scanning microscope (FV1000 Olympus, Hamburg, Germany) additionally equipped with a single photon counting device with picosecond time-resolution (Hydra Harp 400, PicoQuant, Berlin, Germany) with home built extensions for MFD as described in (Weidtkamp-Peters et al., 2009). Using a 60x water immersion objective (Olympus UPlanSApo NA 1.2, diffraction limited focus) the sample was excited with selected wavelengths (GFP at 488 nm with 400 nW, mCherry at 559 nm with 650 nW) of a NCH white light laser with a pulse-repetition rate of 40 MHz. The emitted light was collected and separated into its parallel and perpendicular polarization and into its green and red component (beam splitter 595DCLX, AHF, Germany). GFP fluorescence was then detected by single photon avalanche detectors (PDM50-CTC, Micro Photon Devices, Bolzano, Italy) in a narrow range of its emission spectrum (bandpass filter: BS 520/35, AHF, Tübingen, Germany). mCherry fluorescence was detected by cooled hybrid detectors (HPMC-100-40, Becker&Hickl, Berlin, Germany, with custom designed cooling), of which the detection wavelength range was set by the bandpass filters (HC 607/70, AHF). MFIS images were generated via raster-scanning the sample in a continuously moving beam manner. Images were taken with 20 µs pixel dwell time and a resolution of 103 nm per pixel. With 488 nm excitation, series of 40 frames were merged into one image; with 559 nm excitation, series of 20 frames were merged together. Images were further analyzed using custom-designed software available from our homepage (http://www.mpc.hhu.de/software.html).

5.5.7 Time series experiments of TGR5 stimulation by Taurocholic acid (TC)

To study the effect of bile acid agonists on the FRET parameters we used the water-soluble ligand TC, because addition of DMSO (necessary to dissolve TLC) affects the fluorescence signal significantly. For the time series experiments the time laps viewer function supplied by Olympus LSM was used. The motorized table was calibrated, and three cells were selected and monitored over a 40 minutes time period. FRET measurements were taken every 10 minutes: before the addition of TC immediately after addition (t = 0 min), and after ten and twenty minutes (t = 10 min; t = 20 min). Cells were excited with 488 nm and 559 nm laser light as described above. Where necessary, changes in focus and system drift were corrected.

5.5.8 Microscope calibration

Calibration measurements with Rhodamine 110 delivered the G-factor $G = g_{\perp}/g_{||}$ for the GFP emission wavelength range (green channels). The G-factor accounts for the detection efficiency difference between detectors of both polarizations ($g_{\perp}$ and $g_{||}$). The instrument response function (IRF) was measured with the back-reflection of the laser beam using a mirror and was used for iterative re-convolution in the fitting process.

Furthermore, untransfected cells and water were measured at 488 nm and 559 nm for background determination.

5.5.9 Pixel-wise analysis

To determine fluorescence-weighted lifetimes in a pixel-wise analysis, the histograms presenting the decay of fluorescence intensity after the excitation pulse were built for each pixel with 128 ps per bin. We used a maximum likelihood estimator (MLE) to determine the fluorescence-weighted averaged lifetime of donor molecules ($\langle\tau_{D(A)}\rangle_f$) in a single pixel using a model function containing only two variables, $\langle\tau_{D(A)}\rangle_f$ and the scatter contribution fraction. For experimental anisotropy calculations the fluorescence signals in parallel and perpendicular detection channels were also corrected for dead time of the detection electronics (including detector dead time) as follows:

$$S_{det} = \frac{S_{rec}}{1 - S_{rec} \cdot t_d} \tag{5-1}$$

t_d is the dead time, S_{det} and S_{rec} are the detected and recorded signals, respectively. The dead time of 80 ns of the set-up was determined from the linear auto-correlation curves of detection channels.

5.5.10 MFIS-FRET 2D histograms

For oligomerization analysis, we plotted the 2D histograms of donor lifetime $\langle\tau_{D(A)}\rangle_f$ vs the green to yellow fluorescence intensity ratio (F_D/F_A) (Eq.(5-2) - (5-3)) corrected for crosstalk (characterized by the crosstalk factor α), background $\langle B\rangle$, detection efficiencies of D (g_G) and A (g_Y). The acceptor fluorescence used for 2D-FRET must also be corrected for additional direct acceptor excitation DE and relative concentration dependent brightness DE_{rel}. Furthermore all samples were corrected for distinct fluorescence quantum yields Φ and a spectral shift factor γ (especially for TGR5 Y111A) which is considered in the corrected green detection efficiency (g_G*).

$$F_D = \frac{S_G - \langle B_G \rangle}{g_G *} \tag{5-2}$$

$$F_A = \frac{S_Y - (\langle B_Y \rangle + DE_{rel}) - \alpha(S_G - \langle B_G \rangle)}{g_Y} \tag{5-3}$$

The crosstalk factor is determined as the ratio between donor photons detected in the yellow channels and those detected in the green channels for the Donor only (Donly) labeled sample. The corrected detection efficiency g_G* is determined as the ratio of the spectral shift influenced green detection (0.69) and expected green detection (1.12) multiplied with the quantum yield Φ_{Y111A} obtained from a self-made detection efficiency software. The F_D/F_A parameters for each variant are provided in Table 5-1. The background was determined from untransfected cells.

	α	**⟨B_G⟩ [kHz]**	**⟨B_Y⟩ [kHz]**	**γ**	**Φ**	**DE_{rel} [kHz]**
wt	0.09	0.3	1	1	1	D/A1:10 +0.76 D/A1:40 +3.78
Y111A	0.28	0.3	2	0.61	1.125	D/A1:10 +4.28 D/A1:40 +0
Y111F	0.1	0.3	1	1	1	D/A1:10 +1.76

D/A1:40 +3.02

Table 5-1 Parameters to determine the corrected green-to-yellow fluorescence intensity ratio $F_D/F_{A.}$

The simultaneous reduction in both FRET indicators $\langle\tau_{D(A)}\rangle_f$ and (F_D/F_A) indicates FRET due to proteins interaction.

For a given sub-population selection the donor fluorescence decay histogram with 32 ps time resolution was constructed for further pixel-integrated sub-ensemble analysis, and the species-averaged fluorescence lifetime of the donor $\langle\tau_{D(A)}\rangle_x$ was calculated based on fit results (species fractions x_i and lifetimes $\tau_{D(A)}^{(i)}$)

$$\left\langle \tau_{D(A)} \right\rangle_x = \sum_{i=1}^{n} x_i \cdot \tau_{D(A)}^{(i)} \qquad (5\text{-}4)$$

where n is the number of exponents used in donor fluorescence lifetime fitting.

5.5.11 Pixel-integrated, time-resolved $\varepsilon_{mix}(t)$ illustration

To identify appropriate pixel in the cells for further pixel-integrated analysis, we computed all fluorescence parameters for each pixel (Section 5.5.9) and selected the pixels via two criteria in 2D-histograms of several FRET indicators: (i) green/yellow signal intensity ratio versus donor fluorescence lifetime ($\langle\tau_D\rangle_f$) and (ii) acceptor fluorescence lifetime ($\langle\tau_A\rangle_f$) versus green count rate to identify. A pixel population with homogeneous properties was selected and then integrated for subsequent pixel-integrated sub-ensemble analysis.

The time-dependent FRET parameter, $\varepsilon_{mix}(t)$, contains information on the underlying FRET-rate distribution and is proportional to the probability that FRET occurs at a certain time. After pixel selection, $\varepsilon_{mix}(t)$ was plotted for direct demonstration and visualization of molecular species with different FRET efficiencies in sub-ensemble data.

$\varepsilon_{mix}(t)$, is calculated as the ratio of normalized fluorescence decays of the FRET sample, $f_{mix}(t)$, and donor-only sample, $f_{(D,0)}(t)$.

$$\varepsilon_{mix}(t) = \frac{f_{mix}(t)}{f_{(D,0)}(t)} \tag{5-5}$$

$$\text{with } f_{mix}(t) = \varepsilon_{mix}(t) \cdot f_{(D,0)}(t) \tag{5-6}$$

$\varepsilon_{mix}(t)$ is the probability density function of the occurring FRET governed by FRET rate constant(s), k_{FRET}. The decaying part of $\varepsilon_{mix}(t)$ represents the features of FRET: high- or low-FRET can be directly read out from the decay slope. The amplitude of the decaying part indicates the FRET-active species fraction, x_{FRET}. Accordingly, the offset of $\varepsilon_{mix}(t)$ is the FRET-inactive fraction, $(1 - x_{FRET})$.

5.5.12 Pixel-integrated MFIS-FRET analysis using k_{FRET} models

To determine FRET parameters from pixel-integrated (sub-ensemble) data the donor only reference samples were fitted by a multi-exponential relaxation model accounting for a multi-exponential fluorescence decay of the donor in the absence of FRET:

$$f_{(D,0)}(t) = \sum_{m} x_{D0}^{(m)} \cdot \exp(-t \cdot k_{D0}^{(m)}) \tag{5-7}$$

in which m = 3 considering that FPs in living cells usually show at least bi-exponential characteristic (Heikal et al., 2001). Fit parameters in donor decay include three normalized pre-exponential factors $x_{D0}^{(m)}$ ($\sum x_{D0}^{(m)} = 1$) and three decay rate constants $k_{D0}^{(m)}$, which are the reciprocals of fluorescence lifetimes. The quenched donor decay $f_{D(A)}(t)$ is given by:

$$f_{(D,A)}(t) = \sum_m x_{D0}^{(m)} \cdot \exp\left(-t \cdot \left(k_{D0}^{(m)} + k_{FRET}\right)\right) \tag{5-8}$$

k_{FRET} is the FRET rate constant. The fitted parameters in the 1-k_{FRET} model are x_{FRET} and k_{FRET}. This is only true, if all donor species are quenched by the same FRET rate constant k_{FRET}. From the $\varepsilon_{mix}(t)$ diagrams it's clear that our data have to be fitted with m = 2, then we say it's a two-state model, from which we obtain two FRET rate constants and therefore two apparent distances.

The quenched donor decay $f_{D(A)}(t)$ in Eq. (5-8) is now extended:

$$f_{(D,A)}(t) = \sum_m x_{D0}^{(m)} \cdot \left(x_{FRET}^{(1)} \cdot \exp\left(-t \cdot \left(k_{D0}^{(m)} + k_{FRET}^{(1)}\right)\right) + x_{FRET}^{(2)} \cdot \exp\left(-t \cdot \left(k_{D0}^{(m)} + k_{FRET}^{(2)}\right)\right)\right) \tag{5-9}$$

$k_{FRET}^{(1)}$, $k_{FRET}^{(2)}$ are the FRET rate constants and FRET species fractions $x_{FRET}^{(1)}$, $x_{FRET}^{(2)}$ (the sum normalized to 1). The four fitted parameters in the 2-k_{FRET} model are $x_{FRET}^{(1)}$, $k_{FRET}^{(1)}$, and $x_{FRET}^{(2)}, k_{FRET}^{(2)}$. In the FRET-samples molecules not performing FRET are considered as fraction ($x_{D(0)}$) of Donly molecules.

Each FRET rate constant is converted to an apparent distance, $R_{DA,app}^{(1)}$:

$$R_{DA,app}^{(l)} = R_0 \cdot \left(k_{FRET}^{(l)} \cdot \tau_0\right)^{-\frac{1}{6}} \tag{5-10}$$

in which the unquenched GFP fluorescence lifetime is τ_0 = 2.6 ns and the Förster radius between GFP and mCherry is R_0 = 52 Å (including κ^2 = 2/3).

5.5.13 Mean energy transfer efficiency

The steady state transfer efficiency E is obtained using the FRET fractions and the apparent distances obtained from Eq. (5-10) where $x_{FRET}^{(1)}$, $x_{FRET}^{(2)}$ are fractions of species with FRET apparent distances $R_{DA,app}^{(1)}$ and $R_{DA,app}^{(2)}$, respectively, and R_0 for the GFP-mCherry pair is 52 Å.

$$E = \frac{x_{FRET}^{(1)}}{1+\left(R_{DA,app}^{(1)}/R_0\right)^6} + \frac{x_{FRET}^{(2)}}{1+\left(R_{DA,app}^{(2)}/R_0\right)^6} \tag{5-11}$$

5.5.14 Structural models of TGR5 dimers and tetramers

Dimer models with the interface TM1 and H8 (1/8) were generated by structurally aligning two homology models of TGR5 (Gertzen et al., 2015) onto the dimeric crystal structure of the human κ-opioid receptor (PDB ID: 4DJH (Wu et al., 2012)) via the 'cealign' command in Pymol (Schrödinger, 2010). For dimer models with the 4/5 interface and the 5/6 interface the same procedure was applied using the human CXCR4 receptor (PDB ID: 3ODU (Wu et al., 2010)) and the murine μ-opioid receptor (PDB ID: 4DKL (Manglik et al., 2012)) as alignment templates, respectively.

Tetramer models were built in a similar fashion. Here, two TGR5 dimers with the same dimer interface, e.g. (1/8), were aligned on another TGR5 dimer with a different interface, e.g. (4/5). With this procedure six tetramers were generated: (1/8) and (5/6) dimers with an oligomeric interface of (4/5); (1/8) and (4/5) dimers with an oligomeric interface of

(5/6); (4/5) and (5/6) dimers with an oligomeric interface of (1/8). Subsequently, the interface residues of the respective dimer and tetramer models were energy minimized in Maestro (Maestro, 2014) using the VSGB 2.0 solvation model (Li et al., 2011). Finally, either dimer and tetramer model was submitted to the OPM server (Lomize et al., 2006) to compute its orientation in a membrane.

5.5.15 Explicit linker simulations

5.5.15.1 Molecular dynamics simulations of GFP bound to a linker

For computing a thermodynamic ensemble (TE) of GFP positions with an explicit linker/GFP construct, initially, the structure of the TGR5 C-terminal residues 296-330, for which no experimental structural information is available, and the nine residues that connect the C-terminus to GFP (total sequence: QRCLQGLWGRASRDSPGPSIAYHPSSQSSVDLDLNYGSTG RHVS) was generated with the ‘Protein building’ approach in Maestro. Phi and psi angles of zero were chosen, resulting in a straight peptide conformation and, hence, a structurally unbiased starting structure for the molecular dynamics (MD) simulations. This linker was subsequently fused to enhanced GFP (PDB ID: 4EUL (Arpino et al., 2012)), and the resulting structure was capped with acetyl and *N*-methyl amide groups at the N- and C-termini, respectively, and protonated with PROPKA (Bas et al., 2008) according to pH 7.4. We note that we assumed the thermodynamic ensemble (TE) of mCherry to be identical to that of GFP.

Then, the linker/GFP construct was neutralized by adding counter ions and solvated in an octahedral box of TIP3P water (Jorgensen et al., 1983) with a minimal water shell of 12 Å around the solute. The Amber14 package of molecular simulation software (Case et al., 2005, 2015) and the ff14SB and GAFF (Wang et al., 2004) force fields were used to perform an all-atom MD simulations. To cope with long-range interactions, the “Particle Mesh Ewald” method (Darden et al., 1993) was used, and the SHAKE algorithm (Ryckaert et al., 1977) was applied to bonds involving hydrogen atoms. The time step for all MD simulations was 2 fs with a direct-space, non-bonded cutoff of 8 Å. The first linker residue was fixed with positional harmonic restraints with a force constant of 100 kcal mol^{-1} Å^{-2} throughout the simulations to emulate that this residue would be bound to TGR5 embedded in a membrane. At the beginning, 17500 steps of steepest decent and conjugate gradient minimization were performed; during 2500, 10000, and 5000 steps positional harmonic restraints with force constants of 25 kcal mol^{-1} Å^{-2}, 5 kcal mol^{-1} Å^{-2}, and zero, respectively, were applied to the solute atoms. Thereafter, 50 ps of NVT-MD (MD simulations with a constant number of particles, volume, and temperature) were conducted to heat up the system to 100 K, followed by 300 ps of NPT-MD (MD simulations with a constant number of particles, pressure, and temperature) to adjust the density of the simulation box to a pressure of 1 atm and to heat the system to 300 K. During these steps, a harmonic potential with a force constant of 10 kcal mol^{-1} Å^{-2} was applied to the solute atoms. As the final step in thermalization, 300 ps of NVT-MD simulations were performed while gradually reducing the restraint forces on the solute atoms to zero within the first 100 ps of this step. Afterwards, six independent production runs of NVT-MD simulations with 150 ns length each were performed. For this, the starting temperatures of the simulations at the beginning of the thermalization were varied by a fraction of a Kelvin. The conformations obtained in these simulations were pooled for further analyses.

5.5.15.2 Effective energies of linker/GFP conformations in the presence of TGR5 dimers and an implicit membrane

Snapshots of the MD simulations of the linker/GFP construct extracted in intervals of 50 ps were stripped of water molecules and ions, and the principle axis with the lowest moment of inertia of the first residue of the linker was aligned along the z-axis. The snapshots were then rotated in steps of 90° around the z-axis to increase the sampling density and subsequently placed in proximity to residue 295 of either TGR5 monomer for any of the TGR5 dimers (1/8 interface; 4/5 interface) (Figure 5-14A). For each snapshot, the effective conformational energy $E_{\text{effective, conf}}$ (i.e., the sum of gas phase energy and solvation free energy) was computed using the FEW^{mem} program (Homeyer and Gohlke, 2013, 2015), with the TGR5 dimers embedded in an implicit membrane of 34 Å width and using dielectric constants of 34, 4, and 1 for the outer to inner membrane slabs with a width of 5, 6, and 6 Å, respectively (Figure 5-14A) (Nymeyer and Zhou, 2008; Stern and Feller, 2003); for water and protein, dielectric constants of 80 and 1 were used, respectively. The counter ion concentration for the APBS calculation (Baker et al., 2001) was set to 0.15 mM. For all other parameters, default values as set in FEW^{mem} were used. All snapshots in which GFP penetrated the membrane, or in which GFP or the linker clashed with the TGR5 dimer, were omitted, leaving ~10.000 snapshots for the analysis. The distribution of the C-alpha atom of the central residue of the fluorophore from these snapshots shows that GFP essentially moves within a hemisphere on the cytosolic side of the membrane beneath the dimer (Figure 5-14D, E).

5.5.15.3 Thermodynamic Ensemble (TE) using explicit linker/GFP configurations

From the explicit linker/GFP configurations, the thermodynamic ensemble (TE) distribution is computed as a weighted average of the linker distance. The weights were determined according to a Boltzmann distribution

$$P_{Boltzman} = e^{\frac{-\Delta G}{RT}} \tag{5-12}$$

where R is the gas constant, T is 300 K, and ΔG is the difference between the Gibbs energy of the current snapshot and the energetically most favorable one. G is determined as the difference between $E_{\text{effective, conf.}}$ (see Section 5.5.16) and the contribution from the configurational entropy S:

$$G = E_{effective,conf.} - TS \tag{5-13}$$

We assumed that *S* is dominated by the configurations of the linker, whereas configurations of GFP are assumed to provide no contribution. This seems justified given that GFP is structurally much more stable than the linker: the linker largely consists of the TGR5 C-terminus, a part of GPCRs that has either been not fully resolved in any GPCR structure due to its high flexibility (Hanson et al., 2012; Jaakola et al., 2008; Palczewski et al., 2000) or, when resolved in small parts, shows random coil formation (Wu et al., 2010). Thus, we considered the linker a random hetero-polymer for which low energy conformations can structurally vary largely. Therefore, a random energy model (Wales, 2004) was used to describe its energy landscape. According to the random energy model, the entropy of a configuration with a given $E_{\text{effective, conf.}}$ is (Wales, 2004):

$$S = R \ln \Omega P \tag{5-14}$$

with Ω being the overall number of conformational states. The probability of occurrence *P* for each energy state is obtained from

$$P = \frac{1}{\sqrt{2\pi\sigma^2}} \exp\left(\frac{-\left(E_{effective,conf.} - \mu\right)^2}{2\sigma^2} \right) \tag{5-15}$$

with μ being the mean and σ the standard deviation of the frequency distribution of $E_{\text{effective, conf.}}$. The assumption underlying Eq. (5-15) is that the energy is Gaussian distributed (Wales, 2004), which is approximately fulfilled in our case (data not shown).

MM-PBSA calculations show a range of $E_{\text{effective, conf.}}$ of several hundred kcal mol^{-1} for proteins of sizes similar to that used in the present study (Fogolari and Tosatto, 2005; Gohlke and Case, 2004). In agreement with this, $E_{\text{effective, conf.}}$ computed for the linker/GFP configurations attached to the TGR5 dimer spans a range of ~ 1.000 kcal mol^{-1}. However, such an energy range would lead to unrealistically low probabilities for the higher energy configurations. We thus linearly scaled $E_{\text{effective, conf.}}$ such that the linker/GFP configuration with the highest energy has a probability of occurrence in a Boltzmann distribution of 1/Ω (Figure 5-14B). Finally, with the scaled energies, *P* (Eq. (5-15)), *S* (Eq. (5-14)), and *G* (Eq. (5-13)) were calculated, and from these the weights according to Eq. (5-12) for the weighted average of distances between 35 and 90 Å (Figure 5-14C).

To conclude, the TEs were constructed by explicit peptide linker/GFP MD simulations followed by calculations of conformational free energies (Eq. (5-12) - (5-15)) to weight each linker-GFP configuration. In the TE approach the weights of the points obtained from the explicit linker model were used to assign the weights of the inter-probe distances.

5.5.16 Implicit linker simulations

Inter-dye distance distributions for all TGR5 dimer and tetramer models were calculated using an modified Accessible Volume (AV) approach (Kalinin et al., 2012). Firstly, the different protein models (see Section 5.5.14) were embedded in an explicit membrane via the CHARMM-GUI membrane builder (Jo et al., 2009). Here, a membrane with 5500 lipids of 1,2-dioleoyl-*sn*-glycero-3-phosphocholine (DOPC) per layer was created employing default settings of the CHARMM-GUI. This resulted in a membrane bilayer of about 1.5 million atoms and a side length of about 620 Å to prevent the linker/GFP construct (which has an extended length of about ~229 Å) from wrapping around the edge of the membrane. As neither ions nor water were needed for AV calculations, the steps of ion and water addition were omitted during the creation of the membrane.

For the AV simulations the fluorescent probe was attached to the C-terminal amino acid of the TGR5 via a flexible linker of 203.5 Å corresponding to 55 amino acids (36 amino acids of the TGR5 C-terminus, a 6 amino acid cloning linker, and the first 13 amino acids of the GFP's (PDB ID: 4EUL) N-terminus, see Table 5-3) with a length of 3.7 Å each (Evers et al., 2006). A dye radius of 25 Å was used as an approximation for the GFP size, resulting in a total length of ~229 Å for the linker/GFP construct. The distance between linker attachment points in most of the screened oligomer models was shorter than the effective size of the AVs resulting in AV overlap. The AVs were constructed considering geometric factors in terms of steric exclusion effects caused by the TGR5 oligomer and the membrane. To account for clashes between the dyes, which are not addressed in the AV simulations, the inter-dye distance probability was set to zero for all distances below 25 Å. To account also for entropic effects, we introduced position weights for the implicitly modelled linker according to the Gaussian chain model, so that the non-uniform dye position probability distribution in the AV was scaled (Figure 5-12) (Chiang and Truong, 2006). In the Gaussian chain model a segment length of 7.4 Å was used, as obtained from the calibration aimed to reproduce the accurate end-to-end distance probability distribution from coarse-grained Monte-Carlo simulations of the peptide linker, similar to previously published results for the flexibly linked GFP dimer (Evers et al., 2006).

The obtained AV positional distributions were used to determine the inter-probe distance distribution by measuring all distances from positions in one AV distribution with respect to all positions in the second AV distribution. Considering oligomerization (tetramer) where two acceptors may be present in the vicinity of one donor, we computed the apparent distance distribution shifts towards shorter distances by convolution of the two inter-probe distance distributions ((1/8) and (4/5)) (Figure 5-14).

5.5.17 Statistical analysis

Experiments were performed independently at least three times. For MFIS-FRET at least three to ten cells per series in three independent experiments were measured. Results are expressed as mean ± s.e.. (standard error of the mean) and analysed using the two-sided student t-test. A $p \leq 0.01$ was considered statistically significant.

5.6 Supporting Information

5.6.1 Supplementary Tables

TGR5	Fit	D/A1:3	D/A1:5	D/A1:10	D/A1:20	D/A1:40
wt	b_0:	0.90	0.84	0.89	0.81	0.82
	b_1:	0.01	0.04	0.03	0.04	0.04
	b_2:	0.30	0.18	0.23	0.33	0.46
	b_3:	0.09	0.13	0.08	0.16	0.15
	b_4:	5.70	8.04	1.89	3.80	5.12
Y111A	b_0:	0.42	0.42	0.45	0.43	0.43
	b_1:	0.02	0.01	0.19	0.03	0.03
	b_2:	0.73	0.63	5.28	0.56	0.72
	b_3:	0.55	0.56	0.36	0.55	0.55
	b_4:	6.09	5.02	5.26	4.48	4.90
Y111F	b_0:	0.73	0.74	0.69	0.68	0.77
	b_1:	0.11	0.06	0.18	0.09	0.02
	b_2:	5.73	2.7	3.88	2.30	0.43
	b_3:	0.15	0.19	0.13	0.23	0.21
	b_4:	771.45	90.75	765.84	24.83	2.80

Table 5-2 Parameters for $\varepsilon_{mix}(t)$ diagram in Figure 5-4 for each TGR5 variant. The parameters (b0-b4) were obtained from the fit equation $f = b_0 + b_1 \cdot e^{-\frac{x}{b_2}} + b_3 \cdot e^{-\frac{x}{b_4}}$. b_0 determines the Non-FRET fraction (Donly fraction), b_1 and b_3 are the two FRET fractions and b_2 and b_4 are the corresponding decay times.

	TGR5 wt-FP
5’UTR	none
TGR5	MTPNSTGEVPSPIPKGALGLSLALASLIITANLLLALGIAWDRRLRSPPAGCFFLSLLLAGLLTGLALPTLPGLWNQSRRGYWSCLLVYLAPNFSFLSLLANLLLVHGER**Y**MAVLRPLQPPGSIRLALLLTWAGPLLFASLPALGWNHWTPGANCSSQAIFPAPYLYLEVYGLLLPAVGAAAFLSVRVLATAHRQLQDICRLERAVCRDEPSALARALTWRQARAQAGAMetLLFGLCWGPYVATLLLSVLAYEQRPPLGPGTLLSLLSLGSASAAAVPVAMetGLGDQRYTAPWRAAAQRCLQGLWGRASRDSPGPSIAYHPSSQSSVDLDLNY
Cloning Linker	GSTGRH
GFP (4EUL) = donor (D)	MVSKGEELFTGVVPILVELDGDVNGHKFSVSGEGEGDATYGKLTLKFICTTGKLPVPWPTLVTTFGYGLQCFARYPDHMKQHDFFKSAMPEGYVQERTIFFKDDGNYKTRAEVKFEGDTLVNRIELKGIDFKEDGNILGHKLEYNYNSHNVYIMADKQKNGIKVNFKIRHNIEDGSVQLADHYQQNTPIGDGPVLLPDNHYLSYQSALSKDPNEKRDHMVLLEFVTAAGITLGMDELYK*
mCherry (2H5Q) = acceptor (A)	MVSKGEEDNMAIIKEFMRFKVHMEGSVNGHEFEIEGEGEGRPYEGTQTAKLKVTKGGPLPFAWDILSPQFMYGSKAYVKHPADIPDYLKLSFPEGFKWERVMNFEDGGVVTVTQDSSLQDGEFIYKVKLRGTNFPSDGPVMQKKTMGWEASSERMYPEDGALKGEIKQRLKLKDGGHYDAEVKTTYKAKKPVQLPGAYNVNIKLDITSHNEDYTIVEQYERAEGRHSTGGMDELY

Table 5-3 Sequence Information for AV-simulation. Untranslated region, TGR5 coding sequence, linker and GFP (4EUL) or mCherry (2H5Q) sequence of the analyzed TGR5 variants are summarized and used for TGR5 dimer and oligomer simulations. The position of the Y111 residue in the ERY motif for mutagenesis is highlighted. Sequences with unknown secondary or tertiary structures are underlined and are kept flexible in AV simulations.

	$\langle R_{DA,app} \rangle$, [Å]					
	with G-Protein			without G-Protein		
Label pair	(1/8)-4:5-(1/8)	(1/8)-5:6-(1/8)	(5/6)-4:5-(5/6)	(1/8)-4:5-(1/8)	(1/8)-5:6-(1/8)	(5/6)-4:5-(5/6)
A-B	133	119	**128**	98	94	**103**
A-D	134	**63**	128	97	**64**	120
A-E	**66**	129	65	**58**	93	72
B-D	**59**	108	64	**57**	91	69
B-E	131	**80**	116	99	**71**	106
D-E	136	123	**104**	101	94	**103**

Table 5-4 Overview of the mean distances $\langle R_{DA} \rangle$ calculated for the possible tetramer models with or without G-Protein. The primary interfaces for dimerization are in brackets (x/x) and secondary interfaces for oligomerization are abbreviated –x:x-. The numbers are the corresponding (transmembrane) helices involved in binding interactions. The apparent mean distances $\langle R_{DA,app} \rangle$ of each label pair involved in dimerization are bold. A schematic presentation of the tetramer models is shown in Figure 5-12. For example in the model (1/8)-4:5-(1/8) (with G-Protein always determined as label C, even when it is absent) label pairs A-E and B-D with the primary interfaces (1/8) show a distance 59-66 Å measured between the fluorescent proteins attached to helix 8, and the label pair A-B with the secondary interface -4:5- shows a mean distance of 133 Å. Further calculated distances in this oligomer are measured from label pairs A-D, B-E, B-D and are comparable to the distances obtained from A-B.

	wt[1]		wt		Y111A		Y111F	
	Donly fraction	χ_r^2	Donly fraction	χ_r^2	Donly fraction	χ_r^2	Donly fraction	χ_r^2
2-k_{FRET}	0.74	1.61	0.64	1.59	0.69	1.39	0.62	1.61
dimer (4/5)	0.43	1.65	0.00	1.83	0.00	4.94	0.14	1.54
dimer (1/8)	0.82	1.91	0.67	2.68	0.58	2.61	0.74	1.83
oligomer	n.d	n.d	0.74	2.82	0.65	2.86	0.78	1.88

Table 5-5 Comparison of results from different fit models. Donor fluorescence decay histograms in presence of acceptor in TGR5 variants are fitted based on 2-k_{FRET} and AV simulated distance distributions for different dimer (1/8), (4/5) and oligomer (1/8)-4:5-(1/8) interfaces with only one fit parameter – Donly fraction. Interface dimer (4/5) yields very low Donly fractions compared to all other models: it is known that ~30 % of mCherry acceptor dyes are not active in cells; hence at least ~30 % Donly fractions are expected. Based on this we concluded that interface dimer (4/5) as the primary dimer interface in TGR5 variants are less likely. wt[1] is D/A1:3, all other D/A ratios are 1:20.

5.6.2 Supplementary Figures

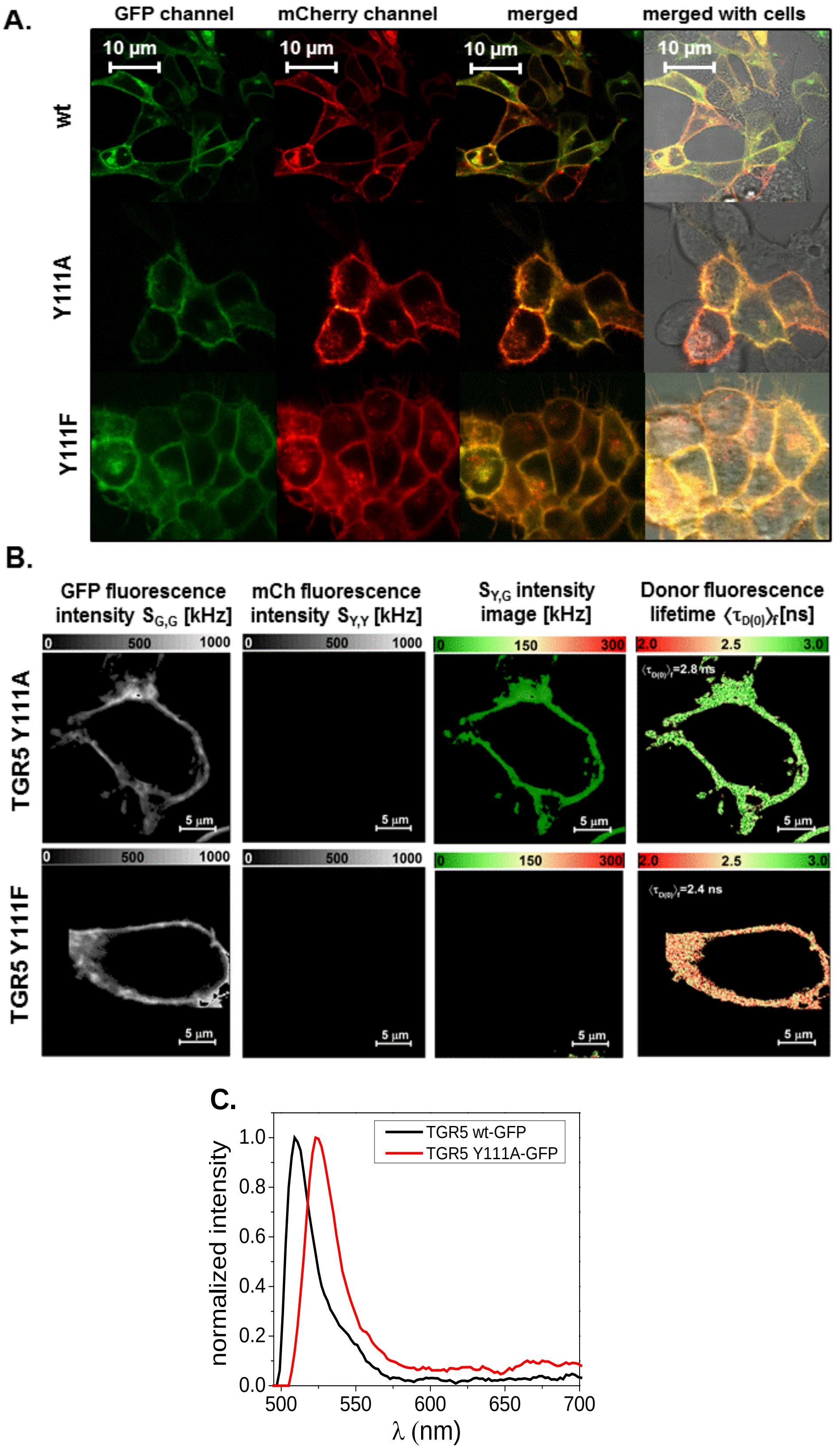

Figure 5-9 Live cell imaging and MFIS analysis of TGR5 donors. (**A**) HEK293 cells, transiently transfected with TGR5-GFP and TGR5-mCherry (transfection ratio 1:10), were imaged for co-localization of GFP and mCherry using sequential scanning and a scanning resolution of 1024 x 1024 pixels. Each TGR5-GFP and TGR5-mCherry picture is shown in a false color saturation mode and then overlaid by using green and yellow intensity colors. TGR5-GFP and TGR5-mCherry wt, Y111A and Y111F (from top to bottom) are clearly co-localized at the cell membrane. Scale bar 10 µm. (**B**) MFIS analysis of TGR5 transfected HEK293 cells by comparing (from left to right and top to bottom row) the GFP fluorescence intensity, mCherry fluorescence intensity, the donor fluorescence lifetime $\langle\tau_{D(0)}\rangle_f$, and mCherry photons after excitation of GFP ($S_{Y,G}$). The fluorescence-averaged donor lifetime in the absence of an acceptor $\langle\tau_{D(0)}\rangle_f$ in the Y111A variant is 2.8 ns compared to 2.4 ns for Y111F. The presence of green photons in the yellow channel is due to a higher crosstalk, background and red shift in the Y111A variant. (**C**) GFP was excited at 488 nm and emission spectrum was measured from 495 nm to 700 nm in a 2 nm step size and a 2 nm spectral band width at Olympus FluoView1000 microscope. TGR5 wt-GFP shows the typical emission maximum at 510 nm, whereas TGR5 Y111A-GFP shows a 13 nm red shift towards 523 nm. Three cells for each curve were measured, the background was subtracted and the average intensity normalized to the maximum. The Y111A MFIS data were corrected for the spectral shift.

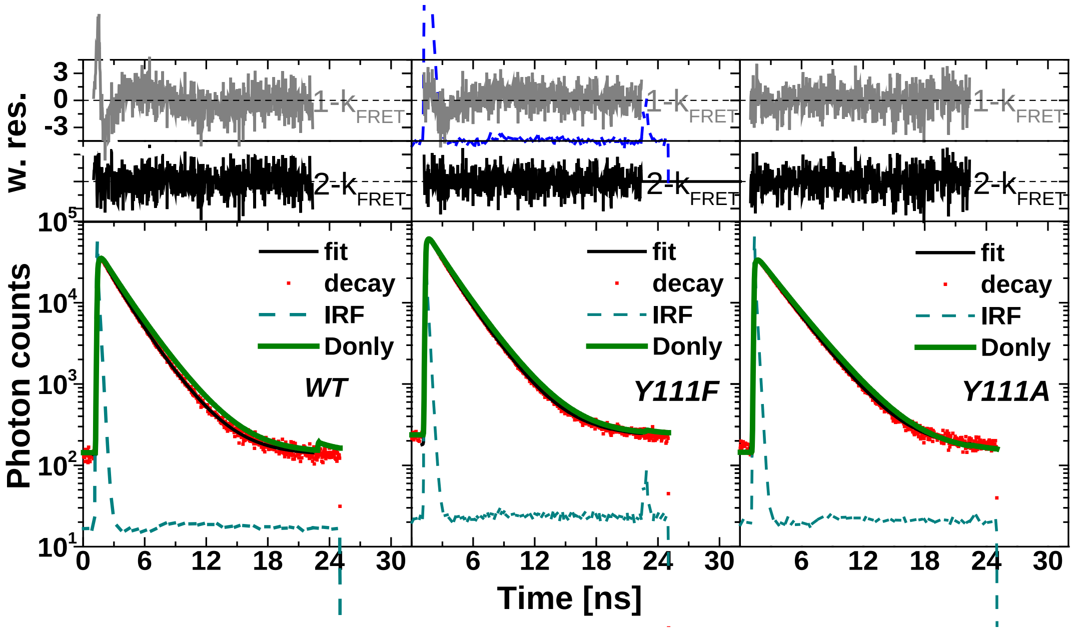

Figure 5-10 Fit fluorescence decays with different models for TGR5 variants. Fitting the sub-ensemble fluorescence decays of the FRET samples (D/A 1:10) with k_{FRET} models (see Section 5.5.12) showed that two FRET rates are necessary to fit these data accurately. The decays of Donly (TGR5-GFP) and FRET samples are in olive and red, respectively. The fitted decay with the 2-k_{FRET} model and the fitting residuals are plotted in black. The fitting residuals with 1-k_{FRET} model are plotted in grey.

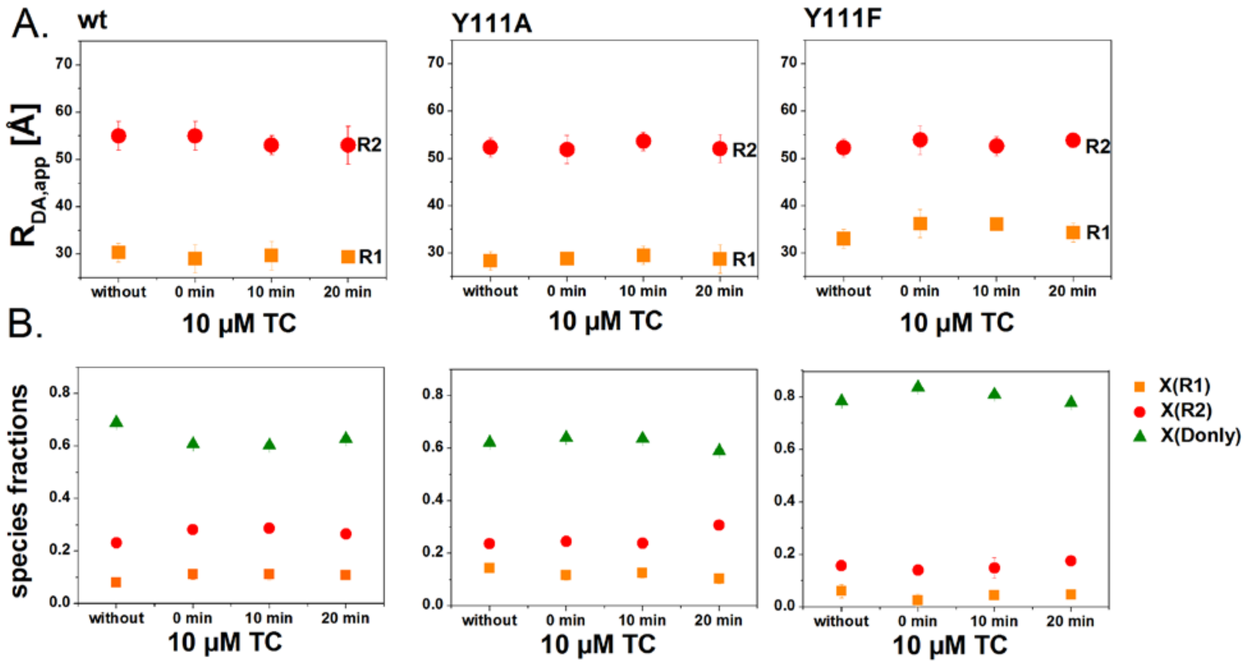

Figure 5-11 Time-series analysis after TC ligand stimulation. HEK293 cells were transiently transfected with TGR5-GFP alone (Donly) or with TGR5-GFP and TGR5-mCherry with the D/A ratio of 1:10. To study changes in FRET after ligand addition, three cells were selected using the Olympus Time laps function and measured at different time points, including before adding 10 µM TC (without), immediately after TC addition (t =0), 10 min after and 20 min after. The apparent distances R_{DA} species fractions were fitted using self-made software. (**A**) The apparent distances are plotted versus time. Each point represents the average of nine cells (three measurements with three cells). (**B**) The species fractions X(R1), X(R2) and the Non-FRET fraction x_{Donly} at four time points (representing without TC, t = 0, t = 10 min and t = 20 min) are plotted, but no substantial change due to ligand addition could be detected. Orange=R1=high FRET distance, red = R2 = low FRET distance, green = Donly fraction.

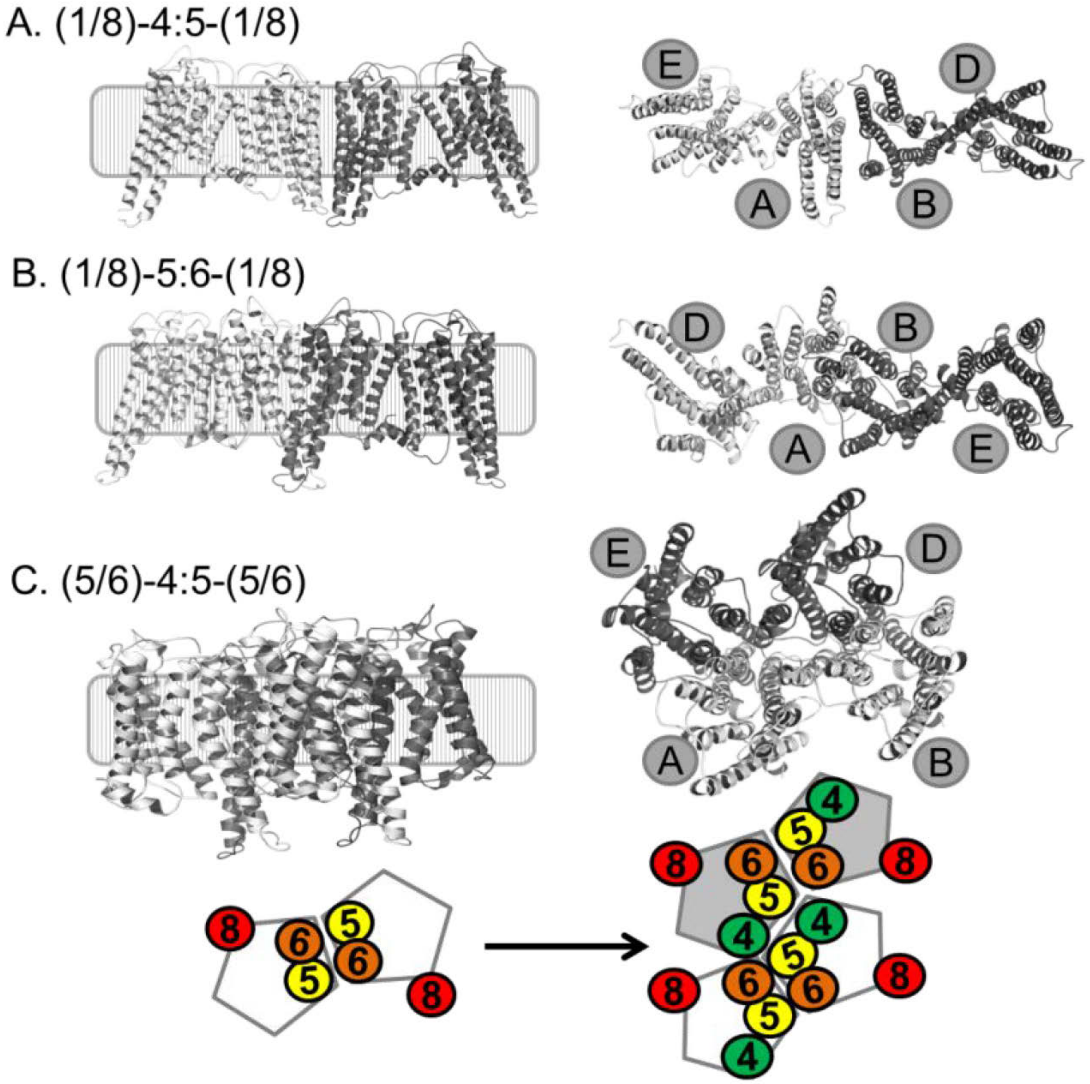

Figure 5-12 GPCR tetramer organization and AV simulations. (**A**-**C**) Cartoon presentation generated in PyMol (DeLano and Lam, 2005; Schrödinger, 2010) from the membrane view (right) and cytoplasmic view (left) for three possible tetramer organizations. The labels A, B, D and E refer to the TGR5 monomers and are used for distance distribution calculations (Table 5-5). The corresponding dimers are colored in light gray or dark gray.

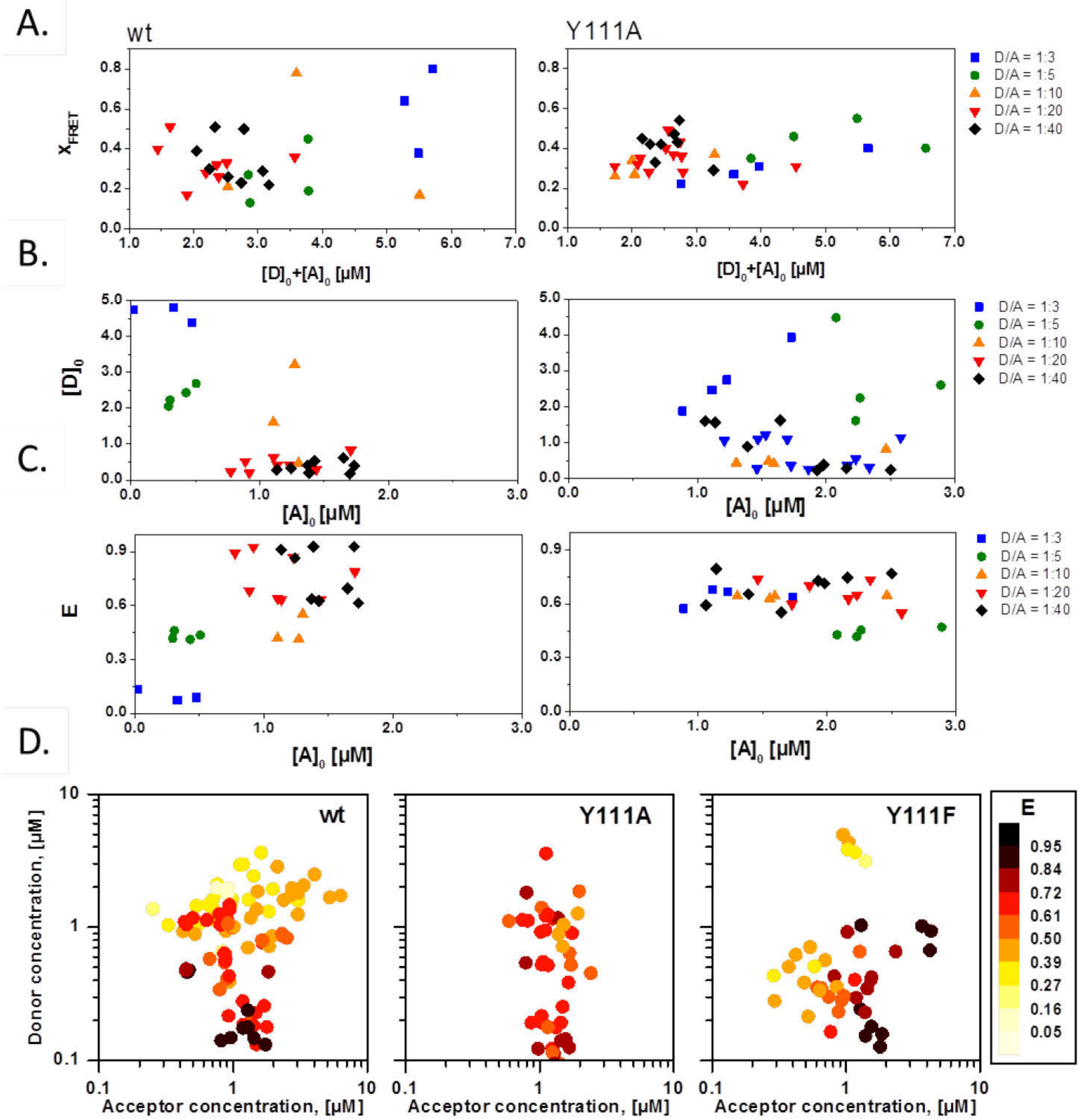
A.
wt
Y111A
x_{FRET}
$[D]_0+[A]_0$ [µM]
D/A = 1:3
D/A = 1:5
D/A = 1:10
D/A = 1:20
D/A = 1:40
B.
$[D]_0$
$[A]_0$ [µM]
C.
E
D.
wt
Y111A
Y111F
Donor concentration, [µM]
Acceptor concentration, [µM]
E
0.95
0.84
0.72
0.61
0.50
0.39
0.27
0.16
0.05

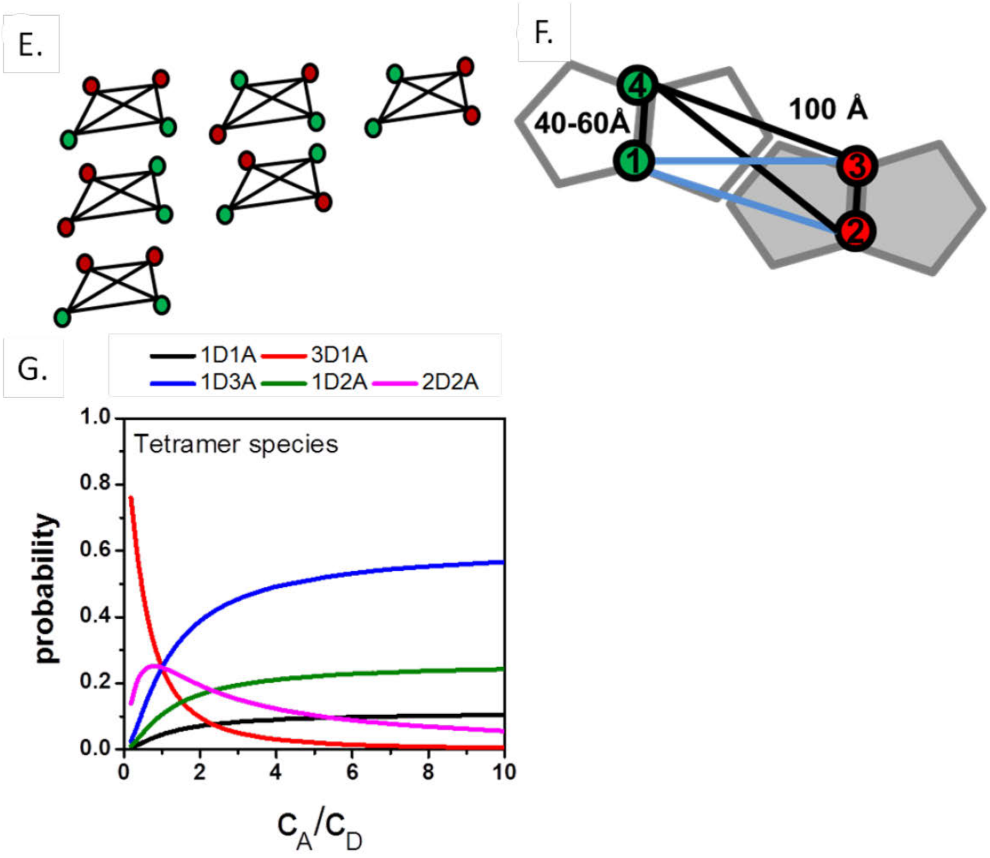

Figure 5-13 Characterization and estimation of the association constants with a dimer/tetramer fit model. HEK293 cells were transiently transfected with TGR5 wt (left plots) or Y111A (right plot) donor to acceptor ratios varying from 1:3 to 1:40. (**A**) The total protein concentration $[D]_0$+$[A]_0$ (calculated as described in Section 5.6.3.1) and the FRET species fractions x_{FRET} were obtained from MFIS measurements and plotted to calculate the dissociation constant K_D. The FRET species fractions calculated from different D/A ratios were distributed equally in a concentration range of 1-7 µM. From these data K_D cannot be directly determined. The upper limit for K_D should be less than 1 µM. **B**. The real donor $[D]_0$ and acceptor $[A]_0$ concentrations from the D/A transfection experiments were plotted for wt and Y111A to estimate differences in experimental and real concentration ratios between donor and acceptor. (**C**) E increases in an $[A]_0$ dependent manner in wt but not in Y111A transfected cells. (**D**) Overview on the concentration ranges of donor and acceptor and its influence on E, whose size is depicted in color. Variant specific interaction patterns are readily visible. (**E**) Description of our data by a minimal dimer/tetramer model to. In this model we assume that a tetramer is constituted of a dimer of dimers. In a tetramer the sum of donor, acceptor and unlabeled molecules is constant (refer to Section 5.6.3.2). Six tetramer configurations for a

case of two acceptor (red) and two donor molecules (green) are possible. (**F**) Composition of a simplified rectangular tetramer molecule with random arrangement of two donors and two acceptors according to a linear organization of the GPCR. The positions of the green and red circles in the pentagram represent the fluorescent proteins attached to helix 8. G. Probabilities of all tetramer species composed of a certain number of donor and acceptors (1D1A, 3D1A, 1D3A, 1D2A, 2D2A) in dependence of the acceptor to donor ratio. In our case the most probable scenario is the 2D2A case which describes our data best.

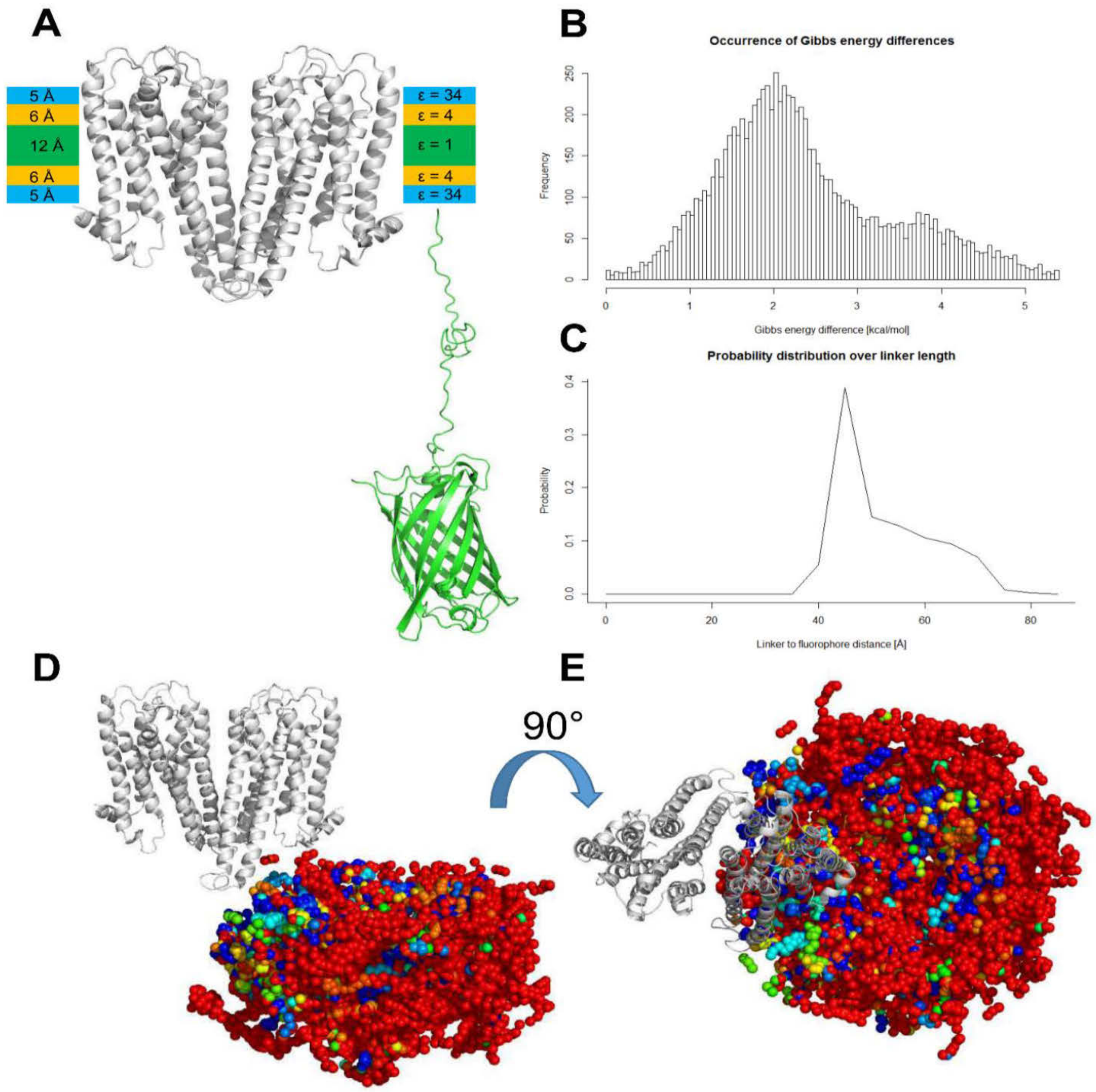

Figure 5-14 Explicit linker/GFP simulation and probability distribution of linker/GFP configurations. (**A**) Starting structure of the TGR5 4/5 dimer (grey) and of the linker and GFP after the initial minimization (green). The linker and GFP were simulated separately from the TGR5 dimer; the structure shown here illustrates one of the composite models used for the MM-PBSA calculations. At the 'wad' in the middle of the linker, several proline residues are present. The positioning of the implicit membrane slabs is shown in colored bars next to the TGR5 dimer. The bars on the left show the thickness of each membrane layer used in the FEWmem calculations, while the bars on the right show the respective electric permittivity. (**B**) Frequency distribution of Gibbs energies (Eq. (5-13) in the main text) relative to the energetically most

favorable snapshot after linear scaling. (**C**) Probability distribution for the Boltzmann-weighted distance between the fluorophore and the N-terminus of the linker. (**D, E**) Ensemble of linker/GFP configurations represented in terms of the C-alpha atom of the central residue of the fluorophore generated by MD simulations with added rotations (see Section 5.5.17) in relation to the TGR5 4/5 dimer (grey) in side (**D**) and exoplasmic view (**E**). The coloring of the C-alpha atoms corresponds to their probability ranging from lowest (blue) to highest (red). Conformations with a low probability are more frequently found in close contact to the dimer.

5.6.3 Supplementary Methods

5.6.3.1 Determination of acceptor and donor concentration from MFIS experiments

TGR5 monomers were either labelled with donor or acceptor fluorescent proteins and transiently transfected into cells with different donor-to-acceptor concentration ratios. The fractions of active donor (denoted as D) and active acceptor (denoted as A) is f_D and f_A respectively. The rest are inactive FPs, which we considered as dark (i.e. no fluorescence emission) and dysfunctional (i.e. FRET-negative). To calculate the protein concentrations from fluorescence intensity, the detection volume of our microscope and GFP and mCherry brightness are required. The detection volume was determined as $1.23{*}10^{-15}$ l from FCS measurements of Cyanine 3B (Cy3B). The fitting model applied to the obtained FCS curve assumes a 3-dimensional Gaussian-shaped volume, and a single diffusing species including transitions to a triplet state as described in (Weidtkamp-Peters et al., 2009). The brightness of enhanced GFP and mCherry *in vivo* were individually characterized from FCS measurements of freely diffusing FPs in cytoplasm. We found that with 0.6 µW of 559 nm laser excitation at the objective, mCherry brightness (Q_A) is 0.68 kcpm in cytoplasm. With 0.4 µW of 485 nm laser excitation at the objective, GFP brightness (Q_D) is 0.56 kcpm in cytoplasm.

The average mCherry fluorescence intensity of an image with mCherry excitation ($S_{Y,Y}$) was first corrected for detector dead time, and then used to calculate the total concentration of mCherry, $[A]_0$, with the determined detection volume ($V_{det\text{-}mCherry}$) and the mCherry brightness:

$$\begin{aligned}[A]_0 &= \frac{S_{Y,Y}^{m}}{Q_A\,[kcpm] * V_{\det - mCherry}\,[fl]} \\ &= \frac{S_{Y,Y}^{m}}{0.68\,kcpm * 0.8\ fl}\end{aligned} \tag{5-16}$$

The average GFP fluorescence intensity of an image with GFP excitation was also corrected for detector dead time, and then the obtained intensity ($S_{G,G}^{m}$) was further corrected for the quenching effect due to FRET:

$$S_{G,G}^{u} = \frac{S_{G,G}^{m}}{(1 - x_{FRET}) + x_{FRET} \cdot (1 - E)} \tag{5-17}$$

$S_{G,G}^{u}$ is the unquenched GFP fluorescence intensity in the absence of FRET, the energy transfer efficiency E and fraction of FRET-active population, x_{FRET}, were calculated as described in the main method sections. $S_{G,G}^{u}$ was then used to calculate the total concentration of GFP, $[D]_0$. The wavelength dependent confocal volume is 0.5 fl.

Assuming the concentration of the FPs reflects the concentration of their host proteins, the TGR5 concentration (without non-fluorescent molecules) in µM was determined as:

$$\text{protein concentration} = [A]_0 + [D]_0 = c_A + c_D \tag{5-18}$$

5.6.3.2 Estimation of the association constants for oligomerization

The total protein concentration and the protein association constants have to be considered to determine the oligomerization state or the chemical speciation. To calculate the transfer-efficiency for a given oligomerization the spatial organization of the molecules within the oligomers and the concentration of donor, acceptor and non-fluorescent molecules has to be considered. The total protein concentration (Eq. (5-19)) is given by the sum of the acceptor, the donor and the unlabeled protein concentration:

$$c_T = c_A + c_D + c_U \tag{5-19}$$

Here the unlabeled protein concentration c_u equals the concentration of immature mCherry. The protein concentrations were calculated using the brightness of free GFP and free mCherry as reference as described in Section 5.6.3.1.

Even though higher-order oligomerization is anticipated we used a simple dimer/tetramer model to describe our data as this allows for a quantitative description. In this model we assume that a tetramer is constituted of a dimer of dimers (Figure 5-13). Hence, starting from a monomer two equilibriums have to be treated:

$$\begin{aligned} o + o \quad &\rightarrow \quad oo \quad K_1 = \frac{[oo]}{[o][o]} \\ oo + oo \quad &\rightarrow \quad (oo)(oo) \quad K_2 = \frac{[(oo)(oo)]}{[oo][oo]} \end{aligned} \tag{5-20}$$

Here o is a monomer, oo a dimer and (oo)(oo) is a tetramer. We use the monomer o as a master species. Then the total protein concentration is given by:

$$c_T = [o] + 2 \cdot [oo] + 4 \cdot [(oo)(oo)] \tag{5-21}$$

Now, the concentrations of the three species o, oo and (oo)(oo) for any given the total protein concentration is obtained by solving the three equations above.

To calculate the transfer efficiency we assume that donor, acceptor and unlabeled molecules behave biochemically identical. Hence, the probability of an oligomer composition is given by the probability of finding a donor, acceptor or unlabeled molecule and the counting statistics. The probabilities of finding a donor, acceptor or unlabeled molecule depend on their respective concentrations. For instance the probability of an acceptor molecule is given by the respective species and total protein concentration:

$$p_A = \frac{c_A}{c_T} \tag{5-22}$$

In a tetramer the sum of donor, acceptor and unlabeled molecules is constant. The probability of a certain tetramer composition is obtained by the multinomial distribution:

$$\begin{aligned} p(n_D, n_A, n_U) &= N \cdot p_D^{n_D} p_A^{n_A} p_U^{n_U} \\ &= \frac{(n_D + n_A + n_U)!}{n_D! n_A! n_U!} \cdot p_D^{n_D} p_A^{n_A} p_U^{n_U} \end{aligned} \tag{5-23}$$

N is the number of combinations for a given composition. Each combination might have a different FRET-rate distribution. Hence, in case of two donors and two acceptors 6 combinations as shown in Figure 5-13C contribute to the signal. If only species with at least one donor and one acceptor are considered the FRET-rate constants of overall 38 distinct species and their respective probabilities and FRET-rate constant distributions have to be calculated. The species probabilities summarized by their donor and acceptor composition in dependence of the acceptor to donor ratio c_A/c_D are illustrated in Figure 5-13F.

FRET-rate constants are additive. Therefore in case of multiple acceptors the total FRET-rate constant experienced by a donor (i) is given by the sum of all FRET-rate constants of all acceptors (j):

$$k_{FRET}^{(i)} = \frac{1}{\tau_0} \cdot \sum_j \left(\frac{R_{DA}^{(ij)}}{R_0} \right)^6 \tag{5-24}$$

Here $R_{DA}^{(ij)}$ is the donor acceptor distance between the donor (i) and the acceptor (j) which is determined by the spatial arrangement of the oligomer. For instance in the case as illustrated in Figure 5-13D the two FRET-rates experienced by the donor at position 1 and the donor at position 4 are given by:

$$\begin{aligned} k_{FRET}^{(1)} &= \frac{1}{\tau_0} \cdot \left(\left(\frac{R_{DA}^{(13)}}{R_0} \right)^6 + \left(\frac{R_{DA}^{(12)}}{R_0} \right)^6 \right) \\ k_{FRET}^{(4)} &= \frac{1}{\tau_0} \cdot \left(\left(\frac{R_{DA}^{(42)}}{R_0} \right)^6 + \left(\frac{R_{DA}^{(43)}}{R_0} \right)^6 \right) \end{aligned} \tag{5-25}$$

These FRET-rates result in first approximation in bi-exponential fluorescence decay, if the coupling between the two donors is not considered.

For a given structural arrangement all FRET-rate constants for all possible compositions (one donor one acceptor, two donors one acceptor, etc.) were calculated (Figure 5-13F). Later the average transfer efficiencies of the tetramer compositions containing at least one donor and one acceptor were calculated.

It has to be considered that the contribution to the fluorescence signal depends on the number of donor molecules. For instance a tetramer constituted out of three donors and one acceptor molecule contributes three times more to the total signal as compared to a tetramer only constituted out of one donor, one acceptor and two unlabeled molecules.

The predicted transfer efficiency for each data point depends now only on the equilibrium association constants K_1, K_2 and the spatial arrangement of the fluorophores in the dimer and the tetramer. To reduce the number of free parameters we assumed that the tetramer can be described by a rectangular geometry where one edge is approximately 100 Å long while the second edge is between 40-50 Å long (Figure 5-13F). This assumption is in line with the homology models (Table 5-4 and Figure 5-12). Furthermore, only FRET molecules have been selected. Therefore, the first equilibrium from monomer to dimer is not monitored and only the equilibrium constant of the tetramer formation is probed. Thus, only K_2 and the dimer distance in the range of 40-60 Å is reflected in the data. For the measurements we find that a short distance of approximately 45 Å describes the data best. For the TGR5 wt and Y111F variant we find predominately a tetrameric or higher-order oligomer configuration while in case of the Y111A mutant the molecules are predominately in a dimeric configuration.

Chapter 6 Conclusions

FRET imaging is the method of choice to study protein interactions in living cells. However, the poor pixel-wise photon statistics hinders detailed, correct and quantitative analysis models to be applied. Moreover, in FRET imaging experiments, donor and acceptor molecules are bulky fluorescent proteins, thus the well-established theory and analysis methods for *in vitro* single-molecule FRET experiments with organic dyes (Kalinin et al., 2012; Sisamakis et al., 2010) are not directly or not entirely applicable. The new global MFIS-FRET analysis workflow introduced in Chapter 2 solves these problems. The photon-integration procedure dramatically improves the photon statistics of MFIS-FRET experiments performed in living cells, so that the fluorescence decay data can reach the quality of traditional *in vitro* cuvette experiments, and be subjected to a thorough analysis. The methodology allows one to extract the maximal information embedded in FRET imaging data, such as protein concentration, structural and conformational features, protein-complex composition and binding affinities. Hence, the study in Chapter 2 enables a comprehensive molecular understanding of protein interactions in living cells.

The newly developed MFIS-FRET methodology was then employed in the study of the initial interaction-events that occurred at the level of the membrane-integrated receptors involved in the CLV and flg signaling pathways in plant cells (Chapter 3). To track the interaction state of receptors in cells following ligand infiltration in real-time, FRET images were recorded in a time series. In addition to the methodology shown in Chapter 2, the two-dimensional MFIS plot r - τ (fluorescence anisotropy – fluorescence lifetime) monitoring hetero- and homo-FRET states in an image (Stahl et al., 2013) is applied. The study reveals that the two pathways adopt different work principles in deploying their receptors for signal perception and transduction: flg22 first triggered receptor-like kinase heterodimerization, and later assembly into larger complexes through homomerization. In contrast, CLV receptor complexes were preformed, and ligand binding stimulated their clustering. These distinct behaviors of the two pathways can be ascribed to their different functions in plant cells.

A novel pattern-based pixel-integrated FRET analysis, in addition to the methodology shown in Chapter 2, is introduced and applied to study the oligomerization of mGBPs at membrane for *T. gondii* defense. This study reveals seminal information regarding: i) the physically separated subcellular reservoirs in which different mGBPs reside; ii) the molecular interactions and dynamics of mGBP2 with further family members (mGBP1, 3, 5, and 6) during *T.gondii* infection; iii) the enrichment of mGBPs at the parasitophorous vacuole membrane (PVM) after *T.gondii* infection, which is accompanied by depletion of vesicle-like structures (VLS); iv) the concentration-dependent structural transitions of mGBP2 from a monomeric, to dimeric and oligomeric state; and v) mGBPs assembly as supramolecular complexes at the parasitophorous vacuole.

MFIS-FRET experiments are performed on TGR5 wild type (wt), TGR5 Y111F and Y111A variants to investigate the structure, oligomerization pattern, and interaction affinities of TGR5 in human cells (Chapter 5). It shows that TGR5 wt and Y111F variant can form higher-order oligomers, but the inserted mutation at TM5 in the Y111A variant hinders the protein oligomerization, allowing only the formation of dimers. TGR5 Y111A dimerizes at an interface between transmembrane helix 1 (TM1) and helix 8 (H8), and

TGR5 wt and Y111F oligomers may still preserve such molecular organization of the TGR5 Y111A as dimer units. Therefore, TGR5 oligomers may consist of a linear arrangement of dimers, and TM5 has a central role in connecting these dimers into oligomers.

To summarize, with different applications in various biological systems (Chapter 3 - 5), this work demonstrates the unique advantages of MFIS-FRET and the new global-analysis workflow (Chapter 2). The methodology introduced in this work allows one to investigate the spatiotemporally regulated protein interactions at a molecular resolution level. Researchers now can efficiently study protein localization, dynamics, concentration, aggregation, protein-complex formation, stoichiometry and binding affinity, and generate a panorama of proteins of interest in living cells.

Acknowledgement

There are many people from whom I learned and *benefited* in these years, without their precious support this thesis would not have been possible. Thus I grateful acknowledge,

Prof. Dr. Claus Seidel who gave me the opportunity to use the state-of-art MFIS instrument and let me engage in very interesting projects that I can present in this thesis. Many thanks to the enthusiastic support during my Ph.D. research.

Prof. Dr. Rüdiger Simon for the long-lasting collaboration and the continuous support, for the useful discussions and the constructive criticism, for always reminding me that there is a life out there.

Prof. Dr. Klaus Pfeffer for the fruitful collaboration, for his intelligence and determination that expedited the publication of Chapter 4.

The International Helmholtz Research School of Biophysics and Soft Matter (IHRS BioSoft) for funding and especially the coordinator Dr. Thorsten Auth for always being helpful.

Dr. Stefanie Weidtkamp-Peters for the continuous support starting from the very beginning to the end in every way, for proofreading Chapter 1, Chapter 2 (cannot remember how many times) and Chapter 6 of this thesis.

Dr. Marc Somssich for bringing a lot of fun to the measurements in the dark and cold lab, for his great talent for cutting tobacco leafs into pieces, for proofreading this thesis, and for the two inspiring books he gave me but I have not put into practice yet.

Dr. Elisabeth Kravets for her hard work in the mGBP project, for her laughter she spread in our office every time she visited, for the tasty chocolates and the nice restaurants she recommended.

Thomas-Otavio Peulen for his great help in molecular simulation and data analysis, for sharing his innovative ideas and giving insightful comments, for the bike he gave me.

Dr. Suren Felekyan for giving me a comprehensive introduction of fluorescence spectroscopy when I first started, for continuously updating and improving the image analysis software that I used in this thesis.

Dr. Ralf Kühnemuth for the useful discussions, for sharing his knowledge in theory and in the lab, for being always available in the late night.

Dr. Annemarie Greife for her hard work in the TGR5 project and for proofreading Chapter 5.

Dr. Daniel Degrandi for the productive collaboration in the mGBP project.

Dr. Stephanie Grabowski for sharing her experience in experiments and data analysis.

Dr. Yvonne Stahl for sharing her expertise and excellent discussions.

Dr. Stanislav Kalinin for his MATLAB script of quantitative FRET analysis that I used during this study.

Peter for sharing an office with me for almost six years, for sharing his experience in the lab, for his daily snack supply, the pizza ordering service, the liquor ordering email list that I want to unsubscribe, and many practical jokes.

Deborah for being an amazing officemate, for the Italian snacks she brought from time to time, for the last bite of Tiramisu in a Christmas party, and for the practical travel guide she prepared for my vacation in Rome.

Olga for the fun we had in every lunch break and coffee break, for the fantastic salad that I cannot stop eating, for the medicine she kindly took together with me when I was sick, which is, of course, vodka.

Aiswaria Prakash for proofreading Chapter 2.

The whole Seidel group, for always being friendly and supportive.

Lastly, I would like to thank my parents and my elder brother for their love and support. I am extremely lucky to have them in my life.

References

Aebersold, R., and Mann, M. (2003). Mass spectrometry-based proteomics. Nature *422*, 198–207.

Akrap, N., Seidel, T., and Barisas, B.G. (2010). Förster distances for fluorescence resonant energy transfer between mCherry and other visible fluorescent proteins. Anal. Biochem. *402*, 105–106.

Albertazzi, L., Arosio, D., Marchetti, L., Ricci, F., and Beltram, F. (2009). Quantitative FRET analysis with the EGFP-mCherry fluorescent protein pair. Photochem. Photobiol. *85*, 287–297.

Albrecht, C., Boutrot, F., Segonzac, C., Schwessinger, B., Gimenez-Ibanez, S., Chinchilla, D., Rathjen, J.P., de Vries, S.C., and Zipfel, C. (2012). Brassinosteroids inhibit pathogen-associated molecular pattern-triggered immune signaling independent of the receptor kinase BAK1. Proc. Natl. Acad. Sci. *109*, 303–308.

Ali, G.S., Prasad, K.V.S.K., Day, I., and Reddy, A.S.N. (2007). Ligand-dependent reduction in the membrane mobility of FLAGELLIN SENSITIVE2, an arabidopsis receptor-like kinase. Plant Cell Physiol. *48*, 1601–1611.

Amaddii, M., Meister, M., Banning, A., Tomasovic, A., Mooz, J., Rajalingam, K., and Tikkanen, R. (2012). Flotillin-1/Reggie-2 protein plays dual role in activation of receptor-tyrosine kinase/mitogen-activated protein kinase signaling. J. Biol. Chem. *287*, 7265–7278.

Arpino, J.A.J., Rizkallah, P.J., and Jones, D.D. (2012). Crystal Structure of Enhanced Green Fluorescent Protein to 1.35 Å Resolution Reveals Alternative Conformations for Glu222. PLoS One *7*, e47132.

Auger, G.A., Pease, J.E., Shen, X., Xanthou, G., and Barker, M.D. (2002). Alanine scanning mutagenesis of CCR3 reveals that the three intracellular loops are essential for functional receptor expression. Eur. J. Immunol. *32*, 1052–1058.

Bacia, K., and Schwille, P. (2007). Practical guidelines for dual-color fluorescence cross-correlation spectroscopy. Nat. Protoc. *2*, 2842–2856.

Baker, N.A., Sept, D., Joseph, S., Holst, M.J., and McCammon, J.A. (2001). Electrostatics of nanosystems: Application to microtubules and the ribosome. Proc. Natl. Acad. Sci. *98*, 10037–10041.

Bas, D.C., Rogers, D.M., and Jensen, J.H. (2008). Very fast prediction and rationalization of pKa values for protein-ligand complexes. Proteins Struct. Funct. Bioinforma. *73*, 765–783.

Bayburt, T.H., Leitz, A.J., Xie, G., Oprian, D.D., and Sligar, S.G. (2007). Transducin Activation by Nanoscale Lipid Bilayers Containing One and Two Rhodopsins. J. Biol. Chem. *282*, 14875–14881.

Becker, W. (2005). Advanced Time-Correlated Single Photon Counting Techniques (Berlin, Heidelberg: Springer Berlin Heidelberg).

Betsuyaku, S., Takahashi, F., Kinoshita, A., Miwa, H., Shinozaki, K., Fukuda, H., and Sawa, S. (2011). Mitogen-activated protein kinase regulated by the CLAVATA receptors contributes to shoot apical meristem homeostasis. Plant Cell Physiol. *52*, 14–29.

Betzig, E., Patterson, G.H., Sougrat, R., Lindwasser, O.W., Olenych, S., Bonifacino, J.S., Davidson, M.W., Lippincott-Schwartz, J., and Hess, H.F. (2006). Imaging intracellular fluorescent proteins at nanometer resolution. Science *313*, 1642–1645.

Bleckmann, A., Weidtkamp-Peters, S., Seidel, C.A.M., and Simon, R. (2010). Stem cell signaling in Arabidopsis requires CRN to localize CLV2 to the plasma membrane. Plant Physiol. *152*, 166–176.

Blom, N., Gammeltoft, S., and Brunak, S. (1999). Sequence and structure-based prediction of eukaryotic protein phosphorylation sites. J. Mol. Biol. *294*, 1351–1362.

Blom, N., Sicheritz-Pontén, T., Gupta, R., Gammeltoft, S., and Brunak, S. (2004). Prediction of post-translational glycosylation and phosphorylation of proteins from the amino acid sequence. Proteomics *4*, 1633–1649.

Boersma, A.J., Zuhorn, I.S., and Poolman, B. (2015). A sensor for quantification of macromolecular crowding in living cells. Nat. Methods *12*, 227–229.

Bonomi, M., Pellarin, R., Kim, S.J., Russel, D., Sundin, B.A., Riffle, M., Jaschob, D., Ramsden, R., Davis, T.N., Muller, E.G.D., et al. (2014). Determining protein complex structures based on a Bayesian model of in vivo Förster resonance energy transfer (FRET) data. Mol. Cell. Proteomics *13*, 2812–2823.

Brand, U., Fletcher, J.C., Hobe, M., Meyerowitz, E.M., and Simon, R. (2000). Dependence of stem cell fate in Arabidopsis on a feedback loop regulated by CLV3 activity. Science *289*, 617–619.

Breitwieser, G.E. (2004). G protein-coupled receptor oligomerization: implications for G protein activation and cell signaling. Circ. Res. *94*, 17–27.

Britzen-Laurent, N., Bauer, M., Berton, V., Fischer, N., Syguda, A., Reipschläger, S., Naschberger, E., Herrmann, C., and Stürzl, M. (2010). Intracellular Trafficking of Guanylate-Binding Proteins Is Regulated by Heterodimerization in a Hierarchical Manner. PLoS One *5*, e14246.

Brown, C.M., Dalal, R.B., Hebert, B., Digman, M.A., Horwitz, A.R., and Gratton, E. (2008). Raster image correlation spectroscopy (RICS) for measuring fast protein dynamics and concentrations with a commercial laser scanning confocal microscope. J. Microsc. *229*, 78–91.

Bücherl, C. a, van Esse, G.W., Kruis, A., Luchtenberg, J., Westphal, A.H., Aker, J., van Hoek, A., Albrecht, C., Borst, J.W., and de Vries, S.C. (2013). Visualization of BRI1 and BAK1(SERK3) membrane receptor heterooligomers during brassinosteroid signaling. Plant Physiol. *162*, 1911–1925.

Calebiro, D., Rieken, F., Wagner, J., Sungkaworn, T., Zabel, U., Borzi, A., Cocucci, E., Zurn, A., and Lohse, M.J. (2013). Single-molecule analysis of fluorescently labeled G-protein-coupled receptors reveals complexes with distinct dynamics and organization. Proc. Natl. Acad. Sci. *110*, 743–748.

Campbell, R.E. (2009). Fluorescent-protein-based biosensors: modulation of energy transfer as a design principle. Anal. Chem. *81*, 5972–5979.

Cao, W., Tian, W., Hong, J., Li, D., Tavares, R., Noble, L., Moss, S.F., and Resnick, M.B. (2013). Expression of bile acid receptor TGR5 in gastric adenocarcinoma. AJP Gastrointest. Liver Physiol. *304*, G322–G327.

Capra, V., Veltri, A., Foglia, C., Crimaldi, L., Habib, A., Parenti, M., and Rovati, G.E. (2004). Mutational analysis of the highly conserved ERY motif of the thromboxane A(2) receptor: Alternative role in G protein-coupled receptor signaling. Mol. Pharmacol. *66*, 880–889.

Case, D.A., Cheatham, T.E., Darden, T., Gohlke, H., Luo, R., Merz, K.M., Onufriev, A., Simmerling, C., Wang, B., and Woods, R.J. (2005). The Amber biomolecular simulation programs. J. Comput. Chem. *26*, 1668–1688.

Case, D.A., Berryman, J.T., Betz, R.M., Cerutti, D.S., T.E. Cheatham, I., Darden, T.A., Duke, R.E., Giese, T.J., Gohlke, H., Goetz, A.W., et al. (2015). AMBER 15.

Chiang, J.J.-H., and Truong, K. (2006). Computational Modeling of a New Fluorescent Biosensor for Caspase Proteolytic Activity Improves Dynamic Range. IEEE Trans. Nanobioscience *5*, 41–45.

Chiang, J., Li, I., Pham, E., and Truong, K. (2006). FPMOD: a modeling tool for sampling the conformational space of fusion proteins. Conf. Proc. Annu. Int. Conf. IEEE Eng. Med. Biol. Soc. IEEE Eng. Med. Biol. Soc. Annu. Conf. *1*, 4111–4114.

Chinchilla, D., Zipfel, C., Robatzek, S., Kemmerling, B., Nürnberger, T., Jones, J.D.G., Felix, G., and Boller, T. (2007). A flagellin-induced complex of the receptor FLS2 and BAK1 initiates plant defence. Nature *448*, 497–500.

Choi, J., Park, S., Biering, S.B., Selleck, E., Liu, C.Y., Zhang, X., Fujita, N., Saitoh, T., Akira, S., Yoshimori, T., et al. (2014). The parasitophorous vacuole membrane of toxoplasma gondii is targeted for disruption by ubiquitin-like conjugation systems of autophagy. Immunity *40*, 924–935.

Choi, W.-T., Kumar, S., Madani, N., Han, X., Tian, S., Dong, C.-Z., Liu, D., Duggineni, S., Yuan, J., Sodroski, J.G., et al. (2012). A Novel Synthetic Bivalent Ligand To Probe Chemokine Receptor CXCR4 Dimerization and Inhibit HIV-1 Entry. Biochemistry *51*, 7078–7086.

Ciruela, F., Vilardaga, J.-P., and Fernández-Dueñas, V. (2010). Lighting up multiprotein complexes: lessons from GPCR oligomerization. Trends Biotechnol. *28*, 407–415.

Clark, S., Running, M., and Meyerowitz, E. (1995). CLAVATA3 is a specific regulator of shoot and floral meristem development affecting the same processes as CLAVATA1. Development *121*, 2057–2067.

Clark, S.E., Running, M.P., and Meyerowitz, E.M. (1993). CLAVATA1, a regulator of meristem and flower development in Arabidopsis. Development *119*, 397–418.

Clark, S.E., Williams, R.W., and Meyerowitz, E.M. (1997). The CLAVATA1 gene encodes a putative receptor kinase that controls shoot and floral meristem size in Arabidopsis. Cell *89*, 575–585.

Cubitt, A.B., Heim, R., Adams, S.R., Boyd, A.E., Gross, L.A., and Tsien, R.Y. (1995). Understanding, improving and using green fluorescent proteins. Trends Biochem. *20*, 448–455.

Curtis, M.D., and Grossniklaus, U. (2003). A gateway cloning vector set for high-throughput functional analysis of genes in planta. Plant Physiol. *133*, 462–469.

D’Amore, C., Di Leva, F.S., Sepe, V., Renga, B., Del Gaudio, C., D’Auria, M.V., Zampella, A., Fiorucci, S., and Limongelli, V. (2014). Design, Synthesis, and Biological Evaluation of Potent Dual Agonists of Nuclear and Membrane Bile Acid Receptors. J. Med. Chem. *57*, 937–954.

Darden, T., York, D., and Pedersen, L. (1993). Particle mesh Ewald: An Nlog(N) method for Ewald sums in large systems. J. Chem. Phys. *98*, 10089.

Decker, T., Stockinger, S., Karaghiosoff, M., Müller, M., and Kovarik, P. (2002). IFNs and STATs in innate immunity to microorganisms. J. Clin. Invest. *109*, 1271–1277.

Degrandi, D., Konermann, C., Beuter-Gunia, C., Kresse, A., Würthner, J., Kurig, S., Beer, S., and Pfeffer, K. (2007). Extensive characterization of IFN-induced GTPases mGBP1 to mGBP10 involved in host defense. J. Immunol. *179*, 7729–7740.

Degrandi, D., Kravets, E., Konermann, C., Beuter-Gunia, C., Klümpers, V., Lahme, S., Wischmann, E., Mausberg, A.K., Beer-Hammer, S., and Pfeffer, K. (2013). Murine guanylate binding protein 2 (mGBP2) controls Toxoplasma gondii replication. Proc. Natl. Acad. Sci. U. S. A. *110*, 294–299.

DeLano, W., and Lam, J. (2005). PyMOL: A communications tool for computational models. Am Chem S *230*, U1371–U1372.

Dickson, R.M., Cubitt, A.B., Tsien, R.Y., and Moerner, W.E. (1997). On/off blinking and switching behaviour of single molecules of green fluorescent protein. Nature *388*, 355–358.

Digman, M.A., Caiolfa, V.R., Zamai, M., and Gratton, E. (2008). The phasor approach to fluorescence lifetime imaging analysis. Biophys. J. *94*, L14–L16.

Dolinsky, T.J., Czodrowski, P., Li, H., Nielsen, J.E., Jensen, J.H., Klebe, G., and Baker, N.A. (2007). PDB2PQR: Expanding and upgrading automated preparation of biomolecular structures for molecular simulations. Nucleic Acids Res. *35*.

Drinkwater, N., Cossins, B.P., Keeble, A.H., Wright, M., Cain, K., Hailu, H., Oxbrow, A., Delgado, J., Shuttleworth, L.K., Kao, M.W.-P., et al. (2014). Human immunoglobulin E flexes between acutely bent and extended conformations. Nat. Struct. Mol. Biol. *21*, 397–404.

Duboc, H., Taché, Y., and Hofmann, A.F. (2014). The bile acid TGR5 membrane receptor: From basic research to clinical application. Dig. Liver Dis. *46*, 302–312.

Evers, T.H., Van Dongen, E.M.W.M., Faesen, A.C., Meijer, E.W., and Merkx, M. (2006).

Quantitative understanding of the energy transfer between fluorescent proteins connected via flexible peptide linkers. Biochemistry *45*, 13183–13192.

Ewald, S.E., Chavarria-Smith, J., and Boothroyd, J.C. (2014). NLRP1 is an inflammasome sensor for Toxoplasma gondii. Infect. Immun. *82*, 460–468.

Faelber, K., Posor, Y., Gao, S., Held, M., Roske, Y., Schulze, D., Haucke, V., Noé, F., and Daumke, O. (2011). Crystal structure of nucleotide-free dynamin. Nature *477*, 556–560.

Felix, G., Duran, J.D., Volko, S., and Boller, T. (1999). Plants have a sensitive perception system for the most conserved domain of bacterial flagellin. Plant J. *18*, 265–276.

Ferre, S., Casado, V., Devi, L.A., Filizola, M., Jockers, R., Lohse, M.J., Milligan, G., Pin, J.-P., and Guitart, X. (2014). G Protein-Coupled Receptor Oligomerization Revisited: Functional and Pharmacological Perspectives. Pharmacol. Rev. *66*, 413–434.

Filizola, M. (2010). Increasingly accurate dynamic molecular models of G-protein coupled receptor oligomers: Panacea or Pandora’s box for novel drug discovery? Life Sci. *86*, 590–597.

Filizola, M., and Weinstein, H. (2005). The study of G-protein coupled receptor oligomerization with computational modeling and bioinformatics. FEBS J. *272*, 2926–2938.

Fiser, A., and Sali, A. (2003). Modeller: generation and refinement of homology-based protein structure models. Methods Enzymol. *374*, 461–491.

Fletcher, J.C., Brand, U., Running, M.P., Simon, R., and Meyerowitz, E.M. (1999). Signaling of cell fate decisions by CLAVATA3 in Arabidopsis shoot meristems. Science *283*, 1911–1914.

Fogolari, F., and Tosatto, S.C.E. (2005). Application of MM/PBSA colony free energy to loop decoy discrimination: toward correlation between energy and root mean square deviation. Protein Sci. *14*, 889–901.

Förster, T. (1948). Zwischenmolekulare Energiewanderung und Fluoreszenz. Ann. Phys. *437*, 55–75.

Förster, T. (1949). Experimentelle und theoretische Untersuchung des zwischenmolekularen Übergangs von Elektronenanregungsenergie. Zeitschrift Für Naturforsch. *4a*, 321–327.

Fotiadis, D., Liang, Y., Filipek, S., Saperstein, D.A., Engel, A., and Palczewski, K. (2003). Atomic-force microscopy: Rhodopsin dimers in native disc membranes. Nature *421*, 127–128.

Gadella, T.W.J., Jovin, T.M., and Clegg, R.M. (1993). Fluorescence lifetime imaging microscopy (FLIM): Spatial resolution of microstructures on the nanosecond time scale. Biophys. Chem. *48*, 221–239.

Gautier, I., Tramier, M., Durieux, C., Coppey, J., Pansu, R.B., Nicolas, J.C., Kemnitz, K., and Coppey-Moisan, M. (2001). Homo-FRET microscopy in living cells to measure monomer-dimer transition of GFP-tagged proteins. Biophys. J. *80*, 3000–3008.

Gazzinelli, R.T., Mendonça-Neto, R., Lilue, J., Howard, J., and Sher, A. (2014). Innate resistance against Toxoplasma gondii: An evolutionary tale of mice, cats, and men. Cell Host Microbe *15*, 132–138.

Gertzen, C.G.W., Spomer, L., Smits, S.H.J., Häussinger, D., Keitel, V., and Gohlke, H. (2015). Mutational mapping of the transmembrane binding site of the G-protein coupled receptor TGR5 and binding mode prediction of TGR5 agonists. Eur. J. Med. Chem. *104*, 57–72.

Ghosh, A., Praefcke, G.J.K., Renault, L., Wittinghofer, A., and Herrmann, C. (2006). How guanylate-binding proteins achieve assembly-stimulated processive cleavage of GTP to GMP. Nature *440*, 101–104.

Giepmans, B.N.G., Adams, S.R., Ellisman, M.H., and Tsien, R.Y. (2006). The fluorescent toolbox for assessing protein location and function. Science *312*, 217–224.

Gish, L.A., Gagne, J.M., Han, L., DeYoung, B.J., and Clark, S.E. (2013). WUSCHEL-Responsive At5g65480 Interacts with CLAVATA Components In Vitro and in Transient Expression. PLoS One *8*.

Gohlke, H., and Case, D.A. (2004). Converging free energy estimates: MM-PB(GB)SA studies on the protein-protein complex Ras-Raf. J. Comput. Chem. *25*, 238–250.

Goldman, R.D., Spector, D.L., and Swedlund, A.C. (2010). Live Cell Imaging: A Laboratory Manual, 2nd Edition (Cold Spring Harbor Laboratory Press, Cold Spring Harbor, NY).

Gómez-Gómez, L., and Boller, T. (2000). FLS2: an LRR receptor-like kinase involved in the perception of the bacterial elicitor flagellin in Arabidopsis. Mol. Cell *5*, 1003–1011.

Gorfu, G., Cirelli, K.M., Melo, M.B., Mayer-Barber, K., Crown, D., Koller, B.H., Masters, S., Sher, A., Leppla, S.H., Moayeri, M., et al. (2014). Dual Role for Inflammasome Sensors NLRP1 and NLRP3 in Murine Resistance to Toxoplasma gondii. MBio *5*, e01117–13 – e01117–13.

Grosberg, A.Y., and Khokhlov, A.R. (1994). Statistical physics of macromolecules (Woodbury, NY, USA: AIP Press).

Grotjohann, T., Testa, I., Leutenegger, M., Bock, H., Urban, N.T., Lavoie-Cardinal, F., Willig, K.I., Eggeling, C., Jakobs, S., and Hell, S.W. (2011). Diffraction-unlimited all-optical imaging and writing with a photochromic GFP. Nature *478*, 204–208.

Grünberg, R., Burnier, J. V, Ferrar, T., Beltran-Sastre, V., Stricher, F., van der Sloot, A.M., Garcia-Olivas, R., Mallabiabarrena, A., Sanjuan, X., Zimmermann, T., et al. (2013). Engineering of weak helper interactions for high-efficiency FRET probes. Nat. Methods *10*, 1021–1027.

Guo, Y., Han, L., Hymes, M., Denver, R., and Clark, S.E. (2010). CLAVATA2 forms a distinct CLE-binding receptor complex regulating Arabidopsis stem cell specification. Plant J. *63*, 889–900.

Gurevich, V. V, and Gurevich, E. V (2008). GPCR monomers and oligomers: it takes all kinds. Trends Neurosci. *31*, 74–81.

Ha, T., Ting, a Y., Liang, J., Caldwell, W.B., Deniz, a a, Chemla, D.S., Schultz, P.G., and Weiss, S. (1999). Single-molecule fluorescence spectroscopy of enzyme conformational dynamics and cleavage mechanism. Proc. Natl. Acad. Sci. U. S. A. *96*, 893–898.

Haldar, A.K., Saka, H.A., Piro, A.S., Da Dunn, J., Henry, S.C., Taylor, G.A., Frickel, E.M., Valdivia, R.H., and Coers, J. (2013). IRG and GBP Host Resistance Factors Target Aberrant, “Non-self” Vacuoles Characterized by the Missing of “Self” IRGM Proteins. PLoS Pathog. *9*.

Haldar, A.K., Piro, A.S., Pilla, D.M., Yamamoto, M., and Coers, J. (2014). The E2-like conjugation enzyme Atg3 promotes binding of IRG and Gbp proteins to Chlamydia- and Toxoplasma- containing vacuoles and host resistance. PLoS One *9*.

Haldar, A.K., Foltz, C., Finethy, R., Piro, A.S., Feeley, E.M., Pilla-Moffett, D.M., Komatsu, M., Frickel, E.-M., and Coers, J. (2015). Ubiquitin systems mark pathogen-containing vacuoles as targets for host defense by guanylate binding proteins. Proc. Natl. Acad. Sci. *112*, E5628–E5637.

Hanson, M.A., Roth, C.B., Jo, E., Griffith, M.T., Scott, F.L., Reinhart, G., Desale, H., Clemons, B., Cahalan, S.M., Schuerer, S.C., et al. (2012). Crystal structure of a lipid G protein-coupled receptor. Science *335*, 851–855.

Heikal, A. a., Hess, S.T., and Webb, W.W. (2001). Multiphoton molecular spectroscopy and excited-state dynamics of enhanced green fluorescent protein (EGFP): Acid-base specificity. Chem. Phys. *274*, 37–55.

Hein, P., Frank, M., Hoffmann, C., Lohse, M.J., and Bünemann, M. (2005). Dynamics of receptor/G protein coupling in living cells. EMBO J. *24*, 4106–4114.

Hell, S.W., and Wichmann, J. (1994). Breaking the diffraction resolution limit by stimulated emission: stimulated-emission-depletion fluorescence microscopy. Opt. Lett. *19*, 780.

Hoi, H., Ding, Y., Campbell, R.E., Algar, W.R., Massey, M., Krull, U.J., van der Meer, B.W., Claussen, J.C., Hildebrandt, N., Medintz, I., et al. (2013). FRET - Förster Resonance Energy Transfer (Weinheim, Germany: Wiley-VCH Verlag GmbH & Co. KGaA).

Homeyer, N., and Gohlke, H. (2013). FEW: A workflow tool for free energy calculations of ligand binding. J. Comput. Chem. *34*, 965–973.

Homeyer, N., and Gohlke, H. (2015). Extension of the free energy workflow FEW towards implicit solvent/implicit membrane MM–PBSA calculations. Biochim. Biophys. Acta *1850*, 972–982.

Hov, J.R., Keitel, V., Laerdahl, J.K., Spomer, L., Ellinghaus, E., ElSharawy, A., Melum, E., Boberg, K.M., Manke, T., Balschun, T., et al. (2010). Mutational Characterization of the Bile Acid Receptor TGR5 in Primary Sclerosing Cholangitis. PLoS One *5*, e12403.

Huang, J., Chen, S., Zhang, J.J., and Huang, X.-Y. (2013). Crystal structure of oligomeric β1-adrenergic G protein–coupled receptors in ligand-free basal state. Nat.

Struct. Mol. Biol. *20*, 419–425.

Hunt, J., Keeble, A.H., Dale, R.E., Corbett, M.K., Beavil, R.L., Levitt, J., Swann, M.J., Suhling, K., Ameer-Beg, S., Sutton, B.J., et al. (2012). A fluorescent biosensor reveals conformational changes in human immunoglobulin E Fc: implications for mechanisms of receptor binding, inhibition, and allergen recognition. J. Biol. Chem. *287*, 17459–17470.

Jaakola, V.-P., Griffith, M.T., Hanson, M.A., Cherezov, V., Chien, E.Y.T., Lane, J.R., Ijzerman, A.P., and Stevens, R.C. (2008). The 2.6 angstrom crystal structure of a human A2A adenosine receptor bound to an antagonist. Science *322*, 1211–1217.

Jares-Erijman, E.A., and Jovin, T.M. (2003). FRET imaging. Nat. Biotechnol. *21*, 1387–1395.

Jensen, D.D., Godfrey, C.B., Niklas, C., Canals, M., Kocan, M., Poole, D.P., Murphy, J.E., Alemi, F., Cottrell, G.S., Korbmacher, C., et al. (2013). The bile acid receptor TGR5 does not interact with β-arrestins or traffic to endosomes but transmits sustained signals from plasma membrane rafts. J. Biol. Chem. *288*, 22942–22960.

Jo, S., Lim, J.B., Klauda, J.B., and Im, W. (2009). CHARMM-GUI Membrane Builder for Mixed Bilayers and Its Application to Yeast Membranes. Biophys. J. *97*, 50–58.

Johnston, J.M., Wang, H., Provasi, D., and Filizola, M. (2012). Assessing the Relative Stability of Dimer Interfaces in G Protein-Coupled Receptors. PLoS Comput. Biol. *8*, e1002649.

Jorgensen, W.L., Chandrasekhar, J., Madura, J.D., Impey, R.W., and Klein, M.L. (1983). Comparison of simple potential functions for simulating liquid water. J. Chem. Phys. *79*, 926.

Jung, G., Wiehler, J., and Zumbusch, A. (2005). The photophysics of green fluorescent protein: influence of the key amino acids at positions 65, 203, and 222. Biophys. J. *88*, 1932–1947.

Kaczor, A.A., Selent, J., and Poso, A. (2013). Structure-based molecular modeling approaches to GPCR oligomerization. Methods Cell Biol. *117*, 91–104.

Kalinin, S., Peulen, T., Sindbert, S., Rothwell, P.J., Berger, S., Restle, T., Goody, R.S., Gohlke, H., and Seidel, C. a M. (2012). A toolkit and benchmark study for FRET-restrained high-precision structural modeling. Nat. Methods *9*, 1218–1225.

Karnik, S.S. (2002). Analysis of structure-function from expression of G protein-coupled receptor fragments. In G Protein Pathways, Pt A, Receptors, pp. 248–259.

Karpova, T.S., Baumann, C.T., He, L., Wu, X., Grammer, A., Lipsky, P., Hager, G.L., and McNally, J.G. (2003). Fluorescence resonance energy transfer from cyan to yellow fluorescent protein detected by acceptor photobleaching using confocal microscopy and a single laser. J. Microsc. *209*, 56–70.

Kask, P., Palo, K., Fay, N., Brand, L., Mets, Ü., Ullmann, D., Jungmann, J., Pschorr, J., and Gall, K. (2000). Two-Dimensional Fluorescence Intensity Distribution Analysis: Theory and Applications. Biophys. J. *78*, 1703–1713.

Kawamata, Y., Fujii, R., Hosoya, M., Harada, M., Yoshida, H., Miwa, M., Fukusumi, S., Habata, Y., Itoh, T., Shintani, Y., et al. (2003). A G protein-coupled receptor responsive to bile acids. J. Biol. Chem. *278*, 9435–9440.

Kayes, J.M., and Clark, S.E. (1998). CLAVATA2, a regulator of meristem and organ development in Arabidopsis. Development *125*, 3843–3851.

Keitel, V., and Häussinger, D. (2012). Perspective: TGR5 (Gpbar-1) in liver physiology and disease. Clin. Res. Hepatol. Gastroenterol. *36*, 412–419.

Keitel, V., Cupisti, K., Ullmer, C., Knoefel, W.T., Kubitz, R., and Häussinger, D. (2009). The membrane-bound bile acid receptor TGR5 is localized in the epithelium of human gallbladders. Hepatology *50*, 861–870.

King, C., Sarabipour, S., Byrne, P., Leahy, D.J., and Hristova, K. (2014). The FRET signatures of noninteracting proteins in membranes: simulations and experiments. Biophys. J. *106*, 1309–1317.

Köllner, M., and Wolfrum, J. (1992). How many photons are necessary for fluorescence-lifetime measurements? Chem. Phys. Lett. *200*, 199–204.

Koshioka, M., Sasaki, K., and Masuhara, H. (1995). Time-Dependent Fluorescence Depolarization Analysis in Three-Dimensional Microspectroscopy. Appl. Spectrosc. *49*, 224–228.

Kozer, N., Barua, D., Orchard, S., Nice, E.C., Burgess, A.W., Hlavacek, W.S., and Clayton, A.H. a (2013). Exploring higher-order EGFR oligomerisation and phosphorylation--a combined experimental and theoretical approach. Mol. Biosyst. *9*, 1849–1863.

Kravets, E., Degrandi, D., Weidtkamp-Peters, S., Ries, B., Konermann, C., Felekyan, S., Dargazanli, J.M., Praefcke, G.J.K., Seidel, C.A.M., Schmitt, L., et al. (2012). The GTPase activity of murine guanylate-binding protein 2 (mGBP2) controls the intracellular localization and recruitment to the parasitophorous vacuole of Toxoplasma gondii. J. Biol. Chem. *287*, 27452–27466.

Kresse, A., Konermann, C., Degrandi, D., Beuter-Gunia, C., Wuerthner, J., Pfeffer, K., and Beer, S. (2008). Analyses of murine GBP homology clusters based on in silico, in vitro and in vivo studies. BMC Genomics *9*, 158.

Kudryavtsev, V., Felekyan, S., Woźniak, A.K., König, M., Sandhagen, C., Kühnemuth, R., Seidel, C.A.M., and Oesterhelt, F. (2006). Monitoring dynamic systems with multiparameter fluorescence imaging. Anal. Bioanal. Chem. *387*, 71–82.

Kudryavtsev, V., Sikor, M., Kalinin, S., Mokranjac, D., Seidel, C.A.M., and Lamb, D.C. (2012). Combining MFD and PIE for accurate single-pair Förster resonance energy transfer measurements. Chemphyschem *13*, 1060–1078.

Kuszak, A.J., Pitchiaya, S., Anand, J.P., Mosberg, H.I., Walter, N.G., and Sunahara, R.K. (2009). Purification and functional reconstitution of monomeric mu-opioid receptors: allosteric modulation of agonist binding by Gi2. J. Biol. Chem. *284*, 26732–26741.

Lagerström, M.C., and Schiöth, H.B. (2008). Structural diversity of G protein-coupled receptors and significance for drug discovery. Nat. Rev. Drug Discov. *7*, 339–357.

Lakowicz, J.R. (2006). Principles of fluorescence spectroscopy, 3rd Edition (Springer).

Laptenok, S.P., Snellenburg, J.J., Bücherl, C.A., Konrad, K.R., and Borst, J.W. (2014). Global analysis of FRET-FLIM data in live plant cells. Methods Mol. Biol. *1076*, 481–502.

Lasker, K., Phillips, J.L., Russel, D., Velazquez-Muriel, J., Schneidman-Duhovny, D., Tjioe, E., Webb, B., Schlessinger, A., and Sali, A. (2010). Integrative Structure Modeling of Macromolecular Assemblies from Proteomics Data. Mol. Cell. Proteomics *9*, 1689–1702.

Li, J., Wen, J., Lease, K.A., Doke, J.T., Tax, F.E., and Walker, J.C. (2002). BAK1, an Arabidopsis LRR Receptor-like Protein Kinase, Interacts with BRI1 and Modulates Brassinosteroid Signaling. Cell *110*, 213–222.

Li, J., Abel, R., Zhu, K., Cao, Y., Zhao, S., and Friesner, R.A. (2011). The VSGB 2.0 model: A next generation energy model for high resolution protein structure modeling. Proteins Struct. Funct. Bioinforma. *79*, 2794–2812.

Liedberg, B., Nylander, C., and Lunström, I. (1983). Surface plasmon resonance for gas detection and biosensing. Sensors and Actuators *4*, 299–304.

Ling, Y.M., Shaw, M.H., Ayala, C., Coppens, I., Taylor, G.A., Ferguson, D.J.P., and Yap, G.S. (2006). Vacuolar and plasma membrane stripping and autophagic elimination of Toxoplasma gondii in primed effector macrophages. J. Cell Biol. *174*, 2063–2071.

Lomize, M.A., Lomize, A.L., Pogozheva, I.D., and Mosberg, H.I. (2006). OPM: Orientations of Proteins in Membranes database. Bioinformatics *22*, 623–625.

Ma, L., Huang, Y.Z., Pitcher, G.M., Valtschanoff, J.G., Ma, Y.H., Feng, L.Y., Lu, B., Xiong, W.C., Salter, M.W., Weinberg, R.J., et al. (2003). Ligand-dependent recruitment of the ErbB4 signaling complex into neuronal lipid rafts. J. Neurosci. *23*, 3164–3175.

MacBeath, G., and Schreiber, S.L. (2000). Printing proteins as microarrays for high-throughput function determination. Science *289*, 1760–1763.

Macchiarulo, A., Gioiello, A., Thomas, C., Pols, T.W.H., Nuti, R., Ferrari, C., Giacchè, N., De Franco, F., Pruzanski, M., Auwerx, J., et al. (2013). Probing the Binding Site of Bile Acids in TGR5. ACS Med. Chem. Lett. *4*, 1158–1162.

MacMicking, J.D. (2012). Interferon-inducible effector mechanisms in cell-autonomous immunity. Nat. Rev. Immunol. *12*, 367–382.

Maestro (2014). Version 9.9.013.

Man, S.M., Karki, R., Malireddi, R.K.S., Neale, G., Vogel, P., Yamamoto, M., Lamkanfi, M., and Kanneganti, T. (2015). The transcription factor IRF1 and guanylate-binding proteins target activation of the AIM2 inflammasome by Francisella infection. Nat. Immunol. *16*, 467–475.

Manglik, A., Kruse, A.C., Kobilka, T.S., Thian, F.S., Mathiesen, J.M., Sunahara, R.K., Pardo, L., Weis, W.I., Kobilka, B.K., and Granier, S. (2012). Crystal structure of the µ-opioid receptor bound to a morphinan antagonist. Nature *485*, 321–326.

Martens, S., Parvanova, I., Zerrahn, J., Griffiths, G., Schell, G., Reichmann, G., and Howard, J.C. (2005). Disruption of Toxoplasma gondii parasitophorous vacuoles by the mouse p47-resistance GTPases. PLoS Pathog. *1*, 0187–0201.

Maurel, D., Comps-Agrar, L., Brock, C., Rives, M.-L., Bourrier, E., Ayoub, M.A., Bazin, H., Tinel, N., Durroux, T., Prézeau, L., et al. (2008). Cell-surface protein-protein interaction analysis with time-resolved FRET and snap-tag technologies: application to GPCR oligomerization. Nat. Methods *5*, 561–567.

Maus, M., Cotlet, M., Hofkens, J., Gensch, T., De Schryver, F.C., Schaffer, J., and Seidel, C.A.M. (2001). An Experimental Comparison of the Maximum Likelihood Estimation and Nonlinear Least-Squares Fluorescence Lifetime Analysis of Single Molecules. Anal. Chem. *73*, 2078–2086.

Mayer, K.F.., Schoof, H., Haecker, A., Lenhard, M., Jürgens, G., and Laux, T. (1998). Role of WUSCHEL in Regulating Stem Cell Fate in the Arabidopsis Shoot Meristem. Cell *95*, 805–815.

van der Meer, B.W., Raymer, M.A., Wagoner, S.L., Hackney, R.L., Beechem, J.M., and Gratton, E. (1993). Designing matrix models for fluorescence energy transfer between moving donors and acceptors. Biophys. J. *64*, 1243–1263.

Melzer, T., Duffy, A., Weiss, L.M., and Halonen, S.K. (2008). The gamma interferon (IFN-??)-inducible GTP-binding protein IGTP is necessary for Toxoplasma vacuolar disruption and induces parasite egression in IFN-??-stimulated astrocytes. Infect. Immun. *76*, 4883–4894.

Meunier, E., Dick, M.S., Dreier, R.F., Schürmann, N., Broz, D.K., Warming, S., Roose-Girma, M., Bumann, D., Kayagaki, N., Takeda, K., et al. (2014). Caspase-11 activation requires lysis of pathogen-containing vacuoles by IFN-induced GTPases. Nature *509*, 366–370.

Meunier, E., Wallet, P., Dreier, R.F., Costanzo, S., Anton, L., Rühl, S., Dussurgey, S., Dick, M.S., Kistner, A., Rigard, M., et al. (2015). Guanylate-binding proteins promote activation of the AIM2 inflammasome during infection with Francisella novicida. Nat. Immunol. *16*, 476–484.

Millington, M., Grindlay, G.J., Altenbach, K., Neely, R.K., Kolch, W., Bencina, M., Read, N.D., Jones, A.C., Dryden, D.T.F., and Magennis, S.W. (2007). High-precision FLIM-FRET in fixed and living cells reveals heterogeneity in a simple CFP-YFP fusion protein. Biophys. Chem. *127*, 155–164.

Miranda, P., Contreras, J.E., Plested, A.J.R., Sigworth, F.J., Holmgren, M., and Giraldez, T. (2013). State-dependent FRET reports calcium- and voltage-dependent gating-ring motions in BK channels. Proc. Natl. Acad. Sci. U. S. A. *110*, 5217–5222.

Moens, P.D.J., Gratton, E., and Salvemini, I.L. (2010). Fluorescence correlation spectroscopy, raster image correlation spectroscopy, and number and brightness on a commercial confocal laser scanning microscope with analog detectors (Nikon C1). Microsc. Res. Tech. *74*, n/a – n/a.

Moreira, I.S. (2014). Structural features of the G-protein/GPCR interactions. Biochim. Biophys. Acta - Gen. Subj. *1840*, 16–33.

Müller, R., Bleckmann, A., and Simon, R. (2008). The receptor kinase CORYNE of

Arabidopsis transmits the stem cell-limiting signal CLAVATA3 independently of CLAVATA1. Plant Cell *20*, 934–946.

Nguyen, T.A., Sarkar, P., Veetil, J. V, Koushik, S. V, and Vogel, S.S. (2012). Fluorescence polarization and fluctuation analysis monitors subunit proximity, stoichiometry, and protein complex hydrodynamics. PLoS One *7*, e38209.

Nimchuk, Z.L., Tarr, P.T., and Meyerowitz, E.M. (2011). An evolutionarily conserved pseudokinase mediates stem cell production in plants. Plant Cell *23*, 851–854.

Ntoukakis, V., Schwessinger, B., Segonzac, C., and Zipfel, C. (2011). Cautionary Notes on the Use of C-Terminal BAK1 Fusion Proteins for Functional Studies. Plant Cell *23*, 3871–3878.

Nymeyer, H., and Zhou, H.-X. (2008). A method to determine dielectric constants in nonhomogeneous systems: application to biological membranes. Biophys. J. *94*, 1185–1193.

Ogawa, M., Shinohara, H., Sakagami, Y., and Matsubayashi, Y. (2008). Arabidopsis CLV3 Peptide Directly Binds CLV1 Ectodomain. Science (80-.). *319*, 294–294.

Ohshima, J., Lee, Y., Sasai, M., Saitoh, T., Su Ma, J., Kamiyama, N., Matsuura, Y., Pann-Ghill, S., Hayashi, M., Ebisu, S., et al. (2014). Role of mouse and human autophagy proteins in IFN-γ-induced cell-autonomous responses against Toxoplasma gondii. J. Immunol. *192*, 3328–3335.

Ohyama, K., Shinohara, H., Ogawa-Ohnishi, M., and Matsubayashi, Y. (2009). A glycopeptide regulating stem cell fate in Arabidopsis thaliana. Nat. Chem. Biol. *5*, 578–580.

Olszewski, M.A., Gray, J., and Vestal, D.J. (2006). In silico genomic analysis of the human and murine guanylate-binding protein (GBP) gene clusters. J. Interferon Cytokine Res. *26*, 328–352.

Overington, J.P., Al-Lazikani, B., and Hopkins, A.L. (2006). How many drug targets are there? Nat. Rev. Drug Discov. *5*, 993–996.

Palczewski, K., Kumasaka, T., Hori, T., Behnke, C.A., Motoshima, H., Fox, B.A., Le Trong, I., Teller, D.C., Okada, T., Stenkamp, R.E., et al. (2000). Crystal structure of rhodopsin: A G protein-coupled receptor. Science *289*, 739–745.

Park, P.S.-H., Filipek, S., Wells, J.W., and Palczewski, K. (2004). Oligomerization of G Protein-Coupled Receptors: Past, Present, and Future †. Biochemistry *43*, 15643–15656.

Parker, M.S., Park, E.A., Sallee, F.R., and Parker, S.L. (2011). Two intracellular helices of G-protein coupling receptors could generally support oligomerization and coupling with transducers. Amino Acids *40*, 261–268.

Patowary, S., Alvarez-Curto, E., Xu, T.-R., Holz, J.D., Oliver, J.A., Milligan, G., and Raicu, V. (2013). The muscarinic M 3 acetylcholine receptor exists as two differently sized complexes at the plasma membrane. Biochem. J. *452*, 303–312.

Perrin, F. (1929). Fluorescence of solutions. Ann. Phys. (Paris). *12*, 169–275.

Pfleger, K.D.G., and Eidne, K.A. (2005). Monitoring the formation of dynamic G-protein-coupled receptor–protein complexes in living cells. Biochem. J. *385*, 625–637.

Pham, E., Chiang, J., Li, I., Shum, W., and Truong, K. (2007). A computational tool for designing FRET protein biosensors by rigid-body sampling of their conformational space. Structure *15*, 515–523.

Pilla, D.M., Hagar, J. a, Haldar, A.K., Mason, A.K., Degrandi, D., Pfeffer, K., Ernst, R.K., Yamamoto, M., Miao, E. a, and Coers, J. (2014). Guanylate binding proteins promote caspase-11-dependent pyroptosis in response to cytoplasmic LPS. Proc. Natl. Acad. Sci. U. S. A. *111*, 6046–6051.

Piston, D.W., and Kremers, G.-J. (2007). Fluorescent protein FRET: the good, the bad and the ugly. Trends Biochem. Sci. *32*, 407–414.

Praefcke, G.J.K., and McMahon, H.T. (2004). The dynamin superfamily: universal membrane tubulation and fission molecules? Nat. Rev. Mol. Cell Biol. *5*, 133–147.

Prakash, B., Renault, L., Praefcke, G.J., Herrmann, C., and Wittinghofer, A. (2000). Triphosphate structure of guanylate-binding protein 1 and implications for nucleotide binding and GTPase mechanism. EMBO J. *19*, 4555–4564.

Prasher, D.C., Eckenrode, V.K., Ward, W.W., Prendergast, F.G., and Cormier, M.J. (1992). Primary structure of the Aequorea victoria green-fluorescent protein. Gene *111*, 229–233.

Qi, Y., Tsuda, K., Nguyen, L. V., Wang, X., Lin, J., Murphy, A.S., Glazebrook, J., Thordal-Christensen, H., and Katagiri, F. (2011). Physical association of Arabidopsis Hypersensitive Induced Reaction proteins (HIRs) with the immune receptor RPS2. J. Biol. Chem. *286*, 31297–31307.

Rice, S., Lin, A.W., Safer, D., Hart, C.L., Naber, N., Carragher, B.O., Cain, S.M., Pechatnikova, E., Wilson-Kubalek, E.M., Whittaker, M., et al. (1999). A structural change in the kinesin motor protein that drives motility. Nature *402*, 778–784.

Ridders, C. (1979). A new algorithm for computing a single root of a real continuous function. IEEE Trans. Circuits Syst. *26*, 979–980.

Robatzek, S., Chinchilla, D., and Boller, T. (2006). Ligand-induced endocytosis of the pattern recognition receptor FLS2 in Arabidopsis. Genes Dev. *20*, 537–542.

Rothwell, P.J., Berger, S., Kensch, O., Felekyan, S., Antonik, M., Wöhrl, B.M., Restle, T., Goody, R.S., and Seidel, C. a M. (2003). Multiparameter single-molecule fluorescence spectroscopy reveals heterogeneity of HIV-1 reverse transcriptase:primer/template complexes. Proc. Natl. Acad. Sci. U. S. A. *100*, 1655–1660.

Rovati, G.E., Capra, V., and Neubig, R.R. (2007). The Highly Conserved DRY Motif of Class A G Protein-Coupled Receptors: Beyond the Ground State. Mol. Pharmacol. *71*, 959–964.

Rust, M.J., Bates, M., and Zhuang, X. (2006). Sub-diffraction-limit imaging by stochastic optical reconstruction microscopy (STORM). Nat. Methods *3*, 793–795.

Ryckaert, J.-P., Ciccotti, G., and Berendsen, H.J.. (1977). Numerical integration of the cartesian equations of motion of a system with constraints: molecular dynamics of nalkanes. J. Comput. Phys. *23*, 327–341.

Sahoo, H., and Schwille, P. (2011). FRET and FCS--friends or foes? Chemphyschem *12*, 532–541.

Salom, D., Lodowski, D.T., Stenkamp, R.E., Trong, I.L., Golczak, M., Jastrzebska, B., Harris, T., Ballesteros, J.A., and Palczewski, K. (2006). Crystal structure of a photoactivated deprotonated intermediate of rhodopsin. Proc. Natl. Acad. Sci. *103*, 16123–16128.

Schaffer, J., Volkmer, A., Eggeling, C., Subramaniam, V., Striker, G., and Seidel, C. a M. (1999). Identification of Single Molecules in Aqueous Solution by Time-Resolved Fluorescence Anisotropy. J. Phys. Chem. A *103*, 331–336.

Schrödinger, L. (2010). The PyMOL molecular graphics system, version 1.3 r1. Py-MOL, The PyMOL Molecular Graphics System, Version 2010.

Schuler, B., and Eaton, W. a. (2008). Protein folding studied by single-molecule FRET. Curr. Opin. Struct. Biol. *18*, 16–26.

Schulze, B., Mentzel, T., Jehle, A.K., Mueller, K., Beeler, S., Boller, T., Felix, G., and Chinchilla, D. (2010). Rapid Heteromerization and Phosphorylation of Ligand-activated Plant Transmembrane Receptors and Their Associated Kinase BAK1. J. Biol. Chem. *285*, 9444–9451.

Selleck, E.M., Fentress, S.J., Beatty, W.L., Degrandi, D., Pfeffer, K., Virgin, H.W., MacMicking, J.D., and Sibley, L.D. (2013). Guanylate-binding Protein 1 (Gbp1) Contributes to Cell-autonomous Immunity against Toxoplasma gondii. PLoS Pathog. *9*, e1003320.

Shaner, N.C., Steinbach, P. a, and Tsien, R.Y. (2005). A guide to choosing fluorescent proteins. Nat. Methods *2*, 905–909.

Shanno, D.F., and Kettler, P.C. (1970). Optimal conditioning of quasi-Newton methods. Math. Comp. *24*, 657–664.

Shimomura, O., Johnson, F.H., and Saiga, Y. (1962). Extraction, Purification and Properties of Aequorin, a Bioluminescent Protein from the Luminous Hydromedusan,Aequorea. J. Cell. Comp. Physiol. *59*, 223–239.

Shinohara, H., and Matsubayashi, Y. (2015). Reevaluation of the CLV3-receptor interaction in the shoot apical meristem: dissection of the CLV3 signaling pathway from a direct ligand-binding point of view. Plant J. *82*, 328–336.

Simons, K., and Toomre, D. (2000). No Title. Nat. Rev. Mol. Cell Biol. *1*, 31–39.

Simpson, L.M., Taddese, B., Wall, I.D., and Reynolds, C.A. (2010). Bioinformatics and molecular modelling approaches to GPCR oligomerization. Curr. Opin. Pharmacol. *10*, 30–37.

Sindbert, S., Kalinin, S., Nguyen, H., Kienzler, A., Clima, L., Bannwarth, W., Appel, B., Müller, S., and Seidel, C.A.M. (2011). Accurate Distance Determination of Nucleic Acids via Förster Resonance Energy Transfer: Implications of Dye Linker Length and Rigidity. J. Am. Chem. Soc. *133*, 2463–2480.

Sindhu, T., and Srinivasan, P. (2015). Exploring the binding properties of agonists interacting with human TGR5 using structural modeling, molecular docking and dynamics simulations. RSC Adv. *5*, 14202–14213.

Sisamakis, E., Valeri, A., Kalinin, S., Rothwell, P.J., and Seidel, C.A.M. (2010). Accurate Single-Molecule FRET Studies Using Multiparameter Fluorescence Detection. In Methods in Enzymology, pp. 455–514.

Somssich, M., Ma, Q., Weidtkamp-Peters, S., Stahl, Y., Felekyan, S., Bleckmann, A., Seidel, C.A.M., and Simon, R. (2015). Real-time dynamics of peptide ligand-dependent receptor complex formation in planta. Sci. Signal. *8*, ra76–ra76.

Spomer, L., Gertzen, C.G.W., Schmitz, B., Häussinger, D., Gohlke, H., and Keitel, V. (2014). A membrane-proximal, C-terminal α-helix is required for plasma membrane localization and function of the G Protein-coupled receptor (GPCR) TGR5. J. Biol. Chem. *289*, 3689–3702.

Stahl, Y., Grabowski, S., Bleckmann, A., Kühnemuth, R., Weidtkamp-Peters, S., Pinto, K.G., Kirschner, G.K., Schmid, J.B., Wink, R.H., Hülsewede, A., et al. (2013). Moderation of Arabidopsis root stemness by CLAVATA1 and ARABIDOPSIS CRINKLY4 receptor kinase complexes. Curr. Biol. *23*, 362–371.

Stern, H.A., and Feller, S.E. (2003). Calculation of the dielectric permittivity profile for a nonuniform system: Application to a lipid bilayer simulation. J. Chem. Phys. *118*, 3401.

Stone, Trotochaud, Walker, and Clark (1998). Control of meristem development by CLAVATA1 receptor kinase and kinase-associated protein phosphatase interactions. Plant Physiol. *117*, 1217–1225.

Striker, G., Subramaniam, V., Seidel, C.A.M., and Volkmer, A. (1999). Photochromicity and Fluorescence Lifetimes of Green Fluorescent Protein. J. Phys. Chem. B *103*, 8612–8617.

Stryer, L., and Haugland, R.P. (1967). Energy transfer: a spectroscopic ruler. Proc. Natl. Acad. Sci. U. S. A. *58*, 719–726.

Sun, W., Cao, Y., Jansen Labby, K., Bittel, P., Boller, T., and Bent, A.F. (2012). Probing the Arabidopsis flagellin receptor: FLS2-FLS2 association and the contributions of specific domains to signaling function. Plant Cell *24*, 1096–1113.

Sun, Y., Day, R.N., and Periasamy, A. (2011). Investigating protein-protein interactions in living cells using fluorescence lifetime imaging microscopy. Nat. Protoc. *6*, 1324–1340.

Terrillon, S., and Bouvier, M. (2004). Roles of G-protein-coupled receptor dimerization. EMBO Rep. *5*, 30–34.

Thelen, M., Muñoz, L.M., Rodríguez-Frade, J.M., and Mellado, M. (2010). Chemokine receptor oligomerization: functional considerations. Curr. Opin. Pharmacol. *10*, 38–43.

Tramier, M., Gautier, I., Piolot, T., Ravalet, S., Kemnitz, K., Coppey, J., Durieux, C., Mignotte, V., and Coppey-Moisan, M. (2002). Picosecond-hetero-FRET microscopy to probe protein-protein interactions in live cells. Biophys. J. *83*, 3570–3577.

Tramier, M., Zahid, M., Mevel, J.-C., Masse, M.-J., and Coppey-Moisan, M. (2006).

Sensitivity of CFP/YFP and GFP/mCherry pairs to donor photobleaching on FRET determination by fluorescence lifetime imaging microscopy in living cells. Microsc. Res. Tech. *69*, 933–939.

Tsien, R.Y. (1998). The green fluorescent protein. Annu. Rev. Biochem. *67*, 509–544.

Unal, H., and Karnik, S.S. (2012). Domain coupling in GPCRs: the engine for induced conformational changes. Trends Pharmacol. Sci. *33*, 79–88.

Vestal, D.J., and Jeyaratnam, J. a (2011). The Guanylate-Binding Proteins: Emerging Insights into the Biochemical Properties and Functions of This Family of Large Interferon-Induced Guanosine Triphosphatase. J. Interf. Cytokine Res. *31*, 89–97.

Vestal, D.J., Gorbacheva, V.Y., and Sen, G.C. (2000). Different Subcellular Localizations for the Related Interferon-Induced GTPases, MuGBP-1 and MuGBP-2: Implications for Different Functions? J. Interf. Cytokine Res. *20*, 991–1000.

Vinogradov, S.A., and Wilson, D.F. (2000). Recursive Maximum Entropy Algorithm and its Application to the Luminescence Lifetime Distribution Recovery. Appl. Spectrosc. *54*, 849–855.

Vogel, S.S., Nguyen, T.A., van der Meer, B.W., and Blank, P.S. (2012). The impact of heterogeneity and dark acceptor states on FRET: implications for using fluorescent protein donors and acceptors. PLoS One *7*, e49593.

Vöpel, T., Hengstenberg, C.S., Peulen, T., Ajaj, Y., Seidel, C.A.M., Herrmann, C., and Klare, J.P. (2014). Triphosphate induced dimerization of human guanylate binding protein 1 involves association of the C-terminal helices: a joint double electron-electron resonance and FRET study. Biochemistry *53*, 4590–4600.

Wales, D.J. (2004). Energy Landscapes: Applications to Clusters, Biomolecules and Glasses (Cambridge, UK: Cambridge Molecular Science).

Wang, J., Wolf, R.M., Caldwell, J.W., Kollman, P.A., and Case, D.A. (2004). Development and testing of a general amber force field. J. Comput. Chem. *25*, 1157–1174.

Weidtkamp-Peters, S., Felekyan, S., Bleckmann, A., Simon, R., Becker, W., Kühnemuth, R., and Seidel, C.A.M. (2009). Multiparameter fluorescence image spectroscopy to study molecular interactions. Photochem. Photobiol. Sci. *8*, 470–480.

White, J.F., Noinaj, N., Shibata, Y., Love, J., Kloss, B., Xu, F., Gvozdenovic-Jeremic, J., Shah, P., Shiloach, J., Tate, C.G., et al. (2012). Structure of the agonist-bound neurotensin receptor. Nature *490*, 508–513.

Whorton, M.R., Jastrzebska, B., Park, P.S.-H., Fotiadis, D., Engel, A., Palczewski, K., and Sunahara, R.K. (2008). Efficient Coupling of Transducin to Monomeric Rhodopsin in a Phospholipid Bilayer. J. Biol. Chem. *283*, 4387–4394.

Widengren, J., Kudryavtsev, V., Antonik, M., Berger, S., Gerken, M., and Seidel, C.A.M. (2006). Single-molecule detection and identification of multiple species by multiparameter fluorescence detection. Anal. Chem. *78*, 2039–2050.

Wu, B., Chen, Y., and Müller, J.D. (2009). Fluorescence fluctuation spectroscopy of mCherry in living cells. Biophys. J. *96*, 2391–2404.

Wu, B., Chien, E.Y.T., Mol, C.D., Fenalti, G., Liu, W., Katritch, V., Abagyan, R., Brooun, A., Wells, P., Bi, F.C., et al. (2010). Structures of the CXCR4 chemokine GPCR with small-molecule and cyclic peptide antagonists. Science *330*, 1066–1071.

Wu, H., Wacker, D., Mileni, M., Katritch, V., Han, G.W., Vardy, E., Liu, W., Thompson, A.A., Huang, X.-P., Carroll, F.I., et al. (2012). Structure of the human κ-opioid receptor in complex with JDTic. Nature *485*, 327–332.

Yamamoto, M., Okuyama, M., Ma, J.S., Kimura, T., Kamiyama, N., Saiga, H., Ohshima, J., Sasai, M., Kayama, H., Okamoto, T., et al. (2012). A cluster of interferon-γ-inducible p65 gtpases plays a critical role in host defense against toxoplasma gondii. Immunity *37*, 302–313.

Yu, D.D., Sousa, K.M., Mattern, D.L., Wagner, J., Fu, X., Vaidehi, N., Forman, B.M., and Huang, W. (2015). Stereoselective synthesis, biological evaluation, and modeling of novel bile acid-derived G-protein coupled Bile acid receptor 1 (GP-BAR1, TGR5) agonists. Bioorg. Med. Chem. *23*, 1613–1628.

Yu, L.P., Miller, A.K., and Clark, S.E. (2003). POLTERGEIST encodes a protein phosphatase 2C that regulates CLAVATA pathways controlling stem cell identity at Arabidopsis shoot and flower meristems. Curr. Biol. *13*, 179–188.

Zhao, Y., Ferguson, D.J.P., Wilson, D., Howard, J.C., Sibley, L.D., and Yap, G.S. (2010). Virulent Toxoplasma gondii Evade Immunity-Related GTPase (IRG)-Mediated Parasite Vacuole Disruption Within Primed Macrophages. J Immunol *182*, 3775–3781.

Zhao, Y.O., Khaminets, A., Hunn, J.P., and Howard, J.C. (2009). Disruption of the Toxoplasma gondii parasitophorous vacuole by IFN??-inducible immunity-related GTPases (IRG proteins) triggers necrotic cell death. PLoS Pathog. *5*.

Zhao, Z., Fux, B., Goodwin, M., Dunay, I.R., Strong, D., Miller, B.C., Cadwell, K., Delgado, M.A., Ponpuak, M., Green, K.G., et al. (2008). Autophagosome-Independent Essential Function for the Autophagy Protein Atg5 in Cellular Immunity to Intracellular Pathogens. Cell Host Microbe *4*, 458–469.

Abbreviations

A	acceptor fluorophore
aa	amino aicd
AC	adenylate cyclase
APB	acceptor photobleaching
APD	avalanche photodiode
AS1, AS2	ASYMMETRIC LEAVES 1, 2
AV	accessible volume
A. thaliana	*Arabidopsis thaliana*
BAK1	BRI1-ASSOCIATED KINASE 1 (BRI1:brassinosteroid-insensitive 1)
BFGS	Broyden–Fletcher–Goldfarb–Shanno
BR	brassinosteroid
BRET	bioluminescence resonance energy transfer
cAMP	cyclic adenosine monophosphate
Co-IP	co- immunoprecipitation
CLE	CLAVATA 3/ENDOSPERM SURROUNDING REGION
CLV	CLAVATA
CREs	cAMP-responsive elements
CRN	CORYNE
CRNΔKi	CRN kinase
CYP5	CYCLOPHILIN 5
Cy3B	Cyanine 3B
D	donor fluorophore
DIC	differential interference contrast

EGFR	EPIDERMAL GROWTH FACTOR RECEPTOR
ER	endoplasmic reticulum
FACS	fluorescence-activated cell sorting
FCCS	fluorescence cross correlation spectroscopy
FCS	fluorescence correlation spectroscopy
FIDA	fluorescence intensity distribution analysis
flg	flagellin
FLIM	fluorescence lifetime image microscopy
FLS2	FLAGELLIN-SENSITIVE 2
FP	fluorescent protein
FRAP	fluorescence recovery after photobleaching
FRET	Förster resonance energy transfer
GBP	guanylate binding protein
GDP	guanosine diphosphate
GFP	green fluorescent protein
GMP	guanosine monophosphate
GPCR	G-PROTEIN COUPLED RECEPTOR
GTP	guanosine triphosphate
hGBP	human guanylate binding protein
ICL	intracellular loop
IFNγ	interferon gamma
IP	immunoprecipitation
IRG	immunity related guanosine triphosphatase
JLO	JAGGED LATERAL ORGAN
kcpm	kilo-count per molecule
LRR	leucine-rich repeat
MAPK	mitogen-activated protein kinase

MC	Monte Carlo
mCherry	A red fluorescent protein. m: monomeric
MD	molecular dynamics
MEFs	mouse embryonic fibroblasts
MFD	multiparameter fluorescence detection
MFIS	multiparameter fluorescence image spectroscopy
mGBP	murine guanylate binding protein
MLE	maximum likelihood estimator
NRG	neuregulin
N. benthamiana	*Nicotiana benthamiana*
OC	organizing center
ppp	photon per pixel
PVM	parasitophorous vacuole membrane
Rh110	Rhodamine 110
RLK	receptor-like kinase
s.e.m.	standard error of the mean
s.d.	standard deviation
TC	taurocholate
TCSPC	time-correlated single photon counting
TE	thermodynamic ensemble
TIRFM	total internal reflection fluorescence microscopy
TLC	taurolithocholic acid
TM	transmembrane
T. gondii	*Toxoplasma gondii*
VLS	vesicle-like structures
WLC	worm-like chain
WT	wild type

WUS	WUSCHEL
YFP	yellow fluorescent protein

Nomenclature

$[A]$	total concentration of unbound acceptor proteins
$[A]_0$	total concentration of acceptor proteins
$ap\ E\%$	apparent FRET efficiency determined via acceptor photobleaching
α	spectral cross-talk from donor detection channel to acceptor detection channel
a_l	intensity-weighted fractional contribution of the l-th component of FRET rate constants
B	background signal intensity
$b_{sc}(t)$	time-resolved scattered background signal
b_l	amplitude of the l-th decay component in time-resolved anisotropy
c or C	concentration
χ_r^2	reduced fitting residue
$[D]_0$	total concentration of donor proteins
$[DA]$	total concentration of donor-acceptor protein complexes
DE	direct acceptor excitation
DE_{rel}	relative acceptor brightness from direct acceptor excitation
E	steady-state FRET efficiency
$E_{effective,conf}$	effective conformational energy
$\varepsilon_{(D,A)}(t)$	FRET-induced donor decay of FRET-active species
$\varepsilon_{mix}(t)$	FRET-induced donor decay of FRET sample

f	laser repetition rate
$f_B(t)$	time-resolved auto-fluorescence signal
$f_\perp(t)$	time-resolved fluorescence intensity of the perpendicular detection channel
$f_\parallel(t)$	time-resolved fluorescence intensity of the parallel detection channel
$f_{(D,0)}(t)$	time-resolved fluorescence intensity of donor-only sample
$f_{(D,\mathrm{A})}(t)$	time-resolved fluorescence intensity of FRET-active species
F	fluorescence intensity
$F_{em,ex}$	$\mathrm{F_{G,G}}$: fluorescence intensity in green detection channels under green excitation, simplified as $\mathrm{F_G}$
	$\mathrm{F_{R,G}}$: fluorescence intensity in red detection channels under green excitation, simplified as $\mathrm{F_R}$
	$\mathrm{F_{Y,G}}$: same as $\mathrm{F_{R,G}}$
	$\mathrm{F_{R,R}}$: fluorescence intensity in red detection channels under red excitation
	$\mathrm{F_{G,R}}$: fluorescence intensity detected in green channels under red excitation
	$\mathrm{F_{Y,Y}}$: same as $\mathrm{F_{R,R}}$
F_D	donor fluorescence intensity
F_A	Intensity of FRET-sensitized acceptor emission
k	rate constant [s^{-1}]
k_D	dissociation constant
$k_{D,app}$	apparent dissociation constant
$k_{D,\mathrm{dim}}$	dissociation constant of a dimer
$k_{D,olig}$	dissociation constant of an oligomer
k_{FRET}	rate constant of energy transfer from a donor to an acceptor fluorophore by FRET [s^{-1}]

$k_{FRET}^{(l)}$	the l-th rate constant of FRET-induced donor decay
$k_{Olig,s}$	FRET rate constant of a small oligomer
$k_{Olig,l}$	FRET rate constant of a large oligomer
$K_{\max}$	the maximum specific GTPase activitiy
κ^2	factor capturing the mutual transition dipole moment orientation
$\left\langle \kappa^2 \right\rangle$	average orientation factor
λ	wavelength [nm]
$l_1,\ l_2$	factors accounting for polarization mixing in a microscope objective
$\hat{\mu}_A,\ \hat{\mu}_D$	unit vector of an acceptor/donor transition dipole moment
Ω	the overall number of conformational states
NA	Avogadro constant (= 6,022·10-23 mol-1)
N	photon count
$\overline{N}$	average photon count
$\left\langle N_{oligo} \right\rangle$	average number of the mGBP2 oligomers
$\left\langle N_{mGBP2} \right\rangle$	average number of mGBP2 units per oligomer
$p(k_{di})$	FRET rate constant distribution of mGBP2 dimer complex
$p(k_{RET})$	probability density of the FRET rate constant
$p(R_{DAi})$	probability density of donor-acceptor distances
p	Pearson's coefficient
Q	brightness
	Q_{GFP} or Q_D: Brightness of a donor protein
	$Q_{mCherry}$ or Q_A: Brightness of an acceptor protein
	Q_{oligo}: Brightness of a protein oligomer

$\langle Q_{oligo} \rangle$	the average brightness of oligomers
Φ	fluorescence quantum yield
θ	fluorescence lifetime heterogeneity
θ_0	fluorescence lifetime heterogeneity in shot-noise limited condition
r	steady-state fluorescence anisotropy
r_D	steady-state donor fluorescence anisotropy
$\langle r_D \rangle_{loc}$	concentration-weighted averaged anisotropy in local area
r_0	fundamental anisotropy
$r(t)$	time-resolved anisotropy
$r_{mix}(t)$	time-resolved anisotropy of FRET sample
R	distance; ideal gas constant (= 8,31 J $mol^{-1}K^{-1}$)
R_0	Förster radius of a FRET pair [Å]
R_{DA}	distance between donor and acceptor fluorophores
$R_{DA,app}$	apparent distance between donor and acceptor fluorophores
$R_{DA,sim}$	simulated distance between donor and acceptor fluorophores
R_{mol}	mean radius of a mCherry in mCherry-mGBPs fusion protein
R_{sim}	distance between donor and acceptor proteins in simulations
ρ	rotational correlation time [ns]
ρ_l	the l-th rotational correlation time in time-resolved anisotropy decay
S	recorded fluorescence signal intensity
$S_{em,ex}$	$S_{G,G}$: signal intensity in green detection channels under green excitation, simplified as S_G $S_{R,G}$: signal intensity in red detection channels under green excitation, simplified as S_R

	$S_{Y,G}$: same as $S_{R,G}$
	$S_{R,R}$: signal intensity in red detection channels under red excitation
	$S_{G,R}$: signal intensity in green detection channels under red excitation
	$S_{Y,Y}$: same as $S_{R,R}$
$S_{G,G}^{m}$	corrected $S_{G,G}$ for detector dead-time
$S_{G,G}^{u}$	corrected $S_{G,G}$ for detector dead-time and FRET-induced donor quenching
σ	standard deviation
t	time
τ	fluorescence lifetime [ns]
$\tau_{D(0)}$	donor fluorescence lifetime of donor-only sample
$\tau_{D(A)}$	donor fluorescence lifetime of in presence of acceptors
$\langle \tau_{D} \rangle_{f}$	mean donor fluorescence-weighted lifetime:
	$\langle \tau_{D(0)} \rangle_{f}$: in the absence of acceptors
	$\langle \tau_{D(A)} \rangle_{f}$: in the presence of acceptors
$\langle \tau \rangle_{x}$	mean species-weighted fluorescence lifetime
$V_{\det - GFP}$, $V_{\det - mCherry}$	detection volume of GFP and mCherry
$w_{DA,appy}$	width of apparent donor-acceptor distance distribution
ϖ	laser angular frequency
ϖ_{0}	$1/e^{2}$-radius in radial (x,y) direction [µm]
x	species fraction
$x_{D0}^{(m)}$	the m-th normalized pre-exponential factor of donor fluorescence intensity decay
$x_{(D,A)}$	species fraction of donor-acceptor complexes
x_{FRET}	species fraction of FRET-active donor-acceptor complexes

$x_{FRET}^{(l)}$	the l-th normalized pre-exponential factor of FRET-induced donor decay
$x_{FRET,s}(t)$	scaled fraction of FRET-active complexes at time t
$\langle x_{FRET}(t) \rangle_n$	mean fraction of FRET-active complexes of n cells at time t
x_{NoFRET}	species fraction of FRET-inactive donor-acceptor complexes
x_{mono}	species fraction of monomers
x_{di}	species fraction of dimers
x_{oligo}	species fraction of oligomers
z_0	1/e^2-radius in axial (z) direction [µm]

Hiermit erkläre ich, dass ich die Promotion mit dem Thema

“Protein interactions in living cells studied by multiparameter fluorescence imaging spectroscopy (MFIS)”

am Institut für Physikalische Chemie II der Heinrich-Heine- Universität Düsseldorf unter der Leitung von Prof. Dr. Claus A.M. Seidel eigenständig und ohne unerlaubte Hilfe angefertigt und in der vorgelegten oder in ähnlicher Form noch bei keiner anderen Institution eingereicht habe.

Es existieren keine vorherigen Promotionsversuche.

Düsseldorf, den 11.02.2016

Qijun Ma